NASA Conference Publication 3343

From Stardust to Planetesimals: Contributed Papers

Edited by
M. E. Kress, A. G. G. M. Tielens, and Y. J. Pendleton

Proceedings of a symposium
held in Santa Clara, California
June 24–26, 1996

NASA Conference Publication 3343

From Stardust to Planetesimals: Contributed Papers

Edited by
M. E. Kress, A. G. G. M. Tielens, and Y. J. Pendleton
Ames Research Center, Moffett Field, California

Proceedings of a symposium
held in Santa Clara, California
June 24–26, 1996

National Aeronautics and
Space Administration

Ames Research Center
Moffett Field, California 94035-1000

1996

PREFACE

On June 24 through 26, 1996, a scientific conference entitled *From Stardust to Planetesimals* was held at the Westin Hotel, Santa Clara, California, as part of the 108th annual meeting of the Astronomical Society of the Pacific. This conference was made possible by generous grants from the Astrophysics and Exobiology programs of the National Aeronautics and Space Administration, and support services rendered by the dedicated staffs of NASA Ames Research Center and the Astronomical Society of the Pacific.

Over the last decade, our understanding of the formation and early evolution of the solar System has advanced considerably due to progress that has been made simultaneously on many fronts. Stardust has been isolated in meteorites and interplanetary dust particles (IDPs), providing us with sample materials which predate the solar system and which offer clues to the processing that has occurred. At the same time, infrared studies have led to a better characterization of the composition of interstellar dust, which is now readily accepted as an important component of the interstellar medium. Infrared observations have also provided a much better view of the star-formation process and the role of dust therein. Recently, the presence of Kuiper Belt planetesimals has been confirmed and spectroscopy of these rather pristine objects may soon become available. Analysis of spacecraft data from the Comet Halley flybys has yielded a wealth of information on the composition of this comet. These observational advances have changed our understanding of planetesimal processing. The launch of the Infrared Space Observatory, the opening of 10-meter class telescopes, and, in the longer term, the Rosetta mission, promise to continue to broaden and deepen our understanding of the evolution from stardust to planetesimals.

For these reasons we considered it timely to organize a meeting focused on the processes that connect stardust and planetesimals. The goal of this meeting was, therefore, to bring together astronomers interested in star- and planet-formation, planetary scientists studying early solar system relics, laboratory scientists studying the processing of analogs, and scientists analyzing meteorites and interplanetary dust particles, grain by grain. As a result of this endeavor, over 200 participants, including 153 scientists from 14 different countries, gathered to discuss the origin and evolution of stardust. We hope that this encounter in Santa Clara will foster an ongoing interchange of information and ideas within this diverse group of scientists.

A major aim of this meeting was to produce conference proceedings which reflect the current situation regarding the evolution from stardust to planetesimals. This volume contains the contributed papers presented at the meeting. The invited review papers will be published separately in the Astronomical Society of the Pacific conference series. We extend special thanks to Greg Sloan, who produced the poster paper abstract book which was a tremendous asset during the meeting.

The conference was dedicated to three outstanding scientists whose untimely deaths left many hearts saddened. James Pollack, Akira Sakata, and Jason Cardelli each contributed significantly to the body of knowledge presented at this conference. Their scientific insight will be missed as we continue to explore the pathway From Stardust to Planetesimals. Tributes to their scientific achievements can be found in the proceedings book of the invited review papers. We thank the Local and Scientific Organizing Committees, NASA Ames Research Center, and the Astronomical Society of the Pacific for making this conference a rewarding endeavor.

M. E. Kress A. G. G. M. Tielens Y. J. Pendleton

Moffett Field, CA
November, 1996

SCIENTIFIC ORGANIZING COMMITTEE

P. Bodenheimer (University of California, Santa Cruz)
Alan Boss (Carnegie Institute, Washington)
Don Brownlee (University of Washington, Seattle)
John Kerridge (University of California, San Diego)
Michael Mumma (Goddard Space Flight Center)
Jane Luu (Harvard University, Boston)
Tobias Owen (University of Hawaii, Honolulu)
Yvonne Pendleton (NASA Ames Research Center, Chair)
T.P. Snow (Univeristy of Colorado, Boulder)
A.G.G.M. Tielens (NASA Ames Research Center)

LOCAL ORGANIZING COMMITTEE

Max Bernstein
Steven Charnley
Michael Kaufman
Monika Kress
Bill Latter
Brent Rogerville
Scott Sandford
Maureen Savage
Jeff Scargle
Greg Sloan
Dave Scimeca
Bob Walker
Juliet Wiesema
Sue Zabor

TABLE OF CONTENTS

page

Preface iii

Scientific and Local Organizing Committees iv

β PIC AND SIMILAR DISK-LIKE OBJECTS

Planetesimals around V536 AQL 3
N. Ageorges & W.J. Duschl

Modelling the dust around Vega-like stars 9
R.J. Sylvester, C.J. Skinner & M.J. Barlow

Examples of comet-like spectra among β Pic-like stars 13
H.M. Butner, H.J. Walker, D.H. Wooden & F.C. Witteborn

Partially crystalline silicate dust in protostellar disks 19
M.L. Sitko, D.K. Lynch, R.W. Russell, M.S. Hanner & C.A. Grady

High-resolution spectroscopy of Vega-like stars: abundances and circumstellar gas 23
S.K. Dunkin, M.J. Barlow & S.G. Ryan

Transient accretion events in Herbig Ae/Be star spectra: the evidence for infalling planetesimals in HD 100546 (B9e) 27
C.A. Grady, M.R. Pérez & K.S. Bjorkman

STAR FORMATION

The remarkable Herbig Ae star V351 Ori 33
M.E. van den Ancker, P.S. Thé & D. de Winter

Dust around Herbig Ae stars: additional constraints from their photometric and polarimetric variability 37
N.A. Krivova, V.B. Il'in & O. Fischer

An infrared study of the juggler nebula..... 41
J.C. Holbrook, P. Temi, D. Rank & J. Bregman

Imaging polarized dust emission in star formation regions with the OVRO mm array..... 45
R. Akeson & J. Carlstrom

The spectral energy distribution of HH 100 IRS 49
R. Siebenmorgen

Externally induced evaporation of young stellar disks in Orion 55
D. Johnstone, D. Hollenbach & F. Shu

CIRCUMSTELLAR DUST

The 11 μm silicon carbide feature in carbon star shells 61
A.K. Speck, M.J. Barlow & C.J. Skinner

On the classification of infrared spectra from circumstellar dust shells 65
G.C. Sloan, I.R. Little-Marenin & S.D. Price

Formation of cosmic carbon dust analogs in partially hydrogenated atmospheres 69
A. Blanco, S. Fonti, A.M. Muci & V Orofino

Time dependent models of grain formation around carbon stars 73
M.P. Egan & R.F. Shipman

The size distribution of stardust injected into the ISM 77
D. Krüger & E. Sedlmayer

Constraints on circumstellar dust grain sizes from high spatial resolution observations in the thermal infrared 81
E.E. Bloemhof, R.M. Danen & C.R. Gwinn

INTERSTELLAR DUST

Revised depletions and new constraints on interstellar dust composition 87
T.P. Snow & A.N. Witt

The interstellar polarization feature associated with the 2175 Å extinction bump 93
G.C. Clayton, M.J. Wolff, S.H. Kim, P.G. Martin & C.M. Anderson

Interstellar extinction, polarization, and grain alignment in high-latitude clouds 97
K.A. Larson & D.C.B. Whittet

The extinction properties of heavily-reddened lines of sight in the Galaxy 101
M.G. Rawlings, A.J. Adamson & D.C.B. Whittet

HAC: band gap, photoluminescence, and optical/near-infrared absorption 105
A.N. Witt, D. Ryutov & D.G. Furton

The role of hydrogen in small amorphous carbon grains: the IR spectrum 109
V. Mennella, L. Colangeli, C. Cecchi Pestellini, E. Palomba, P Palumbo, A. Rotundi & E. Bussoletti

Observations of two nonstandard grain components 113
R.F. Shipman, S.J. Carey & F.O. Clark

IRAS colors of the Pleiades 117
S.J. Carey, R.F. Shipman & F.O. Clark

PAH emission in the Orion Bar 121
J. Bregman & G.C. Sloan

Laboratory experiments on the reactions of PAH cations with molecules and atoms of interstellar interest 125
V. LePage, H.S. Lee, V.M. Bierbaum & T.P. Snow

Processing of icy mantles in protostellar envelopes 131
J.E. Chiar, D.C.B. Whittet, P.A. Gerakines, A.C.A. Boogert & A.J. Adamson

The ice and silicate spectral features for dust aggregates 135
A.E. Ilin

Evidence for the evolution of grain properties in the NGC 2024 star forming ridge 139
C.J. Chandler, J.E. Carlstrom, J.S. Richer, A. Visser & R. Padman

The abundances of charged particles in protostellar cores 143
S.J. Desch

THE PROTOSOLAR NEBULA

Catalysis by dust grains in the solar nebula 149
M.E. Kress & A.G.G.M. Tielens

Restructuring of dust aggregates in the solar nebula 155
C. Dominik & A.G.G.M. Tielens

Effect of dust coagulation dynamics on the geometry of aggregates 159
R. Nakamura

Self-consistent simulation of the Brownian stage of dust growth 163
S. Kempf, S. Pfalzner & Th. Henning

Dust coagulation in protoplanetary accretion disks 167
W. Schmitt, Th. Henning & R. Mucha

Size segregation and number density enhancement of particles in accretion disk eddies 171
H.H. Klahr & Th. Henning

From chondrules to planetesimals: solids and turbulence in the solar nebula .. 175
A. R. Dobrovolskis, J.S. Dacles-Mariani & J.N. Cuzzi

Vortices and planetesimals 179
P. Barge & J. Sommeria

The role of vortices in the formation of the solar system 183
A.V. Mehta & G.R. Flierl

The global perspective on the evolution of solids in a protoplanetary disk 187
T.F. Stepinski & P. Valageas

Toward an astrophysical theory of chondrites 191
H. Shang, F.H. Shu & T. Lee

Planetesimal formation in the outer solar nebula 195
K.D. Supulver

PLANETESIMALS AND COMETS

The mass of large impactors 201
M.G. Parisi & A. Brunini

Tidal breakup of asteroids by the earth and moon 205
D.C. Richardson & W.F. Bottke, Jr.

On the dynamics of the zodiacal dust cloud close to the sun 209
K. Scherer, I. Mann & G. Reaves

Dust and sputtered particle streams in cometary atmosphere 213
S.B. Svirschevsky

Preliminary results of observations of comets de Vico and Hyakutake by the Ulysses comet watch network 217
C.C. Petersen, J.C. Brandt & Y. Yi

Porosity and permeability of chondritic materials 221
M.E. Zolensky, C.M. Corrigan, J. Dahl & M. Long

Raman spectrum of quenched carbonaceous composite 227
S. Wada, S. Hayashi, H. Miyaoka & A.T. Tokunaga

Author Index 231

Subject Index 233

Object Index 237

Addresses of Participants 239

β PIC AND SIMILAR DISK-LIKE OBJECTS

PLANETESIMALS AROUND V536 AQL

N. AGEORGES *ESO, Karl-Schwarzschild-Straße 2, D-85748 Garching, Germany*
W. J. DUSCHL *ITA, Heidelberg & MPIfR, Bonn, Germany*

1. INTRODUCTION

The pre-main sequence star V536 Aql, classified as a K7 classical T Tauri star by Cohen & Kuhi (1979) has been resolved, by high angular resolution near-infrared speckle observations, as a close binary (0.52" separation at 17°) surrounded by extended structures (Ageorges et al. 1994). These structures seen, both in the July 1993 and April 1994 observations, are not at the same position in the reconstructed image (Fig. 2) and do not present exactly the same shape at both times. Altough it is unlikely that the presence of these structures is due to seeing calibration problems, the exact shape might be affected by it. We cannot presently make a final interpretation of the observations but can formulate different possibilities: the 'circumstellar' material seen in our images can be an independent cloud, or simply gas or dust, in front of the system on our line of sight, but close enough to still be illuminated by the binary; this material may be 'by chance' there or be a remnant of the material in which the star was born.

We propose a model to explain the position variation of the extended structures. New observations are under reduction and should help to determine the exact value of this motion. At their distance from the star, motions of the extended matter would correspond to velocities much higher than the Kepler velocities. To explain this, we have developed a model based on a 'torch-light' effect. The possibility that the observed elongated structures belong to a circumstellar or circumbinary disk are also discussed below.

2. OBSERVATIONS

Near-infrared observations

The observations were done with the near-infrared speckle camera SHARP (System for High Angular Resolution Pictures, Hofmann et al. 1995) installed at the ESO NTT (3.5 m telescope equipped with an active optic system). The detector of SHARP is a NICMOS 3, 256 × 256 pixels corresponding to a 12.8^{2}" field of view. The data were analysed using the MPE speckle reduction software package (Eckart & Duhoux 1990). We kept the frames obtained under the best similar seeing conditions for both the source and the reference (SAO 105091, used as point spread function to deconvolve the target source data), to accumulate both simple shift-and-add (SSA) images (Christou 1991) and power spectra. Images in all wavebands were obtained

by linear deconvolution of the SSA images and of the power spectrum followed by 200 Fienup iterations (Fienup 1982) with a loop gain of 0.3 and starting with phases taken from the deconvolved SSA images. To compensate for the somewhat distorted PSF in 1994, we use the northern component, noticed to be a point source at our resolution, as a refence star and did 200 Lucy deconvolution on the images. The images presented in Fig. 2 results from exactly the same data reduction procedure for both years.

10μm detection of an envelope
The 'torch-light' model need some circumstellar material around the source so that the light escaping through the 'tunnels' can be reflected. As this material is expected to be situated further from the stars, we expect it to reradiate at longer wavelengths (longer as near-infrared). So in a first attempt to detect it, we made 10μm observations, to the courtesy of Th. Henning & R. Launhardt, with the ESO-TIMMI camera (Käufl et al. 1994). The observations have been carried out in April 1996 at 10.10μm (N band). 28 frames have been acquired in chopping mode with a total integration time per frame on the source of 15.54s. The source HR6630 has been used as calibrator. Its image obtained with the same integration time is perfectly circular. The resulting 10.10 μm image for V536 Aql is presented in Fig. 1. This image clearly shows an extension with P.A. (major axis) $\approx 17 \pm 1°$, i.e the same direction as the position angle of the binary system. The size of this structure is of the order of a few 100AU. Further data reduction will give us the exact value.

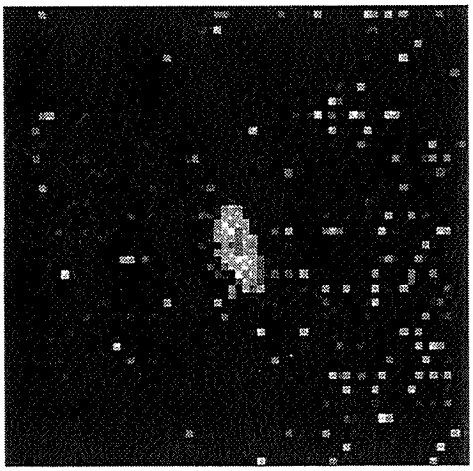

Figure 1. TIMMI 10μm image of V536 Aql. The field of view is 42.24× 42.24". The North is to the top and the East to the left. This image is the sum of 28 frames acquired in choping mode, each of which being integrated 15.5 sec. on source.

3. INTERPRETATION

Could the observed elongation be part of a circumbinary disk? Considerations on the spectral energy distribution (SED) assuming a circumbinary (CB) disk and heating of the dust by the system luminosity shows that one should investigate alternative explanations for the distribution of matter in the vicinity of V536 Aql. Indeed a CB disk would correspond to a peak of the SED around 70μm, which is not observed.

Could a circumstellar accretion disk exist about one or both of the stars?

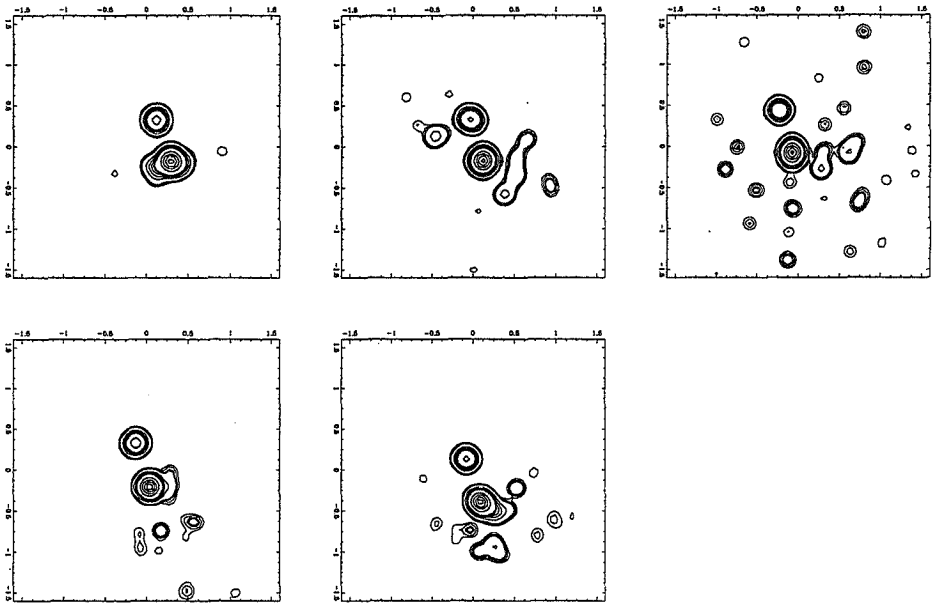

Figure 2. Contour plot of V536 Aql in J, H and K (from the left to the right) in August 1993 (above) and April 1994 (below). The contours are at: 0.5 - 1 - 2 - 3 - 4 - 5 - 6 - 7 - 8 - 9 - 10 - 50 and 100 % of the maximum peak value.

If we are dealing with a viscous accretion disk that liberates gravitational energy through dissipative processes, and if the disk masses are small compared to the respective central star's mass (see e.g. Beckwith 1994), we get local effective temperatures in the disk of:

$$T_{eff,disk}(r) = 150\,K \left(\frac{M_*}{M_\odot}\right)^{1/4} \left(\frac{\dot{M}}{10^{-7} M_\odot/yr}\right)^{1/4} \left(\frac{r}{1\,AU}\right)^{-3/4} \quad (1)$$

(M_*: mass of the accreting star; $\dot{M}$: mass accretion rate; r distance to the accretor). For pre-main sequence accretion disks, the mass flow rate is typically of the order of $10^{-7} M_\odot/yr$, leading to $T_{eff,disk}$ in the range of 150 K (at $r = 1\,AU$) to 10 K (at 40 AU). The bulk of the radiation of such an accretion disk will be observable in the sub-mm wavelength range. Thus the currently available observations do not allow us to confirm or to rule it out.

4. AN ALTERNATIVE EXPLANATION: OPTICALLY THICK CONDENSATIONS AROUND ONE OR BOTH COMPONENTS

4.1. Physical description of the model

Besides of the two stars, we have two more ingredients in our model that play important roles: spatially resolved circumstellar material that is visible and that shows strong indications for variability and optically thick condensations around one or both components of the binary system. In the following, we will simply call them 'blobs' or

'planetesimals'. Those ones are spatially unresolved. The variations in the distribution of the circumstellar material between the two observing epochs imply velocities much higher than the Kepler velocity. To explain this, our idea is that the variations are due to a 'torchlight effect', i.e. the radiation from at least one of the central stars proper can reach the circumstellar material only along some 'tunnels' along which it is not blocked by planetesimals that otherwise obscure the stars, absorbe the radiation and re-radiate it in the infrared (IR) spectral range. To get such an effect the number density of optically thick blobs has to be around unity along each individual radius from the stars. Only then one can expect that a sizeable fraction of the direct light is absorbed while there remains still a reasonably big chance for such tunnels to be present.

4.2. Working the model out

We envisage each of the two stars being surrounded by a spherically symmetric distribution (in a first approximation) of planetesimals. The individual blobs are assumed to be optically thick in all relevant wavelength regions, and to have all the same radius, R_{blob} (*free parameter*). For the following order of magnitude calculations we also assume the individual Roche lobes to be spherically symmetric of radius r_{RL} (Paczyński 1971). We get for the two components of V536Aql: $r_{RL,A} = 44\,AU$ and $r_{RL,B} = 32\,AU$, assuming a distance of 200 pc and using the mass, luminosity and stars'radius as derived by Ageorges et al. (1994). The blob distribution is assumed to range from an inner radius (*free parameter*) $r_i \geq R_*$ (R_*: stellar radius) to a fraction χ (*free parameter*) of the Roche Lobe's radius. As we will see later, its exact value is only of importance if $r_i \approx \chi r_{RL}$, i.e., if the blobs are confined to narrow radial range.

In the following, we treat a star with mass M_*, stellar radius R_*, and Roche lobe radius r_{RL}. We assume the number density $n(r)$ of the planetesimals to follow a power law distribution:

$$n(r) = n_0 \left(\frac{r}{r_0}\right)^{-x} \tag{2}$$

We identify r_0 with the inner radius of the distribution, $r_0 :=: r_i$, and we envisage the sky above the star to be almost fully covered by blobs. This allows us to estimate the coverage fraction $y_{tot} \approx 1$. For the given blob distribution $n(r)$ we then, after some algebra, get for the total number of planetesimals N within the Roche lobe around the star:

$N = \int_{r_i}^{\chi r_{RL}} 4\pi r^2 n(r) dr = 4\pi n_0 r_i^x \int_{r_i}^{\chi r_{RL}} r^{2-x} dr$ and for the fraction Φ of the Roche Lobe's volume occupied by blobs:

$$\Phi = \frac{4\beta\delta}{r_{RL}^2} \frac{\int_{r_i}^{\chi r_{RL}} r^{2-x} dr}{\int_{r_i}^{\chi r_{RL}} r^{-x} dr} \tag{3}$$

Here, we introduced $r_i = \delta r_{RL}$ and $R_{Blob} = \beta r_i$. Φ has to be considerably smaller than unity. If Φ were comparable to unity, we would not have the situation of a star with a cloud of planetesimals around it but rather a very extended atmosphere filling almost all of the Roche Lobe. There are no observational indications for such a configuration in V536 Aql.

The characteristic angular frequency ω_{char} of a blob about the star is given by $(\omega_{Kepler}(r) = \sqrt{GM_* r^{-3}})$

$$\omega_{char} = \frac{1}{N} \int_{r_i}^{\chi r_{RL}} 4\pi r^2 \omega_{Kepler}(r) n(r) dr \quad (4)$$

As all blobs individually rotate with Keplerian angular frequency, the typical distance r_ω of a blob from the star is

$$r_\omega = \left(\frac{GM_*}{\omega_{char}^2} \right)^{1/3} \quad (5)$$

The characteristic radius r_ω is determined by weighing the distribution $n(r)$ with the angular frequency. This is the typical radius for describing the motion of the planetesimals. We regard v_ω as the velocity that is also characteristic for the motion of the 'tunnels' through which stellar light reaches the circumstellar dust directly.

4.3. Results for the Dynamics

In Fig 3 is an example of a typical model for component A.

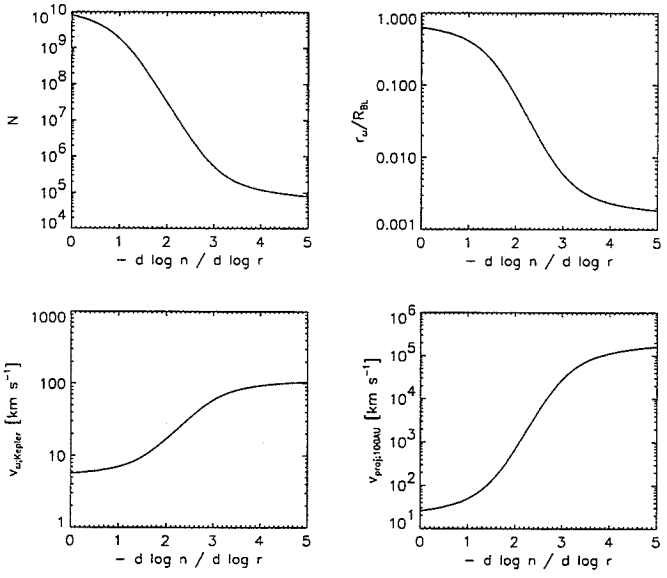

Figure 3. Results of model calculations for a planetesimal distribution around a $0.8M_\odot$, 4.8 $R_\odot$ star (typical for V536 Aql-A). The blob distribution extends from 2 R_* to 35.2 AU. The planetesimals have radii of $10^{-2}R_*$. We give as a function of $x = -d\log n/d\log r$ the total number of blobs (N, top left), the typical distance of planetesimals from the star (r_ω/R_{RL}; top right), their characteristic Keplerian velocity ($r_\omega\omega_{char}$; bottom left) and their projected velocity at 100AU (bottom right). We achieve the required projected velocity of $\approx$ 500 km/s for x$\approx$ 1.9. This places the planetesimals characteristically to a distance $r_\omega \approx$ 3.1 AU.

The general characteristics of the solutions can be summarized as follows:

- Projected velocities at projected distances of the order of 10^2 AU ($v_{proj,100\,AU}$) amount to several 10^2 km/s.

  This leads to an exponent $x \approx -2$ for the radial number distribution of blobs. This in turn indicates a characteristic radius of the distribution of planetesimals of a few percent of r_{RL}, i.e., of the order of a few AU. This is consistent with the extent of the 'stars' in the NIR observations. For the model shown in Fig 3 we get $x \approx 1.9$, $r_\omega \approx 3.1$ AU.

- Variations of the size of the blobs does not really modify the results. The only difference is the number of the planetesimals and their filling factor.
- The fraction χ of the Roche Lobe radius over which the blobs are distributed is only of importance if χr_{RL} becomes small enough to enforce small r_ω and, in turn, large $v_{proj,100\,AU}$. As long as χ is not too different from unity, its actual value is not of great importance.
- For a different stellar mass and radius (corresponding to component B of V536 Aql) the results are very similar.

An independent 'order of magnitude' check can be obtained from a study of the energetics of the system. The observed maximum of the SED, in the far IR, at $\approx$ 18 μm leads to a blob temperature of the order of 200K. Energy conservation and equipartition arguments then give characteristic distances, r_{FIR}, between each of the two stars and the respective blob distributions of $\approx$ 10AU. This is in remarkable good agreement with $r_\omega \approx 3.1$ AU as deduced from the dynamics of the system.

References

Ageorges N., Ménard F., Monin J.L., Eckart A., 1994, Å, **283**, L5

Ageorges N., 1995, PhD Thesis of the University Paris VII.

Bastien P.,Landstreet J.D., 1979, *Ap. J.*, **229**, L137

Beckwith S.V.W., 1994, in *Theory of accretion disk – 2*, eds. W.J. Duschl et al., (Dordrecht: Kluwer), p. 1

Christou J.C., 1991, Experimental Astr., **2**, 27

Cohen M., Kuhi L.V., 1979, *Ap. J. Suppl.*, **41**, 743

Eckart A., Duhoux P.R.M., 1990, in *Astrophysics with infrared arrays*, eds. Elston R., Astronomical Society of the Pacific Conference Series, p. 336

Fienup J.R., 1982, Applied Optics, **21**, 2758

Hofmann R. et al., 1995, in *SPIE international symposium, Infraed detectors and instrumentation for astronomy*, in press

Käufl H.U. et al., 1994, Infrared Phys. Tech., **35**, 203

Paczyński B., 1971, ARA&A, **9**, 183

MODELLING THE DUST AROUND VEGA-LIKE STARS

ROGER J. SYLVESTER *Department of Physics and Astronomy, University College London, Gower Street, London WC1E 6BT, UK*
C.J. SKINNER *Space Telescope Science Institute, 3700 San Martin Drive, Baltimore, MD21218, USA*
M.J. BARLOW *Department of Physics and Astronomy, University College London, Gower Street, London WC1E 6BT, UK*

ABSTRACT. Models are presented of four Vega-like stars: main-sequence stars with infrared emission from circumstellar dust. The dusty environments of the four stars are rather diverse, as shown by their spectral energy distributions. Good fits to the observations were obtained for all four stars.

1. INTRODUCTION

Vega-like stars are main-sequence stars with excess mid- and far-infrared emission due to circumstellar dust, which is thought to be distributed in discs. We have recently undertaken an observational survey of Vega-like stars, taken mainly from the list of Walker & Wolstencroft (1988). Our observations include optical, near-IR and millimetre-wave photometry, and mid-IR spectroscopy (Sylvester et al 1996). Similar observations of a number of these sources have also been published by Walker & Butner (1995) and Butner et al (1996). In parallel with our observing programme, we have modelled several of our targets using a radiative transfer code based on that developed by Skinner, Barlow & Justtanont (1992) to model SAO 179815 (=HD 98800).

2. TECHNIQUE AND RESULTS

The model uses multiple grain sizes (typically 15 sizes are used) and dust materials (usually silicate and/or amorphous carbon). Power laws are used to describe the grain-size distribution and the variation of dust density in the disc with distance from the star. The power-law indices are treated as free parameters. The grain optical properties, such as absorption efficiency, are calculated from the bulk optical constants using Mie theory, and the discs are treated as optically thin. Some results of the modelling are presented in Table 1 and Figures 1–4. A fuller account of the model technique and results may be found in Sylvester & Skinner (1996).

The four stars presented here have rather different spectral energy distributions (SEDs), and give some idea of the variety of properties displayed by Vega-like stars. SAO 158350 has the smallest fractional excess luminosity ($L_{\rm exc}/L_*$), and the smallest derived dust mass (see Table 1). Its mid-IR spectrum is consistent with there being

Table 1 Best-fitting model parameters for four Vega-like stars. Tabulated are star names and spectral types, grain size distribution power-law index (α), density distribution power-law index (β), inner and outer disc radii, and the dust mass. The minimum grain size was 50Å, and the maximum grain size was 1mm (0.1mm for SAO 140789).

SAO	HD	Spectral Type	α	β	$R_{\rm in}$ (AU)	$R_{\rm out}$ (AU)	$M_{\rm disc}$ ($M_\odot$)
140789	141569	A0Ve	4	2	670	5700	7×10^{-6}
158350	123160	G5	4	3	190	470	1×10^{-7}
179815	98800	K5Ve	3.2	1.6	1.1	230	4×10^{-7}
184124	144432	A9/F0Ve	3	1.3	4.0	1100	2×10^{-5}

only photospheric emission in the 10-μm region. The predicted mm-wave flux is greater than the observed upper limits obtained with the JCMT; however, when the model flux is convolved with the 20-arcsec JCMT beam, the predicted in-beam flux is consistent with the observations.

SAO 140789 shows UIR-band emission in its mid-IR spectrum, ascribed to PAH-like hydrocarbon species. No attempt was made to model these emission features; a good fit to the other observations was obtained (see Figure 2).

SAO 179815 (HD 98800) was found by Skinner, Barlow, and Justtanont (1992) to show silicate emission at 10 μm. The model presented in Figure 3 is generally similar to their model. As noted by Torres et al (1995), the visual companion star to SAO 179815 may pass through the predicted location of the disc, if it is on a bound orbit.

SAO 184124 has the largest fractional excess luminosity, and the largest derived dust mass of the four stars presented here. Its SED shows excess near-IR emission and a strong silicate feature. It was found that no single combination of size and spatial density power-law distributions could provide a fit to the entire optical-mm SED. The use of a second component of small, hot silicate grains allowed a good fit to be made to all the data. The effect of adding this component is shown in Figure 4. Given the large dust luminosity, it is possible that optical depth effects should be taken into account when modelling this source.

References

Butner, H. M., et al., 1996, this volume.

Skinner, C. J. Barlow, M.J., and Justtanont, K., 1992, *M. N. R. A. S.*, **255**, 31P.

Sylvester, R. J., and Skinner, C. J., 1996, *M. N. R. A. S.*, in press.

Sylvester, R. J., Skinner, C. J., Barlow, M.J., and Mannings, V., *M. N. R. A. S.*, **279**, 915.

Torres, G., Stefanik, R. P., Latham, D. W., and Mazeh, T., 1995, *Ap. J.*, **452**, 870.

Walker, H. J., and Butner, H. M., 1995, *Ap. Space Sci.*, **224**, 389.

Walker, H. J., and Wolstencroft, R. D., 1988, *Pub. A. S. P.*, **100** 1509.

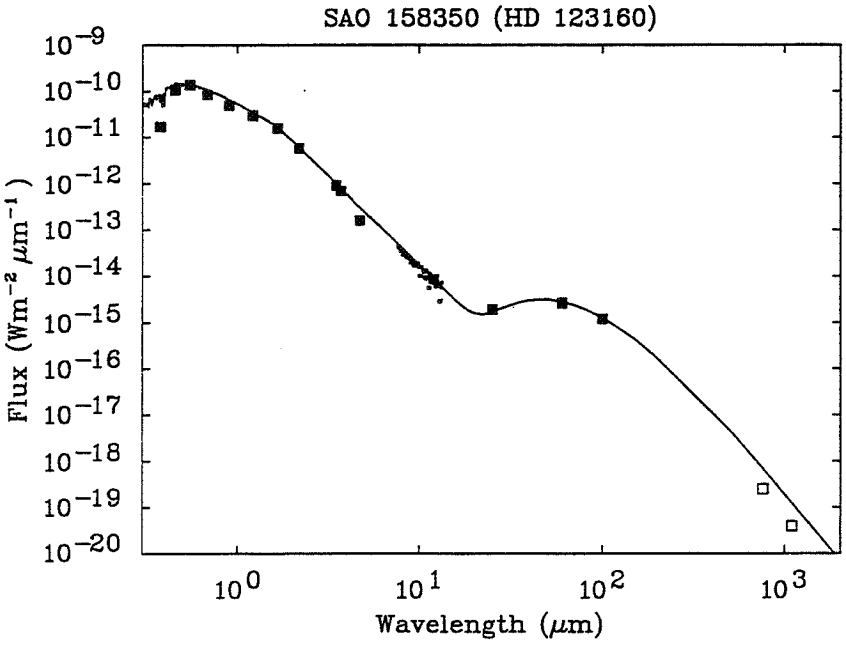

Figure 1. Model fit to the spectral energy distribution (SED) of SAO 158350. Large filled squares: photometric data, open squares: upper limits, small squares: UKIRT-CGS3 spectrum, line: model fit.

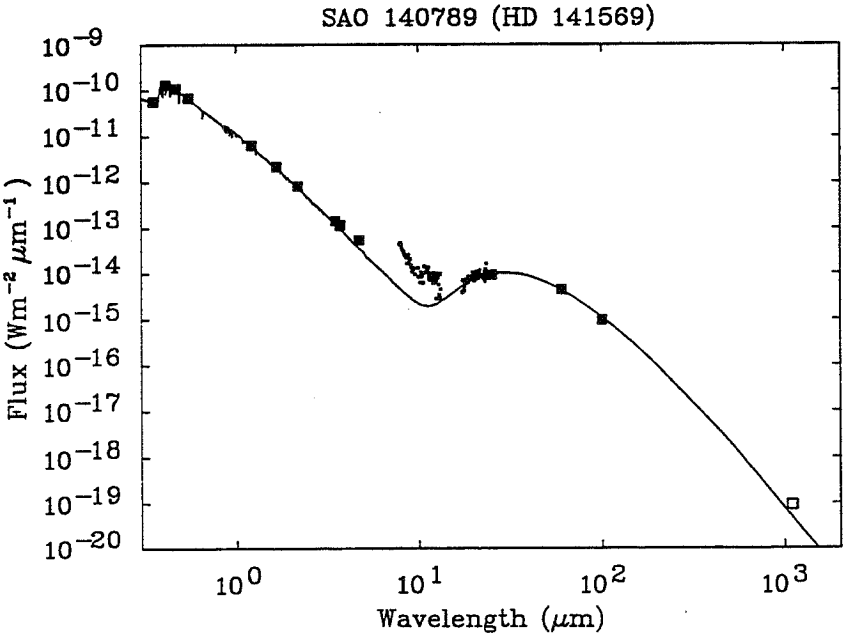

Figure 2. Model fit to the SED of SAO 140789. Symbols as for Figure 1.

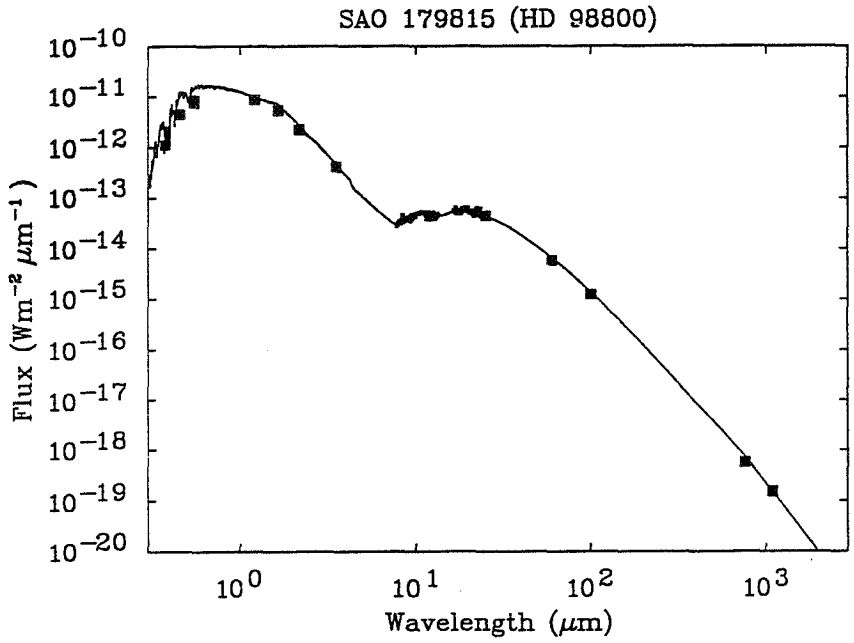

Figure 3. Model fit for SAO 179815 (HD 98800). Weak silicate emission peaks are seen at 10 and 18 μm.

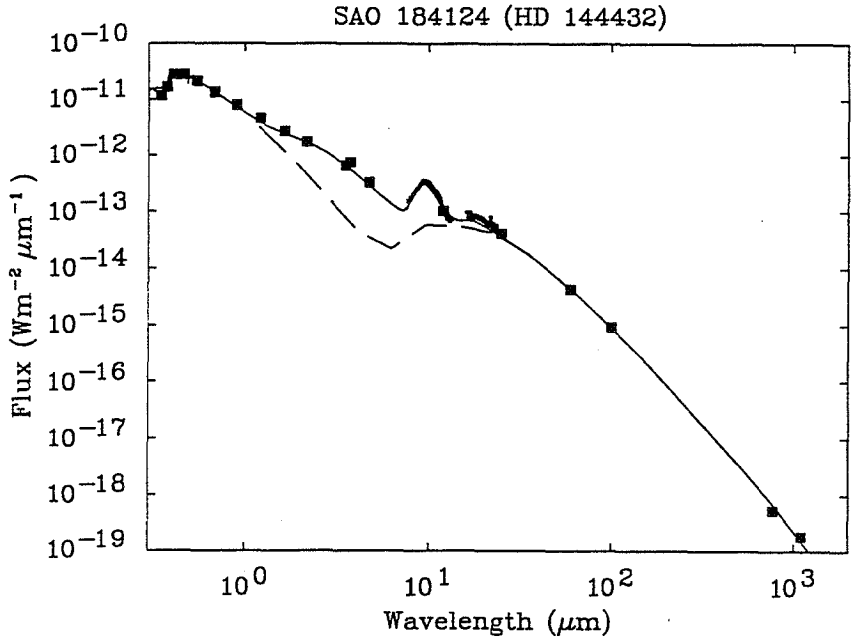

Figure 4. Model fit for SAO 184124. Symbols as for Figure 1; the dashed line shows the model without the additional hot component. See text for details

EXAMPLES OF COMET-LIKE SPECTRA AMONG β PIC-LIKE STARS

H. M. BUTNER *DTM Carnegie Inst. of Washington, Washington, DC, USA*
H. J. WALKER *CLRC Rutherford Appleton Laboratory, Didcot, UK*
D. H. WOODEN *NASA Ames Research Center, Moffett Field, CA, USA*
F. C. WITTEBORN *NASA Ames Research Center, Moffett Field, CA, USA*

ABSTRACT. β Pic is a nearby main-sequence star with an extended dust disk, large infrared excess, and mid-infrared emission similar to that seen in some cometary spectra. We selected a sample of stars whose infrared properties resemble β Pic and obtained 8 to 13 μm spectra (resolution 200). We find a variety of silicate emission features among the stars in our sample, ranging from classic interstellar dust features to spectra similar to that of comet P/Halley and and the laboratory spectra of Interplanetary Dust Particles (IDPs).

1. INTRODUCTION

In 1984, a new class of stars was identified by IRAS. These stars, named Vega-like stars after their prototype (Vega), were first classified as main-sequence stars with significant excess infrared emission. The infrared emission was consistent with that expected from thermal emission from dust grains surrounding the stars. The lack of optical extinction and large infrared excesses suggested that the emission might arise from dust arranged in a disk-like geometry as opposed to a spherical distribution. Visual images of β Pic (Smith and Terrile 1984) dramatically confirmed the disk hypothesis, revealing a disk radius in excess of 200 AU. More recently, β Pic has been imaged at a variety of wavelengths ranging from the optical (Burrows *et al.* 1996) to 10 μm (Lagage and Pantin (1994).

Other Vega-like stars have been identified in the IRAS database (Aumann 1985, Walker and Wolstencroft 1988). The traditional method is to examine a sample of stars (such as all A-stars within 25 parsecs) for evidence of excess emission in the IRAS bands. Most of the stars identified have turned out to have very small excesses compared to the proto-types, making them difficult to study. See Backman and Paresce (1993) for a review of these objects. Among the many areas of study is the actual age of individual Vega-like candidates. For example, β Pic might be as young as 10 million years old (Jura *et al.* 1993), though the age estimates are far from certain. Even if these disk systems turn out to be younger than initially thought, they represent a unique opportunity to study actual disks around nearby stars.

2. β Pic-like SYSTEMS

One of the great difficulties in studying Vega-like systems is that by and large the disks are not very massive. In addition, even among the proto-types, 3 out of 4 have excess emission only at wavelengths longer than 20 μm. The lack of 12 μm emission indicates that the dust is very cold, and the disk is probably does not extend close to the star. The obvious exception is β Pic where the disk is massive, extends close to the central star, and is oriented edge-on (favorable for study by earth-based observers). It is thus no surprise that searches for other disk systems has proved difficult. For example, numerous optical searches have failed to find counterparts among other suspected Vega-like stars to the disk seen around β Pic.

One possibility is to restrict one's observational program to systems that are β Pic-like, not just Vega-like. Walker and Wolstencroft (1988-henceforth WW) identified a number of candidates with significant infrared excess similar to β Pic. Most of these are at distances further away than β Pic itself. The larger distances imply that the disks surrounding these stars are likely to be more massive than β Pic. As part of a multi-wavelength program, we have selected a number of WW-stars for followup studies at 10 μm.

3. SILICATE EMISSION

Of particular interest is the 8 - 13 μm region. This wavelength region is accessible from the ground and has a number of spectral features that can be used to study the dust composition. One of the most important is the silicate feature at 10 μm. The feature is a band that arises due to the presence of silicates in the dust. Such features have been seen in either absorption or emission towards a number of astronomical objects, including M-stars, young stars, and comets. In absorption, the silicate feature traces the presence of cold dust projected against a bright background. In emission, it indicates hot dust grains are present and that the dust is optically thin.

The silicate emission feature can be used to study the composition of the silicate grains. If crystalline silicates are present, the feature has a much different shape than in the case of an amphorous mixture. Observations of comets such as P/Halley and P/Bradfield 1987 revealed a twin peaked structure seen in laboratory spectra of interplanetary dust particles (IDPs - Bradley *et al.* 1992), but not not seen in most interstellar sources (Bregman *et al.* 1987, Hanner *et al.* 1993). In the case of β Pic, silicate emission was first detected in its disk by Telesco and Knacke (1991) using spectrophometry. They compared the feature they found with the Halley spectra, and found a plausible match. More recent spectra of β Pic were taken by Knacke *et al.* (1993) to a variety of astronomical and cometary spectra. They found that the cometary and IDP spectra matched best.

4. OBSERVATIONS

To study the mid-infrared spectra of the WW-sample, we used the NASA Ames HIFOGS (High Resolution Faint Object Grating Spectrograph) at the NASA 3 meter IRTF (Infrared Telescope Facility). HIFOGS works in the region of 8 to 13 μm, see Witteborn *et al.* (1991) for a full description. There are 120 detectors, covering the 8 to 13 μm atmospherice window, with a spectral resolution of 0.05 μm/pixel. In June

1995, we observed 6 stars from the WW list. Weather conditions were very good, with little or no problems from cirrus. To calibrate the data, we observed known spectral standards and applied additional corrections to correct for the atmospheric transmission (such as the 10 μm ozone feature). Overall the stability from one night to the next was excellent. Our general procedure is to observe one grating setting on one night. The setting then is shifted slightly (to fill in gaps caused by bad pixels) and the observations repeated the second night. This allows us to have two independent spectra that can then be interweaved to provide Nyquist sampling.

5. DISCUSSION

We observed α PsA, β Cas, HD 188037, HD 14432, HD 142666, and 51 Oph. Both α PsA and β Cas show no evidence of silicate features but a hint of the onset of a thermal dust continuum at 12 μm. HD 188037 has been reported to have an M star companion, which would explain the observed "astronomical" silicate feature we see. HD 144432 has a feature reminiscent of that seen towards GW Ori (a binary young stellar object thought to have disk). HD 142666 has a broad silicate feature, similar to that that Sylvester *et al.* (1995) report for HD 98800. Our data show no examples of PAH-like emission features, though Sylvester *et al.* report PAH features for three other sources (HD 169142, HD135344, and HD 141596).

51 Oph, thought to be a Be star with a dust disk, was reported by Fajardo-Acosta *et al.* (1993) to have silicate emission features similar to β Pic and comet P/Halley. They found that the dust around 51 Oph was warmer than β Pic and argued that the grains would be larger than the grains around β Pic. Sylvester *et al.* (1995) also observed 51 Oph, but make no comment about the emission other than to note it is silicate emission. Our own data has been carefully reduced, and a 550 K blackbody removed from the continuum. The feature appears to have an unusual broad shoulder in the emission beyond 10 μm (Figure 1). One of the glass-rich IDPs discussed by Bradley *et al.* (1992) is similar to the 51 Oph spectra. We applied similar continuum removal to the HD 142666 and HD 144432 spectra and find prominent bumps in both spectra at 11 μm. Comparison of the 51 Oph, HD 142666, and HD 144432 spectra with examples of cometary spectra (Hanner *et al.* 1993) shows that the P/Halley and P/Bradfield-87 spectra are very simlar. A detailed analysis of the spectral features for each star awaits full models, but it would appear that we can use the comets and IDPs as analogs for the average silicate dust found in some of these systems.

The results to date suggest that many of the β Pic-like stars have dust that has undergone processing similar to that seen in cometary dust.

Acknowledgements. HMB wishes to acknowledge the support of the NASA Origins of the Solar System Program (NAGW-4097) and the Carnegie Institution of Washington.

References

Aumann, H. 1985, *Pub. A. S. P.*, **97**, 885.

Backman, D. E., and Paresce, F. 1993, in Protostars and Planets III, eds. E. H. Levy, J. I. Lunine, and M. S. Matthews, (Univ. of Arizona: Tucson), p. 1253.

Bradley, J. P., Humecki, H. J., and Germani, M. S. 1992, *Ap. J.*, **394**, 643.

Bregman, J. D., Campins, H., Witteborn, F. C., Wooden, D. H., Rank, D. M., Allamandola, L. J., Cohen, M., and Tielens, A. G. G. M. 1987, Å, **187**, 616.

Burrows, C. J., Krist, J. E., Stapelfeldt, K. R., WFPC2 Investigation Team 1995, *BAAS*, **187**, 3205.

Fajardo-Acosta, Telesco, C. M., and Knacke, R. F. 1993, *Ap. J. (Letters)*, **417**, L33.

Hanner, M. S., Lynch, D. K., and Russell, R. W. 1994, *Ap. J.*, **425**, 274.

Knacke, R. F., Fajardo-Acosta, S. B., Telesco, C. M., Hackwell, J. A., Lynch, D. K., and Russell, R. W. 1993, *Ap. J.*, **418**, 440.

Jura, M., Zuckerman, B., Becklin, E. E., and Smith, R. C. 1993, *Ap. J. (Letters)*, 418, L37.

Lagage, P. O. and Pantin, E. 1994, *Nature*, **369**, 552.

Smith, B. A., and Terrile, R. J. 1984, *Science*, **226**, 1421.

Sylvester, R. J., Barlow, M. J., and Skinner, C. J. 1995, *Ap. Space Sci.*, **224**, 405.

Telesco, C. M., and Knacke, R. F. 1988, *Ap. J.*, **372**, L29.

Walker, H. J., and Wolstencroft, R. D. 1988, *Pub. A. S. P.*, **100**, 1509.

Witteborn, F., C., Bregman, J. D., Rank, D. M., and Cohen, M. 1991, in *Proceedings of the 1991 North American Workshop on Infrared Spectroscopy*, ed. R. E. Stencel, (Boulder: Colorado), p. 29.

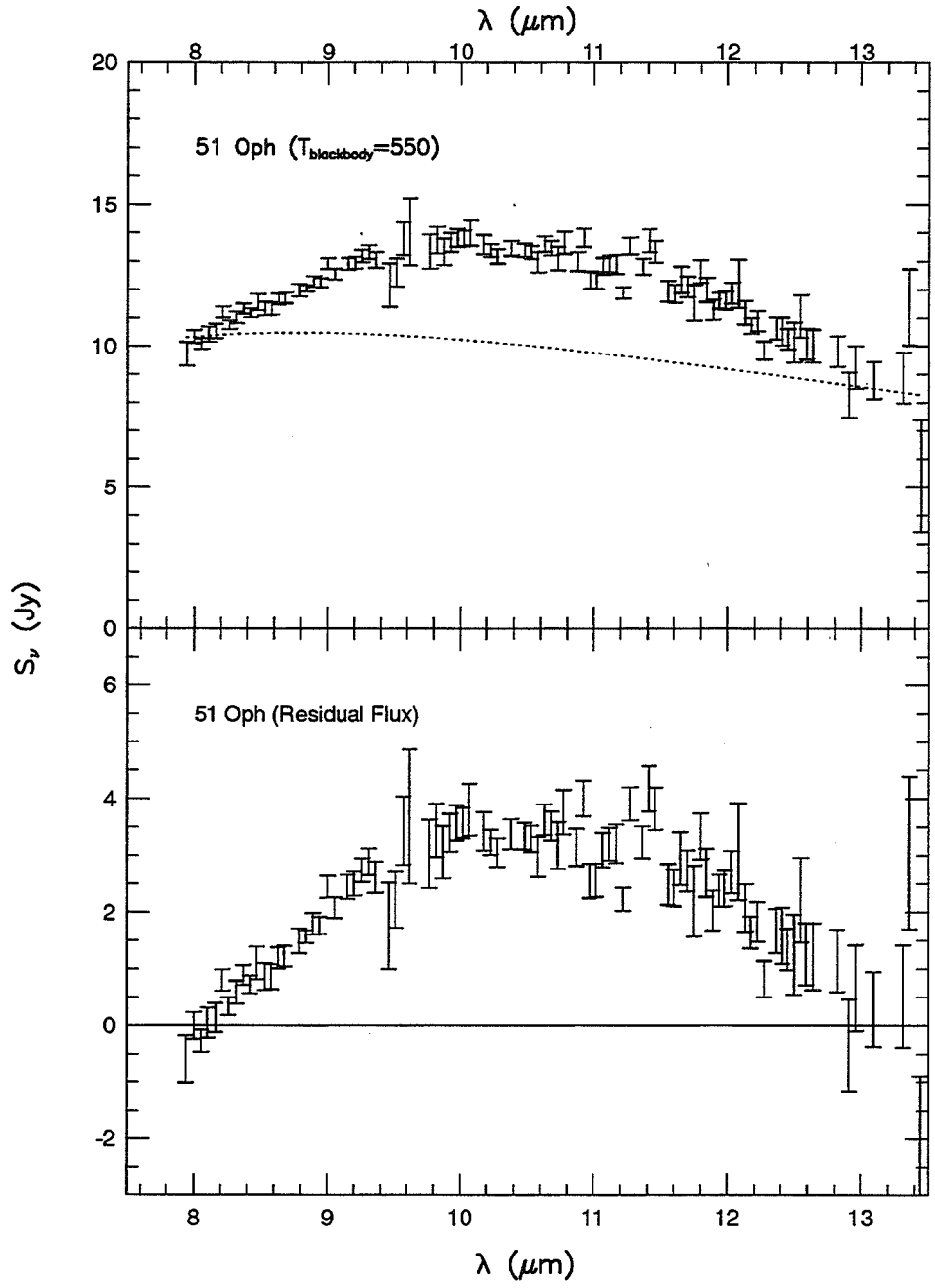

Figure 1. 51 Oph: (top) Spectra with superimposed 550 K Blackbody (dashed lines), (b) Residual flux after subtraction of the 550 K blackbody. Flux is in Jy.

PARTIALLY CRYSTALLINE SILICATE DUST IN PROTOSTELLAR DISKS

M. L. SITKO *University of Cincinnati, Cincinnati, OH 45221, USA*
D. K. LYNCH & R. W. RUSSELL *The Aerospace Corporation, Los Angeles, CA 90009, USA*
M. S. HANNER *Jet Propulsion Laboratory, Pasadena, CA 91109, USA*
C. A. GRADY *Eureka Scientific, Oakland, CA 96402, USA*

ABSTRACT. We examine the infrared emission of the Herbig Ae/Be stars and show that some possess characteristics indicative of partially crystalline grains similar to those seen in β Pictoris and some solar system comets.

1. INTRODUCTION

Stars with debris disks like β Pictoris must have had evolutionary precursors. The stars that most resemble what such a precursor was probably like are the Herbig Ae/Be stars (HAEBEs). In the past few years a considerable amount of evidence has been amassed that clearly indicates that a large fraction of these systems must be actively accreting material, that the accretion is largely confined to a disk, and that in a significant number of cases we must be viewing the disk essentially edge-on, as we do β Pic (Grady et al. 1996). Specifically, we see that: (1) a large fraction of the stars exhibit spectroscopic evidence of gas inflow; (2) the stellar rotational velocities suggest that the gas inflow is preferentially located near the stellar equatorial plane; (3) dust shares in the inflow process and is probably the source of some of the gaseous species seen; (4) flux and polarization variations are seen which are most easily explained by changing obscuration in dusty disks viewed edge-on; (5) polarization position angles differ by 90 degrees at different wavelengths.

2. DUST MINEROLOGY IN HAEBES

Because stars like the HAEBEs possess many characteristics suggesting that they are likely precursors to β Pic systems, studying the composition of the dust in their disks would provide valuable information on how the dust in β Pic systems evolves.

β Pic has a flat-toppped silicate emission band, with a peak near 11.2 μm indicative of crystalline olivine (Knacke et al. 1993). This feature is also present in the spectra of many, but not all, comets (Hanner, Lynch, and Russell 1994). Since crystalline olivine condenses at the high temperatures (>1200 K) that might have been typical of the inner solar nebula, it could, in principle, have formed by condensation during the formation of the solar system. But the difficulty of transporting the

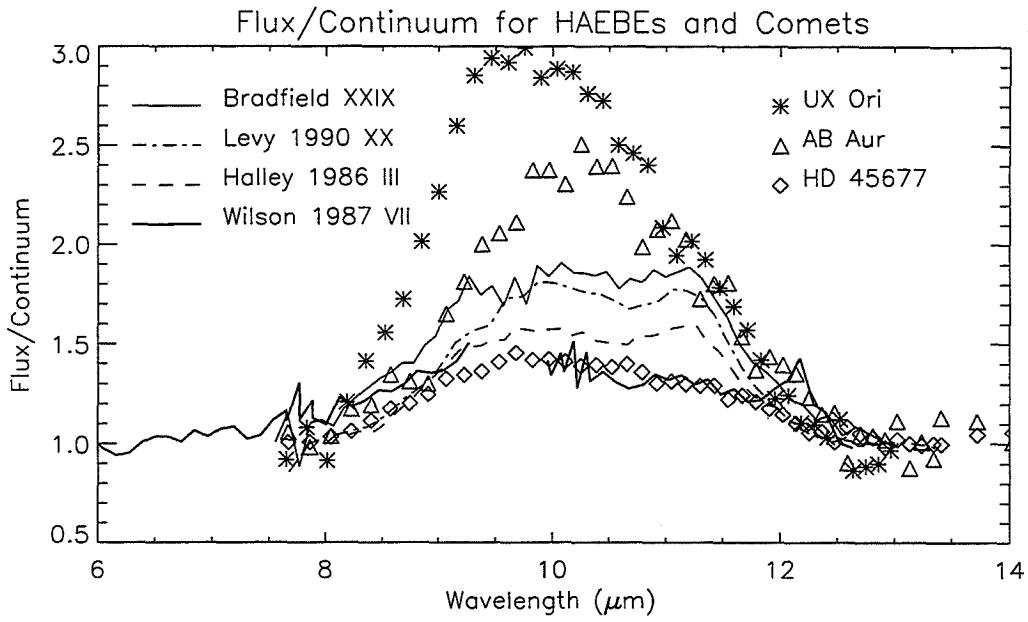

Figure 1. The spectra of 3 HAEBE stars compared to 4 comets with strong silicate features. Each spectrum has been normalized to the underlying continuum by fitting a single-temperature blackbody at 8 and 13 μm. The comet data is from Hanner, Lynch, and Russell (1994); the data on AB Aur and HD 45677 are IRAS LRS; the UX Ori data were obtained with the Aerospace BASS spectrometer.

grains to the outer nebula where comets formed suggests a presolar origin instead. However, although crystalline olivine is seen in the ouflows in some stars (Waelkens 1996), it has not been seen in most young stellar regions. We just don't know where it comes from (Hanner et al. 1994). And by contrast with β Pic and many comets, the silicate bands of most HAEBEs do not seem to exhibit the 11.2 μm olivine feature. In Figure 1 we show the emission (normalized to the continuum) of three HAEBEs, three comets that exhibit the olivine feature, and one that does not.

3. CRYSTALLINE SILICATES IN HAEBES

While the bulk of the HAEBEs observed so far have 10 μm silicate emission features indicative of relatively amorphous material, a few have emission bands that would seem to require a significant component of partially crystalline grains. Among these is HD 100546. In addition to showing emission due to organics (ISO spectra confirm that the shoulder at 8.6 μm and part of the peak at 11.3 μm are probably organics; Waelkens 1996), the main component of the emission, due to silicates, seems to peak longward of 10 μm. Its 20 μm band also shows some structure. In Figure 2 we show

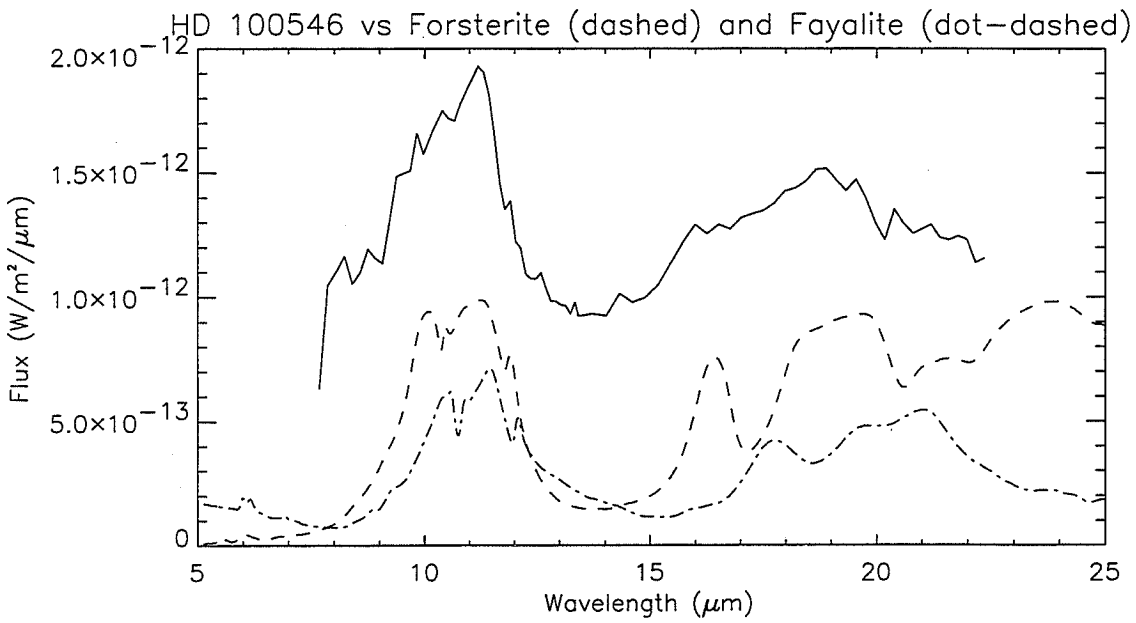

Figure 2. HD 100546 (solid line) compared to absorption (inverted transmission) spectra of forsterite (dashed curve) and fayalite (dot-dashed curve)

the IRAS LRS spectrum of HD 100546 along with inverted transmission spectra of two terrestrial olivines (data from Salisbury et al. 1991), one Mg-rich and the other Fe-rich. The feature at 16 μm, if real, is indicative of Mg-rich olivine (forsterite). In objects where Mg/Fe < 1 (fayalite), the feature shifts to longer wavelengths. ISO spectra between 20 and 50 μm confirm this identification (Waelkens 1996). The spectrum of this star is also very similar to some of the glassy silicate IDPs studied by Bradley, Humecki and Germani (1992).

β Pic is known to exhibit evidence of infalling evaporating bodies (Buest and Tagger 1993; Buest and Lissauer 1995; Vidal-Madjar et al. 1994). If HAEBEs are "baby β Pics", then the same process might be observed in them. Such events may explain the anticorrelated UV/IR variability seen in some of them (such as HD 45677; Sitko et al. 1992). Perhaps the crystalline olivine is being produced by the partial annealing of grains or removal of coatings in infalling objects with elongated (star-grazing?) orbits whose grains are then dispersed to larger distances by a combination of orbital dynamics (large grains) and radiation pressure (small grains). If so, we expect that objects exhibiting such silicate band structure will also exhibit evidence for compact infalling objects if viewed in the disk plane. HD 100546 seems to be such a system (Grady, Pérez, and Bjorkman 1996).

4. CONCLUSIONS

If HAEBEs are the natural evolutionary precursors to main sequence stars with debris disks such as β Pic, we expect that some of the HAEBEs (perhaps those in the latest stages of pre-main sequence evolution) should have similar grain emission characteristics to β Pic, and might resemble the dust seen in solar system comets.

While β Pic and many solar system comets possess IR emission indicative of at least partially crystalline silicates, this feature is weak or absent in most HAEBEs. In a few of them, however, the feature is strong, and these may be the "missing link" in the this evolutionary scenario. In one of these objects, HD 100546, we see evidence for a significant degree of crystallinity, and can use the presence of a feature at 16μm to infer that the grains are rich in Mg. We expect that such systems, if their disk is suitably oriented, will exhibit evidence for the infalling evaporating bodies observed in β Pic, and HD 100546 would seem to fall into this catagory. It may be that these bodies provide a possible source for the crystalline grains, either through partial annealing of more amorphous material or the removal of coatings that may supress the expression of the feature.

Acknowledgements. This work has been suported at the University of Cincinnati by the Physics Department and the University Research Council, and at The Aerospace Corporation by the Aerospace Sponsored Research program.

References

Beust, H. and Tagger, M. 1993, Icarus, **106**, 42.

Beust, H. and Lissauer, J. 1995, *Astr. Ap.*, **247**, 505.

Bradley, J.P., Humecki, H.J., and Germani, M.S. 1992, *Ap. J.*, **394**, 643.

Grady, C.A., Pérez, M.R., and Bjorkman, K.S. 1996, this volume.

Grady, C.A., Pérez, M.R., Talavera, A., Bjorknman, K.S., de Winter, D., Th, P.S., Molster, F., van der Anker, M., Sitko, M.L., Grinin, V.P., Calvet, N., Morrison, N., McCollum, B., and Castelaz, M. 1996, *Astr. Ap.*, in press.

Hanner, M.S., Hackwell, J.A., Russell, R.W., and Lynch, D.K. 1994, Icarus, **112**, 490.

Hanner, M.S., Lynch, D.K., and Russell, R.W. 1994, *Ap. J.*, **425**, 274.

Knacke, R.F., Fajardo-Acosta, S.B., Telesco, C.M., Hackwell, J.A., Lynch, D.K., and Russell, R.W. 1993, *Ap. J.*, **418**, 440.

Salisbury, J.W., Walter, L.S., Vergo, N., and D'Aria, D.M. *Infrared (2.1-25μm) Spectra of Minerals.* The Johns Hopkins University Press, 1991.

Sitko, M.L., Halbedel, E.M., Lawrence, G., Smith, J.A., and Yanow, K. 1994, *Ap. J.*, **432**, 753.

Vidal-Madjar, A., Lagrange-Henri, A.-M., Feldman, P.D., Beust, H., Lissauer, J.J., Deleuil, M. Ferlet, R., Gry, C., Hobbs, L.M., McGrath, M.A., McPhate, J.B., and Moos, H.W. 1994, *Astr. Ap.*, **290**, 245.

Waelkens, C. 1996, *From Stardust to Planetesimals*, ASP Conference series, in press.

HIGH RESOLUTION SPECTROSCOPY OF VEGA-LIKE STARS: ABUNDANCES AND CIRCUMSTELLAR GAS

S. K. DUNKIN & M. J. BARLOW *Dept. of Physics and Astronomy, University College London, Gower Street, London WC1E 6BT, England*
SEAN G. RYAN *Anglo-Australian Observatory, PO Box 296 Epping, NSW 2121 Australia*

ABSTRACT. Vega-like stars are main-sequence stars exhibiting excess infrared emission. In an effort to improve the information available on this class of star, 13 stars have been analysed which have been classed as Vega-like, or have an infra-red excess attributable to dust in their circumstellar environment. In a separate paper (Dunkin, Barlow and Ryan 1996a) stellar properties such as effective temperature and log g have been derived and in this poster we highlight the results of the photospheric abundance analysis also carried out during this work.

King (1994) recently drew attention to the possible link between Vega-like stars and the photospheric metal-depleted class of A-stars, the λ Bootis stars. Since Vega-like stars are thought to have disks of dust, it might be expected that accretion of depleted gas onto the surface of these stars may cause this same phenomenon. In the 6 stars studied for depletions, none showed the extreme underabundance patterns observed in λ Bootis stars. However, depletions of silicon and magnesium were found in two of the sample, suggesting that these elements are in silicate dust grains in the circumstellar environment of these stars.

Absorption lines attributed to circumstellar gas have been positively identified in three stars in our sample. Individual cases show evidence either of high-velocity outflowing gas, variability in the circumstellar lines observed, or evidence of circumstellar gas in excited lines of Fe II. No previous identification of circumstellar material has been made for two of the stars in question.

1. INTRODUCTION AND OBSERVATIONS

Vega-like stars get their name from the prototype of their class, Vega (α Lyr). During a routine calibration scan of this star, the Infrared Astronomical Satellite (*IRAS*) detected excess flux at wavelengths centered at 25, 60 and 100μm, above that expected for a blackbody at the temperature of the star (Aumann et al., 1984). During the course of the mission, three other bright main-sequence stars were found to exhibit this infrared (IR) excess: α PsA (Fomalhaut), ϵ Eri and β Pic which, together with Vega, have become known as the prototypes of the "Vega-like" phenomenon. Subsequent searches of the *IRAS* database (e.g. Aumann, 1985, Walker and Wolstencroft, 1988) have since expanded the known membership of the class significantly. The excess emission from these main sequence stars has been attributed to circumstellar dust in

the form of a disk, toroid or envelope, somewhat similar to that postulated for our own Solar System. Studies of the β Pic system reveal an extensive disk, a possible nursery for newly formed planets, increasing the interest in this fascinating class of star.

Spectra of a sample of Vega-like stars, selected mainly from the list of Walker and Wolstencroft (1988), were obtained using the UCL echelle spectrograph at the Anglo-Australian Telescope and the ROESC echelle spectrograph at the Observatorio Astronomico Nacional, Mexico in 1993. Wavelength coverage extended from approximately 3300Å to 9000Å and the resolving power of the spectra was R($=\lambda/\Delta\lambda$)$\sim$44,000 and 15,000 respectively. Full details can be found in Dunkin, Barlow and Ryan (1996a,b).

2. EVIDENCE FOR CIRCUMSTELLAR GAS

Gas in the circumstellar environment can be studied by looking at characteristic narrow absorption lines superimposed on the easily distinguishable stellar lines from the parent star. Establishing an interstellar or circumstellar (CS) origin for the line is a difficult task, and often the CS lines can only be positively identified if they are variable, or at very high velocities relative to the star, or show narrow absorption in excited state lines which are not present in interstellar sightlines.

We studied the lines of Ca II K (3933.663Å) and Na I D (5889.951Å and 5895.924Å) for evidence of narrow absorption lines. Most of the sample had some evidence for such lines, but the majority could not be positively identified as circumstellar. However, three stars were found which had lines that were highly likely to be of circumstellar origin. One of them, HD 35187 has been previously studied by Grady et al. (1996), who classify it as a Herbig Ae star. Their spectrum of the Na doublet is distinctly different from ours (Figure 1), in that another narrow absorption line has appeared in our spectrum in the time between the two observations. Such variability does not occur in the interstellar medium on these timescales, and we therefore ascribe a circumstellar origin to this variable narrow absorption line in HD 35187. HD 144432 is obviously an active star, judging by its prominent P Cygni profiles in the Na D and Ca K lines. In addition to two probable interstellar lines visible in the the Na D profile (Figure 1), a weaker, high velocity component is also seen. Its high velocity of approximately –84 km s^{-1} would suggest that its origin is circumstellar, rather than interstellar. This component is also visible in the Ca K line, after the observed profile has been divided through by a standard model for its spectral type (Figure 1,centre frame). 51 Oph has been previously studied (i.e. Lagrange-Henri et al., 1990) where a narrow absorption was found in the Ca II K line and, as it is also a shell star, was thought likely to have some component of this narrow line emanating from its circumstellar environment. We confirm this by discovering the presence of narrow absorption lines in excited state lines of Fe II (4549.474Å and 4583.837Å). These lines are not expected to appear in the interstellar medium, so must originate from the circumstellar environment of 51 Oph.

3. PHOTOSPHERIC ABUNDANCES

λ Bootis stars are chemically peculiar A-stars, exhibiting large underabundances in elements such as magnesium, calcium and iron. The accretion of dust-depleted gas from the circumstellar environment onto the stellar surface has been proposed as an explanation for the λ Bootis phenomenon (Venn and Lambert, 1990). In terms of this

accretion hypothesis, King (1994) investigated the possible link between the λ Bootis phenomenon and Vega-like stars, with inconclusive results. We investigated such a link by carrying out an abundance analysis on some of our sample of A-type Vega-like stars.

Model spectra were produced using the LTE-spectrum synthesis program UCLSYN (Smith, 1992). Using atomic data from Kurucz (1995), UCLSYN initially assumes solar abundances. Upon provision of the observed equivalent widths, revised abundances are derived until a satisfactory fit to the observed equivalent widths and line profiles is found.

In our full analysis of four Vega-like stars and partial analysis of two, we found no correlation between the abundances in λ Bootis stars, or in the interstellar medium, with those in the Vega-like stars in our sample. Underabundances were found in Si and Mg for two of our stars. HD 169142 has a Si depletion of 0.86 dex (relative to solar) and 0.56 dex in Mg, whilst HD 139614 has a Si depletion of 0.52 dex below solar. Silicon and magnesium are the two main constituents of silicate dust grains. These have already been detected around HD 169142 (from the presence of the 18μm silicate feature, Sylvester et al., 1996); HD 139614 has yet to be studied for the presence of this feature in its spectrum. However, the absence of depletion of other elements such as Fe, Ca and Ti is puzzling, as these would normally be expected to be even more depleted than Mg and Si.

References

Aumann H.H., Gillett F.C., Beichman C.A., de Jong T., Houck J.R., Low F.J., Neugebauer G., Walker R.G., Wesselius P.R., 1984, *Ap. J.*, **278**, L23

Aumann H.H., 1985, *Pub. A. S. P.*, **97**, 885

Dunkin S.K., Barlow M.J., Ryan S.G., 1996, *M. N. R. A. S.*, submitted

Dunkin S.K., Barlow M.J., Ryan S.G., 1996, *M. N. R. A. S.*, submitted

Grady C.A. et al., 1996, *A. J.*, in press

King J.R., 1994, *M. N. R. A. S.*, **269**, 209

Kurucz R.L., 1995, ASP Conference Series, **78**, 205

Lagrange-Henri A.M., Ferlet R., Vidal-Madjar A., Beust H., Gry C., Lallement R., 1990, *A. J.*, **85**, 1089

Smith K.C., 1992, Ph.D. Thesis, University of London, Chapter 5

Sylvester R.J., Skinner C.J., Barlow M.J., Mannings V., 1996, *M. N. R. A. S.*, in press

Venn K.A., Lambert D. L., 1990, *Ap. J.*, **363**, 234

Walker H.J., Wolstencroft R.D., 1988, *Pub. A. S. P.*, **100**, 1509

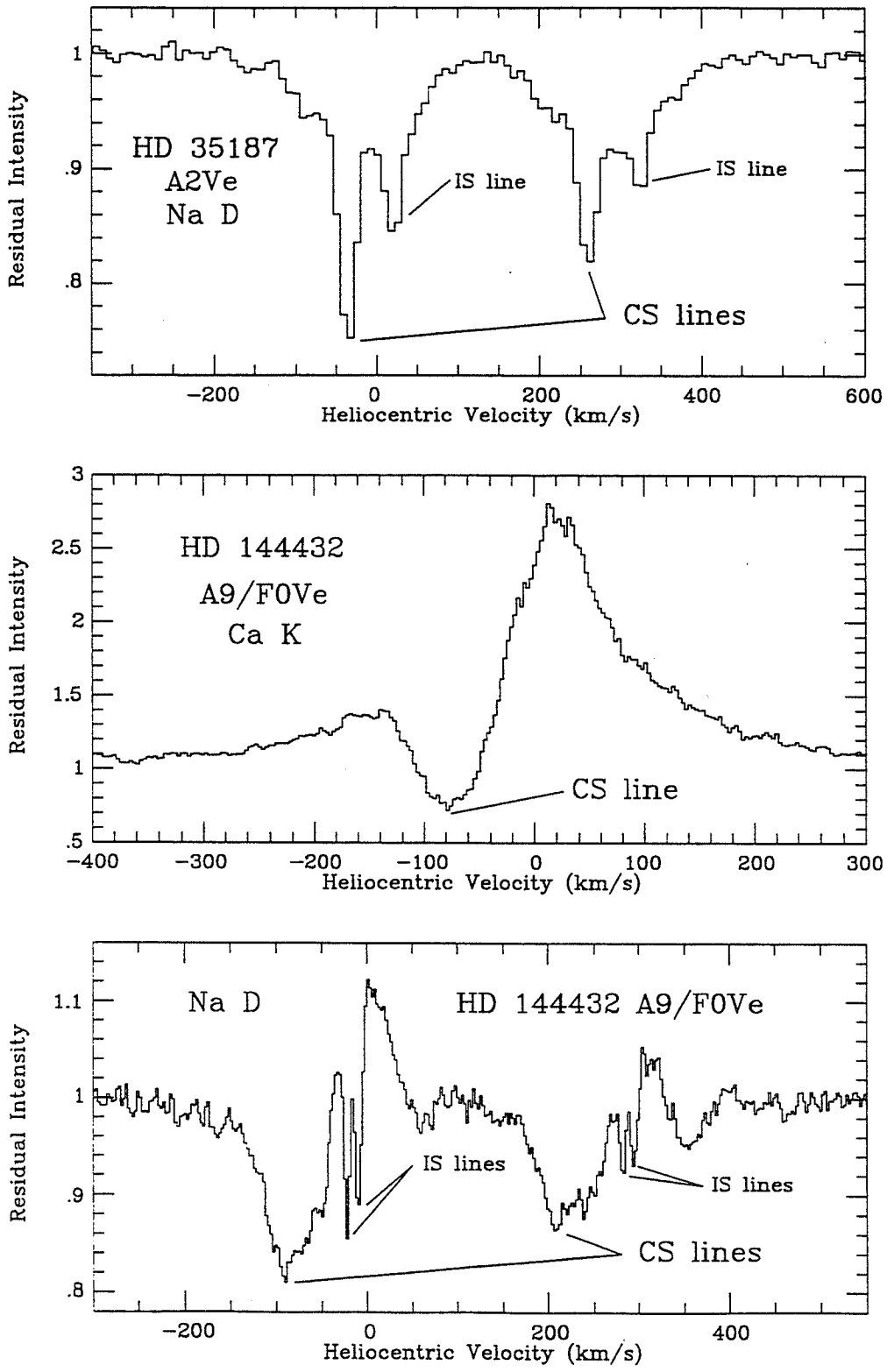

Figure 1. Circumstellar lines detected in HD 35187 and HD 144432. The Ca II spectrum of HD 144432 is the result of the observed spectrum having been divided through by a model for the photospheric spectrum.

TRANSIENT ACCRETION EVENTS IN HERBIG AE/BE STAR SPECTRA: THE EVIDENCE FOR INFALLING PLANETESIMALS IN HD 100546 (B9E)

C.A. GRADY *Eureka Scientific, Oakland, CA 96402,*
M.R. PÉREZ *Applied Research Corporation, Landover MD 20785*
K.S. BJORKMAN *SAL, University of Wisconsin, Madison WI 53706-1390*

ABSTRACT. Enhanced gaseous absorption resembling the high velocity circumstellar gas features in the spectrum of β Pic have been detected in IUE high dispersion spectra of the 2 Myr-old Herbig Be star, HD 100546, on 1995 March 9. The presence of atomic gas features in transitions of C I and O I implies that the material is produced by the pyrolysis of an unseen, solid body in a star-grazing orbit. The presence of weak Fe II absorption in the same spectrum with heavily saturated magnesium, aluminum, and silicon features is consistent with an origin in the sublimation of the olivenes detected in IRAS LRS and ISO SWS spectra of this star. The C I and O I detections suggest that, compared to β Pic, the planetesimals in this system contain substantial amounts of carbonaceous material. The presence of mildly refractory species such as Zn II and S II suggests that the planetesimal had not been substantially heated above 700 K during its previous lifetime.

1. INTRODUCTION

Recent moderate resolution (25 $\mathrm{km\,s^{-1}}$) UV and optical spectral studies of Herbig Ae/Be (HAeBe) stars have revealed the presence of systematically redshifted absorption features in approximately 33% of the stars studied (Grady et al. 1996). These features are preferentially observed in the spectra of stars with comparatively high $v \sin i$, double-peaked Hα emission, and histories of large amplitude photometric and polarimetric variability (Grinin & Rostopchina 1996).

Where multiple spectra are available, striking line profile changes are observed in the accreting gas, reminiscent of those routinely observed in spectra of β Pic. The identification of these stars, together with their high luminosity from the far UV through mm wavelengths provides us with a laboratory for probing the nature of circumstellar material in close proximity to the star in objects as young as 2-3 Myr. We present IUE spectra of a transient accretion event observed on 9 March 1995 toward the B9 Ve star, HD 100546. HD 100546 is an isolated Herbig Be (HBe) star (Hu et al. 1989) with a mm flux consistent with a dust and gas disk extending some 665 AU from the star (Henning et al. 1994). Accreting circumstellar gas is routinely detectable in all of the available IUE spectra (Grady et al. 1996). When observed in high dispersion with IUE on 1995 March 7, enhanced redshifted absorption centered at approximately 100-150 $\mathrm{km\,s^{-1}}$ was detected, compared to observations made in

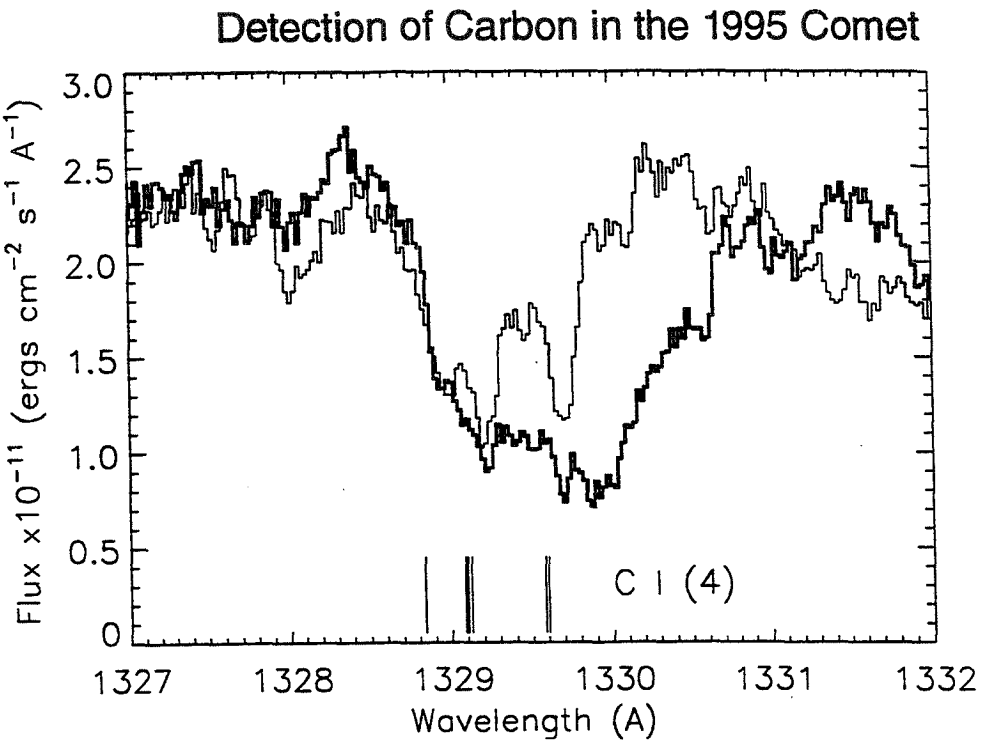

Figure 1. Detection of accreting, atomic carbon as seen in C I (4) in the spectrum of HD 100546 on 7 March 1995 compared to a quiescent state spectrum from 1993.

more quiescent states. The high velocity feature (HVF) is visible in high oscillator strength transitions of S II, O I, Si II, Si IV, C I, C II, C IV, Al II, Zn II, Mg II, and Fe II (see figure 1).

2. RESULTS:

Size of Gas Cloud: Mg II, the carbon ions, Al II, and the higher oscillator strength Si II transitions all have saturated absorption profiles with covering factors of 55%, which enables us to infer that the gas cloud had a projected area of 55% of the visible stellar surface, or for a 3 solar mass star with an estimated radius of 3 $R_{\odot}$, a size of a few times 10^6 km. This is comparable to the size of the gas clouds seen in Na I toward the Herbig Ae stars RR Tau, BF Ori, and UX Ori, and is also comparable to the inferred size of the HVF clouds in the line of sight to β Pic.

Association with Infalling, Evaporating, Bodies: When normalized to quiescent state spectra of HD 100546, the bulk of the circumstellar gas transitions have absorption profiles indistinguishable in shape from those routinely detected toward β Pic, which have been modelled (Beust et al. 1989; 1995) as the gaseous comae of infalling, evaporating bodies. Vidal-Madjar (1994) has noted that additional support for an origin of the gas features in the β Pic system from infalling, solid bodies, is provided by the presence of atomic and or molecular gas features at the system velocity for elements with first ionization potentials below that of hydrogen (e.g. they can

be ionized by the stellar radiation field, or the ISM, and hence are not equilibrium species). The IUE data demonstrate that C I and O I are routinely detected at the system velocity, together with a marginal detection of S I. The 1995 March 7 HVF also shows C I to +225 km s^{-1}, O I to 300 km s^{-1}, and N I to +300 km s^{-1}. Optical spectra of HD 100546 (Böhm & Catala 1995; Grady et al. 1996) also show He I λ5876 absorption over the same velocity range. Grinin et al. (1995) noted that the presence of atomic gas species at high velocity with photoionization lifetimes within a few stellar radii of the star of seconds to at most minutes indicates that the atomic gas is being continuously produced *in situ* and must originate from either the dissociation of molecules or the sublimation of large grains.

A Link to the Grains: While Si, Al, Mg, C, and O show saturated absorption profiles with a 55% covering factor except in the lowest oscillator strength transitions of Si II (1) and Si IV (1), the Fe II absorption is anomalously weak. Absorption from transitions of multiplet (1) are not in the ratio of the oscillator strengths, but are also not 1:1, indicating that this material is probably only just becoming optically thick. The IUE data, therefore, are consistent with Mg>Fe, which is supported by both Sitko et al.'s (1996) finding of silicate emission consistent with Mg-rich olivene, and detection of olivene features (e.g. forsterite) in ISO SWS data (Waelkens 1996). The similarity of the carbon and oxygen HVF profiles to those from more refractory species, and especially those which are likely the dissociation products of silicates suggests that these species behave as refractory elements rather than volatiles and may be associated with CHON particles. The IUE data for this object, therefore indicate that the bulk of the really high velocity gas is associated with the dissociation of solid bodies. While the covering factor for the HVF is similar to that seen toward other HAeBe stars with accreting gas and is comparable to that routinely observed toward β Pic, it is a factor of $\geq$100 higher than is observed for single Sun-grazing comets (e.g. C/1996 b2). This suggests that we may have detected a planetesimal swarm.

Limits on Prior Heating: In contrast to β Pic, the HVF seen toward HD 100546 shows Zn II, S II, and in optical spectra (Böhm & Catala 1995; Grady et al. 1996) routinely shows He I 5876 Å absorption to +400 km s^{-1}. The presence of the mildly refractory elements Zn, and S, indicates that the grains and parent body associated with the HVF has not been uniformly heated to much more than 700 K (Jenkins 1987). The presence of olivenes and He I further suggests that the bulk of the parent body for the grains and dust has not been previously heated above 1000 K, and suggests a further similarity between the composition of the parent body of the HD 100546 HVF and solar system inteplanetary dust particles.

Comparison with Other HAeBe Stars: The other HAeBe stars with accreting gas and IUE high dispersion data tend to show strong Fe II absorption with covering factors comparable to that seen in Mg II. IR spectrometry of the 9.7 micron silicate emission profile for these objects suggests either Halley-like grains , or features more closely resembling the ISM (UX Ori, Sitko et al. 1995), implying the presence of both iron-rich and magnesium-rich silicates. Circumstellar C I absorption is present (and very saturated) in HD 163296 and is present, but less saturated in HD 95881.

3. IMPLICATIONS

The IUE data, supplemented by non-contemporary optical spectra, suggest much of the accreting gas seen in the line of sight to the 2 Myr-old HBe star HD 100546 is asso-

ciated with star-grazing planetesimals which produce, at comparable distance to the star, gas comae similar to those routinely observed in the β Pic system. This is consistent with the inferred clumpiness of the near-stellar circumstellar gas in other HAeBe stars (Graham 1992, 1994), and may explain why boundary layer emission, such as would be expected from accretion of predominantly gaseous material, is not typically observed in association with the less-embedded HAeBe stars. The HD 100546 planetesimal differs from those seen toward β Pic by retaining mildly refractory species which sublimate at temperatures above 700 K (Jenkins 1987), and by having large amounts of carbon, nitrogen, and oxygen. The refractory species seen in the UV spectra are consistent with the silicates in this system being dominated by Mg-rich olivenes and show a deficiency of siderophile elements.

If the planetesimal seen toward this object is representative of 2 Myr-old bodies associated with other intermediate-mass PMS stars, comparison of the HD 100546 data with β Pic suggests that substantial modification of planetesimals which become star-grazers occurs between 2-3 Myr and 12 Myr, the inferred age of the β Pic system (Lanz et al. 1995).

Acknowledgements. Support for this study was provided by the NASA Long-Term Space Astrophysics Program to Eureka Scientific under NASA Contract NASW 4756. Data analysis facilities were provided by the IUE Data Analysis Center located in the Laboratory for Astronomy & Solar Physics, NASA/GSFC.

References

Beust, H. et al. 1989, *Astr. Ap.***223**, 304.

Beust, H. 1995 in *Circumstellar Dust Disks and Planet Formation*, ed. R. Ferlet, and A. Vidal-Madjar (Paris: Editions Frontières), p. 35.

Böhm, T. and Catala, C. 1995, *Astr. Ap.***301**, 155.

Grady, C.A. et al. 1996, *Astr. Ap. Suppl. Ser.*(in press).

Graham, J.A. 1992, *Pub. A. S. P.*, **104**, 479.

Graham, J.A. 1994, ASP Conf. Ser. **62**, 363.

Grinin, V.P. et al. 1994, *Astr. Ap.***292**, 165.

Grinin, V.P., and Rostopchina, A.N. 1996, Astron. Rep. **40**, 171.

Henning, T. et al. 1994 *Astr. Ap.***291**, 546.

Hu, J.Y., Thé, P.-S., and de Winter, D. 1989, *Astr. Ap.***208**, 213.

Jenkins, E.B. 1987 in *Interstellar Processes*, eds. D.J. Hollenbach and H.A. Thronson (Dordrecht: Reidel), p. 533.

Lanz, T. et al. 1995, *Ap. J.***447**,L41.

Sitko, M.L. et al. 1995 in *Circumstellar Dust Disks and Planet Formation*, ed. R. Ferlet, and A. Vidal-Madjar (Paris: Editions Frontières), p, 389.

Sitko, M.L. et al. 1996 (this conference).

Vidal-Madjar, A. et al. 1994 *Astr. Ap.***290**,245.

Waelkens, C. 1996 (this conference).

STAR FORMATION

THE REMARKABLE HERBIG AE STAR V351 ORI

M.E. VAN DEN ANCKER *University of Amsterdam, Amsterdam, The Netherlands*
P.S. THÉ *University of Amsterdam, Amsterdam, The Netherlands*
D. DE WINTER *Universidad Autónoma de Madrid, Madrid, Spain*

ABSTRACT. The photometric behaviour of the Herbig Ae star V351 Ori was investigated combining data from the literature with new photometry. It is shown that this object changed from a Herbig Ae star with strong photometric variations, due to extinction by circumstellar dust clouds, to that of an almost non-variable star. Such a behaviour is not unique; it has been found also in the star BN Ori. This suggests that such transitions as well as the opposite must occur quite often during the evolution of these intermediate mass stars towards the main-sequence. A provisional model to explain V351 Ori's behaviour, in which it is assumed that a temporarily strong accretion of matter onto the star took place, is proposed.

1. INTRODUCTION

V351 Ori = HD 38238 is an irregular variable Hα-emission line star, located in the direction of the Lynds 1630 dark cloud region. Although V351 Ori fulfills all primary criteria for membership of the Herbig Ae/Be stellar group (A or B-type emission-line star with infrared excess, located in a plausible region of recent star formation), as well as many secondary ones (large brightness variations, spectral signatures of mass accretion), it was only first recognized by Koval'chuk (1985) and by Zajtseva (1986) to belong to this special class of intermediate-mass pre-main sequence objects. As a consequence of this late discovery, the star was not well studied and a more careful analysis of all available photometric and spectroscopic data of this object was in place, the results of which are presented in this paper.

2. PHOTOMETRIC BEHAVIOUR

During the last seven years, V351 Ori was monitored by the ESO "Long Term Photometry of Variables"-group, using the Strömgren Automatic Telescope at La Silla, Chile. The new y data are, together with visual photometry of V351 Ori collected from literature, plotted in Fig. 1. Colour-magnitude diagrams with these data are shown in Fig. 2. When we examine the lightcurve in Fig. 1, we notice that V351 Ori has changed its photometric behaviour drastically over the period of 14 years covered by this diagram. In the period before JD 2446000 the star shows large brightness variations. When we look at the colour-magnitude diagrams in the Johnson $UBVRI$ system over this period (Fig. 2b), we notice that for $V < 10\overset{m}{.}0$ there seems to be a linear relation between the V magnitude and the colour-indices, in which the colours

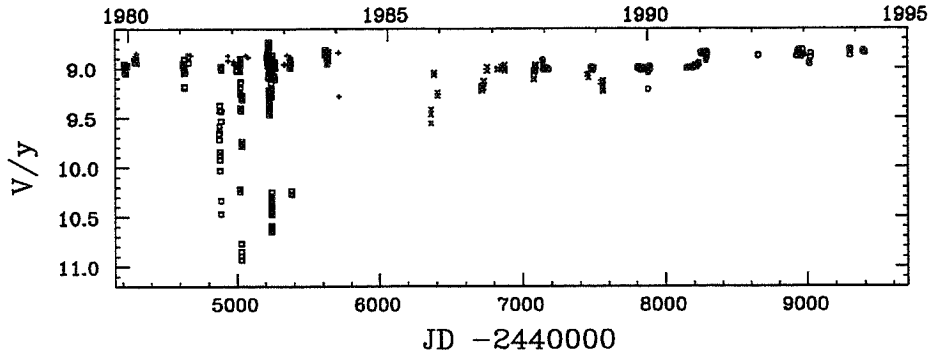

Figure 1. Lightcurve of V351 Ori. Squares represent data of Koval'chuk (1985), plus signs those of Kilkenny et al. (1985), crosses those of Chkhikvadze (1990) and open circles are data of the LTPV group.

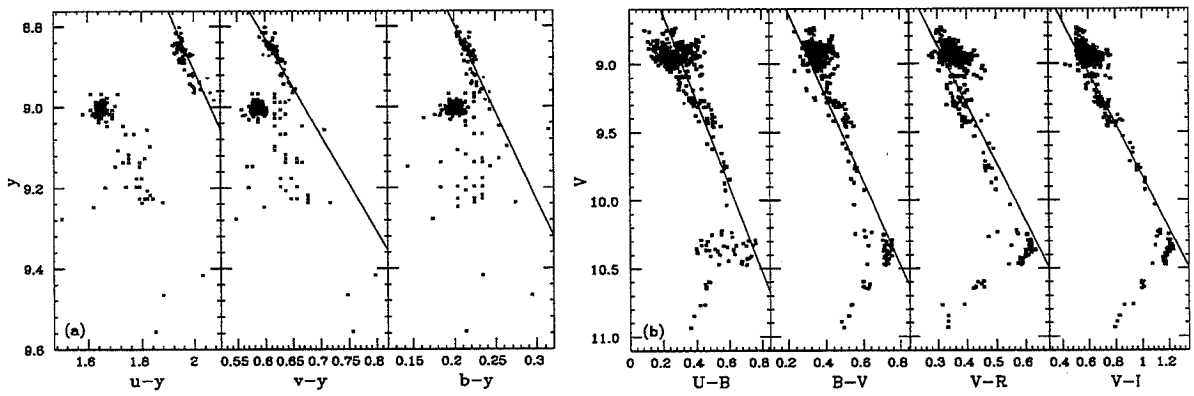

Figure 2. (a) Colour-magnitude diagrams of V351 Ori in the Strömgren *uvby* system. (b) Colour-magnitude diagrams of V351 Ori in the Johnson $UBVRI$ system. Plot symbols have the same meaning as in Fig. 1. The solid lines indicate the interstellar reddening direction.

become redder as V increases. The slope of this relation is compatible with that of the normal (i.e. $R_V = A_V/E(B-V) = 3.1$) interstellar extinction law. This suggests that these variations are caused by variable amounts of extinction of the starlight.

As the stellar brightness decreases even further, we see the blueing effect; with increasing V, the colours now become bluer. Such an effect can be explained by assuming the presence of a dust envelope around V351 Ori. The radii of the particles in this envelope are small enough to scatter the blue photons of the stellar radiation, producing a faint blue emission. The complete colour-magnitude diagram in Fig. 2b can now be explained by assuming the passing by of obscuring dust clouds, revolving around the star. Due to extinction by the particles in the cloud, the light from the star becomes fainter and redder. Below some brightness level, the scattered blue light from the dust envelope dominates, and produces the observed blueing effect.

If we only look at the first part of the light curve in Fig. 1 and the colour-magnitude diagrams in Fig. 2b, we would come to the conclusion that the photometric behaviour of V351 Ori is like that of a typical Herbig Ae star with large photometric variations, such as UX Ori. However, in Fig. 1 we can see that *V351 Ori changed its photometric behaviour from that of a Herbig Ae star showing large photometric variations to that of a nearly constant one.* This process seems to have started around JD 2446000. Before

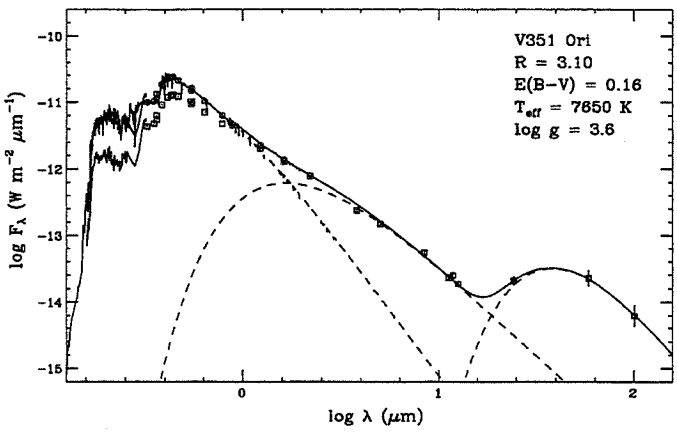

Figure 3. Observed (squares) and extinction-corrected (circles) SEDs for V351 Ori. Also shown are the Kurucz model (left dashed line), the disk model (middle dashed line) and the Planckian (right dashed line) fitted to the infrared excess and the total model (solid line), fitted to the extinction-free SED.

this date, the star showed large ($> 2^m$) variations in y with a maximum brightness of $\approx 8\overset{m}{.}8$ in this passband. Between JD 2446000 and JD 2448200, V351 Ori only varied by several tenths of a magnitude in y, and the star's maximum visual brightness dims by $0\overset{m}{.}16$ to $y \approx 9\overset{m}{.}0$. Between JD 2448200 and JD 2448250, the maximum brightness of V351 Ori rapidly increases to $y \approx 8\overset{m}{.}84$, equal to its level before JD 2446000. After JD 2448250, the variations in brightness nearly vanished.

3. STELLAR PARAMETERS

Using newly obtained low-resolution spectra, we determined V351 Ori to be an A6 or A7 weak emission-line star, well in agreement with the spectral type of A7 III given by Zajtseva (1986). From new high-resolution ($R = 55,000$) spectra of V351 Ori in the Hα and Na I D lines, we notice that the Hα emission has a very strong reversed P Cygni profile, indicating accretion of matter towards the star. Indications for the presence of a disk-like structure around V351 Ori come from the presence of a weak and broad component in the sodium lines.

The extinction-free spectral energy distribution (SED) of V351 Ori, employing only data taken near maximum brightness, was analyzed by comparing it with a Kurucz (1991) model with $T_{eff} = 7650$ K and $\log g = 3.6$, corresponding to the spectral type of A7 III. The photometry used in the construction of this SED were taken from literature and were all obtained in the period when the star still showed strong photometric variations. The resulting SED of V351 Ori is shown in Fig. 3.

As can be seen from this plot, the quality of the fit to the Kurucz model is very good in the ultraviolet and the optical wavelength ranges, with a large amount of excess radiation in the infrared. The fact that the SED in the near infrared can be approximated by a straight line indicates the presence of an extended disk or dust shell around the star, whereas the strong bump in the far-infrared suggests the presence of an additional cooler component. We modelled this SED using a simple parametrized disk model, with $T \propto r^{-0.9}$, similar to the ones by Beckwith et al. (1990). An additional Planckian component with a temperature of 78 ± 4 K represents the dust shell. These two models are also shown in Fig. 3.

4. DISCUSSION AND CONCLUSIONS

We have shown that V351 Ori changed from a Herbig Ae star with strong photometric variations to a almost non-variable one. Such a change had previously only been observed in the Herbig Ae star BN Ori around 1947 (Shevchenko et al. 1996). A first conclusion that can be drawn from the fact that we have actually been able to observe such transitions in the relatively short period these stars have been observed systematically, is that *such transitions from Herbig Ae stars with strong photometric variations to almost non-variable ones must occur quite often during the evolution of such stars towards the main-sequence.* This also implies that the reverse process must occur frequently.

Since before JD 2446000 the photometric variations of V351 Ori were caused by dust clouds orbiting the star, it seems that around this date some event started which either destroyed the dust in these clouds, or moved the dust clouds from our line of sight. This event continued until JD 2448200, after which the star rapidly became nearly constant in brightness. So far, we can only speculate about the cause of this event. It could be that it is correlated with a temporarily strong accretion of dust onto the star. Such an event will be accompanied by shock-fronts which create an extremely hot gaseous disk near the equatorial plane close to the star. This hot optically thick gaseous disk blocked part of the visual and blue light of the star, causing a visual brightness decrease of about $0^m.2$. At the same time, this hot object radiates ultraviolet energy superposed on that of the central star. This is causing the increase of the ultraviolet brightness of the star. When the accretion of dust stops, the visual and blue stellar light regain its maximum brightness, whereas the ultraviolet contribution of the hot disk disappears, and the ultraviolet brightness drops.

Since all infrared observations of V351 Ori were made during the period in which the star still showed photometric variations, it is very important to obtain new infrared photometry of this object. If the dust clouds close to the star have indeed accreted onto the central star, we should expect to see a clear decrease of the infrared excess of the star. Further optical monitoring of V351 Ori remains necessary to see whether the dust clouds start to re-occur, in which case the star will become variable once more.

References

Beckwith, S.V.W., Sargent, A.I., Chini, R.S., Güsten, R. 1990, *A. J.* **99**, 924

Chkhikvadze, J.N. 1990, *Bull. Abastumani Astroph. Obs.* **68**, 43

Kilkenny, D., Whittet, D.C.B., Davies, J.K., Evans, A., Bode, M.F., Robson, E.I., Banfield, R.M. 1985, *SAAO Circ.* **9**, 55

Koval'chuk, G.U. 1985, *Kinem. Fizika Nebesn. Tel.* **1**, 30

Kurucz, R.L. 1991, in *Precision photometry: Astrophysics of the galaxy*, ed. A.G. Davis Philip, A.R. Upgren, K.A. Janes, L. Davis press, Schenectady, New York

Shevchenko, V.S., Ezhkova, O., Tjin A Djie, H.R.E., van den Ancker, M.E., Blondel, P.F.C., de Winter, D. 1996, *Astr. Ap.*, in press

Zajtseva, G.V. 1986, *Astrofizika* **25**, 471

DUST AROUND HERBIG AE STARS: ADDITIONAL CONSTRAINTS FROM THEIR PHOTOMETRIC AND POLARIMETRIC VARIABILITY

N. A. KRIVOVA *Institute of Astronomy, Nicholas Copernicus University, Toruń, Poland*
V. B. IL'IN *MPG Research Unit "Dust in Star-Forming Regions", Jena, Germany*
O. FISCHER *Astrophysical Institute, Jena University, Jena, Germany*

ABSTRACT. For the Herbig Ae stars with Algol-like minima (UX Ori, WW Vul, etc), the effects of circumstellar dust include: excess infrared emission, anomalous ultraviolet extinction, the "blueing" of the stars in minima accompanying by an increase of intrinsic polarization. Using a Monte-Carlo code for polarized radiation transfer we have simulated these effects and compared the results obtained for different models with the observational data available. We found that the photometric and polarimetric behaviour of the stars provided essential additional constraints on the circumstellar dust models. The models with spheroidal shell geometry and compact (non-fluffy) dust grains do not appear to be able to explain all the data.

1. INTRODUCTION

The dust in the vicinity of Herbig Ae stars (HAe) is responsible for the majority of the observational manifestations of the objects — *excess emission* in the infrared (IR), *anomalous extinction* in the ultraviolet (UV) and visual, and *intrinsic polarization* — and is thought to be a possible source material for the formation of planetesimals and planets. For a numerous group of HAe stars with large (up to 2 mag) brightness variations (UX Ori, WW Vul, etc.), *the "blueing" effect* in the color-magnitude diagrams (CMD) and *the increase of the intrinsic polarization* are also observed in deep minima.

The best studied objects of this group are BF Ori, UX Ori, WW Vul, and CQ Tau. Table 1 gives some observed parameters of the stars: visual magnitude in the bright states (m), the range of the brightness falls (Δm_{max}), the polarization degree in the bright (P_b) and faint (P_f) states, and the degree of interstellar polarization (P_{IS}).

To simulate the observational effects mentioned above we apply spheroidal models of the shell. Our main intention here is to examine whether such models are able to account for the data available for the stars.

2. SHELL MODEL

The dusty envelope is assumed to be an oblate spheroid with a power-law density distribution

$$n(\vec{r}) \propto \left(r_x^2 + r_y^2 + r_z^2 \frac{a^2}{b^2} \right)^{-\alpha/2}, \quad (1)$$

where a and b are the semiaxes of the shell (so that the isodenses are ellipses).

The dust-free innermost spherical region around the star is adopted to be due to evaporation of the grains. The outer radius of the shell has little effect on the results and is chosen large enough to be not in conflict with the observed far-IR flux.

The dust grain model is a MRN-like one: a mixture of silicate and graphite spherical grains having a power-law size distribution $n(a) = n_0\, a^{-q}$ with the minimum and maximum radii a_{min} and a_{max}.

We believe that the photometric and polarimetric variability of the objects is caused by the dense dust clumps orbiting the stars and screening them from the observers (Grinin, 1988). It is assumed that the clumps do not affect spectral energy distribution (SED) and other characteristics of the objects significantly.

For modelling of the observational data listed in Sect. 1, we use a 2D Monte-Carlo code (Fischer, 1995). To derive the dust temperature distribution for the Monte-Carlo simulations, spherical shells of the same volume are considered with a 1D radiation transfer code (Men'shchikov & Henning, 1996).

3. RESULTS AND DISCUSSION

At first, we have considered the SED's in the IR and the stellar tracks in the CMD's and restricted the set of the models fitting both types of the data. Such a procedure gives the reliable estimates of the optical thickness of the shells τ_{sh} (Krivova, 1996). The obtained values of τ_{sh} are presented in Table 1.

The observed polarization of the stars with the shells presumably involves three components: the interstellar polarization $\vec{P}_{IS}$, the polarization caused by optical dichroism of the shell $\vec{P}_{CS}$, and the polarization due to light scattering in the non-spherical shell $\vec{P}_{sh}$ (see e. g. Berdiugin et al., 1990). For the "variable circumstellar extinction" model accepted, the polarization at given wavelength should vary with brightness variations as follows:

$$\vec{P}(\Delta m) = \vec{P}_{\rm IS} + \vec{P}_{sh} \frac{I_{sh}}{I_0 \cdot 10^{-0.4\Delta m}} + \vec{P}_{CS} \left(1 - \frac{I_{sh}}{I_0 \cdot 10^{-0.4\Delta m}} \right), \quad (2)$$

where Δm is the stellar brightness decrease, I_{sh} is the flux of the scattered radiation, and $I_0 = I_* \exp(-\tau_{sh}) + I_{sh}$ is the total flux of the object (star+envelope) at the maximum brightness level.

The ratio I_{sh}/I_0 can be estimated as the maximum brightness fall is limited by the scattered light

$$(\Delta m)_{max} \leq -2.5 \log \frac{I_{sh}}{I_0}. \quad (3)$$

Table 1 Observational characteristics of the stars and derived parameters of the models

Star	BF Ori	UX Ori	WW Vul	CQ Tau
m, mag	~9.5	~9.6	~10.2	~9.5
$(\Delta m)_{max}$	3.0	2.7	2.4	1.8
P_b, % (m)	0.2 (9.82)	0.7 (9.86)	0.6 (10.25)	2.7 (9.48)
P_f, % (m)	5.1 (12.15)	7.2 (12.12)	5.9 (12.26)	6.7 (11.25)
P_{IS}, %	0.5	0.5	0.7	1.5
τ_{sh}	0.2	0.3	0.3	0.7
I_{sh}/I_0	$\leq$0.06	$\leq$0.08	$\leq$0.10	$\leq$0.19
P_{sh}, %	7.6	8.8	7.7	7.4
P_{CS}, %	1.0	0.8	1.2	2.8
Λ	~0.2	~0.2	~0.3	>0.2

Note: all values for the optical wavelength

Taking for $(\Delta m)_{max}$ the maximum difference between the ever observed values, we arrive at an upper limit for the ratio I_{sh}/I_0 (see Table 1). For $(\Delta m)_{max}$ as large as 2^m, this limit provides a good approximation to the ratio.

Having the polarimetric and photometric measurements for two brightness levels, the estimates of $\vec{P}_{IS}$ from the literature and of I_{sh}/I_0 from the above consideration, we can evaluate the components $\vec{P}_{CS}$ and $\vec{P}_{sh}$ (see Table 1). The former component is determined by the processes in the shells which are poorly known; our models can provide information about the latter component only.

We have calculated the intrinsic polarization $\vec{P}_{sh}$ for different models that satisfactorily explain the observed SED and the stellar tracks in the CMDs. We found that all of them gave too low polarization degree even for the shell semiaxis ratio $a/b = 5$. It should be pointed out that the polarization degree P_{sh} is known to have a maximum at $a/b \approx 5$, and the maximum mainly depends on the dust grain parameters (see e. g. Voshchinnikov and Karjukin, 1994).

On the other hand, our calculations show that the models able to fit the polarization data (with the ratio I_{sh}/I_0 given in Table 1) have the IR flux which is several times smaller than the observed one.

We see the following ways of creating a dust shell model capable to explain both the IR spectra and the polarization behaviour simultaneously:

– *A disk-like geometry.* To test this point we have considered a variant with a disk-like shell (a sphere without two cones). The polarization degree obtained was about 13% whereas the spheroidal shell with all other parameters being the same gave 6%. A possible tool for identification of the geometry of the shells can be offered by a comparison of the observational and theoretical polarization and intensity maps. Such maps have been calculated by us and will be discussed elsewhere.

– *"Fluffiness" of dust particles.* There is some evidence that the dust grains around young stars may differ from the MRN-like ones (see e.g. Greenberg & Li, 1996). Perhaps, the following may be considered as another indication. For the objects under consideration, the optical thickness $\tau_{sh} < 1$. It is well known that for $\tau_{sh} < 0.3$–0.5 the following simple relation is kept (see e. g. Voshchinnikov and Karjukin, 1994)

$$\frac{I_{sh}}{I_*} \approx \tau_{sh}\Lambda, \tag{4}$$

where Λ is grain albedo. The Λ values obtained from Eq. (4) (see Table 1) show that the albedo is rather low and typical of fluffy grains. Unfortunately, in contrast to the "compact" dust particles adopted here the grain fluffiness adds several unknown model parameters while we have already too many free parameters and too few observational constraints.

4. CONCLUSIONS

– The behaviour of the brightness and polarization of the UX Ori-like stars during their minima provides essential constraints on the circumstellar dust models.
– The models with the spheroidal shell and compact ("non-fluffy") dust particles cannot explain all the observational data available for the HAe stars with Algol-like minima.
– The models with a disk-like geometry of the shell and/or with fluffy grains could remove the problem. High-resolution polarization maps could provide a critical test for the shell geometry.

Acknowledgements. N.K. is grateful to Prof. J. Krelowski for warm hospitality and offering excellent working conditions during her stay at the UMK (Torun). She also acknowledges the support by the US-Poland M.Sklodowska-Curie Joint Fund (grant MEN/NSF-94-196). Participation of N.K. in the Conference was funded by the ISF and NASA. She thanks Dr. Y. Pendleton for kind help in travel arrangements. V.I. is thankful to the Alexander von Humboldt Foundation for the financial support of the work.

References

Berdiugin, A. V., Berdiugina, S. V. et al. 1990, *Astron. Zh.*, **67**, 812.

Fischer, O. 1995, *Rev. Mod. Astr.*, **8**, 103.

Greenberg, J. M., Li, A. 1996, *Astr. Ap.*, preprint.

Grinin, V. P. 1988, *Pis'ma Astron. Zh.*, **14**, 27.

Krivova, N. A. 1996, *Pis'ma Astron. Zh.*, submitted.

Men'shchikov, A. B., Henning, Th. 1996, *Astr. Ap.*, in press.

Voshchinnikov, N. V., Karjukin, V. V. 1994, *Astr. Ap.*, **288**, 883.

AN INFRARED STUDY OF THE JUGGLER NEBULA

J. C. HOLBROOK *University of California, Santa Cruz, California, USA*
P. TEMI *University of California, Santa Cruz, California, USA*
D. RANK *University of California, Santa Cruz, California, USA*
J. BREGMAN *NASA Ames Research Center, MS 245-6, Moffet Field, CA 94035-1000*

ABSTRACT. This work is an examination of the infrared reflection nebula surrounding a protostellar source, IRS 1, in the CRL 2136 region at 2.2, 3.08, and 3.45 μm. The greatest absorption due to water ice occurs within 5 arcsec (10,000 AU, D = 2000pc) of IRS 1. The water ice absorption decreases with increasing radius from IRS 1. This τ_{ice} structure suggests that the water ice is primarily associated with IRS 1. The flux from IRS 1 has a [2.2] - [3.45] color of 5, much redder than the nebula. The color structure combined with the τ_{ice} structure suggests the presence of an icy-dusty disk around IRS 1 orientated NE to SW. Radio CO maps presented by Kastner *et al.*(1994) reveal a molecular outflow orientated perpendicular to the disk. The south and east reflection lobes line the conical cavity created by the blueshifted molecular outflow.

1. INTRODUCTION

Previous studies of GL 2136 (1950: 18 19 39.3 -13 31 18) reveal a protostellar object, IRS 1 ($L \approx 7.2 \times 10^3 L_\odot$) which is the source of a massive molecular outflow (Kastner 1994). At near infrared wavelengths, three reflection lobes are visible which give the region its name: The Juggler Nebula. The polarization at 2.2 μm has an elliptical structure which suggests the presence of a disk around IRS 1 and that IRS 1 is the sole illuminating source for the reflection nebula (Minchin 1991, Kastner 1992).

The spectral energy distribution of GL 2136 has a prominent absorption feature at 3.08 μm due to water ice (Willner 1982). The polarization study of Hough *et al.*(1989) concludes that the near infrared continuum in the nebula arises from aligned grains and that the polarization in the 'ice band' arises from icy grains which are not uniformly distributed along the line-of-sight towards IRS 1. Kastner *et al.*(1992) propose that the water ice absorption originates from a circumstellar disk around IRS 1.

This paper presents the $M_{2.2}$ - $M_{3.45}$ color structure and the water ice, τ_{ice}, absorption structure of GL 2136. The 2.2 μm data is compared to a simple single scattering calculation. The implications of the color and τ_{ice} maps and the single scattering analysis are discussed in §3. The conclusions are presented in §4.

2. OBSERVATIONS

The observations were made at the Lick 3 m telescope on Mt. Hamilton on September 18 and 19, 1992. An infrared camera with an Amber Engineering 128x128 InSb array was used at solid nitrogen temperatures ($\sim 55^o$) for data collection. The plate scale of the images is 0.32 arcsec per pixel. The images were taken in staring mode with exposure times of 30 seconds at 2.2 μm, 6 seconds at 3.45 μm, and 20 seconds at 3.08 μm. An optical camera with autoguider was used for accurate pointing. The 2.2 μm, K band filter measures the continuum between 2.05-2.45 μm. The 3.08 μm filter measures the ice absorption band with $\Delta\lambda/\lambda = 1.9\%$. The 3.45 μm filter, with $\Delta\lambda/\lambda = 3\%$, measures the continuum longward of the ice band. The Image Reduction and Analysis Facility (IRAF) and the Interactive Data Language (IDL) were used for the reduction and analysis of the data. Image reduction began with the subtraction of sky frames from the object frames. A flat field was created using images of the illuminated dome with the bias and dark current removed. After flat-fielding, the object images were registered and co-added to produce one frame for each filter. The combined exposure times for GL 2136 are 60 seconds at 2.2 μm, 240 seconds at 3.09 μm, and 60 seconds at 3.45 μm. The final images were flux calibrated using the star Alpha Cygnus, with absolute flux values taken from the IRTF Observor's Guide.

3. ANALYSIS

Calculating the $M_{2.2}$ - $M_{3.45}$ color for the reflection nebula discloses the reddening due to dust extinction. The $M_{2.2}$ - $M_{3.45}$ color structure is presented in Figure 1 as a grayscaled image. The protostellar object has the 'reddest' value of $\approx$ 5. The south and east lobes are 'bluer' with values of <3. The contours near the protostar are elongated in the NE-SW direction.

From radiative transfer, $I_{observed}=I_o e^{-\tau_{ice}}$. From the 2.2 μm and 3.45 μm data it is possible to create a linearly interpolated 3.08 μm image. This interpolated image represents the continuum that should be observed at 3.08 μm if there were no water ice in the nebula. The interpolated 3.08 μm data is used for I_o, while the observed 3.08 μm data is $I_{observed}$. The τ_{ice} structure is presented in Figure 1 (contours). The south lobe has a maximum ice optical depth of 2.56, while the east lobe is relatively featureless with an average τ_{ice} of 1.46. The highest values of τ_{ice} ($\approx$2.8) occur within 5 arcsec (10,000 AU) of IRS 1. The τ_{ice} contours near the protostar are elongated in the NE-SW direction and τ_{ice} generally decreases with distance from IRS 1. The fact that majority of the ice and dust absorption is associated with IRS 1 suggest the presence of an icy-dusty disk. The NE-SW elongation is consistent with the semi-major axis of the polarization ellipse at 2.2 μm (Kastner 1992, Minchin 1991). There is a possibility that some of the absorption is due to ice grains in the intervening molecular cloud.

Given the bolometric luminosity of IRS 1 and the 2.2 μm flux observed in the reflection nebula, an effective protostellar temperature and grain albedo can be estimated. These values (graphite grains: T_{eff}=675 K, $\omega_{2.2}$=.38) are used to calculate what the surface brightness should be at a projected distance from IRS 1, given a uniform distribution of scatters. In Figure 2 the calculated values are compared to the observed surface brightness at 2.2 μm. A value of "1" indicates that the observed and calculated surface brightnesses are equal, while values <1 indicate that the observed nebula is fainter than expected. The low comparison values (<.5) can be explained by tilting the nebula to the line of sight and/or by extinction between

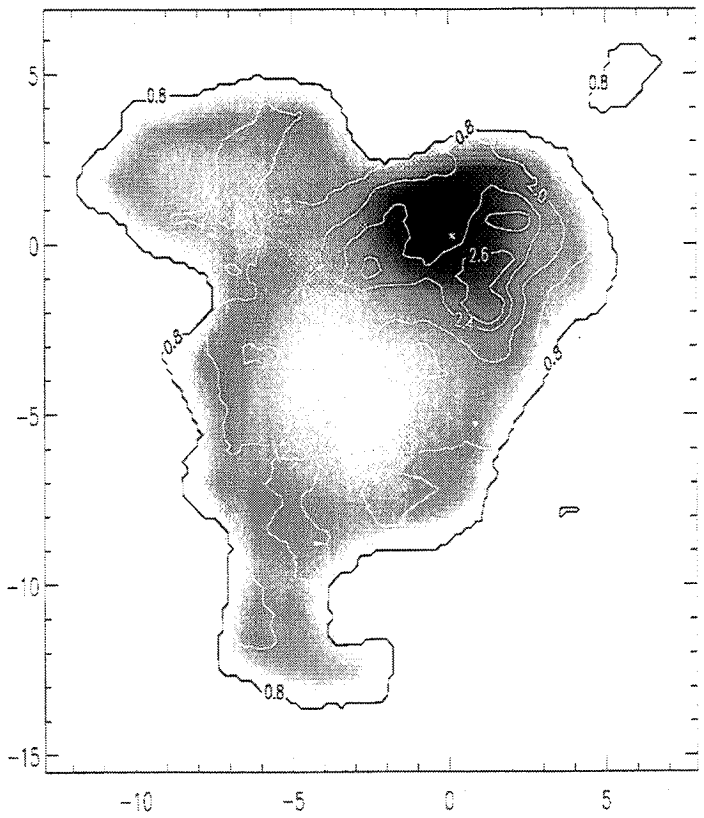

Figure 1. $M_{2.2}$ - $M_{3.45}$ with τ_{ice}: A grayscaled image of the $M_{2.2}$ - $M_{3.45}$ structure with τ_{ice} contours overlaid. A 3 σ mask has been applied to the data in both Figure 1 and Figure 2. IRS 1, at (0,0), is marked by "*". The maximum reddening value of 5 occurs at IRS 1. The south lobe is 'blue' and has a τ_{ice} maximum value of 2.56. The majority of the ice absorption appears to be associated with IRS 1.

a point on the nebula and IRS 1. Figure 2 shows scattering enhancements at the east, south and west lobes. The scattering enhancements are due to either a clearer line of light to IRS 1 or a higher density of scatterers. The scattering enhancements border the molecular outflow which is known to have a wide opening angle, and the west enhancement may be associated with the redshifted molecular outflow (Kastner 1994.)

4. CONCLUSIONS

- The τ_{ice} structure suggests that the majority of the water ice is associated with IRS 1. However, a percentage of the τ_{ice} structure could be due to foreground extinction.
- The $M_{2.2}$ - $M_{3.45}$ color has a maximum value of 5.0 at IRS 1. The color and τ_{ice} structure suggest the presence of an icy-dusty disk around IRS 1.
- The strong scattering enhancements in the east and south lobes in Figure 2 define the boundary of the cavity produced by the molecular outflow. The small scattering enhancement at the west lobe may be associated with the red shifted molecular outflow (Kastner 1994). The estimated opening angle of the blueshifted outflow from the 2.2 μm data is $\approx 45^o$.

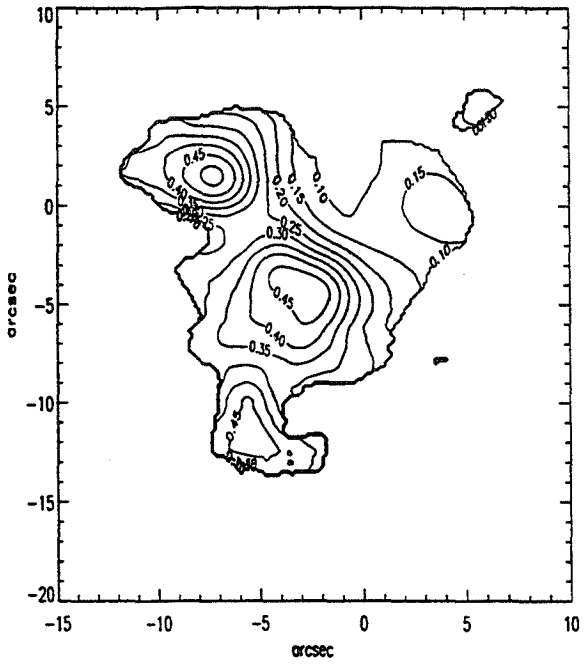

Figure 2. Comparison between a single scattering calculation and the 2.2 μm data. Scattering enhancements are seen at the east, south, and west lobes. The enhancement are due to a less obscured line of sight between IRS 1 and the lobe and/or a higher density of scatterers.

- The single scattering analysis used shows itself to be a powerful tool for defining the geometric structure of the circumstellar region and the molecular outflows. The maximum contour values of .45 as opposed to 1.0 are interpreted as due to further extinction arising within the outflow cavity plus the 40° inclination of the system.

References

Fukui, Y., Iwata, T., Mizuno, A., Bally, J., and Lane, A.P. 1993, in *Protostars and Planets III*, eds. E. H. Leby, and J. I. Lunine, (Tuscon: University of Arizona Press), p. 603.

Hough, J., Whittet, D., Sato, S., Yamashita, T., Tamura, M., Ngata, T., Aitken, D., and Roche, P. 1989, *M. N. R. A. S.*, **241**, 71.

Kastner, J., Weintraub, D., and Aspin, C. 1992, *Ap. J.*, **389**, 357.

Kastner, J., Weintraub, D., Snell, R., Sandell, G., Aspin, C., Hughes, D., and Baas, F. 1994, *Ap. J.*, **425**, 695.

Lada, C. 1985, *Ann. Rev. Astr. Ap.*, **23**, 267.

Minchin, N., Hough, J., Burton, M., and Yamashita, T. 1991, *M. N. R. A. S.*,**251**, 522.

Willner, S., Gillett, F., Herter, T., Jones, B., Krassner, J., Merrill, K., Pipher, J., Puetter, R., Rudy, R., Russell, R., and Soifer, B. 1982, *Ap. J.*,**253**, 174.

Uchida, Y., and Shibata, K. 1985, *Pub. Astr. Soc. Japan*, **37**, 515.

quarter-wavelength farther than the reflected component and the two components have equal magnitudes, circular polarization is transformed to linear. To measure all 4 Stokes parameters, we cross-correlate the four combinations of right and left circular on each baseline. As there is only one receiver on each telescope, we time-multiplex between right and left circular to obtain all correlations.

3. NGC 1333/IRAS 4A

The molecular cloud NGC 1333 lies at a distance of ~350 pc and is a site of active star formation. The young stellar object IRAS4A is part of a widely spaced (~10,000 AU) binary system. Millimeter continuum observations reveal several $M_\odot$ of circumstellar material around IRAS4A. This material may correspond to the magnetically supported envelopes predicted by theoretical models. A well-collimated bipolar molecular outflow extends over 2′ from the central source. Recent CSO-JCMT submillimeter interferometer measurements by Lay et al. (1995) revealed a 1.″8 binary at a position angle of 132°. Polarization emission from IRAS 4A has been detected in single-dish observations by Minchin et al. (1995). They measured 3.2% polarization with a magnetic field direction of 42°.

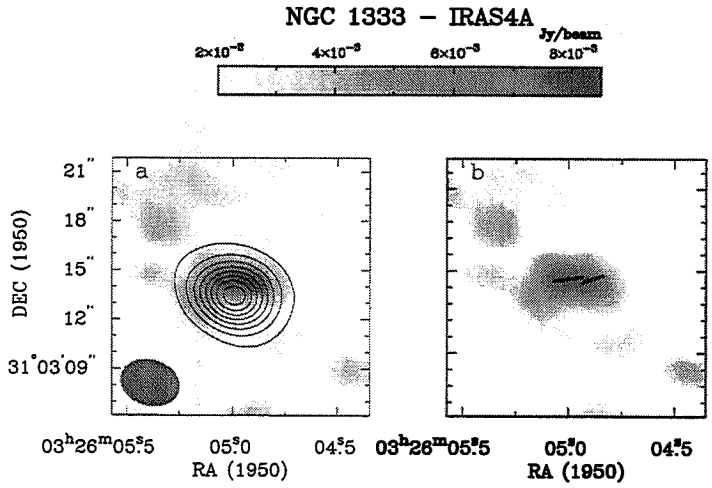

Figure 1. Polarized emission toward NGC 1333/IRAS4A. a) The polarized emission (grey scale) and the total intensity (contours). The counter levels are 25 mJy beam^{-1}. b) The polarized emission (grey scale) and polarization vectors for two positions.

Significant polarization emission is detected toward NGC 1333-IRAS4A (Akeson et al. 1996). The total intensity measured in the map is 270 mJy and the peak polarization is 8.6 ± 1.4 mJy beam^{-1} (Figure 1). The average polarized emission is 4.2% ± 0.8% of the continuum level. The polarization is extended in an east-west direction and the linear polarization peak is located north of the total intensity peak. The magnetic field direction at the peak linear polarization position is 7° ± 6°. The large scale outflow direction is roughly 45°, while near IRAS 4A it is directed almost north-south (Blake et al., 1995). The outflow position angle close to the source is

IMAGING POLARIZED DUST EMISSION IN STAR FORMATION REGIONS WITH THE OVRO MM ARRAY

RACHEL AKESON AND JOHN CARLSTROM *California Institute of Technology, Owens Valley Radio Observatory, Pasadena, California, USA*

ABSTRACT. We present OVRO interferometric observations of linearly polarized emission from magnetically aligned dust grains which allow the magnetic field geometry in nearby star formation regions to be probed on scales ranging from 100 to 3000 AU. Current results include observations of the young stellar objects NGC1333/IRAS 4A, IRAS 16293-2422 and Orion IRc2-KL.

1. INTRODUCTION

Magnetic fields are involved in all stages of star formation, from the collapse of the molecular cloud to the dynamics of accretion disks and outflows. Ambipolar diffusion may eventually remove most of the magnetic flux, but in the protostellar phase the field is dynamically important. Recent models of magnetized core collapse show that the curving field lines will produce a magnetically supported envelope of material (Galli and Shu, 1993; Fiedler and Mouschovias, 1993).

Observations of selective extinction from magnetically aligned dust grains have provided most of the information about magnetic field structure in molecular clouds. While this method is good for measuring the large scale fields in molecular clouds, it is ineffective in the highly obscured regions where star formation takes place. An ideal method of determining the magnetic field structure in protostellar disks and envelopes is to observe the polarized emission from the aligned dust. While single-dish far-infrared and sub-millimeter observations have detected polarized emission from aligned grains, these measurements can not resolve structures on protostellar size scales. Accordingly, we have installed polarimeters at the Owens Valley Radio Observatory Millimeter Array to investigate the magnetic field structure on size scales relevant to protostellar envelopes and outflows.

2. POLARIMETRY AT THE OVRO MILLIMETER ARRAY

The most sensitive measure of weak linear polarization, such as that produced by aligned dust grains, is to cross-correlate circular polarizations. At OVRO, the receivers are equipped with one linear feed. To produce circular polarization we placed adjustable wave plates in the optics path of each telescope. The wave plates consist of a wire grid which can be set at any angle and a flat mirror with adjustable spacing. When the spacing is set such that the transmitted component travels a

parallel to the magnetic field direction as predicted for core collapse along the field lines. Large scale ($\sim$1 pc) infrared selective extinction observations of NGC 1333 indicate a field direction of 125° (Tamura et al., 1988). The non-alignment between parsec and 1000 AU scales suggests substantial structure of the magnetic field deep within molecular cloud cores that should be further pursued.

3.1. Model for IRAS 4A

The offset of the linearly polarized emission from the total intensity can be explained by a magnetic field morphology in which the field has an hourglass shape (Figure 2) inclined from the plane of the sky and the optical depth of the emission is $\gtrsim 1$. In this model the field lines of the blue-shifted lobe are inclined toward the line of sight on the near side. Thus, more polarized emission is observed from the red lobe, in which the field lines are nearly in the plane of the sky.

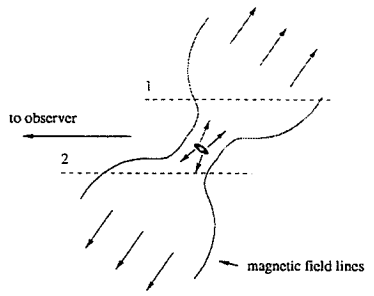

Figure 2. The hourglass magnetic field morphology used in the models.

Shown in Figure 3 are the total intensity and polarized emission for a model envelope with a density profile $n \propto r^{-2}$, temperature profile $T \propto r^{-0.5}$ and an hourglass field geometry as shown above. The envelope has an inner cutoff of 500 AU, set by the binary, and the density at this radius was chosen so that the maximum optical depth was $\sim$ 1. As seen in the figure the polarized emission peaks toward the red-shifted outflow lobe (top of figure) and is extended perpendicular to the outflow. The images have been smoothed with a 3″ Gaussian beam.

4. OTHER RESULTS

Polarized emission has also been detected toward the young binary source IRAS 16293-2422. The polarized emission is located between the continuum emission peaks of the two components. The implied magnetic field direction is along the major axis of the circumbinary disk.

Observations have been made toward the Orion KL region, though no polarized emission was detected with a 3σ upper limit of 3% in a 2.″5 beam. Single dish polarization surveys at far-infrared and sub-millimeter wavelengths have revealed a decrease in the polarization percentage toward the position of the high mass object IRc2 and

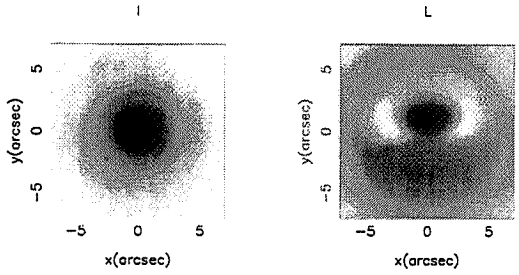

Figure 3. The total intensity (left) and the polarized emission (right) for the model described in the text.

the dense molecular gas referred to as the 'hot core'. Our millimeter polarization results suggest that this decrease is not due to field line tangling on 1000 AU scales.

5. CONCLUSIONS

We have detected linearly polarized emission from magnetically aligned dust toward the young stellar objects NGC 1333/IRAS4A and IRAS 16293-2422. The significant polarization levels detected require that the dust alignment mechanism is still effective at densities greater than 10^8 cm^{-3}. These observations have demonstrated the usefulness of millimeter interferometric polarimetry for investigating the magnetic field structure in the dense envelopes surrounding young stellar objects. Reflecting polarizers for the 1 mm band have been constructed and will be installed on the array in August, 1996. The maximum resolution of the OVRO mm array at 1 mm is 1″, allowing structures on scales of < 200 AU to be resolved at the distance of the nearest star forming regions (Ophiuchus, Taurus). Polarization studies at OVRO are supported by a NASA Origins grant.

References

Akeson, R., Carlstrom, J., Woody, D., and Phillips, J. 1996 *Ap. J. (Letters)*, **456**, L45.

Blake, G.A., Sandell, G., van Dishoeck, E.F., Groesbeck, T.D., Mundy, L.G., and Aspin, C. 1995, *Ap. J.*, **441**, 689.

Fiedler, R.A. and Mouschovias, T.Ch., 1993, *Ap. J.*, **415**, 680.

Galli, D. and Shu, F.H., 1993, *Ap. J.*, **417**, 220.

Lay, O.P., Carlstrom, J.E., Hills, R.E., and Phillips, T.G. 1995, *Ap. J. (Letters)*, **452**, L73.

Minchin, N.R., Sandell, G., and Murray, A.G. 1995, *Astr. Ap.*, **293**, L61.

Tamura, M., Yamashita, T., Sato, S., Nagata, T., and Gatley, I. 1988, *M. N. R. A. S.*, **231**, 445.

THE SPECTRAL ENERGY DISTRIBUTION OF HH 100 IRS

RALF SIEBENMORGEN *ISO Science Operations Centre, Astrophysics Division of ESA, Villafranca del Castillo, P.O. Box 50727, 28080 Madrid, Spain, rsiebenm@iso.vilspa.esa.es*

ABSTRACT. Recent progress in the modeling of the radiative transfer in star forming regions has lead to improved dusty envelope models. Such models can now explain in great detail the observed infrared spectrum. The success of such models suggests that input parameters correspond to the true physical situation of the environment of the young stellar object. However, so far only minor attention has been given to models which include the spectroscopic signature of ice bands. Such models are applied to the Herbig-Haro energy source HH100 IRS. Calculations have been performed to interpret the spectral energy distribution as a function of dust parameters such as the grain size, the ice volume fraction, and the "fluffiness" of the particles. The infrared spectrum together with the strength of the water ice band of HH 100 IRS is successfully reproduced if an upper limit of the grain size below 1 μm is used. Comet-like grains, with sizes above 1μm, result in a poor fit of the observations.

1. INTRODUCTION

Recently, Krügel & Siebenmorgen (1994) have proposed a new grain model for protostellar environments. They introduced the concept of fluffy grains, composed of subparticles of silicates and amorphous carbon, with an admixture of frozen ices. The authors assumed a power law grain size distribution ($n(a) \propto a^{-3.5}$), with a lower size limit of $a_- \geq 300$Å. The optical constants of Draine (1985) were used for the silicates, those by Preibisch et al. (1993) for amorphous carbon ices. In order to calculate the spectral energy distribution of HH 100 IRS, their model is modified as follows: To obtain the optical depth between between $2.5\mu\text{m} \leq \lambda \leq 11\mu\text{m}$, we use the optical constants of an ice mixture by Hudgins et al. (1993). As there is no good theoretical description to obtain the synthetic optical depths for fluffy particles (Ossenkopf 1993), we use the Bruggeman mixing rule. We use four component conglomerates for the dust. The relative volume fraction for silicates (f_{Si}), for amorphous carbon (f_{aC}), for ice (f_{ice}) and the "fluffiness" represented by vacuum (f_{vac}), satisfies $f_{Si} + f_{aC} + f_{ice} + f_{vac} = 1$. We assume the same cosmic abundances in dense regions as in the ISM and use $f_{Si}/f_{aC} = 1.41$. The other two volume parameters are not well constrained and we use $f_{vac} = 0.5$ and for the mass ratio of ice to refractive material $M_{ice}/M_{ref} \approx 0.5$. The optical constants of ices are a function of the temperature history. To estimate the strength of this effect, we adopt two temperatures, $T_{ice} = 100$ and 10K. Figure 1 demonstrates the effects of varying degree of vacuum fraction with values of $f_{vac} =$

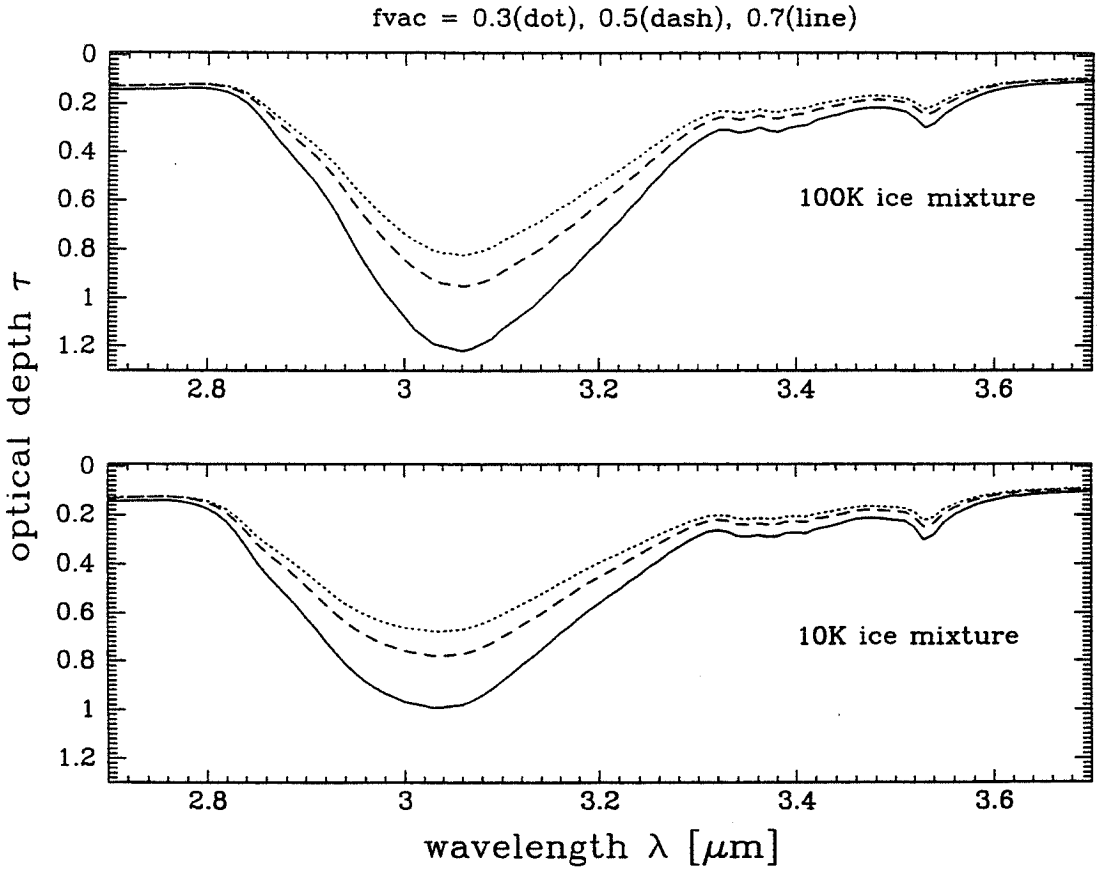

Figure 1. Influence of fluffiness on the optical depth. Models are shown for ice mixture with optical constants measured at temperature T_{ice} = 100 K (top) and 10 K (bottom) and with vacuum volume fraction f_{vac} = 0.3 (dotted), 0.5 (dashed line) and 0.7 (full line). The mass ratio M_{ice}/M_{ref} = 1 and and the upper grain size is $a_+ = 0.3\mu$m

0.3, 0.5, 0.7. It can be seen that the more fluffy particles increase the H_2O band strength. Perrin & Lamy (1990) have noted a similar effect on the Si-O stretch. Note that a certain dependence of the volume fractions on physical parameters of the environment is expected. In Figure 2 we show variations for $a_+ = 0.3, 1$ and $3\ \mu m$. For model calculations with $a_+ = 3\mu m$, mixtures of larger grains have increased band strength and for grain radii $a \approx \lambda$, scattering becomes important.

2. RADIATIVE TRANSFER MODELS OF HH 100 IRS

We have employed the dust model described above to calculate the spectral energy distribution of HH 100 IRS. We assume that HH 100 is embedded in an optically thick and spherical dusty envelope. The transfer problem is treated following the numerical approximation given in Siebenmorgen (1993). The radial dependence of the source function is written as:

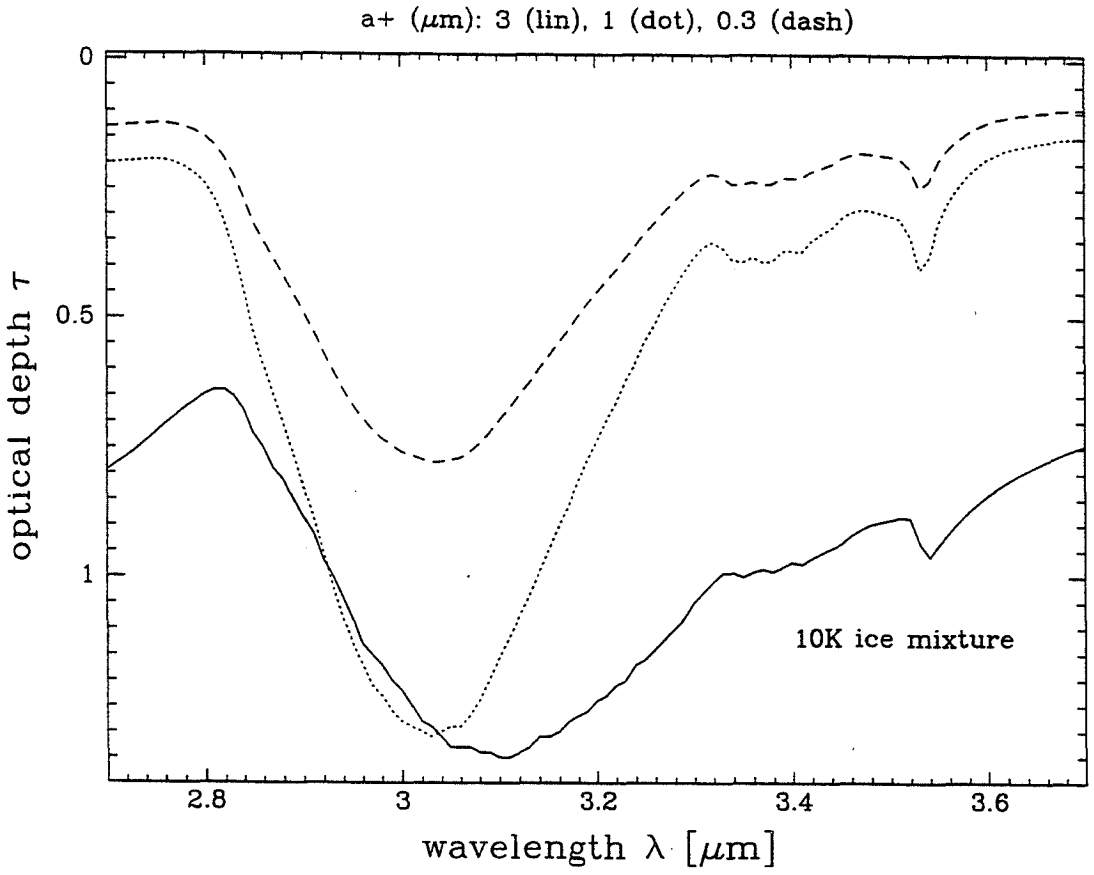

Figure 2. Influence of the upper limit of the grain size distribution on the optical depth. Models are shown for $a_+ = 0.3$ (dashed), 1.0 (dotted) and 3 μm (full line) with optical constants for ice mixtures measured at temperature $T_{ice} = 10$ K, vacuum volume fraction $f_{vac} = 0.5$ and mass ratio $M_{ice}/M_{ref} = 1$

$$S_\nu(r) = \frac{\kappa_\nu^{\rm abs}(T) B_\nu(T) + J_\nu(r) \cdot \kappa_\nu^{\rm sca}(T)}{\kappa_\nu^{\rm ext}(T)} \qquad (1)$$

The properties of our new dust model are incorporated into the radiative transfer code via the scattering ($\kappa_\nu^{\rm sca}$) and the extinction ($\kappa_\nu^{\rm ext}$) coefficients of the grains. We compute self consistently the change of temperature of the dust with distance from the star. In the outer parts of the cloud where the dust grains have temperatures below $T_{ice}^{evap} < 125K$, we use a four component dust model as described above, with dust parameters $a_- = 300$Å, $a_+ = 0.3\mu m$, f_{vac}= 0.5, $M_{ice}/M_{ref} = 0.5$. At distances closer to the center, where $T(a) > T_{ice}^{evap}$, we set $M_{ice} = 0$, but keep the remaining dust parameters unaltered. Our model does not consider a temperature history for the ice mixture, we use $\epsilon_{ice}(T) = \epsilon_{ice}(100K)$. The vacuum volume fractions are held constant, but an increase towards denser regions of the cloud is expected. We adopt the observed bolometric luminosity of L = 6.4 $L_\odot$ for HH 100 IRS and a distance of D = 130pc. The inner boundary r_i of the cloud follows from the adopted sublimation temperature, 1600K assumed here, and is $r_i \approx 0.3$ AU. In our model cloud we apply a dust density distribution $\rho(r) \propto 1/r$. For HH100, Reipurth et al.

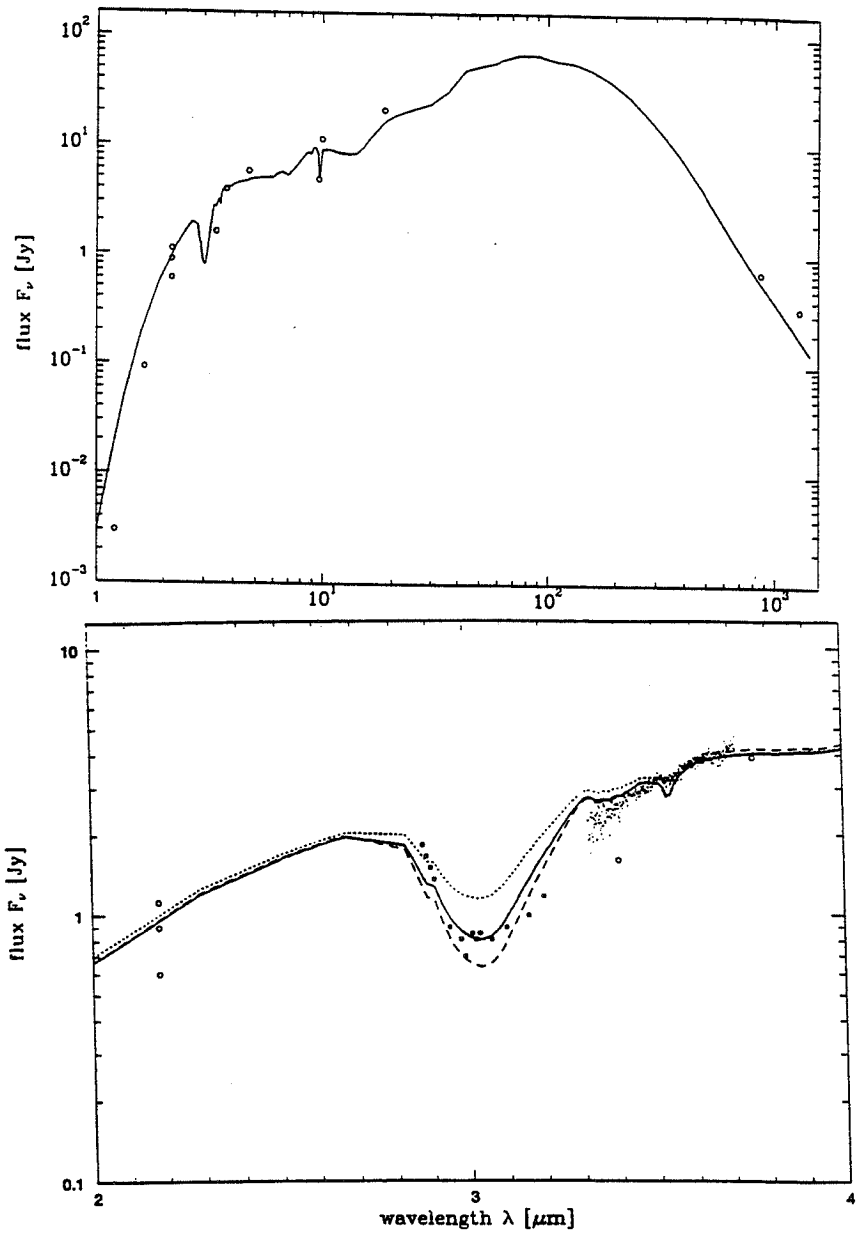

Figure 3. Spectral energy distribution of HH100–IR. a) Data by Molinari et al. (1993) and Reipurth et al. (1993) (circles) and model for $T_{ice}^{evap} = 125$ K (full line). b) Data by Molinari et al. (1993), circles, by Chen & Graham (1993), filled squares and Siebenmorgen et al. (1996), dots. The model is shown for ice evaporation temperatures $T_{ice}^{evap} = 200$ K (short dashed line), 125 K (full line) and 75 K (long dashed line).

(1993) obtain a value of $M_g \cdot \kappa^{ext}(1300\mu m) \approx 0.0054$ for the product of gas mass and dust extinction at 1300μm. This implies an outer boundary of $r_o \approx 2700$ AU and a mass of $M_g \approx 0.03 M_\odot$. The evaporation temperature of the ice within the multi-component grain mixture is taken as $T_{ice}^{evap} = 125K$ (Preibisch et al. 1993), which results in an ice evaporation zone with extension $r \leq 23$AU. The spectral energy distribution of HH 100 IRS is shown in Figure 3a together with bolometric observations. Figure 3b include high resolution observations. Models are shown for ice evaporation temperatures of $T_{ice}^{evap} = 200$, 125 and 75 K. As expected, a decrease of the ice evaporation temperature results in a decrease of the band strength of the ice mixture.

We have tried to fit the observations towards HH 100 IRS using larger grains. For this purpose we calculated synthetic spectra by varying the volume fraction of the vacuum, the ice mass as well as the upper limit of the grain size distribution. In particular we tried to fit the observations using *comet* like grains as proposed for β Pic by Greenberg & Li (1995). These grains have a sizes of typically larger than 1μm. In our exploration of the parameter space, we were unable to find a satisfactory fit of the observed SED of HH 100 IRS using micron sized grains.

References

Chen W.P., Graham J.A., 1993, ApJ 409, 319.

Draine B., 1985, ApJ Suppl 57, 587.

Greenberg J.M. Li, 1995, "The role of dust in the formation of stars", ESO workshop held in Garching, eds. Käufl & Siebenmorgen, Springer.

Hudgins D.M., Sandford S.A, Allamandola L.J., Tielens A.G.G.M. 1993, ApJS 86, 713.

Krügel E., Siebenmorgen R., 1994, AA 288, 929.

Molinari S., Liseau R., Lorenzetti D. 1993, AA Suppl. 101, 59.

Ossenkopf V., 1993, å280, 617.

Perrin J.M., Lamy, P.L., 1990, ApJ 364, 146.

Preibisch Th, Ossenkopf V., Yorke H.W., Henning Th., 1993, AA 279, 577.

Reipurth B., Chini R., Krügel E., Kreysa E., Sievers A., 1993, AA 273, 221.

Siebenmorgen R., 1993, ApJ 408, 218.

Siebenmorgen R., Starck J.L., Gredel R., 1996, "The role of dust in the formation of stars", ESO workshop held in Garching, eds. Käufl & Siebenmorgen, Springer.

EXTERNALLY INDUCED EVAPORATION OF YOUNG STELLAR DISKS IN ORION

D. JOHNSTONE *CITA, University of Toronto*
D. HOLLENBACH *NASA/Ames Research Center, Moffett Field*
F. SHU *Astronomy Department, University of California at Berkeley*

ABSTRACT. In this paper we propose a model for the evaporation of disks around young low-mass stars by external sources of high energy photons. Two evaporation techniques are possible. Lyman continuum radiation can ionize hydrogen at the disk surface powering a steady thermal ionized disk-wind or FUV radiation can heat the disk through photo-electric grain processes powering a slower thermal neutral disk-wind. Applying these two models to the evaporating objects in the Trapezium produces a satisfactory solution to both the mass-loss rate and size of the ionized envelopes.

1. OBSERVATIONAL CONSTRAINTS

Perhaps the most exciting discovery of star formation research has been the conclusion that most, if not all, stars are born with circumstellar disks. Through analogy with our own Solar System, one posits that these disks are the prenatal environs of extra-solar planets. In the quest for direct evidence of these protoplanetary disks, HST observations of the Orion nebula have provided the best optical evidence (see paper by McCaughrean in this volume and O'Dell and Wen 1994).

The shape and pointing direction of the extended optical emission around the young low-mass stars seen in the HST images incriminate $\theta^1 C$ (sp. type Oep) as the ionization source. The electron density in the ionized envelopes as determined from the radio emission measure (Felli *et al.* 1993) yields $n_e \sim 10^6$ cm^{-3} which is significantly greater than the diffuse nebular material $n_e \lesssim 10^4$ cm^{-3}. Such overpressure would lead to expansion of any fully ionized condensation on a dynamical time $r/c_s \sim 100$ yrs; thus, a steady evaporative flow is assumed to originate from the low-mass star-disk system. Flowing at the sound speed in the ionized gas, $c_s \sim 10$ km/s, the mass-loss rate can be determined: $\dot{M} \sim m_H n_e r^2 c_s \sim 10^{-7} M_\odot$/yr. Maintaining such a flow over the million year lifetime of the Trapezium region requires a neutral hydrogen source mass of $M > \dot{M} \tau_O \sim 0.1 M_\odot$.

Recent ground based adaptive optics observations (McCullough *et al.* 1995) determine a relationship between the size r of the extended objects, and the distance d from the ionization source, yielding a relation $r \propto d^{2/3}$. Any explanation for the mass-loss mechanism from the low-mass star-disk system must satisfy this observational constraint.

2. EXTERNALLY INDUCED EVAPORATION

Explaining mass-loss rates of order $10^{-7} M_{\odot}$/yr through internal processes in the low-mass star-disk systems proves difficult. Powerful outflows from young stars yield $\dot{M} \sim 10^{-6} M_{\odot}$/yr but are collimated and quick moving. Thus, they would not be expected to produces the shapes seen in the Trapezium region. No other internal mass-loss mechanisms are known to produce such high mass-loss rates.

Given the nearby proximity of the energetic star $\theta^1 C$, which is responsible for much of the Orion nebula appearance, it is worthwhile considering its externally induced effect on the low-mass star-disk systems. In particular, the high energy photons produced by $\theta^1 C$ are capable of heating disk surfaces and creating thermally driven disk-winds. For extreme ultraviolet radiation (EUV) the hydrogen at the surface of the disk is ionized directly and an HII region equilibrium of 10^4 K is produced. Less energetic, far ultraviolet, photons (FUV) heat the disk surface predominantly through photo-electric grain processes, equilibrating at about 10^3 K and producing a structure similar to those found in photo-dissociation regions (Tielens and Hollenbach 1985).

The next sections outline order of magnitude solutions to both the EUV and FUV externally induced evaporation discussed in Johnstone (1995) (see also Bertoldi and McKee 1990) following the approach for internally induced evaporation (Shu *et al.* 1993 and Hollenbach *et al.* 1994). Particular attention is paid to the mass-loss rate and the observable size of the extended emission.

3. EUV HEATING

1. The total number of ionizing photons from $\theta^1 C$, an O6 spectral type star, is $\Phi_* \sim 10^{49}$ s^{-1}. At a distance d from $\theta^1 C$ the incident flux is $F_i = \Phi_* / 4\pi d^2$.

2. A one-dimensional model for time-independent equilibrium requires that the incident flux of ionizing photons F_i equal the number of recombinations $n_e^2 \alpha l$ plus the number of ion pairs $n_e c_s$ created at the disk surface. That is, $F_i = n_e^2 \alpha l + n_e c_s$.

3. Two regimes are evident from the above equation. For $d < d_c$, the ionization is 'flux limited' and

$$n_e \sim \left(\frac{\Phi_*}{4\pi\alpha} \right)^{1/2} d^{-1} r_d^{-1/2}. \tag{1}$$

Integrating over the disk surface r_d yields the mass-loss rate,

$$\dot{M} \sim \left(\frac{4\pi\Phi_*}{\alpha} \right)^{1/2} m_H c_s d^{-1} r_d^{3/2}. \tag{2}$$

For star-disk systems in the Trapezium, the mass-loss rate as a function of distance is shown as the solid line in Figure 1. For $d > d_c$, the ionization is 'particle-flux limited' and the density drops as d^{-2}. yielding a steeper mass-loss rate with distance.

4. The size of the emission region formed around EUV heated disks should be $r_e \sim r_d$ since the ionization front coincides with the disk surface and the ion density drops as $n_e \propto r^{-2}$ in the disk-wind.

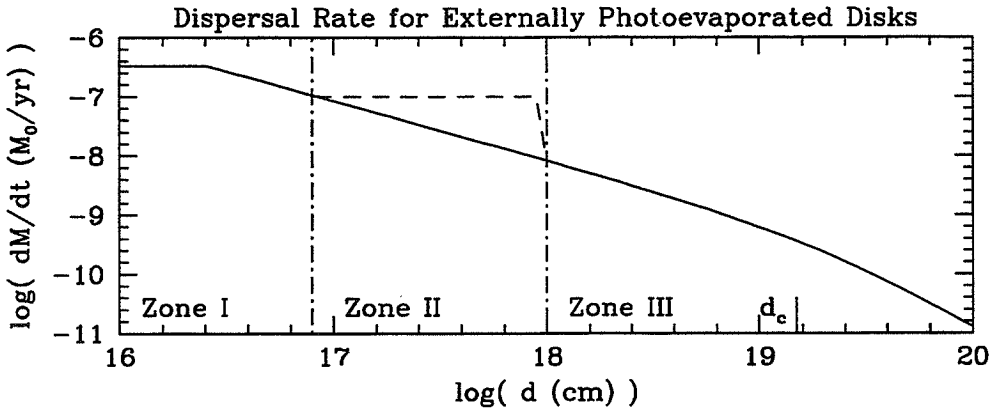

Figure 1. Mass-loss rates for externally evaporated disks. The solid line indicates the mass-loss rate due to photoionization heating and the dashed line indicates the enhancement when FUV heating dominates.

4. FUV HEATING

1. Opacity to FUV photons is produced through dust attenuation; thus, the atmosphere formed above the disk maintains an optical depth unity for FUV photons. That is, $\tau_{UV} \sim 1 \sim n_H \sigma l$.

2. For a standard dust to gas ratio the grain cross section is $\sigma \sim 10^{-21}$ cm^2. The pathlength is comparable to the size of the disk, $l \sim r_d \sim 10^{15}$ cm. Thus the number density in the evaporative flow is $n_H \sim 10^6$ cm^{-3}. Integrating over the disk the mass-loss due to FUV heating is

$$\dot{M} \sim 10^{-7} \left(\frac{r_d}{10^{15} \text{ cm}} \right)^2 M_\odot/\text{yr}. \quad (3)$$

The mass-loss rate is independent of distance from the FUV source $\theta^1 C$ as long as sufficient FUV flux is available for heating the gas to 10^3 K. The increased mass-loss rate due to FUV heating is shown as the dashed line in Figure 1. The inclusion of FUV heating introduces a plateau region into the mass-loss versus distance plot.

3. When FUV heating produces a higher mass-loss rate than EUV heating the ionization front moves off the surface of the disk (ionizing photons are unable to penetrate the entire outflow). The ionization front occurs at the position r_e along the path where $F_i = \int n_e^2 \alpha dl$. Due to spherical divergence $n_e \propto l^{-2}$ and conservation across the ionization front requires $n_e/n_H = (T_n/T_e)^{1/2}$ at the boundary. Since $F_i \propto d^{-2}$, $r_e \propto d^{2/3}$. The theoretical emission size versus distance from $\theta^1 C$ is shown in Figure 2 along with the sizes and positions of 13 evaporating objects observed in Orion by McCullough *et al.* (1995).

5. CONCLUSIONS AND REFINEMENTS

In this paper we have demonstrated that external FUV and EUV heating of young low-mass star-disk systems is capable of producing thermal disk-winds with appro-

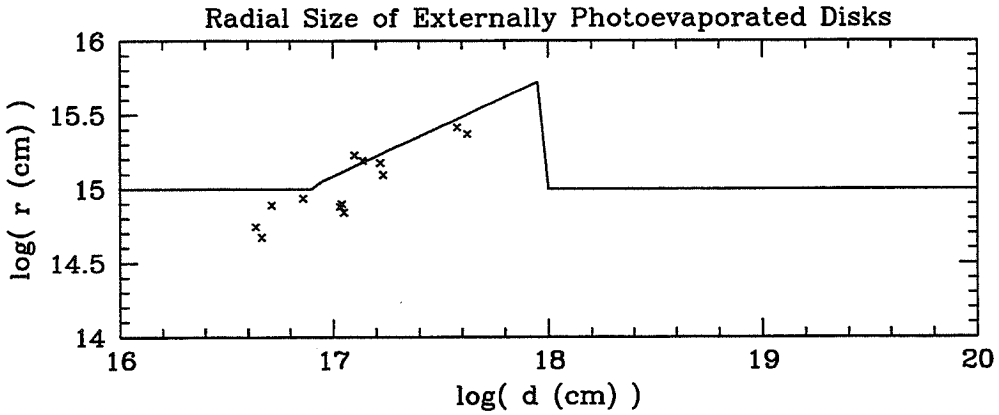

Figure 2. Size of the emission region around externally heated, star-disk systems. The sizes and positions of the evaporating objects observed by McCullough *et al.* (1995) are noted with crosses.

priate mass-loss rates. Further, when ionized by the EUV photons from $\theta^1 C$ these outflows produce the characteristic size-distance relation observed. Determination of the initial disk masses will enable specific age constraints to placed on the gestation period for planet embryos around stars in dense clusters.

Further modeling concentrates on reproducing the hydrodynamic effects within the wind for a technical determination of the velocity and density structure in the the thermal outflow. Radiation pressure on the outflow accelerates dust and gas away from $\theta^1 C$ presumably producing the head-tail structures seen in Orion. Finally, ongoing time dependent PDR calculations (with Antonella Natta and Herbert Stoerzer) of the FUV heated outflow will determine the temperature and composition within the neutral hydrogen wind.

References

Bertoldi, F. and McKee, C. F. 1990, *Ap. J.*, 354, 529.

Felli, M., Churchwell, E., Wilson, T., and Taylor, G. B. 1993, *Astr. Ap. Suppl. Ser.*, 98, 137.

Hollenbach, D., Johnstone, D., Lizano, S., and Shu, F. 1994, *Ap. J.*, 428, 654.

Johnstone, D. 1995 *UC Berkeley Thesis.*

McCaughrean, M. J. 1996, *this volume.*

McCullough, P. R., Fugate, R. Q., Chirtou, J. C., Ellerbroek, B. L., Higgins, C. H., Spinhirne, J. M., Cleis, R. A., and Moroney, J. F. 1995, *Ap. J.*, 438, 394.

O'Dell, C. R. and Wen, Z. 1994, *Ap. J.*, 435L, 149.

Shu, F. H., Johnstone, D., and Hollenbach, D. 1993, *Icarus*, 106, 92.

Tielens, A. G. G. M., and Hollenbach, D. 1985, *Ap. J.*, 291, 722.

CIRCUMSTELLAR DUST

THE 11 μm SILICON CARBIDE FEATURE IN CARBON STAR SHELLS

A.K. SPECK & M.J.BARLOW *Department of Physics and Astronomy, University College London, Gower Street, London WC1E 6BT, UK*
C.J.SKINNER *Space Telescope Science Institute, 3700 San Martin Drive, Baltimore, MD 21218, USA*

ABSTRACT. Silicon carbide (SiC) is known to form in circumstellar shells around carbon stars. SiC can come in two basic types - hexagonal α-SiC or cubic β-SiC. Laboratory studies have shown that both types of SiC exhibit an emission feature in the 11-11.5 μm region, the size and shape of the feature varying with type, size and shape of the SiC grains. Such a feature can be seen in the spectra of carbon stars. Silicon carbide grains have also been found in meteorites. The aim of the current work is to identify the type(s) of SiC found in circumstellar shells and how they might relate to meteoritic SiC samples. We have used the CGS3 spectrometer at the 3.8m UKIRT to obtain 7.5-13.5 μm spectra of 31 definite or proposed carbon stars. After flux-calibration, each spectrum was fitted using a χ^2-minimisation routine equipped with the published laboratory optical constants of six different samples of small SiC particles, together with the ability to fit the underlying continuum using a range of grain emissivity laws. It was found that the majority of observed SiC emission features could only be fitted by α-SiC grains. The lack of β-SiC is surprising, as this is the form most commonly found in meteorites. Included in the sample were four sources, all of which have been proposed to be carbon stars, that appear to show the SiC feature in absorption.

1. INTRODUCTION

It is widely accepted that dust particles form in the atmospheres of cool stars and are ejected into the interstellar medium, c.f. Gilra (1971), Woolf (1973), Stephens (1980), Mathis (1990). In this context there has been a great deal of work published on silicon carbide (SiC). From equilibrium condensation models, Friedemann (1969) and Gilman (1969) showed that silicon carbide should condense in the atmospheres of carbon stars. Following the work of Gilra & Code (1971), Hackwell (1972) and Treffers & Cohen (1974), a broad infrared emission feature seen in the spectra of many carbon stars, peaking at between about 11.0 and 11.5 μm, has been attributed to solid SiC particles. SiC is therefore believed to be a significant constituent of the dust around carbon stars. There are many different forms of SiC, but these can be divided into 2 basic types - alpha (α) and beta (β). α-SiC has a hexagonal or rhombohedric crystal structure and is very stable up to approximately 2700°C. β-SiC has a cubic structure and is also very stable, but will transform into α-SiC at temperatures above 2100°C. This transformation is unlikely to happen in reverse. The aim of this paper is

Table 1 SiC features and the Temperatures of the Sources

Source	$T_{BB}(K)$	SiC type (1)	SiC type (2)	SiC type (3)	SiC type (4)
AFGL 341	385	SiC-N	SiC-600	SiC-N	SiC-600
IRAS 21489+5301	455	SiC-600	SiC-600	SiC-N	Peg-SiC
AFGL 2699	475	SiC-N	SiC-600	SiC-N	SiC-1200
IRAS 02345+5422	525	SiC-600	SiC-600	SiC-N	Peg-SiC
IRAS 19594+4047	525	SiC-600	SiC-600	SiC-N	Peg-SiC
AFGL 3099	600	SiC-600	SiC-1200	SiC-N	SiC-600
AFGL 5102	600	SiC-600	SiC-600	SiC-N	SiC-600
AFGL 2155	615	Peg-SiC	Peg-SiC	SiC-N	SiC-600
IRAS 02152+2822	675	SiC-600	SiC-600	SiC-N	SiC-N
IRC+40540	680	SiC-600	SiC-600	SiC-N	SiC-600
AFGL 2368	800	SiC-600	SiC-600	SiC-N	SiC-600
V Hya	865	SiC-600	Peg-SiC	SiC-N	SiC-N
AFGL 2233	975	SiC-600	SiC-600	SiC-N	SiC-N
CIT 6	1100	SiC-600	SiC-600	SiC-1200	SiC-N
TU Tau	1100	—	SiC-600	SiC-N	SiC-600
IRC+50096	1200	SiC-600	SiC-600	SiC-600	SiC-600
Y Cvn	1350	Peg-SiC	SiC-600	SiC-N	SiC-600
R For	1400	beta-SiC	beta-SiC	SiC-600	SiC-600
R Lep	1500	—	—	SiC-600	SiC-600
UU Aur	1500	beta-SiC	Peg-SiC	SiC-600	SiC-600
UV Aur	1500	beta-SiC	SiC-600	SiC-600	SiC-600
V Cyg	1500	—	—	SiC-600	SiC-600
CS 776	1600	beta-SiC	—	SiC-600	SiC-600
V414 Per	1600	SiC-600	SiC-600	SiC-600	Peg-SiC
V Aql	2250	—	—	SiC-N	SiC-600

SiC-Type (1) = χ^2 fitting results for the flux-calibrated spectra over 7.5-13.5 μm.
SiC-Type (2) = χ^2 fitting results for the flux-calibrated spectra over 9.5-13.5 μm.
SiC-Type (3) = χ^2 fitting results for the normalised spectra over 7.5-13.5 μm.
SiC-Type (4) = χ^2 fitting results for the normalised spectra over 9.5-13.5 μm.

to determine whether either type predominates in the circumstellar outflows around carbon stars.

2. OBSERVATIONS

The stars in the sample were observed between October 1990 and November 1993. All observations were made using the United Kingdom Infrared Telescope (UKIRT) with the common-user spectrometer CGS3 (see Cohen & Davies 1995). The spectral resolution of these observations is 0.17 μm.

3. FITTING THE SPECTRA

We have fitted our observed spectra using a χ^2-minimization routine which includes the published optical constants for six forms of silicon carbide, taken from Friedemann et al. (1981) (α-SiC), Pégourié (1987) (Peg-SiC) and Borghesi et al. (1985) (SiC-1200, SiC-600, SiC-N; all forms of α-SiC; & β-SiC). We attempted to fit all 31 of the spectra taken. All attempted fits involved either a pure blackbody or a blackbody times a λ^{-1} emissivity, together with one form of silicon carbide. A problem with using the fitting routine over the 7.5 to 13.5 μm range is that some carbon stars have

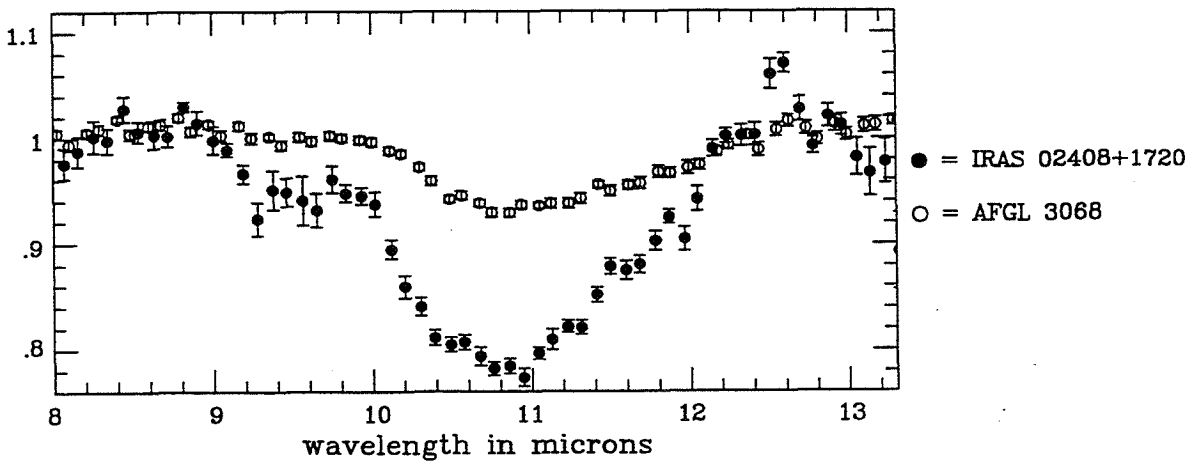

Figure 1. Absorption feature in the spectra of AFGL 3068 & IRAS 02408+1720

a feature at about 8.5 μm in their spectra, which has been attributed to amorphous hydrogenated carbon (α:C-H) dust in their circumstellar shells (Goebel et al. 1995). At this time the fitting program is not capable of including this feature into its minimisation routine. To overcome this problem the fitting program was used in several different ways for each spectrum in the sample.

Initially the routine was used over the whole wavelength range (7.5–13.5 μm). A second attempt at was restricted to wavelength longwards of 9.5 μm in order to avoid the α:C-H feature. Each of the spectra was also divided by a suitable blackbody in order to see the spectral features more clearly. The χ^2-fitting routine was then applied to these normalised spectra over both wavelength ranges (7.5–13.5 μm and 9.5–13.5 μm). The results of the fits are given in Table 1, together with the temperature of the blackbody that fitted the underlying energy distribution of the flux-calibrated spectra over 7.5–13.5 μm.

4. RESULTS – THE PREDOMINANCE OF α-SiC

Table 1 lists the sources in order of ascending blackbody temperature for the 8-13 μm continuum. There is an obvious predominance of the α-SiC form of silicon carbide. In particular the SiC-600 form of silicon carbide dominates the fits. This is the purest form of α-SiC treated by Borghesi et al. (1985) paper. The lack of β-SiC is surprising, given that this is the form most commonly found in meteorites – all α-SiC found in meteorites is believed to be due to contamination. Further work needs to be done to reconcile these findings.

5. ABSORPTION FEATURES

During our investigation we found four carbon stars which exhibit possible SiC absorption features. These can be split into two groups. AFGL 3068 and IRAS 02408+1720

have very similar absorption features, although IRAS 02408+1720 is much stronger (see figure 1). The feature seen in AFGL 3068 has previously been attributed to SiC in absorption (Jones et al. 1978, Justtanont et al. 1996) . Unfortunately the χ^2 minimisation routine is not equipped to deal with absorption, so the type of SiC responsible for these features is unknown. IRAS 19548+3035 and IRAS 21318+5631 also show very similar features, but are significantly different from AFGL 3068 and IRAS 02408+1720. They have a distinct double feature. For both objects the longer wavelength minimum is very similar to the feature seen in the spectra of AFGL 3068 and IRAS 02408+1720. It is plausible that these longer wavelength peaks are also due to SiC absorption. The cause of the shorter wavelength trough (with a minimum at 9.7μm) is unknown but may be due to silicates, which have characteristic bands between 9.5–10 μm. All these features need to be investigated more thoroughly.

References

Aitken, D.K., Roche, P.F., 1982, *M. N. R. A. S.*, **200**, 217.

Blanco, A., Borghesi, A., Fonti, S., Orofino, V., 1994, *Astr. Ap.*, **283**, 561.

Borghesi, A., Bussoletti, E., Colangeli, L., De Blasi, C., 1985, *Astr. Ap.*, **153**, 1.

Chan, S.J., Kwok, S., 1990, *Astr. Ap.*, bf 237, 354.

Cohen, M., Davies, K., 1995, *M. N. R. A. S.*, **276**, 715.

Friedemann, G., 1969, *Astron. Nachr.*, **291**, 177.

Friedemann, G., Gürtler, J., Schmidt, R., Dorschner, J., 1981, *Astrophys. & Space Science*, **79**, 405.

Gilman, 1969, *Ap. J. (Letters)*, **155**, 185.

Gilra, D.P., 1971, *Nature*, **229**, 237.

Gilra, D.P., Code, A.D., 1971, *Bull. Amer. Astr. Soc.*, **3**, 379.

Goebel, J.H., Cheeseman, P., Gerbault, F., 1995, *Ap. J.*, **449**, 246.

Hackwell, J.A., 1972, *Astr. Ap.*, **21**, 239.

Hoppe, P., Amari, S., Zinner, E., Ireland, T., Lewis, R.S., 1994, *Ap. J.*, **430**, 870.

Jones, B., Merrill, K.M., Puetter, R.C., Willner, S.P., 1978, *Astron. J.*, **83**, 1437

Justtanont, K., Barlow, M.J., Skinner, C.J., Roche, P.F., Aitken, D.K., Smith, C.H., 1996, *Astr. Ap.*, **309**, 612.

Mathis, J.S., 1990, *Ann. Rev. Astr. Ap.*, **28**, 37.

Pégourié, B., 1988, *Astr. Ap.*, **194**, 335.

Stephens, J.R., 1980, *Ap. J.*, **237**, 450.

Treffers, R., Cohen, M., 1974, *Ap. J.*, **188**, 545.

Whittet, D.C.B., Duley, W.W., Martin, P.G., 1990, *M. N. R. A. S.*, **244**, 427.

Woolf, N.J., 1973, in *IAU Symposium No.52, Interstellar Dust and Related Topics*, eds. J.M. Greenberg and H.C. van de Hulst (Boston:Reidel), p. 485.

ON THE CLASSIFICATION OF INFRARED SPECTRA FROM CIRCUMSTELLAR DUST SHELLS

G.C. SLOAN *NASA Ames Research Center, Moffett Field, CA*
I.R. LITTLE-MARENIN *Wellesley College, Wellesley, MA*
S.D. PRICE *Phillips Laboratory, Hanscom AFB, MA*

1. INTRODUCTION

We present results from an ongoing effort to classify the infrared spectra produced by circumstellar dust shells. Earlier efforts (described by Sloan et al. 1994) concentrated on oxygen-rich dust shells from sources associated with the asymptotic giant branch (AGB). Here, we describe the expansion of our classification to include S stars, supergiants, and carbon stars.

Sloan & Price (1995) defined a sample of bright AGB sources found by cross-referencing the General Catalog of Variable Stars (Kholopov et al. 1985-1988) with the IRAS Point Source Catalog (1988). Their sample contained 546 Mira, SRa, SRb, and Lb variables classified as M or K stars optically. For each source they classified the spectrum from the IRAS Low-Resolution Spectrometer by first removing the contribution from the stellar photosphere and then assigning the spectrum to one of several general emission classes (see Table 1).

Table 1. Infrared emission classes

Class	Description
N	**N**aked (no dust)
SE	**S**ilicate (and oxygen-rich dust) **E**mission
SB	**S**ilicate self-a**B**sorbed emission
SA	**S**ilicate **A**bsorption
CE	**C**arbon-rich dust **E**mission
H	very red spectrum (**H** II region)
P	**P**eculiar (or noisy)

For SE sources, they used the flux ratios of the dust emission at 10, 11, and 12 μm to classify the spectrum. They found that when plotting F_{10}/F_{12} vs. F_{10}/F_{11}, the spectra defined a narrow curve, which they identified as the *silicate dust sequence.* They used this sequence to improve on the classification system introduced by Little-Marenin & Little (1988, 1990), dividing it into eight segments, labelled SE1–8. SE1 spectra have low flux ratios and could be described as broad, low-contrast features peaking $\sim$12 μm. SE8 spectra have high flux ratios and represent the classic, narrow silicate feature at 10 μm. In between are the structured silicate emission classes. Figure 1 illustrates all eight SE classes.

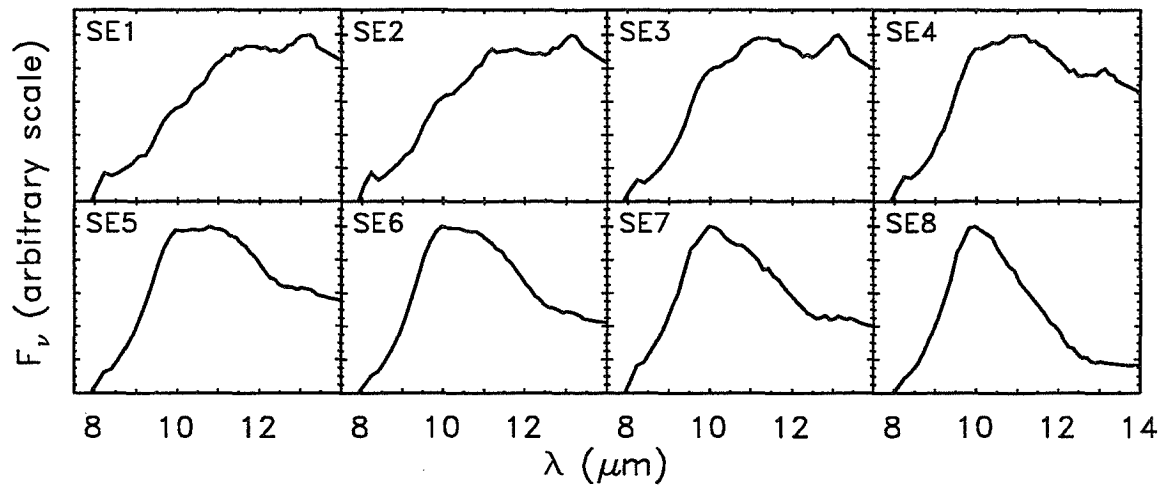

Figure 1. Sample dust spectra for each SE class. Each spectrum is the sum of all AGB sources of that class, after removal of the stellar contribution.

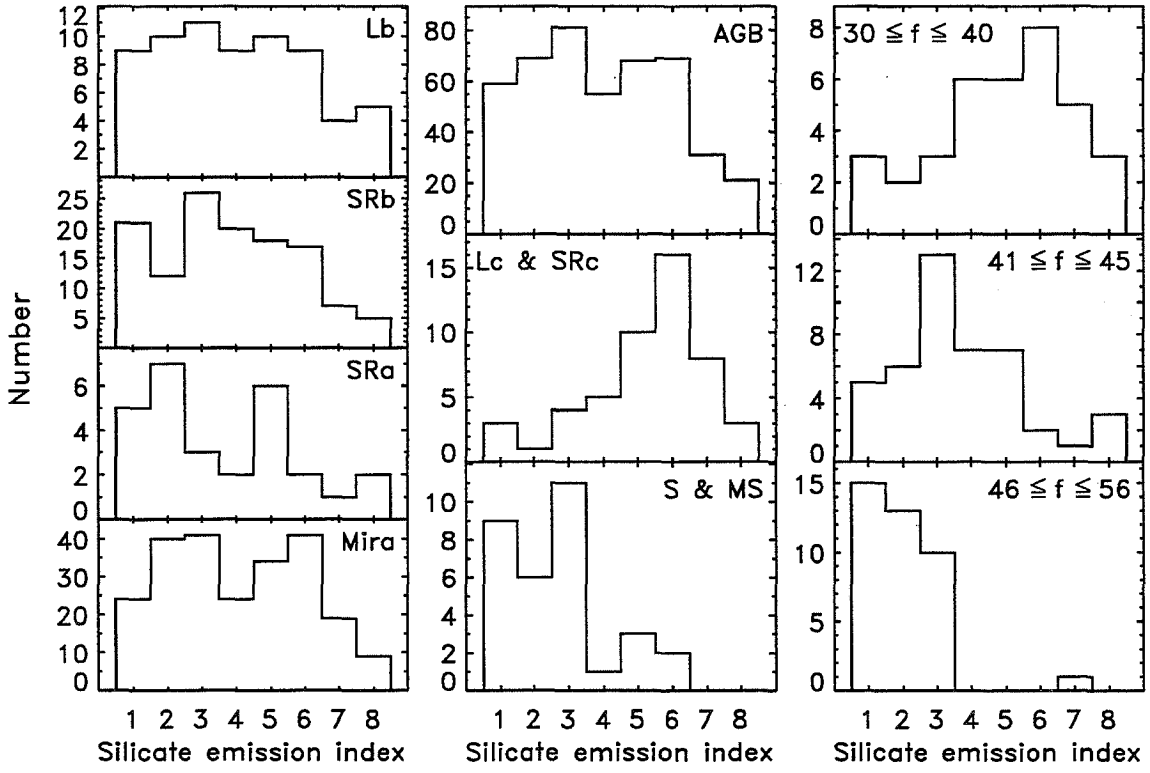

Figure 2. *Left:* The distribution of SE classes for the variables associated with the AGB. *Center:* A comparison of the AGB sample with the supergiants and S and MS stars. *Right:* The Miras separated by the asymmetry of their light curve ($f = 100 \times$ rise time/total period). Miras with the most asymmetric light curves and the supergiants tend to show classic silicate emission (SE6–8) while Miras with more symmetric light curves and the S and MS stars tend to show broad emission profiles (SE1–3).

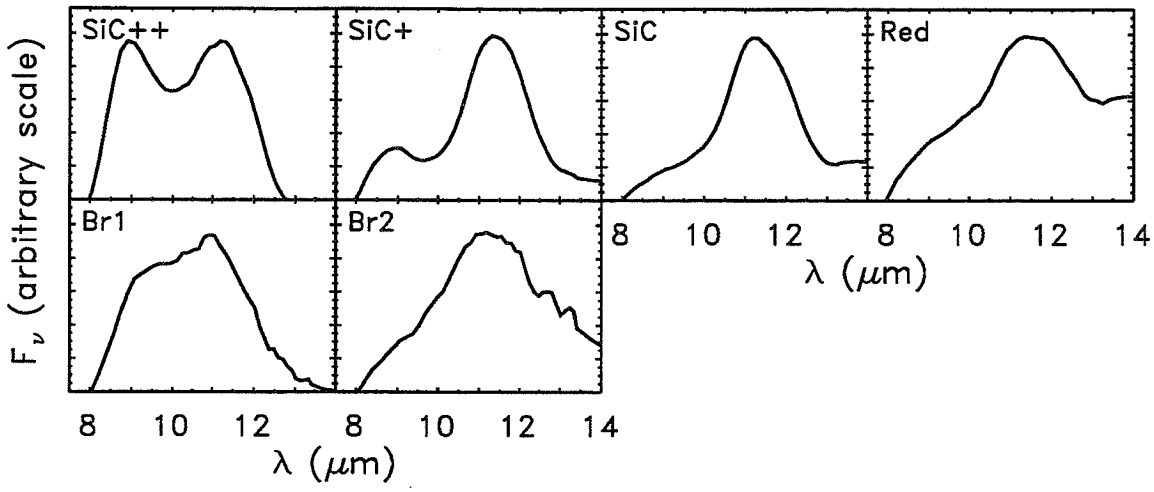

Figure 3. The classes of carbon-rich dust emission, determined as in Fig. 1 and smoothed slightly.

As discussed in more detail by Sloan & Price (1995, 1996), amorphous silicates produce classic silicate emission, amorphous alumina may explain the broad SE spectra, and crystalline silicates provide the best explanation for the structured SE spectra.

Sloan, LeVan, & Little-Marenin (1996) presented the results of a search for sources of the 13 μm emission feature (readily visible in the SE1–4 spectra in Fig. 1). They found that all types of emission spectra from oxygen-rich dust (broad, structured and classic) show a 13 μm feature. They estimated that up to ~50% of all SE spectra exhibit this feature, though low signal/noise prevents its detection in many sources. Among the bright SRb variables, over 90% showed a 13 μm feature, compared to only 20% of the bright Miras. The carrier of this feature seems to be diminished when the central star shows the strong and steady pulsations associated with Mira variables. One possible candidate for the carrier is crystalline alumina.

2. EXPANDING THE OXYGEN-RICH SAMPLE

Sloan & Price (1996) expand the AGB sample to include 24 S stars and 65 supergiants (variability class SRc or Lc). They supplement the small S star sample with 19 MS stars from the AGB sample. As shown in Figure 2, the distributions of classes of oxygen-rich dust spectra among the four variability classes in the AGB sample show no obvious differences. However, the AGB sample as a whole differs significantly from the supergiants, which tend to show classic silicate emission, and the S and MS stars, which concentrate strongly in the broad emission classes. Furthermore, separating the Mira variables by the shape of their light curves reveals that stars with symmetric light curves ($f \sim 50$) show only broad emission while stars with more asymmetric light curves have more classic silicate emission (as first pointed out by Vardya et al. 1986). It is suprising that the four variability classes in the AGB sample have such similar spectral distributions when considering how the distributions vary with the shape of the light curve among the Miras and how the percentage of 13 μm sources changes with variability class.

3. CARBON STARS

Sloan, Little-Marenin, & Price (1996) examine the sample of 96 carbon stars associated with the AGB (see also Little-Marenin, Sloan, & Price 1996). Nearly all of the sample show dust emission, although three sources have oxygen-rich dust (two are the well-known silicate/carbon stars BM Gem and V778 Cyg). The remainder of the sample belong to one of six classes (Fig. 3).

Four classes fall along a sequence: SiC++ $\rightarrow$ SiC+ $\rightarrow$ SiC $\rightarrow$ Red. The SiC++ and SiC+ sources have an emission feature near 8.5–9.0 μm accompanying the more common 11.2 μm emission feature attributed to SiC. Moving along the sequence to SiC and Red, the percentage of Miras increases while the feature around 9 μm decreases in strength, to be replaced by a cool continuum attributed to graphite or amorphous carbon. The 9 μm feature may arise from a precursor to graphite (Goebel et al. 1995). This sequence may represent the evolution from a thin to a thick shell produced as the pulsation of the central star steadies, increases in period and amplitude, and drives the mass-loss to extremely high rates.

Two additional classes, identified as Broad 1 and Broad 2, show unusual spectral emission which may be related to the 11.2 μm SiC feature.

References

Goebel, J.H., Cheeseman, P., & Gerbault, F. 1995, *Ap. J.*, **449**, 246.

IRAS Point Source Catalog, Version 2.0. 1988, Joint IRAS Science Working Group (Washington: GPO).

Kholopov, P.N., et al. 1985-1988, *General Catalogue of Variable Stars,* (4th Ed.; Moscow: Nauka and Greenbelt: NASA Astronomical Data Center) (GCVS).

Little-Marenin, I.R., & Little, S.J. 1988, *Ap. J.*, **333**, 305.

——. 1990, *A. J.*, **90**, 1173.

Little-Marenin, I.R., Sloan, G.C., & Price, S.D. 1996, in *IAU Symposium 177: The Carbon Star Phenomenon,* ed. R.F. Wing, in press.

Sloan, G.C., LeVan, P.D., & Little-Marenin, I.R. 1996, *Ap. J.*, **463**, 310.

Sloan, G.C., Little-Marenin, I.R., LeVan, P.D., & Price S.D. 1994, in *Airborne Astronomy Symposium on the Galactic Ecosystem: From Gas to Stars to Dust,* ed. M.R. Haas, J.A. Davidson, & E.F. Erickson (San Francisco: ASP), 425.

Sloan, G.C., Little-Marenin, I.R., & Price, S.D. 1996, in preparation.

Sloan, G.C., & Price, S.D. 1995, *Ap. J.*, **451**, 758.

——. 1996, in preparation.

Vardya, M., de Jong, T., & Willems, F. 1986, *Ap. J.*, **304**, L29.

FORMATION OF COSMIC CARBON DUST ANALOGS IN PARTIALLY HYDROGENATED ATMOSPHERES

A. BLANCO, S. FONTI, A. M. MUCI, AND V. OROFINO *Department of Physics, University of Lecce C.P. 193, 73100 LECCE (Italy)*

ABSTRACT. We present here UV-visible spectra of carbon grains produced by direct condensation of the carbon vapors in partially hydrogenated atmospheres. The freshly formed grains exhibit an extinction peak in the wavelength range 200-240 nm whose exact position depends on the hydrogen abundance. The results are discussed in terms of formation and evolution of circumstellar and interstellar cosmic dust.

1. INTRODUCTION

Recently in a series of works we have shown that the carbon grains produced and studied in our laboratory (Muci et al. 1994; Blanco et. al. 1995, 1996) may be good cosmic dust analogs. In particular, by producing and thermally processing fully hydrogenated amorphous carbon grains (Blanco et al. 1993; Mennella et al. 1995a), we have shown that the heat treatment of the particles can be a reasonable simulation of the grain processing active in space as modeled by other authors. The heat treatment decreases the hydrogen content of the grains which, for this reason, change their internal structure and their optical properties in the 190-260 nm range. An ultraviolet extinction bump, absent in the fully hydrogenated carbon grains, appears and becomes more and more pronounced as the annealing temperature increases, while at the same time the position of the peak shifts toward longer wavelengths.

In this work we show that similar results can be obtained if carbon grains are produced by direct condensation of the carbon vapors in partially hydrogenated atmospheres. By changing the contribution of the hydrogen gas to the total pressure inside the condensation chamber, the resulting grains exhibit an extinction peak whose wavelength position shifts toward longer wavelengths as the hydrogen abundance decreases.

The results presented in this work may explain the spectral differences in the ultraviolet extinction observed toward some circumstellar regions without invoking any kind of dust evolution and, at the same time, confirm the importance of the hydrogen abundance during the dust formation processes. This means that our findings may have important consequences for the nucleation/condensation theories and evolution of dust grains as well as for the study of dust formation regions.

2. EXPERIMENTAL RESULTS

The carbon grains studied in this work were prepared using the arc discharge technique (for further details on the production method, see Bussoletti et al. 1987, and

references therein). The arc discharge occurred between two amorphous carbon electrodes at a total pressure of 10 mbar and, in this work, the quenching atmosphere has been varied to obtain the condensation of grains directly in pure H_2, pure Ar, or in mixtures of the two gases. Several samples have been produced and their transmission spectra measured in the interval 190-900 nm by means of a dispersive double-beam spectrophotometer. Transmission electron microscopy (TEM) was used to estimate the mean size of the condensed grains and to identify diffracting phases. Also in this case of particles formed in mixtures of H_2 and Ar, there exist clustered spheroidal amorphous carbon grains having an average diameter of about 10 nm.

As expected from the results obtained in previous works (Blanco et al. 1991, 1993), the extinction spectra of carbon grains formed in pure H_2 atmosphere show a monotonic behavior with the absorbance decreasing with increasing wavelength (see fig. 1) while the spectra of carbon particles produced in a pure Ar atmosphere exhibit an extinction peak at about 240 nm. Starting from this well known situation, we have varied the composition of the ambient atmosphere, by changing the relative contribution of H_2 and Ar to the total pressure of the gas mixture, and we have produced several samples. The aim was to see if and how the H_2 abundance could influence the optical behavior of the carbon particles and in particular the position of the bump. In this way we have found that, if the partial pressure of hydrogen exceeds 2% of the total pressure (10 mbar) in the condensation chamber, the formation of the bump in the range 190-900 nm is inhibited and only a shoulder is present. For lower partial pressures the bump appears and becomes more and more pronounced and shifted toward longer wavelengths as the contribution of H_2 decreases (see Figure 1 and Table 1).

From the above results, it is clear that the abundance of gaseous hydrogen during the condensation process of the carbon grains influences the amount of hydrogen atoms locked up by the freshly formed particles and hence their optical properties (Mennella et al. 1995a, 1995b). We recall that, up to now, to vary the hydrogen content of the grains a thermal annealing process was used on particles freshly formed in an ambient atmosphere composed of pure H_2 (Blanco et al. 1993; Mennella et al. 1995a). The heat treatment decreases the hydrogen content of the grains which, for this reason, change their internal structure and their optical properties in the 190-260 nm range. An ultraviolet extinction bump, absent in the fully hydrogenated carbon grains, appears and becomes more and more pronounced as the annealing temperature increases, while at the same time the position of the peak shifts toward longer wavelengths (see fig. 2).

3. CONSEQUENCES ON COSMIC CARBON DUST

The experimental results reported in the previous section show that the same amount of hydrogen locked up by carbon grains can be obtained either by thermal processes or by direct condensation of the particles in partially hydrogenated atmosphere. Moreover, as already mentioned, the experimental results presented in this work may explain the spectral differences in the ultraviolet extinction observed toward some circumstellar regions without invoking any kind of dust evolution and, at the same time, confirm the importance of the hydrogen abundance during the dust formation processes. In such a case an alternative point of view, supported by our present experimental data and by the observational evidence, is that the carbon grains responsible for the circumstellar extinction do not change their hydrogen content with time so that their spectral properties can be regarded as a direct indication of the

actual hydrogen abundance in the ambient atmospheres in which they formed. If this hypothesis turns out to be real, then the observation of the spectral behavior of extinction caused by dust particles around carbon-rich sources can be a valuable tool to probe the hydrogen abundances in regions in which the carbon grains form.

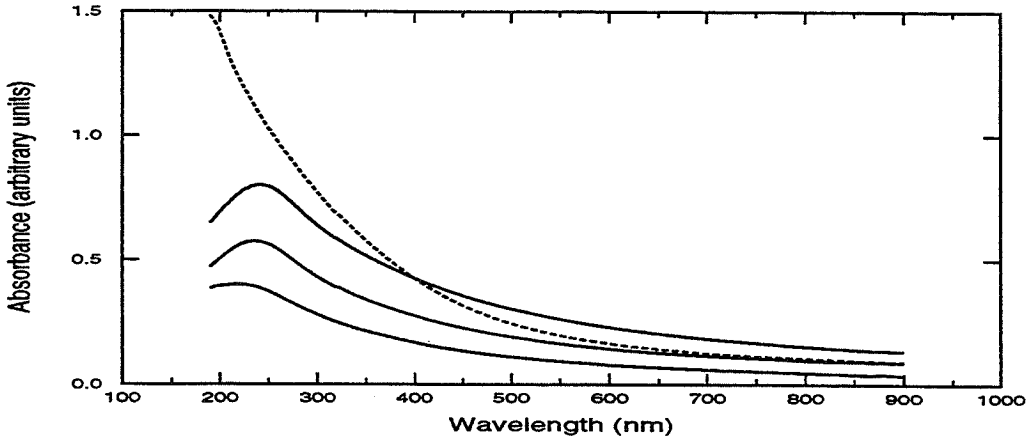

Figure 1. Absorbance of freshly formed carbon grains produced in pure H_2 atmosphere (dashed line), in two gas mixtures composed respectively by 1% of H_2 and 99% of Ar (bottom solid line) and by 0.27% of H_2 and 99.73% of Ar (medium solid line), and in pure Ar (top solid line). The curves have been arbitrarily shifted for clarity.

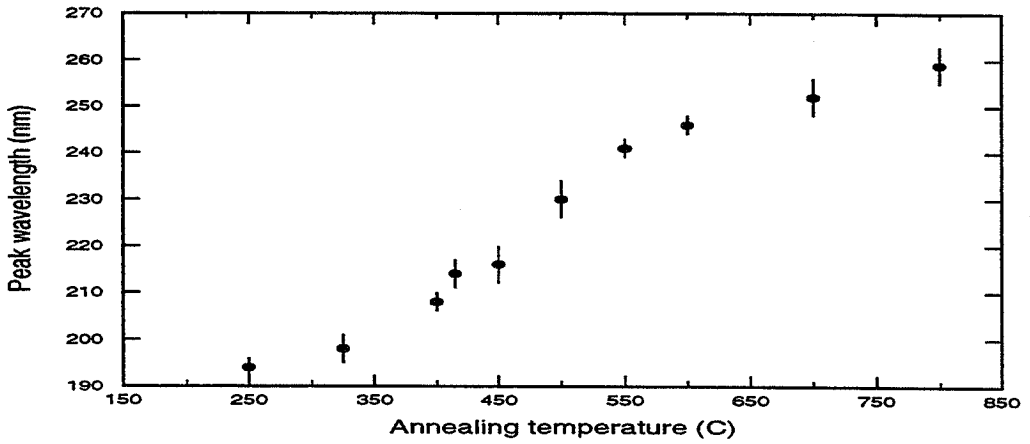

Figure 2. UV peak position of hydrogenated carbon grains annealed for 3 hr as a function of the annealing temperature. The error bars represent the uncertainties determined from repeated experiments on different samples.

As far as the 217.5 nm interstellar feature is concerned, if we assume that it is due to carbonaceous grains, then it follows that the grains must originate in the envelopes of carbon-rich sources. Once again, our experimental results corroborate the hypothesis of Hecht (1986) and Sorrell (1990) on the importance of the hydrogen content of the particles responsible for the 217.5 nm feature. The data presented in this work, however, change the point of view on the origin of such particles or at least

the time scale of their evolution: they need not be the result of the evolution of fully hydrogenated grains, but they can be formed in all the stellar environments in which the hydrogen abundance is low enough to produce grains with an absorption peak below 217.5 nm. This means that all these kinds of sources are the potential suppliers of future interstellar particles that undergo little or no evolution at all.

Table1

Peak wavelength, λ_p, of the absorbance measured for samples of freshly formed carbon grains produced in different gas mixture (see also Fig.1)

H_2(%)	Ar(%)	λ_p(nm)
0.00	100.00	240 ± 1
0.18	99.82	237 ± 1
0.27	99.73	235 ± 1
0.45	99.55	228 ± 2
1.00	99.00	217 ± 2

Acknowledgements. This work has been partly supported by ASI, CNR-GIFCO, and MURST.

References

Blanco, A., Bussoletti, E., Colangeli, L., Fonti , S. and Stephens, J.R. 1991, ApJ, 382, L97

Blanco, A., Bussoletti, E., Colangeli, L., Fonti, S., Mennella, V. and Stephens, J.R. 1993, ApJ, 406, 739

Blanco, A., Fonti, S. and Orofino, V. 1995, ApJ, 448, 339

Blanco, A., Fonti, S. and Orofino, V. 1996, ApJ, 462, 1020.

Bussoletti, E., Colangeli, L., Borghesi, A. and Orofino V. 1987, A & AS, 70, 257

Hecht, J. 1986, ApJ, 305, 817

Mennella, V., Colangeli, L., Blanco, A., Bussoletti, E., Fonti, S., Palumbo, P. and Mertins, H. C. 1995a, ApJ, 444, 288

Mennella, V., Colangeli, L., Bussoletti, E., Monaco G., Palumbo, P. and Rotundi, A. 1995b, ApJS, 100, 149

Muci, A. M., Blanco, A., Fonti, S. and Orofino, V. 1994, ApJ, 436, 831

Sorrell, W.H. 1990, MNRAS, 243, 570

TIME DEPENDENT MODELS OF GRAIN FORMATION AROUND CARBON STARS

M. P. EGAN *Phillips Laboratory, Hanscom AFB, Massachusetts, USA*
R. F. SHIPMAN *Phillips Laboratory, Hanscom AFB, Massachusetts, USA*

ABSTRACT. Carbon-rich Asymptotic Giant Branch stars are sites of dust formation and undergo mass loss at rates ranging from 10^{-7} to 10^{-4} $M_{\odot}/yr$. The state-of-the-art in modeling these processes is time-dependent models which simultaneously solve the grain formation and gas dynamics problem. We present results from such a model, which also includes an exact solution of the radiative transfer within the system.

1. INTRODUCTION

Modeling the physical properties of the AGB mass loss have until recently concentrated on either the gas outflow - assuming the existence of dust grains, or the grain formation process - assuming a steady state outflow. This ignores the fact that these processes are highly coupled. Woodrow and Auman (1982) solved the continuity and momentum equations for a two component (gas and grains) model. In the first half of this decade, a number of authors (Fleischer, *et al.* 1992, 1995; Dorfi & Hoefner 1991, Hoefner, Feuchtinger & Dorfi 1995; Egan 1993) have attempted to solve the problem of dusty outflows around carbon stars from first principles.

In the models of Fleischer *et al.* and Dorfi & Hofner and Hofner *et al*, grain nucleation is computed under the assumptions of classical nucleation theory. Egan & Leung (1995) demonstrate that classical nucleation theory is an inadequate description of the conditions encountered in circumstellar shells. As an alternative, we developed a combined master equation/moment equation method to accurately calculate grain formation and growth valid for the wide range of density conditions in circumstellar shells. For the models presented here, we combine this method of calculating grain formation with the partial differential equations governing the dynamics of the outflow. Gravity, radiative forces, and drag effects are taken into account. The resulting model yields a time-dependent model of circumstellar envelope development, detailing grain growth, velocity structure, and gas and grain density distributions.

2. METHODS

In Egan & Leung (1995) grain formation is described with a truncated set of kinetic equations (determining grain nucleation) coupled to moment equations similar to those derived in Gail & Sedlmayr (1988). The kinetic equations do not necessarily rely on equilibrium assumptions to calculate the classical nucleation rate, and are

easily amended for any chemical species and reaction rates. In these models, however, we are using simple carbon clusters and collisional rates in the reaction network. In reality the rates are more dependent on chemical bonding than this approach allows (at least for small N values; Donn & Nuth 1985).

2.1. Shell Dynamics

To model grain formation and outflow dynamics self-consistently, we solve the hydrodynamics equations of the circumstellar shell as amended to account for grain formation. It is necessary to solve these equations for the carrier gas (H_2), each molecular level considered in the master equation calculations, and the zeroeth moment, which represents the number density of our "average" grain. The higher moments are required only to satisfy the continuity equation. Thus, normalizing by the particle masses, and writing out the equations in full in terms of the number density n, the momentum μ, and the internal energy e of each component yields the system of equations (for 1-D spherically symmetric geometry)

$$\frac{\partial n_i}{\partial t} + \frac{\partial(\mu_i)}{\partial r} + \frac{2\mu_i}{r} = G_i(\mathbf{n}), \tag{1}$$

$$\frac{\partial(\mu_i)}{\partial t} + \frac{\partial(\mu_i^2/n_i)}{\partial r} + \frac{2\mu_i^2}{rn_i} = -F_i + R_i - n_i g(r) + G_i(\mu), \tag{2}$$

$$\begin{aligned} &\frac{\partial e_i}{\partial t} + \frac{\partial[\mu_i\{\gamma e_i - \frac{1}{2}(\gamma-1)\mu_i^2/n_i\}/n_i]}{\partial r} + \frac{2[\mu_i\{\gamma e_i - \frac{1}{2}(\gamma-1)\mu_i^2/n_i\}/n_i]}{r} \\ &\quad = \tfrac{1}{2}G_i(\mathbf{n})\mu_i^2/n_i^2 + G_i(\mathbf{n})kT/[(\gamma-1)M_i]. \end{aligned} \tag{3}$$

Here $G_i(\mathbf{n})$ represents the grain formation terms, $G_i(\mu)$ represent the equivalent processes governing momentum conservation, F the drag force due to other particles, R the force due to radiation pressure, $g(r)$ the acceleration of gravity, γ the ratio of specific heats for each gas component, and M_i the mass of each component particle.

2.2. Radiation Pressure

The radiation pressure felt by a grain is a function of its extinction cross section and the radiation field. Ideally, we would solve the radiative transfer equation for the medium in question and have complete knowledge of the radiation field. In this case, the force due to radiation pressure on grains can be written as

$$F_{rad}(r) = \frac{4\pi}{c}\int_0^\infty Q_{ext}(a,\lambda)\pi a^2 H_\lambda(r)d\lambda, \tag{4}$$

where $Q_{ext}\pi a^2$ is the extinction cross section of a grain of radius a, and H_λ is the Eddington flux at wavelength λ. Dominik *et al.* (1989) simplify this expression by making the following assumptions. With effective temperatures of around 2500 K, the radiation from cool AGB stars peaks at a wavelength of about 1 μm. Replacing $Q_{ext}(a,\lambda)$ with its value at 1 μm, and assuming the flux is only directed radially outward (which applies in optically thin material), the expression simplifies to

$$F_{rad}(r) = Q_{ext}(a, 1\mu m)\pi a^2 \frac{L_*}{4\pi r^2 c}. \tag{5}$$

For the grains, we use results from Mie theory to determine the extinction efficiency for amorphous carbon.

3. NUMERICAL METHOD

In solving numerically the partial differential equations (PDEs) for spherical flow, we are interested in obtaining accurate solutions for all components of our outflow. There exist several standard finite difference methods for solving such problems (for a review and comparison of these methods see Sod 1978). The grain formation problem is more complex because the grain formation term depends on the particle density of the gas components, *i.e.*, we have strongly coupled equations. Using a finite difference method introduces numerical dissipation into the solution. In the grain formation problem, we expect very sharp changes in density as grain formation takes place. Numerical dissipation has the effect of smoothing out this sharpness, thus destroying the validity of the solution. Techniques to reduce dissipation, such as artificial viscosity are available, but these require the addition of terms to the finite difference equations, along with the selection of coefficients for each term. In addition to being costly in terms of time and effort in picking these coefficients, these methods typically introduce oscillatory behavior into the solution (Sod, 1978). This would also give spurious results in our grain formation code which could be misinterpreted as actual physical structure. As an alternative, we are using the random choice method, or Glimm's method, to solve the hydrodynamics. Because Glimm's method can only solve the conservative form of the hydrodynamics equations (Sod 1977), we must split the equations into appropriate parts. This is accomplished by the method known as fractional steps, or operator splitting.

The splitting technique leaves us with the conservative form of the hydrodynamics equations, plus an ordinary differential equation (ODE) which contains the non-homogeneous terms from our original PDEs. Because Glimm's method is at best first order, we choose to use an implicit Euler method to solve this ODE.

For one of the models discussed here we also solve the equation of radiative transfer at each timestep. We use a 3-D Monte Carlo method, using a photon-bundling technique to accurately determine of temperature and Eddington flux (H_λ) with a minimum number of simulated photon paths.

4. RESULTS

In this paper, we primarily wish to investigate the effect on grain formation calculations of including a full radiative transfer treatment versus using the optically thin assumption. The differences in the models manifest themselves in the temperature distribution in the circumstellar shell and in the structure of the radiation field. If the dust is optically thin, the temperature distribution follows an r^{-p} law. This is seen in the dashed line in Fig. 1. As dust condenses and the shell opacity rises, the radiative transfer model calculates that the material beyond the condensation point, partially shielded from the stellar radiation, is at a temperature 50 K lower (solid line, Fig. 1) than the optically thin assumption predicts. For grain formation, this leads to a higher supersaturation ratio. Thus the grains which have formed are more stable against evaporation.

The optically thin assumption also leads to an over-estimation of the outflow velocity. The simplified radiation pressure term used in Eqn (5) does not take into account radiation emitted and scattered out of the radial direction when the dust opacity is high. The transfer model determines the Eddington flux in Eqn. (4)

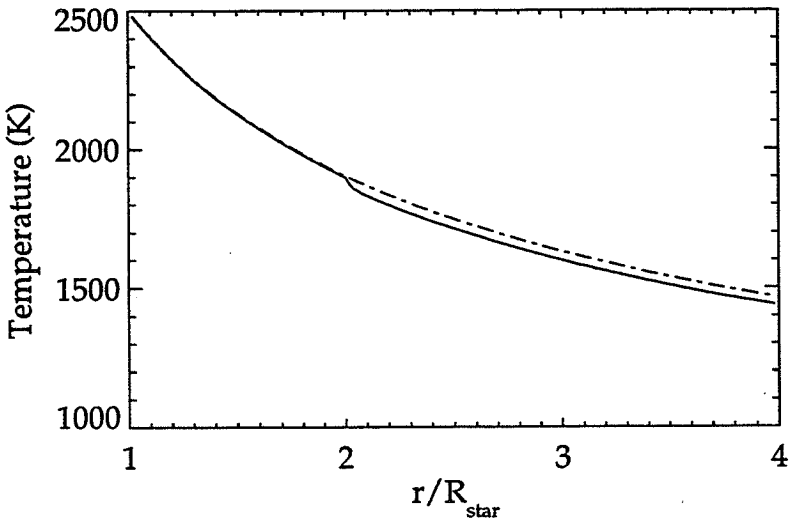

Figure 1. Temperature profile for grain formation models. Dashed line is temperature under optically thin assumption. Solid line is the temperature from solution of the radiative transfer equation at a time shortly after the onset of dust formation..

directly, and we find that the radiation pressure is less than that expected from the optically thin assumption.

References

Dominik, C., Gail, H.-P., and Sedlmayr 1989, *Astr. Ap.*, **223**, 227.

Donn, B. and Nuth, J. A. 1985, *Ap. J.*, **288**, 187.

Dorfi, E. A. and Hoefner, S. 1991, *Astr. Ap.*, **248**, 105.

Egan, M. P. 1993, PhD Thesis, Rensselaer Polytechnic Institute.

Egan, M. P. and Leung, C. M. 1995, *Ap. J.*, **444**, 251.

Fleischer, A. J., Gauger, A., and Sedlmayr, E. 1992, *Astr. Ap.*, **266**, 321.

Fleischer, A. J., Gauger, A., and Sedlmayr, E. 1995, *Astr. Ap.*, **297**, 543.

Gail, H.-P. and Sedlmayr, E. 1988, *Astr. Ap.*, **206**, 153.

Hoefner, S., Feuchtinger, M. U., and Dorfi, E. A. 1995, *Astr. Ap.*, **297**, 815.

Sod, G. A. 1977, *J. Fluid Mech.*, **83**, 785.

Sod, G. A. 1978, *J. Comp. Phys.*, **27**, 1.

Woodrow, J. E. J. and Auman, J. R. 1982, *Ap. J.*, **257**, 247.

THE SIZE DISTRIBUTION OF STARDUST INJECTED INTO THE ISM

D. KRÜGER *Institut für Astronomie und Astrophysik, Berlin. Germany*
E. SEDLMAYR *Institut für Astronomie und Astrophysik, Berlin. Germany*

ABSTRACT. A multi-component method for the description of the evolution of the grain size distribution in consideration of a size dependent grain drift and growth rate is applied in order to model dust driven winds around cool C-stars.

Grain drift introduces several modifications concerning dust growth: On the one hand the residence time in the region of efficient growth is reduced, on the other hand the growth efficiency is higher due to an increased collisional rate. For carbon grains the surface density of radical sites is increased, but on the other hand there is a reduction of the sticking efficiency of the growth species for drift velocities larger than a few $\mathrm{km\,s^{-1}}$.

It is found that the consideration of drift results in a considerable distortion of the size distribution as compared to the case of zero drift velocity. Generally, there are less, but larger grains if drift is included.

1. INTRODUCTION

The extended atmospheres of cool red giants are places of considerable dust formation accompanied by substantial mass loss. Radiation pressure on the dust grains with subsequent momentum transfer to the gas via grain-gas collisions is often discussed as a mechanism to drive these massive stellar winds (e. g.Gail & Sedlmayr, 1987).

Although the photon momentum absorbed by the dust is completely transfered to the bulk of the gas, i. e.complete momentum coupling may be assumed (e. g.Krüger *et al.*, 1994), the grains are not position coupled to the gas but move with a size-dependent drift velocity instead. This introduces several modifications concerning dust formation and growth: Since the grain drifts out of the gas element where it has been created, the time of residence in a region of efficient growth is reduced. On the other hand, the growth rate of grains is increased due to a larger collisional rate, and for carbonaceous grains the surface density of reactive radical sites increases with the drift velocity. However, for drift velocities larger than $\sim 5\ \mathrm{km\,s^{-1}}$there is a reduction of the sticking efficiency of the growth species. Last not least: Since the flux of grains is conserved the dust component becomes increasingly dynamically diluted for high drift velocities.

To study the effects of grain drift on dust formation and growth in circumstellar dust shells we have applied a new multi-component method for the description of the evolution of the grain size distribution (Krüger *et al.*, 1995) and calculated self-consistent models of stationary dust driven winds around cool C-stars.

2. METHOD

The stellar wind model is characterized by a combined eigen- and boundary value problem for a system of ordinary differential equations with an internal singularity (this is the critical or sonic point). The resulting wind solution is completely determined by the stellar mass M_*, the stellar luminosity L_*, the effective temperature T_* and the elemental abundances ϵ_i. The mass loss rate $\dot{M}$ follows as an eigenvalue.

By means of the multi-component method of Krüger *et al.*(1995) the grain size distribution can be determined on a non-uniform grid which is moving in grain size space. This grid is constructed by following the size evolution of a large, successively incremented number of grains (typically $N_{\max} \sim 300$) originating from appropriately chosen radii in the stellar envelope. A detailed description of carbonaceous grain growth according to a hydrogen–abstraction/acetylene–addition surface reaction scheme (Krüger *et al.*, 1996) was also included.

Further details on the self-consistent treatment of a multi-component dust driven wind and the method of solution can be found in Krüger & Sedlmayr (1996).

3. RESULTS AND DISCUSSION

For the construction of an exemplary model of a cool C-star envelope we adopted parameter values of $M_* = 1\,\mathrm{M}_\odot$, $L_* = 4\,10^4\,\mathrm{L}_\odot$, and $T_* = 2100$ K. The elemental abundances have been taken to be solar except for $\epsilon_\mathrm{C} = 1.7\epsilon_\mathrm{O}$. The corresponding mass loss rate is $\dot{M} = 3.6\,10^{-5}\mathrm{M}_\odot/\mathrm{yr}$. For comparison, the model was recalculated with the drift velocity of the grains artificially set equal to zero.

Figure 1a shows the radial course of the relevant velocities in the resulting wind model. Although the mean drift velocity $v_{\mathrm{dr},0}$ is rather small and comparable to the isothermal sound velocity c_T, the center of mass of the dust component drifts with a velocity $v_{\mathrm{dr},3}$ that is clearly supersonic. In the inner region of the wind the drift velocity may even be much higher than the gas velocity v_g. Remarkably, the general hydro- and thermodynamical structure of the envelope is quite similar, regardless of whether drift is considered or neglected. This is also true for the values of the mass loss rate and the terminal outflow velocity $v_{\mathrm{g},\infty}$ of the gas.

However, grain drift decisively influences the growth efficiency of the dust. In the subsonic regime close to the star the growth efficiency is depressed by a factor of up to 10, since the grains quickly drift away from their point of creation outwards to less efficient growth regions. The majority of the grains is created around the sonic point. Here, the two drift effects of "sweeping up" the condensable material and "drifting away" approximately cancel for these small grains ($a \sim 20$ nm). However, further growth of the larger grains is quite suppressed: Although the large drift velocity of these grains somewhat increases their surface radical density, the sticking efficiency is reduced. In the outer region ($r \gtrsim 3\,R_*$) growth is enhanced by a factor of up to 3 for the small and medium sized grains mainly due to the "sweeping up" of condensable material. No further growth of large particles takes place in the supersonic region.

Eventually the stardust will be injected into the interstellar medium (ISM). As has been shown by Woitke *et al.*(1993) dust destruction in the transition region of the red giant wind into the ISM is negligible. However, after the grains have come to rest in the ISM grain densities are increased by a size dependent factor $(v_{\mathrm{g},\infty} + v_{\mathrm{drift}}(a))/v_{\mathrm{g},\infty}$.

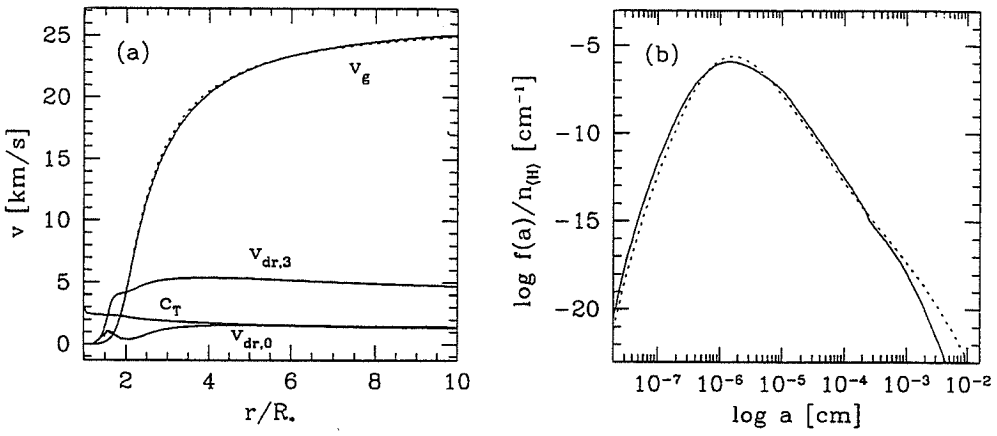

Figure 1. a Dynamical structure of the exemplary windmodel. b Grain size distribution after injection into the ISM. Dashed lines indicate the results neglecting drift.

The resulting size distribution after injection into the ISM is shown in Fig. 1b. Compared to the model neglecting drift (dashed line), the size distribution appears somewhat flattened. There is a pronounced decrease of the distribution at medium grain sizes (10 nm $< a <$ 50 nm). Furthermore, the amount of ultrasmall particles ($a \lesssim 10$ Å) is increased by almost an an order of magnitude. The existence of such an ultrasmall grain component in the ISM has been suggested on the ground of observations of 1–25 μm infrared emission from interstellar clouds (Sellgren *et al.*. 1983).

To first order, the distribution function can be fitted piece-wise by power laws of the form a^γ. The relevant part of the size distribution of the exemplary model including drift can be fitted by power laws with spectral indices $\gamma_1 \approx -2.5$ (20 nm $< a < 0.1\mu$m) and $\gamma_2 \approx -5.1$ ($a > 0.1\mu$m), respectively. Though tempting in this context, we think it is not apt to compare the obtained spectral indices with the one deduced for the size spectrum of the carbonaceous grain component in the interstellar medium (Mathis *et al.*, 1977) which is $\gamma \sim -3.5$. The latter is bound to result from the superposition of many size distributions originating from distinct dust forming objects, and is furthermore subject to repeated processing by interstellar shock waves.

We also present plots of $f(a)$ multiplied by a and a^4. In the left panel of Fig. 2 the area below the curve is proportional to the *number* of grains in a corresponding size interval. Obviously, in the negligible drift case the total number of grains is much higher than in the case where drift is included, although the position of the maximum, i. e.the most probable grain radius, does not vary much.

This reduction of the grain density due to drift by a factor of almost 2 can be explained by the nucleation rate peaking at a lower value. This is due to the fact that comparatively many large grains are formed in the inner region consuming a significant portion of condensable material (and therefore suppressing further efficient nucleation) without efficiently driving the wind (since these grains are dynamically diluted). This effect of drift should be quite independent of the the specific nucleation mechanism adopted here, since every realistic expression for the nucleation rate will to *some* degree be dependent on the amount of condensable material.

In the right panel of Fig. 2 the area below the curve corresponds to the *mass*

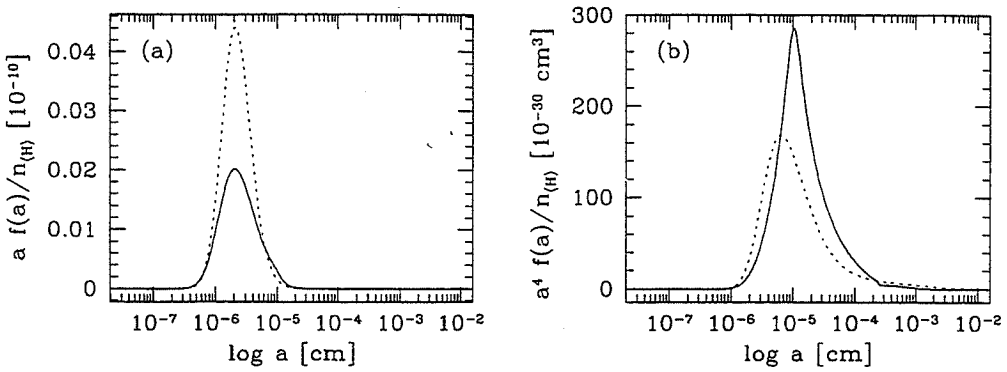

Figure 2. Grain size distribution after injection into the ISM. a Weighted by a. b Weighted by a^4. Dashed lines indicate the results neglecting drift.

contained in the grains. The consideration of drift leads to a significant shift of the distribution of condensed matter towards larger grain radii. The average grain mass is more than twice as large, and the dust-to-gas mass ratio $\dot{M}_d/\dot{M}_g$ injected into the ISM is increased by about 30% compared to the case of neglected drift.

4. CONCLUSIONS

To summarize, it can be said that although the consideration of grain drift does not greatly affect the resulting general hydro- and thermodynamical structure of the circumstellar envelope it has an decisive influence on the resulting grain size spectrum. Generally, less but more massive grains are being formed when drift is included. Concerning microscopic processes, drift mainly reduces the sticking efficiency of the growth species acetylene on large grains with significant drift velocities, although for carbon grains the surface density of radical sites is somewhat increased.

In conclusio, it seems that grain drift directly affects the modelling of observational quantities like the mass density ratio ρ_d/ρ_g of dust and gas, the prediction of the amount $\dot{M}_d$ of dust injected into the ISM, as well as the modelling of the optical appearence of circumstellar dust shells.

References

Gail, H.-P., and Sedlmayr, E. 1987, *Astr. Ap.***171**, 197.

Krüger, D., Gauger, A., and Sedlmayr, E. 1994, *Astr. Ap.*, **290**, 573.

Krüger, D., Woitke, P., and Sedlmayr, E. 1995, *Astr. Ap. Suppl. Ser.*, **113**, 593.

Krüger, D., Patzer, A. B. C., and Sedlmayr, E. 1996, *Astr. Ap.*, **in press.**

Krüger, D., and Sedlmayr, E. 1996, *Astr. Ap.*, **submitted.**

Mathis, J. S., Rumpl, W., and Nordsieck, K. H., 1977, *Ap. J.*, **217**, 425.

Sellgren, K., Werner, M., and Dinerstein, H. L., 1983, *Ap. J. (Letters)*, **271**, L13.

Woitke, P., Dominik, C., and Sedlmayr, E. 1993, *Astr. Ap.*, **274**, 451.

CONSTRAINTS ON CIRCUMSTELLAR DUST GRAIN SIZES FROM HIGH SPATIAL RESOLUTION OBSERVATIONS IN THE THERMAL INFRARED

E. E. BLOEMHOF *California Institute of Technology, Pasadena, California, USA*
R. M. DANEN, C. R. GWINN *University of California, Santa Barbara, California, USA*

ABSTRACT. We describe how high spatial resolution imaging of circumstellar dust at a wavelength of about 10 μm, combined with knowledge of the source spectral energy distribution, can yield useful information about the sizes of the individual dust grains responsible for the infrared emission. Much can be learned even when only upper limits to source size are available. In parallel with high-resolution single-telescope imaging that may resolve the more extended mid-infrared sources, we plan to apply these less direct techniques to interpretation of future observations from two-element optical interferometers, where quite general arguments may be made despite only crude imaging capability.

Results to date (e.g. Bloemhof and Danen, 1995; Danen, Gwinn, and Bloemhof, 1995) indicate a tendency for circumstellar grain sizes to be rather large compared to the Mathis-Rumpl-Nordsieck size distribution traditionally thought to characterize dust in the general interstellar medium. This may mean that processing of grains after their initial formation and ejection from circumstellar atmospheres adjusts their size distribution to the ISM curve; further mid-infrared observations of grains in various environments would help to confirm this conjecture.

1. INTRODUCTION

To obtain very high spatial resolution on large ground-based telescopes, we have used an instrument of our own design and construction that features a linear array of infrared photodetectors (Bloemhof, Townes, and Vanderwyck, 1986). Two-dimensional images are obtained by spatially scanning the linear array in the direction perpendicular to its axis, either through earth rotation or with an articulating secondary mirror. Detector pixels are sufficiently small to sample the diffraction-limited point-spread function (PSF) of a 3 meter telescope, with FWHM ~ 0.7", at somewhat more than the Nyquist rate; readout of the array is very rapid, so that images are heavily oversampled in the scan direction. The low duty cycle of earth rotation ("drift") scanning is not a problem for observations of relatively bright stellar sources, and this technique delivers high dynamic range and image fidelity. With the very high signal-to-noise ratio obtained on brighter sources, deconvolution to spatial scales of order 0.35" is possible.

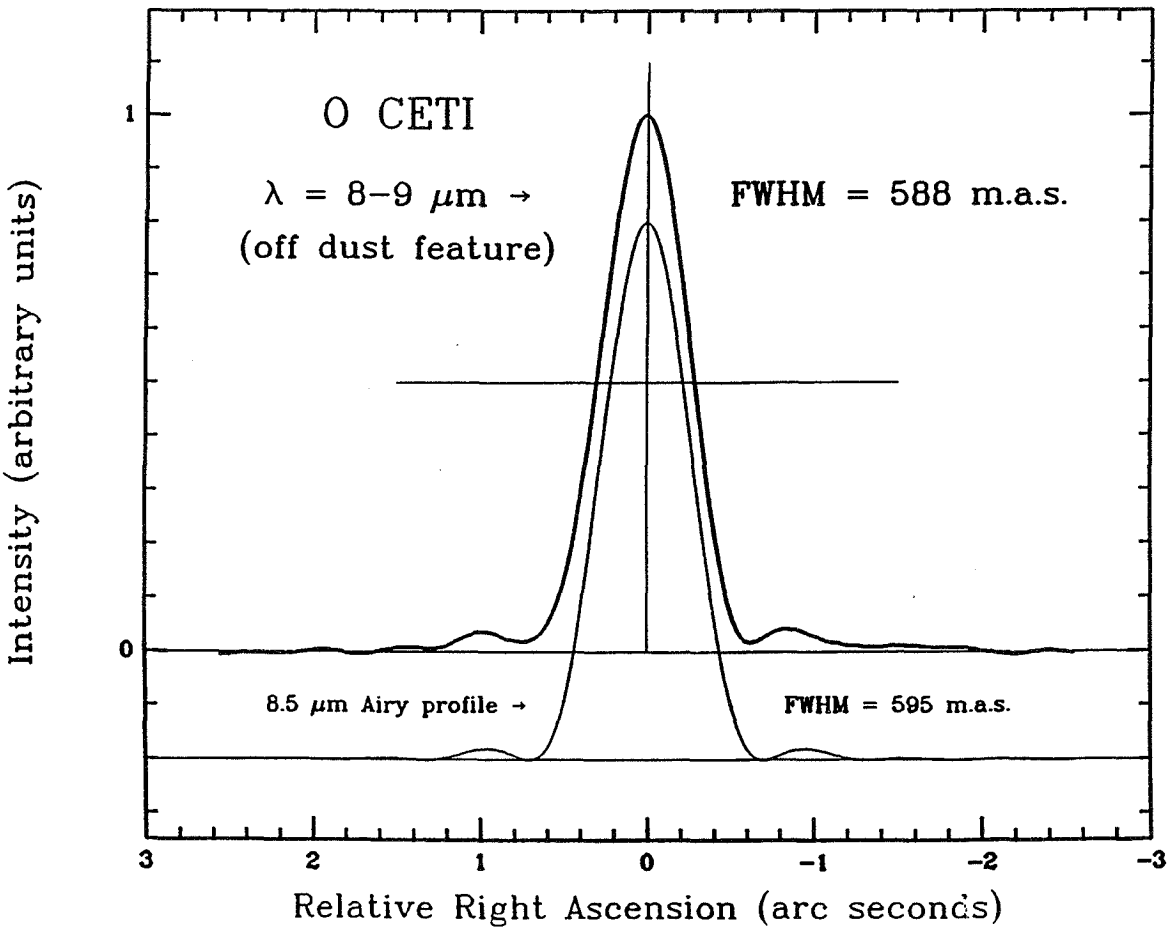

Figure 1. Measured point-spread function of the imaging system on the 3 m IRTF vs. the diffraction-limited response (Airy pattern). A filter that blocks emission due to spatially extended dust was used

Particularly precise east-west image profiles are obtained by examining the response of a single detector in the array as earth rotation scans it over the source. Figure 1 shows a high-quality image profile of an unresolved source, O Ceti, obtained in this way on the 3 meter Infrared Telescope Facility (IRTF) on Mauna Kea. For comparison, a profile through the theoretical diffraction-limited point-spread function of the telescope (Airy pattern) is also plotted. The quality of the experimental PSF is outstanding, permitting very accurate searches for faint, spatially extended dust emission close to bright stellar photospheres.

The achievement of such clean diffraction-limited images at 10 μm under conditions of sub-arc second visible seeing on Mauna Kea was not a surprise, given the well-known $\lambda^{-1/5}$ wavelength dependence of seeing blur circles in the standard (Kolmogorov) theory. Moreover, our drift scans are completed in a few tenths of a second, so our images constitute short exposures at 10 μm. It has been surprising, however, to obtain excellent short exposures even under conditions of only moderate seeing at lower-altitude observing sites: eg. the unresolved image profiles of LkHα 101 to be discussed in § 3 show some low-level structure arising in the optics of the Shane 3 meter telescope at Lick, but variations due to seeing in successive scans are small.

2. DUST AROUND A COOL STAR: α SCO

An example of a cool star surrounded by copious dust is the type-M supergiant α Sco. We have imaged this star using the IRTF, and the excess 10 μm emission arising from spatially extended dust may be seen directly in our image profiles. As is discussed in Bloemhof and Danen (1995), the close agreement between the inner part of these image profiles and that of a point source implies an inner radius of dust formation that is quite far from the central star: roughly 0.6" (110 AU). The temperature of dust grains in radiative equilibrium that far from the star will be rather low, suggesting that dust formation proceeds under supersaturated conditions, which may support models of rapid, episodic grain growth.

We may reasonably assume that the spatially extended infrared emission is coming from optically thin grains, and we may use the emissivities characteristic of silicates to make deductions concerning the size of individual grains. Although the measured 10 μm radiation of the circumstellar dust depends explicitly on grain size, it may be related to the total mass of dust and the grain material density, with only an implicit dependence on grain size through the temperature of the grains (details of this and following arguments are in Bloemhof and Danen, 1995). Large grains and small grains will have different temperatures at a given circumstellar distance, owing to their different optical properties, and so different estimates of the mass of the circumstellar dust may be given depending on grain size. These may be compared to independent mass-loss rates, using the velocity of the outflow in α Sco that is well-known from optical measurements; when this is done, our measurements favor grain radii that are large by ISM standards...roughly, larger than $a \sim 0.08$ μm.

3. DUST AROUND A YOUNG STAR: LKHα 101

The young stellar object LkHα 101 is a Herbig Ae/Be star surrounded by an extensive nebula of gas and dust. The spectral energy distribution (SED) of the source, a composite of observations made at a number of different spatial scales, shows several components of various effective temperatures and equivalent sizes. Observations with a 26" beam reveal a peak of infrared emission at around 10 μm that may be expected to arise in spatially extended circumstellar dust (or perhaps a disk, depending on the stage of evolution of the object and the correctness of YSO disk models).

Our high spatial resolution drift scans of LkHα 101, obtained with the Shane 3 meter telescope at Lick Observatory, are indistinguishable from profiles of the star α Tau used as a comparison point source. We obtained multiple scans of each source, permitting the determination of experimental error bars on the measured sizes. The high signal-to-noise ratio permits an analytic deconvolution that puts a 95%-confidence upper limit to the source diameter of 0.34" (270 AU), and our measured flux (325 Jy) accounts for most of the 10 μm emission from the central arc minute.

The arguments used to extract grain sizes are given in detail by Danen, Gwinn, and Bloemhof, 1995. Briefly, the SED allows us to deduce that the unresolved 10 μm core accounts for $\sim$ 12% of the total luminosity of LkHα 101, so the dust in this core must be either optically thin or anisotropically distributed around the star. In the optically thin case, the $\sim$ 12% energy absorbed by the dust core is balanced by our observed 10 μm reradiation that may be related to the grains' circumstellar distance and to their mid-infrared absorption efficiencies; these efficiencies in turn depend on grain composition and size (e.g. Draine and Lee, 1984; Draine and Lee, 1987).

Examining a number of grain types, we find that our stringent upper limit to the size of the 10 μm-emitting core may be translated into a general lower limit on grain radius a (for graphite grains, $a \geq 0.2$ μm; for glassy carbon grains, $a \geq 0.15$ μm; for silicate grains, $a \geq 0.3$ μm). Consideration of a spherically symmetric r^{-2} dust distribution, which is strongly suggested by the spectral index near 0.6 seen at radio wavelengths in the source SED, raises the lower limit for carbon grains to about 0.3 μm and places an upper limit on grain size of 0.5 μm, so that this model is very nearly excluded by our measurements. If the dust core we observe is composed of optically thick agglomerations, then sensitivity to grain type or size is lost. It appears, however, that a range of circumstellar radii is not consistent with our data, and hence neither are conventional disk models.

4. FUTURE OBSERVATIONS: LARGER TELESCOPES, INTERFEROMETRY

In view of the tight constraints that we were able to set on LkHα 101 with a 3 meter telescope, it would be of great interest to observe that source with one of the Keck 10 meter telescopes. The instrument of choice is the Long Wavelength Spectrometer (Jones and Puetter, 1993), with pixel size 0.12". The nominal PSF diameter is 0.25", so it should be possible with good signal-to-noise ratio either to image the circumstellar dust or to constrain its size to less than about 0.13", which would rule out the r^{-2} outflow model.

Another interesting possibility is using IRIS, a new 4-25 μm imager and spectrometer being built by George Rieke at the University of Arizona, on the upgraded 6.5 meter MMT (an initial optical design is contained in Bloemhof and Rieke, 1995). This instrument will use a 256×256 BIB array, and will be capable of very high spatial resolution: in imaging mode, each pixel is 0.127", Nyquist-sampling the diffraction-limited resolution of the telescope. Obtaining the highest spatial resolution may yet be aided by a scanned imaging technique, although this would be a non-standard observing mode placing extreme demands on array readout and data handling.

The general arguments we have outlined here may be particularly useful when applied to the analysis of data from the new generation of optical interferometers, such as the planned Keck interferometer. At least in the early stages, such instruments will have poor UV coverage, and may be more suited to determining few-parameter models of the source brightness distribution, rather than true images.

References

Bloemhof, E. E., and Danen, R. M. 1995, *Ap. J. (Letters)*, **440**, L93.

Bloemhof, E. E., and Rieke, G. H. 1995, *P. S. P. I. E.*, **2540**, 236.

Bloemhof, E. E., Townes, C. H., and Vanderwyck, A. H. B. 1986, *P. S. P. I. E.*, **627**, 473.

Danen, R. M., Gwinn, C. R., and Bloemhof, E. E. 1995, *Ap. J.*, **447**, 391.

Draine, B. T., and Lee, H. M. 1984, *Ap. J.*, **285**, 89.

Draine, B. T., and Lee, H. M. 1987, *Ap. J.*, **318**, 485.

Jones, B., and Puetter, R. 1993, *P. S. P. I. E.*, **1946**, 610.

INTERSTELLAR DUST

REVISED DEPLETIONS AND NEW CONSTRAINTS ON INTERSTELLAR DUST COMPOSITON

THEODORE P. SNOW *University of Colorado*
ADOLF N. WITT *University of Toledo*

ABSTRACT. We have reviewed the literature on composition of young stars, both hot and cool, as well as older solar-type stars. We find that all these classes of stars have lower abundances of the heavy elements (specifically C, N, O, Mg, Si, and Fe) than the sun. Therefore studies of interstellar depletions in which the solar composition is used as the reference standard are probably in error, tending to overestimate the total quantities of these elements, hence the depletions. We have revised the depletion estimates, using stellar abundances as the reference standard and making use of recent IS gas-phase abundance measurements. As a result of our revised depletions, we can place new and stringent constraints on several published models for the interstellar dust.

1. INTRODUCTION

Most studies of gas-phase abundances in the diffuse interstellar medium are based on the assumption that the overall composition of the ISM is the same as that of the sun. Depletion estimates in particular depend on this assumption, because a reference standard must be adopted in order to determine how much of an element is "missing" from the gas and therefore presumed to be resident in the dust.

We have questioned the assumption that the solar system should be used as the abundance standard, because we find that stars generally do not match the sun's chemical makeup. Furthermore, accurate interstellar gas-phase column density data are now available for a number of elements (observed with the GHRS on the *HST*), making this a good time to reassess diffuse ISM depletions and compare them with dust models. This is what we have done. The results presented here are included in two recent publications (Snow & Witt 1995, 1996; hereafter referred to as Papers I and II), which can be consulted for more details. Here we present tabular results with very little discussion, because the essence of our message lies in the tables, and because page limits prevent us from repeating much of the discussion from the cited papers. We urge the interested reader to look up the more complete papers.

2. DATA AND RESULTS

Our data are contained in the two tables below. Table 1 provides a summary of the compositions of stars falling into several groups: field B stars, cluster B stars, and young disk F and G stars (more details are provided in Papers I and II). All of the

stellar groups represented in Table 1 are, in our opinion, more relevent as reference standards for the ISM than the sun is, because these are young stars recently formed from the ISM and because there is other evidence that the solar system has anomalous abundances, possibly as the result of enhancements due to a nearby supernova explosion close to the time of solar system formation (see discussion and literature citations in Papers I and II).

Table 1 includes our recommended "cosmic" abundances for several elements which are commonly thought to be major grain constituents, along with the implied depletions, taking into account recent, accurate GHRS gas-phase measurements. The depletions are expressed in terms of the number of atoms of each element (per 10^6 hydrogen atoms) that are missing from the gas (these are expressed as "$N_{Dust}/10^6$ H" in the final column of the table).

Table 2 lists several standard dust models and the abundances of the elements that are required to satisfy extinction observations, again expressed in terms of number of atoms per 10^6 hydrogen atoms. This facilitates comparisons between what is available (Table 1) and what is needed (Table 2).

3. CONCLUSIONS

We argue that depletions of elements from the gas phase onto the dust in the diffuse ISM have been systematically overestimated, largely because the solar system has been used as the reference standard for assessing "cosmic"abundances, and the solar system has enhanced abundances of most of the relevent elements. We have reviewed the literature on stellar compositions, emphasizing young, unevolved stars, and we find a very uniform picture in which stars that form from the ISM have lower heavy element abundances than the solar system. Adopting stellar abundances as the reference standard, combined with recent, accurate data on gas-phase abundances in the diffuse ISM, leads to new constraints on dust models.

These new constraints tend to rule out models that rely on amorphous carbon to explain the general extinction, while still allowing models that invoke carbon in ordered form (e.g. graphite or PAHs), because these forms of carbon are more optically efficient and can produce the observed extinction with less carbon. The most viable class of models appears to be those in which ordered carbon is used to explain the far-UV extinction (as well as spectral features such as the 2175Å bump) while silicates are invoked for the visible portion of the extinction curve.

It is noteworthy that others who have recognized the disparity between solar and stellar abundances have begun work to find new dust models which can accomodate the revised depletions, with some initial success (e.g. Mathis 1996). These new models tend to require fluffy or porous grains which have high optical efficiency per unit of mass. Therefore we may anticipate a change in general thinking about dust in the direction of such models.

Table 1. Revised stellar and interstellar abundances

Element	Sun	Field B Stars[a]	Cluster B Stars[b]	Disk F, G Stars[c]	Adopted IS Value	$N_{Dust}/10^6$ H[d]
C	8.60	8.31	8.35	8.32	8.33	79
N	8.05	7.83	7.80	-	7.82	0
O	8.93	8.58	8.69	8.69	8.66	126
Mg	7.58	7.37	7.32	7.48	7.40	19
Si	7.55	7.20	7.20	7.38	7.27	17
S	7.21	7.07	7.11	-	7.09	0
Ca	6.36	6.23	-	6.16	6.20	1.6
Ti	4.99	4.76	-	4.85	4.81	0.06
Cr	5.67	5.51	-	-	5.51	0.3
Fe	7.67	7.49	7.51	7.26	7.43	27
Ni	6.25	6.06	-	6.03	6.05	1.1

[a] References for field B stars: Kilian 1992, 1994; Adelman *et al.* 1993; Gies & Lambert 1992.

[b] References for cluster B stars: Lennon & Dufton 1983; Keenan *et al.* 1984; Gehren *et al.* 1985; Montenbruck 1987; Cunha & Lambert 1994; Kilian *et al.* 1994.

[c] References for F and G field stars: Edvardsson *et al.* 1993; Tomkin *et al.* 1995.

[d] The quantities available for dust are based on a recent compliation of depletions for ζ Ophiuchi by Snow & Witt (1996)

Table 2. Requirements of selected dust models.

Model[a]	Reference	C	N	O	Mg	Si	Fe
Si + G	Mathis *et al.* 1977	≥240	-	-	33	31	26
Si/O	Hong & Greenberg 1980	280	57	444	33	30	26
Si + G	Draine & Lee 1984	300	-	-	-	32	-
Si/O + PAH + Fe	Chlewicki & Laureijs 1988	262	52	145	36	35	42
HAC + graphite	Duley *et al.* 1989	185					
PAH + graphite	Puget & Léger 1989	101					
Composite grains	Mathis & Whiffen 1989	265					
HAC + solid PAH	Jones 1990	185					
Si + C + PAH	Désert *et al.* 1990	150	-	160	20	40	20
Si + C + G	Sorrell 1990	109	-	-	-	27	-
Si + C + G	Rowan-Robinson 1992	271	-	-	-	33	-
Si + C + G	Siebenmorgen & Krügel 1992	300	-	-	-	31	-
Si + G + PAH	Aannestad 1995	245	-	-	-	32	-

[a] Notes to Table 3: In column 1, Si means silicates; G indicates graphite; C means amorphous carbon; O indicates organic refratory material; PAH means polycyclic aromatic hydrocarbons (gas phase); and Fe means metallic iron. The plus (+) sign between grain materials indicates that distinct grain populations are invoked; a slash (/) denotes core-mantle grains.

The required abundances listed in columns 3 through 8 are in units of atoms per 10^6 hydrogen nuclei.

References

Aannestad, P. 1995, ApJ, 443, 653

Adelman, S. J., Robinson, R. D., & Wahlgren, G. M. 1993, PASP, 105, 327

Chlewicki, G. & Laureijs, R. J. 1988, A&A, 207, L11

Cunha, K. & Lambert, D. L. 1994, ApJ, 426, 170

Dèsert, F.-X., Boulanger, F., & Puget, J.-L. 1990, A&A, 237, 215

Draine, B. T. & Lee, H. M. 1984, ApJ, 285, 89

Duley, W. W., A. P. Jones, & D. A. Williams, 1989, MNRAS, 236, 709

Edvardsson, B., Anderson, J., Gustafsson, B., Lambert, D. L., Nissen, P. E., & Tomkin, J. 1993, A&A, 275, 101

Gehren, T., Nissen, P.E., Kudritzki, R. P., & Butler, K. 1985, *Production and Distribution of CNO Elements; ESO Conf. & Workshop Proc. No. 21*, eds. I. J. Danziger, F. Matteucci, & K. Kjaer, p. 171

Gies, D. R. & Lambert, D. L. 1992, ApJ, 387, 673

Hong, S. S. & Greenberg, J. M. 1980, A&A, 88, 194

Jones, A. P. 1990, MNRAS, 247, 305

Keenan, F. P., Brown, P. J. F., Dufton, P. L., & Lennon, D. J. 1984, ApJL, 279, L11

Kilian, J. 1992, A&A, 262, 171

Kilian, J. 1994, A&A, A&A, 282, 867

Kilian, J., Montenbruck, O., & Nissen, P. E. 1994 A&A, 284, 437

Kilian-Montenbruck J., Gehren, T., & Nissen, P. E. 1994, A&A, 291, 757

Lennon, D. J. & Dufton, P. L. 1983, MNRAS, 203, 443

Mathis, J. S. 1996, ApJ, in press

Mathis, J. S., Rumpl, W., & Nordsieck, K. H. 1977, ApJ, 217, 425

Mathis, J. S. & Whiffen, G,. 1989, ApJ, 341, 808

Montenbruck, O. 1987 *Diplomarbeit Universität München*

Puget, J. & A. Léger, 1989, *Ann. Rev. Astr. Ap.*, 27, 161

Rowan-Robinson, M. 1992, MNRAS, 258, 787

Siebenmorgen, R. & Krügel, E. 1992, A&A, 259, 614

Snow, T. P. & Witt, A. N. 1995, *Science*, 270, 1455

Snow, T. P. & Witt, A. N. 1995, ApJL, 468, L65

Sorrell, W. H. 1990, MNRAS, 243, 570

Tomkin, J., Woolf, V. M., & Lambert, D. L. 1995, AJ, 109, 2204

THE INTERSTELLAR POLARIZATION FEATURE ASSOCIATED WITH THE 2175 Å EXTINCTION BUMP

GEOFFREY C. CLAYTON *Department of Physics and Astronomy, Louisiana State University, Baton Rouge, LA 70803*
MICHAEL J. WOLFF *Space Science Institute, Suite 294, 1234 Innovation Dr., Boulder, CO 80303-7814*
S. H. KIM *Korea Astronomy Observatory, 36-1, Whaamdong Yuseonggu, Daejon, 305-348, Korea*
P. G. MARTIN *Canadian Institute for Theoretical Astrophysics, University of Toronto, Toronto, ON Canada, M5S 1A1*
C. M. ANDERSON *Space Astronomy Laboratory, University of Wisconsin, 1150 University Ave., Madison, WI 53706*

1. ULTRAVIOLET POLARIZATION

Clayton et al. (1992) presented the first detailed measurements of the wavelength dependence of interstellar polarization in the ultraviolet (UV). Among the six lines of sight observed, one, HD 197770, showed an apparent polarization feature centered near 2175 Å, the location of the well-known extinction "bump" seen along all dusty sightlines in the Galaxy (Mathis 1990; 1994). Subsequent studies more than doubled the number of sightlines studied, none of which showed UV polarization features (Wolff, Clayton & Meade 1993; Somerville et al. 1994; Clayton et al. 1995). The existence of one polarized feature detected at modest signal-to-noise (S/N) among 14 lines of sight raised doubts as to its reality, and if real as to whether it had any relation to the 2175 Å extinction bump (Martin 1995). The recent Astro-2 space shuttle mission provided the opportunity to both double the observed UV sample yet again and to re-observe the single polarized bump star, HD 197770.

Anderson et al. (1996) presented these new UV interstellar polarization data bringing the total sample to about 30 stars. The reality of the polarization feature toward HD 197770 was confirmed at much higher S/N (See Figure 1). In addition, another polarization feature was detected at high S/N toward HD 147933-4 (ρ Oph AB) (See Figure 2). With the exception of these two stars, the observed sample displays a smooth wavelength dependence of polarization in the UV. The magnitude of the UV polarization along any sightline is correlated with a single parameter, the wavelength at which the interstellar polarization is a maximum, λ_{max} (Clayton et al. 1995; Anderson et al. 1996). This correlation implies there may be a mean interstellar polarization law analogous to the mean interstellar extinction law of Cardelli, Clayton & Mathis (CCM) (1989). The CCM law depends on only one parameter, the ratio

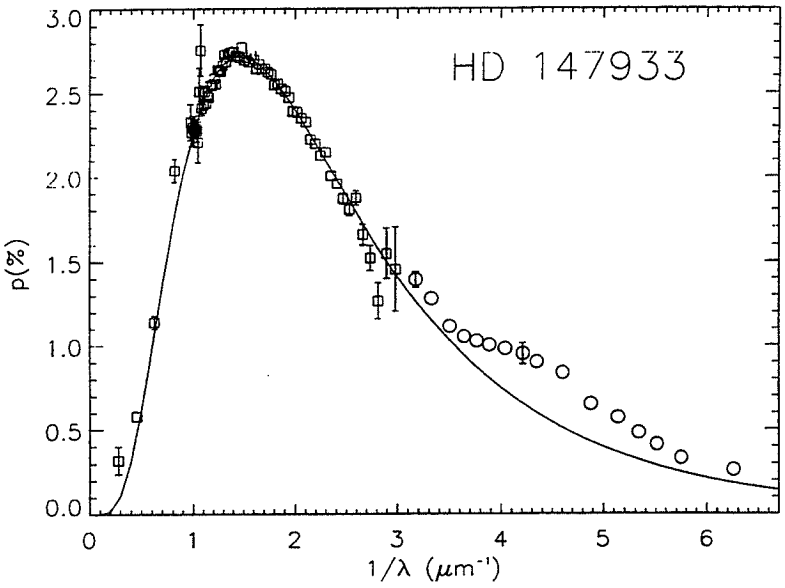

Figure 1. Combination of Astro-2 (circles) and ground-based (squared) data for HD 147933. The solid line represents the best-fit three-parameter Serkowski Law. The error bars are 1–σ, and those smaller than the size of the symbol are not shown.

of total-to-selective extinction, R_V. The parameters, R_V and λ_{max}, are both crude measures of the size distribution of interstellar dust.

The most successful model at fitting the wavelength dependence of interstellar extinction consists of two populations of bare silicate and graphite grains (Mathis, Rumpl & Nordsieck 1977 (MRN)). The graphite grains are needed to fit the strong 2175 Å extinction bump, with the silicates providing most of the smooth extinction seen at other wavelengths. From observations of the IR silicate absorption features, it was inferred that the silicate grains, non-spherical and aligned to the Galactic magnetic field, were responsible for the interstellar polarization (Mathis 1990). Aligned silicate grains make a very good fit to the smooth featureless UV polarization curves that comprise most of the observed sample (cf. Wolff et al. 1993; Kim & Martin 1995). The lines of sight showing a UV polarization feature require something different, perhaps a second population of grains as do the fits to the extinction curve. The polarization wavelength dependence of HD 197770 can be fit by a MRN-like mixture of aligned bare silicate and graphite grains (Wolff et al. 1993; Draine 1988). However, none of the popular grain models including MRN envisaged an aligned bump grain population (Mathis 1990). It has been suggested that the extinction bump is not due to graphite but rather to a population of polycyclic aromatic hydrocarbons (PAHs). If the observed UV polarization features could be associated with the 2175 Å bump then it would strengthen the argument that the bump must be due to grains rather than PAHs which are not likely to be aligned to the Galactic Magnetic field (Draine & Malhotra 1993).

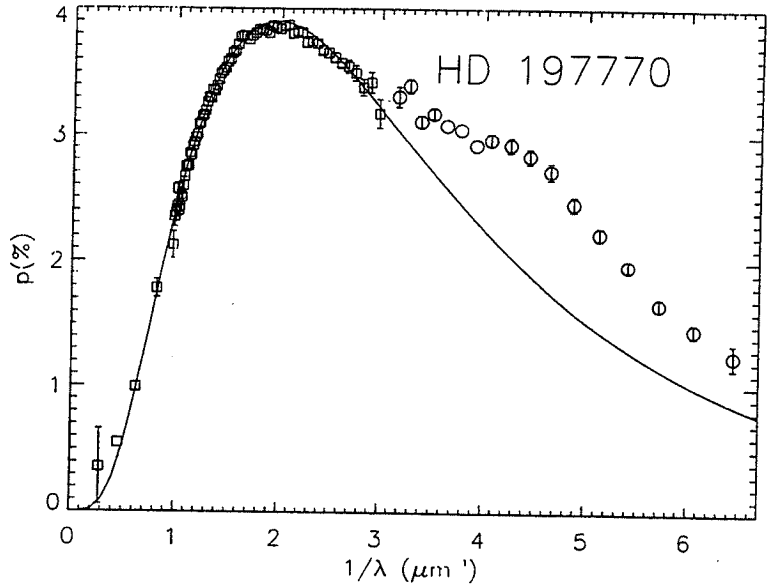

Figure 2. Combination of Astro-2 (circles) and ground-based (squared) data for HD 197770. The solid line represents the best-fit three-parameter Serkowski Law. The error bars are 1–σ, and those smaller than the size of the symbol are not shown.

2. NEW RESULTS

The reality of Ultraviolet polarization features has been confirmed by observations with Astro-2. Two sightlines out of 30 now observed show significant features. The original detection toward HD 197770 has been confirmed and a new feature has been dete cted toward HD 147933-4 (See Figures 1 and 2). Both features have centroids lying close to 2175 Å the location of the UV extinction bump. Two possibilities are considered for the source of the polarization bump, alignment of graphite grains responsib le for the extinction bump or changes in the size distribution of the aligned silicate grains responsible for the continuum polarization. The location and width of the HD 147933-4 polarization bump corresponds closely to that of its extinction bump and cannot be easily fit by altering the silicate size distribution. The HD 197770 bump appears wider and can be accounted for by either the graphite or silicate grains. Taken together, it seems the graphite grains are a more likely source of the polarizati on Computer models show that aligned 200 Å graphite disks produce a consistent fit to the measured polarization bumps. Both polarization bumps have amplitudes which are very small compared to the amount of additional extinction present in the 2175 Å bump, implying poor polarization efficiency. Several other sightlines have been observed at S/N where features should have been clearly detected if the same polarization efficiency applied. So real variations in the alignment or shape of the grains responsible seem to occu r from one sightline to another.

References

Anderson, C.M. et al. 1996, AJ, submitted

Cardelli, J.A., Clayton, G.C., & Mathis, J.S. 1989, *Ap. J.*, 345, 245

Clayton, G.C., Wolff, M.J., Allen, R.G., & Lupie, O.L. 1995, *Ap. J.*, 445, 947

Clayton, G.C., et al. 1992, *Ap. J.*, 385, L53

Draine, B.T. 1988, *Ap. J.*, 333, 848

Draine, B.T, & Malhotra, S. 1993, ApJ, 414, 632

Kim, S.-H. & Martin, P.G. 1995, ApJ, 442, 172

Martin, P.G. 1995, in The Diffuse Interstellar Bands, eds. A.G.G.M. Tielens & T.P. Snow, (Dordrecht: Kluwer), p, 263

Mathis, J.S., Rumpl, W., & Nordsieck, K.H. 1977, *Ap. J.*, 217, 425

Mathis, J.S. 1990, ARA&A, 28, 37

Mathis, J.S. 1994, 422, 176

Somerville, W.B. et al. 1994, *Ap. J.*, 427, L47

Wolff, M.J., Clayton, G.C., & Meade, M.R. 1993, *Ap. J.*, 403, 722

INTERSTELLAR EXTINCTION, POLARIZATION, AND GRAIN ALIGNMENT IN HIGH-LATITUDE CLOUDS

K. A. LARSON AND D. C. B. WHITTET
Department of Physics, Applied Physics, and Astronomy, Rensselaer Polytechnic Institute, Troy, New York 12180, USA

ABSTRACT. From new near-infrared photometry and optical and near-infrared polarimetry, we determine the ratio of total-to-selective extinction and the wavelength of maximum polarization for a sample of stars behind molecular clouds at high Galactic latitude. In general, we find that at high latitude, these parameters have values comparable to those observed closer to the Galactic plane. One notable exception is the line of sight towards HD 210121, where unusually small values of these parameters suggest an abundance of small grains in the foreground cloud.

1. INTRODUCTION

The presence of molecular clouds at high Galactic latitude is a topic of much current interest. Discovered first as diffuse cirrus in IRAS emission, many of these clouds have also been shown to have a rich molecular content at moderately low visual extinction. The clouds have been identified in CO survey catalogs of Magnani *et al.* (1985) and Keto and Meyers (1986), and in the infrared catalogs of Désert *et al.* (1988). Local, isolated high-latitude clouds provide a laboratory in which to study the optical properties and alignment of interstellar matter in a controlled, quiescent environment. In addition, if the environmental conditions far from the Galactic plane are distinct from conditions in the plane, observations of high-latitude clouds will help to constrain models of the evolution of interstellar dust across a wider range of environmental conditions. This poster presents preliminary results of an ongoing investigation into both the physical conditions at high Galactic latitude and the effect of those conditions on the interstellar grains in high-latitude clouds. We will compare calculations of the ratio of total-to-selective extinction ($R_V = A_V/E_{B-V}$) and the wavelength of maximum polarization ($\lambda_{\rm max}$) at high latitude to average values in the Galactic diffuse interstellar medium.

2. OBSERVATIONS

Program stars were selected primarily from an extensive photometric and spectroscopic survey by Penprase (1992) of extinction towards high-latitude clouds. We have obtained near-infrared photometry and near-infrared and optical polarimetry of a reddened, southern-hemisphere subset of these stars.

2.1. Extinction

Infrared photometry of 81 stars was obtained at the South African Astronomical Observatory in July 1994, April 1995, and January 1996. The Mark III InSb Infrared Photometer was used on the 1.9m telescope to give magnitudes in standard *JHKL* passbands. Spectral type, blue-visual reddening (E_{B-V}), and V magnitude (Penprase, 1992; except HD 210121, Welty and Fowler, 1992) were used to evaluate the ratio of total-to-selective extinction,

$$R_V \simeq 1.1(E_{V-K}/E_{B-V})$$

towards each star (Whittet and van Breda, 1978). Future work on this data will include the more rigorous method of fitting an offset power law to the relative extinction and determining R_V from the intercept as $\lambda \to \infty$.

With the high-latitude stars for which R_V can be calculated from a combination of well-determined spectral type, V and K magnitudes, and significant reddening ($E_{B-V} > 0.10$ mag), we determine a mean value of $R_V = 3.3$. This value is similar to the diffuse Galactic average value of 3.1. However, values of R_V for stars in our sample have a standard deviation of 0.7 about the mean value, which suggests that these lines of sight sample a variety of environmental conditions.

The ratio of total-to-selective extinction can be used to characterize the size of interstellar dust. The convergence of absolute extinction to a common form in the infrared suggests that variations in relative extinction as characterized by R_V are due to environmental variations in blue-visual reddening (Martin and Whittet, 1990). Grains causing blue-visual reddening are smaller than those causing infrared extinction and are more sensitive to physical conditions. Furthermore, R_V can be used to characterize variations in the extinction curve out to ultraviolet wavelengths due to systematic evolution of the entire grain size distribution (Cardelli, Clayton, and Mathis, 1989). Large values of R_V are consistent with a lack of small grains due to coagulation, while small values are due to a relative abundance of small grains.

2.2. Polarization

Polarimetry of 29 stars was obtained at the 3.9m Anglo-Australian Telescope at Siding Spring Observatory in September 1995 and March 1996. The Hatfield Polarimeter was used to measure percent linear polarization and position angle in *UBVRIJHK* passbands. The Serkowski-Wilking relation,

$$p_\lambda/p_{\max} = \exp(-K \ln^2(\lambda_{\max}/\lambda))$$

(e. g. Whittet *et al.* 1992) was fit to the data. Since aligned dust grains most effectively polarize those wavelengths that are comparable to the grain radius, $\lambda_{\max}$ may be considered a size parameter of the aligned dust component. Details of the relationship between grain size distribution and $\lambda_{\max}$ will depend on the size dependence of the alignment mechanism, which may include a size-dependent grain shape and/or composition.

Of the observed program, 13 stars are both clearly polarized ($p_{\max} > 1.0\%$) and well-characterized by the Serkowski-Wilking relation. We determine a mean value of $\lambda_{\max} = 0.56\,\mu$m for these stars, very close to the diffuse Galactic average value of $0.55\,\mu$m. However, this is still a statistically small sample in which one "anomalous" star may bias calculations of the mean.

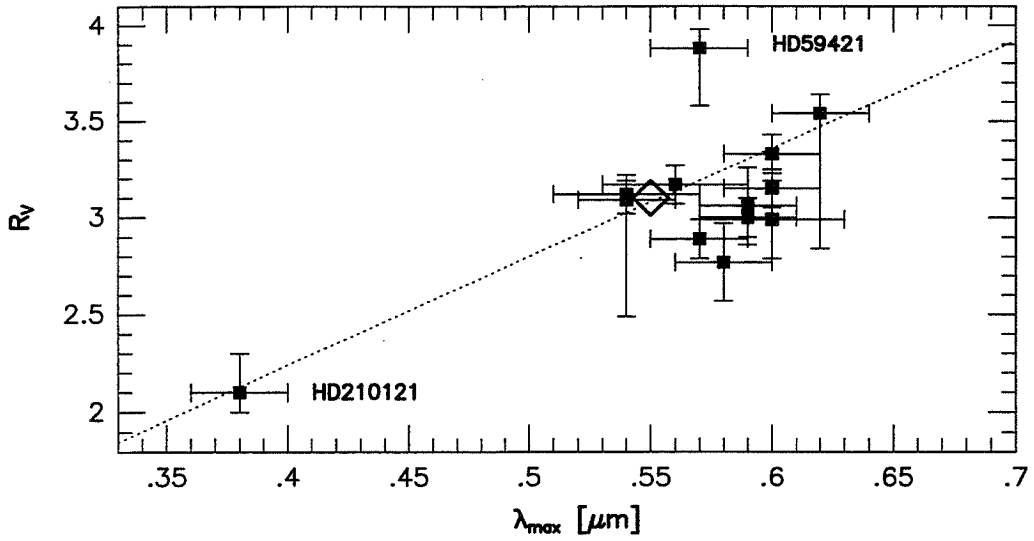

Figure 1. R_V and $\lambda_{\max}$ for stars towards high-latitude molecular clouds. Diamond symbol and dotted line indicate Galactic diffuse average values and linear correlation, respectively.

3. DISCUSSION

In figure 1, we present results for the stars in our observing program that have well-determined values of both R_V and $\lambda_{\max}$. These stars represent lines of sight to six different clouds in which molecular species such as CO and CH have been detected. With extinction $A_V = R_V E_{B-V} = 0.8$–1.6 mag, these clouds exist at the transition between the diffuse and dense cloud environments. Polarization efficiency ranges from $p_{\max}/A_V = 1.0\%$ mag^{-1} to nearly 3.0% mag^{-1}, the observed Galactic upper limit.

The diamond symbol in figure 1 represents the diffuse Galactic average, $R_V = 3.1$ and $\lambda_{\max} = 0.55\,\mu$m. In general, variations in these two independently-determined parameters are linearly correlated, as first shown by Serkowski *et al.* (1975). This relationship suggests that the population of grains producing extinction and the subset of that population producing polarization respond to prevailing physical conditions in a correlated way. For the much larger Galactic data set of Whittet and van Breda (1978), this correlation can be described by the fit $R_V = 5.6\,\lambda_{\max}$, shown as a dotted line in figure 1. A fit to the high-latitude stars in figure 1 yields $R_V = (5.47 \pm 0.10)\lambda_{\max}$, which is consistent with the Galactic correlation. Most of the high-latitude stars in this sample agree with the least-squares fit to within uncertainty in photometry and spectral type. However, as can be seen from figure 1, the set of R_V and $\lambda_{\max}$ for these stars is not well characterized by a line. While average values of both parameters are generally consistent with the Galactic averages, there is a cluster of points in figure 1 with large $\lambda_{\max}$ for corresponding R_V, i. e. to the right of the diamond symbol. On the other hand, the star HD 59421 appears to show the opposite behavior, with a normal value of $\lambda_{\max}$ and relatively large value of R_V.

The most notable star in figure 1 is HD 210121, which has among the lowest known values of $R_V = 2.1$ and $\lambda_{\max} = 0.38\,\mu$m, yet is in excellent agreement with the Galactic correlation (Larson *et al.*, 1996). These small values suggest an abundance of small grains in the foreground cloud DBB 80, which is consistent with the steep far-ultraviolet extinction and the high molecular abundances measured towards this

star (see Welty and Fowler (1992) and references therein). The distinguishing characteristic of this cloud with respect to the other clouds in figure 1 may be its large distance from the plane. Using distances determined by Penprase (1992), we note that the "normal" molecular high-latitude clouds in our sample are from 25 pc to 130 pc from the plane, whereas Welty and Fowler (1992) estimate that DBB 80 is about 150 pc from the plane, located at about two molecular scale heights in a significantly reduced interstellar radiation field.

4. CONCLUSIONS

We have determined that high-latitude molecular clouds have extinction and polarization properties that are generally not significantly different from diffuse clouds closer to the Galactic plane. The values of R_V and $\lambda_{\rm max}$ are similar to Galactic average values, and while not exactly linearly correlated, are fairly consistent with observed Galactic correlation. New measurements towards HD 210121 extend the range of values for which the previously observed correlation between R_V and $\lambda_{\rm max}$ appears to be valid. These data will be used to address several remaining questions. For example, specifying the grain-size distribution, the dust-to-gas ratio, and the alignment efficiency at high Galactic latitude and how these cloud parameters correlate with environmental conditions may contribute to the understanding of the evolution of high-latitude clouds and ultimately of the conditions leading to star formation. Finally, it will be important to observe other clouds at distances from the Galactic plane that are equal to and greater than the cloud towards HD 210121 to firmly establish the effect that distance from the plane has on cloud environment.

Acknowledgements. This research was partly funded by the NSF through grant AST–9419690 and by NASA through grant GO–2245.01–87A. K. A. L. thanks S. Desch, S. Carey, and J. Bregman for helpful suggestions at the symposium, and the organizing committee for financial support to attend.

References

Cardelli, J. A., Clayton, G. C., and Mathis J. S. 1989, *Ap. J.*, **345**, 245.

Martin, P. G., and Whittet, D. C. B. 1990, *Ap. J.*, **357**, 113.

Désert, F. X., Bazell, D., and Boulanger, F. 1988, *Ap. J.*, **334**, 815.

Magnani, L., Blitz, L., and Mundy, L. 1985, *Ap. J.*, **295**, 402.

Keto, E. R., and Myers, P. C. 1986, *Ap. J.*, **304**, 446.

Penprase, B. E., 1992, *Ap. J. Suppl.*, **83**, 273.

Serkowski, K., Mathewson, D. S., and Ford, V. L. 1975, *Ap. J.*, **196**, 261.

Larson, K. A., Whittet, D. C. B., and Hough, J. H. 1996, *Ap. J.*, in press.

Whittet, D. C. B., Martin, P. G., Hough, J. H., Rouse, M. F., Bailey, J. A., and Axon, D. J. 1992, *Ap. J.*, **386**, 562.

Whittet, D. C. B., and van Breda, I. G. 1978, *Astr. Ap.*, **66**, 57.

Welty, D. E., and Fowler, J. R. 1992, *Ap. J.*, **393**, 193.

THE EXTINCTION PROPERTIES OF HEAVILY-REDDENED LINES OF SIGHT IN THE GALAXY

M. G. RAWLINGS *University of Central Lancashire, Preston, UK*
A. J. ADAMSON *University of Central Lancashire, Preston, UK*
D. C. B. WHITTET *Rensselaer Polytechnic Institute, Troy, USA*

ABSTRACT.

Recent studies of the 3.4μm C-H stretch absorption feature (Sandford et al. 1995) indicate a strong correlation between it and the 10μm silicate band over a wide range of extinctions (A_V = 3.9 - 31 magnitudes), but the relationships between their optical depths and the visual extinction are particularly poorly constrained at intermediate extinctions between 15 and 20 magnitudes. The objective prism survey published by Stephenson (1992) may help to alleviate this difficulty. It lists more than 400 extremely red stars lacking molecular absorption bands, suggesting that these are hot blue stars reddened by long path lengths of the Galactic ISM. The intrinsic properties of these stars are unfortunately only loosely constrained, and *JHK* photometry therefore does not accurately determine the interstellar extinction. Using the POSS I plates, we have attempted to produce self-consistent spectral types, luminosity classes and extinctions for the stars which Stephenson claims to be most heavily reddened. 14 out of 25 sources studied are consistent with OB supergiants. The results are highly sensitive to upper limits in the blue plate, and are not always consistent with Stephenson's claims of much higher reddening than that of a typical member of the Cygnus OB2 association. For the most heavily-reddened sources studied, a *B*-magnitude based on the faintest measurable value on the blue plate yielded a lower limit of about 9 magnitudes on the extinction.

1. INTRODUCTION

The physical properties and chemical composition of solid grains in the dusty interstellar medium can be constrained by observing the grains' effect on transmitted starlight. Major advances in our understanding of interstellar grains have arisen through observations of spectral features in lines of sight with extreme extinctions. For example, the intrinsically weak 3.4μm absorption due to aliphatic hydrocarbons was first detected in the long path length to the Galactic Centre (Butchart et al. 1986). Due to the intrinsic weakness of this band, it was not detected in any other line of sight for several years (Adamson, Whittet & Duley 1990). Such shortcomings are serious, since we do not know the galactic distribution of the various particulate solids. The detection of widely-distributed lines of sight in the Galaxy, with a range of extinctions, would therefore be useful in determining the physical relationship between interstellar silicates and carbonaceous materials.

The current state of knowledge is best represented by the work of Sandford et al. (1995). 3.4μm C-H stretch absorption correlates well with the 10μm interstellar silicate band over a wide range of extinctions (A_V=3.9-31). Both features increase in strength nonlinearly with increasing A_V. However, the relationship between the band optical depths and A_V is poorly constrained at the crucial extinctions between 15 and 20 magnitudes. This relationship bears upon the distribution of the various types of hydrocarbon material, and its rapid increase at the highest visual extinctions studied (at the Galactic Centre) may reflect a variation in the relative density of CH-bearing molecules as a function of galactocentric radus. However, observational data currently exist for only thirteen stars and poorly sample exactly the region where the models most require constraint (see Fig. 3, 4 & 5 of Sandford et al. 1995). The identification of additional heavily-reddened lines of sight away from the Galactic Centre would therefore be desirable.

2. THE STEPHENSON SURVEY

The *I*-band objective prism survey published by Stephenson (1992) contains more than 400 Galactic-plane stars with extremely red colours but which appear to exhibit no molecular bands in the near-infrared. The absence of (for example) near-IR molecular absorption suggests that these are hot stars which are intrinsically blue, and that their colours reflect dust reddening in a long path of the Galactic ISM. Since such stars are essentially featureless throughout the majority of their infrared spectrum, they are ideal background sources against which to silhouette interstellar absorption features. Creese et al. (1995) obtained *VRIJHK* polarimetry and *JHK* photometry for subsets of the survey, but were unable to determine the spectral type of individual stars. This is a requirement for correct selection of intrinsic colours and hence accurate determination of A_V. The problem is illustrated in the *J-H* versus *H-K* two-colour plane presented by Creese et al.: the Stephenson sources are distributed diagonally along the plane to about the same extent as the spread along the locus of unreddened field stars. This could potentially produce an uncertainty of more than 5 magnitudes in the inferred value of A_V, according to the adopted intrinsic spectral type.

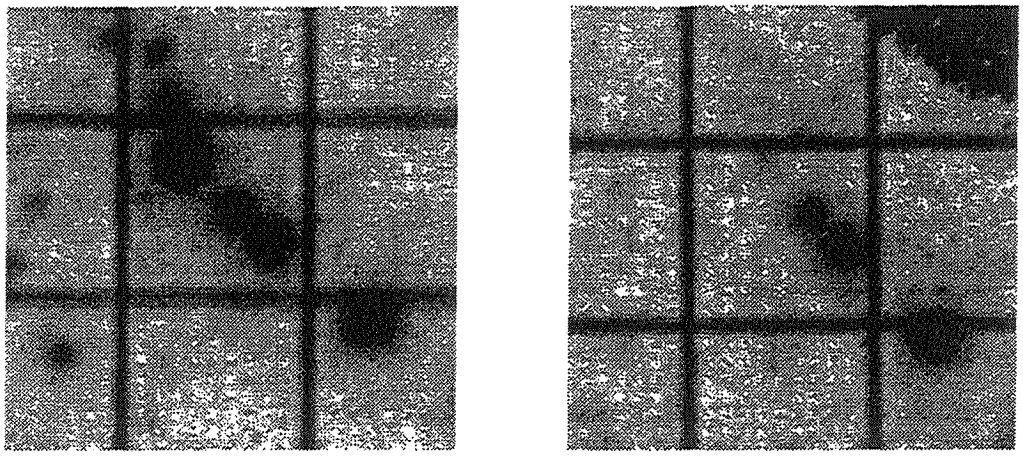

Figure 1. POSS images of StRS154. The left-hand image is taken from the E plate, and the right is from the O plate. The Stephenson source is towards the top left of the central square, which has a side length of 0.5 mm on the plate ($\simeq$ 30 arcsec).

3. ANALYSIS

Using a Quantimet Q520 image processing system, images of the most-reddened Stephenson sources were digitized from the POSS I plates. The image diameters were measured and calibrated using a magnitude-diameter relation derived from similar POSS I studies by Humphreys et al. (1991) to determine effective E and O magnitudes. These were converted to approximate R and B photometric magnitudes respectively, using a linear relationship determined using calibrated test sources from Humphreys et al (1991). Using these magnitudes with standard intrinsic colour indices from Johnson (1966), Bessell & Brett (1988) and Wegner (1994) and an average extinction curve (e.g. Whittet 1992), approximate values of A_V and predicted R-band magnitudes were calculated for the sample over a range of spectral types and luminosity classes.

The parameters which produced the closest agreement with the measured R-band magnitude were adopted as the true spectral type and luminosity class. This method is sensitively dependent on the lowest measurable blue plate image diameters (corresponding to a magnitude of $\simeq$ 20.7); measurements of the degree of interstellar reddening in the reddest sources were taken as lower limits.

4. RESULTS

A range of spectral types and luminosity classes were tested, from O9Ia through to G5V. Results for the 31 sources listed by Stephenson as most heavily-reddened, are summarized in the table. About 5 sources could not be classified, producing ambiguous results. The majority of the remaining objects were consistent with early-type stars with A_V of $\sim$ 9 magnitudes at least, suitable for studies of the Galactic distribution of particulate solids. The spectral resolution of the Stephenson survey is low, and our implicit assumption that these objects are not late-type giants may not be justified in all cases. Optical spectroscopy will be carried out in August 1996, to settle this question for 50% of the Stephenson survey.

StRS	Spectrum	A_V	StRS	Spectrum	A_V
5	O9 Ia	7.3	224	B5 Ia	10.7
12	B5 Ia	9.0	226	O9 V	9.8
108	O9 V	4.4	229	B5 III	7.7
119	B5 Ia	9.1	231	O9 Ia	9.2
136	B5 Ia	10.3	239	G5 III	5.1
151	O9 V	9.4	253	B5 Ia	10.3
154	A5 Ia	11.1	297	A5 V	4.0
161	B5 Ia	9.7	318	B5 Ia	10.6
163	O9 Ia	5.2	326	B5 Ia	11.4
164	A5 Ia	10.6	337	B5 Ia	10.3
202	O9 V	9.3	383	O9 Ia	10.1
211	B5 Ia	7.4	439	O9 V	5.6
217	A5 Ia	11.3			

Table 1 Stephenson source designations, and self-consistent spectral types and visual extinctions.

Acknowledgements.

MGR is funded by a PPARC studentship. AJA is partly funded by the UK Starlink project and partly by the University of Central Lancashire. MGR is grateful to the conference organizers for help with expenses. We acknowledge useful discussions with colleagues in the UCLan Centre for Astrophysics.

References

Adamson, A. J., Whittet, D. C. B., & Duley, W. W. 1990, MNRAS, **243**, 400

Bessell, M. S., Brett, J. M. 1988, PASP, **100**, 1134

Butchart, I., McFadzean, A. D., Whittet, D. C. B., Geballe, T. R., & Greenberg, J. M. 1986, A&A, **154**, L5

Creese, M., Jones, T. J., Kobulnicky, H. A. 1995, AJ, **110**, 268

Humphreys, R. M., Landau, R., Ghigo, F. D., Zumach, W., LaBonte, A. E. 1991, AJ, **102**, 395

Johnson, H. L. 1966, ARA&A, **4**, 193

Sandford, S. A., Pendleton, Y. J., Allamandola, L. 1995, ApJ, **440**, 697

Stephenson, C. B. 1992, AJ, **103**, 263

Wegner, W. 1994, MNRAS, **270**, 229

Whittet, D. C. B. 1992, *Dust in the Galactic Environment*, (Bristol: Inst. Physics)

HAC: BAND GAP, PHOTOLUMINESCENCE, AND OPTICAL/NEAR-INFRARED ABSORPTION

ADOLF N. WITT AND DIMITRI RYUTOV *The University of Toledo, Toledo, Ohio, USA*
DOUGLAS G. FURTON *Rhode Island College, Providence, Rhode Island, USA*

ABSTRACT. We report results of laboratory measurements which illustrate the wide range of physical properties found among hydrogenated amorphous carbon (HAC) solids. Within this range, HAC can match quantitatively the astronomical phenomena ascribed to carbonaceous coatings on interstellar grains. We find the optical band gap of HAC to be well correlated with other physical properties of HAC of astronomical interest, and conclude that interstellar HAC must be fairly hydrogen-rich with a band gap of $E_g \gtrsim 2.0$ eV.

1. INTRODUCTION

Hydrogenated amorphous carbon (HAC) is widely thought to be a constituent of interstellar grains (Tielens *et al.* 1996), most likely in the form of grain mantles (Duley *et al.* 1989; Sorrell 1991). The most direct observational evidence supporting this view is the extended red emission (ERE) seen in many dusty astrophysical environments (Witt and Schild 1998; Guhathakurta and Tyson 1989; Witt and Malin 1989; Witt and Boroson 1990; Furton and Witt 1990, 1992; Perrin and Sivan 1992; Perrin *et al.* 1995) and the interstellar 3.4 μm band (Soifer *et al.* 1976: Sandford *et al.* 1991; Allamandola *et al.* 1992; Pendleton *et al.* 1994; Duley 1994, 1995; Sandford *et al.* 1995) seen in absorption along lines of sight through the diffuse interstellar medium of the Galaxy. In this work we produced and characterized HAC thin films with a wide range of physical characteristics with the aim to use the observational constraints derived from observations of the ERE and the 3.4 μm absorption band to determine the properties of those HACs which resemble the interstellar hydrocarbon solids most closely.

2. EXPERIMENTS

Nine different HAC samples were grown in a DC glow discharge reactor at 200 mTorr pressure in a -1 kV potential. The hydrocarbon feed gas was methane. The deposition conditions were varied by adding UV photons, Ar, or H_2 to the deposition environment, both singly and in combination. The following optical and physical measurements were conducted: 1) UV/Vis absorption spectroscopy (190-820 nm),

2) Absolute photoluminescence (PL) spectroscopy (500-820 nm), 3) Near-IR absorption spectroscopy (2500-3200 cm^{-1}), and 4) Film thickness measurements. From these measurements we derived the following characteristics: 1) Tauc band gaps (Tauc 1973), 2) Total photoluminescence (PL) efficiencies, 3) Ratio of visible to 3.4 μm band absorption optical depths, 4) 3.4 μm band mass absorption coefficients, and 5) 3.4 μm band component structure.

3. RESULTS

3.1. Bandgaps and Photoluminescence

We found the band gaps of different HAC films to vary over the range 1.3 eV to 2.9 eV; the largest gap resulted from the deposition of pure CH_4 plasma onto a room-temperature substrate. The PL efficiency, defined as the conversion efficiency of monochromatic (488 nm) Ar laser radiation into PL band photons, varied over two and a half orders of magnitude and proved to correlate well with the band gaps (Figure 1).

The HAC PL efficiencies of the laboratory samples match the observed interstellar ERE efficiency (~2%, Furton 1993) without difficulty, However, when doing so, HAC has a band gap of ~2.1 eV and the resulting PL band peaks at a wavelength about 80 nm shorter than the corresponding ERE peaks (Witt and Boroson 1990). Interstellar depletion studies (Sofia *et al.* 1994) indicate that a substantial fraction of interstellar silicon is likely residing in grain mantles rather than in grain cores. We consider it possible, therefore, that grain mantles responsible for the ERE do not contain pure HAC but rather the amorphous ternary alloy a-Si(x)C(1-x):H. The photoluminescence spectrum of this material consists of a single broad band with peak emission in the 600-800 nm wavelength region (Sussmann and Ogden 1991), more in agreement with ERE observations. The PL efficiencies of a-Si(x)C(1-x):H have yet to be determined.

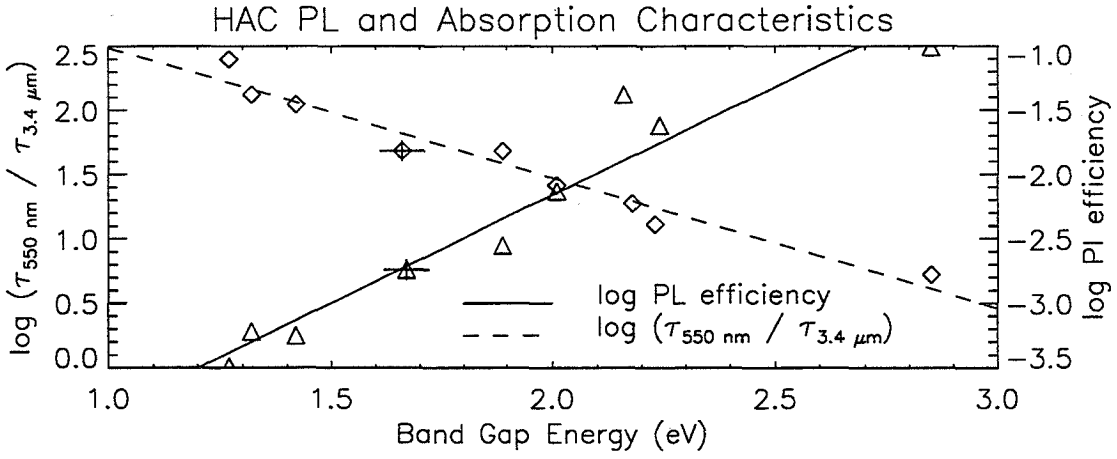

Figure 1. The photoluminescence and absorption characteristics of HAC.

3.2. The 3.4 micron Absorption Band

We compared the observed interstellar 3.4 μm band profile toward GC IRS 6E (Pendleton *et al.* 1994) with the 3.4 μm absorption bands of our HAC samples. The best, almost perfect match was provided by the pure CH_4 HAC sample with a bandgap of 2.85 eV (Figure 2). The principal absorption contributions come from three bonding configurations: sp^3 CH_3 (asym) 2960 cm−1 (30%); sp^3 CH_2 (asym) 2925 cm−1 (~45%); sp^3 CH_3 (sym) 2870 cm−1 (~25%).

The 3.4 μm band mass absorption coefficients of our samples ranged from 500-2000 cm^2 g^{-1}. The wider-band gap, more hydrogen rich HAC occupy the upper end of this range, and they meet the 3.4 μm mass absorption coefficient estimated by Whittet (1992) for the Cyg OB2 No. 12 line of sight of $\kappa_{3.4} > 1300$ cm^2 g^{-1}.

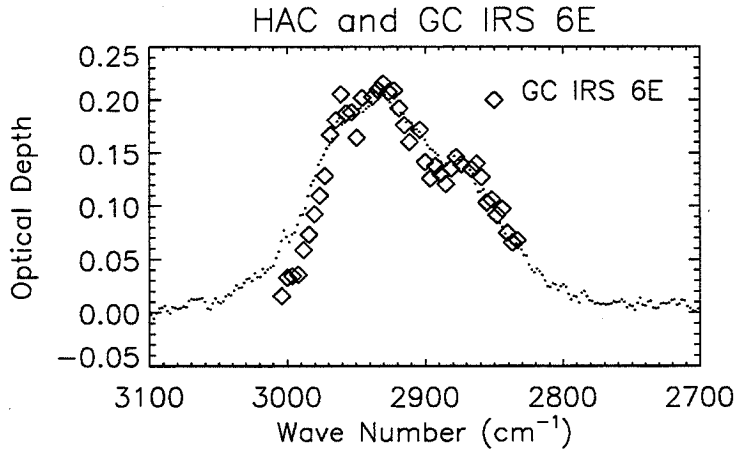

Figure 2. A comparison of the IR absorption profile of highly hydrogenated HAC with that observed toward GC IRS 6E. The GC data is curtesy Pendleton *et al.* 1994.

3.3. The Ratio of Visual Absorption to 3.4 micron Optical Depth

In Figure 1 we also display our measurements of the ratio of the visible absorption τ(550 nm) and the 3.4 μm optical depth as a function of the Tauc band gap. The remarkably close correlation is easily understood because all three quantities depend on the degree of hydrogenation of the HAC. As the hydrogenation decreases, τ(550 nm) increases, τ(3.4 μm) decreases, and the band gap decreases. As a consequence, the ratio τ(550 nm)/τ(3.4 μm) varies over two orders of magnitude for our nine samples. Yet, in interstellar space, the ratio A_V/τ(3.4 μm) is remarkably constant at about 250, with the exception of the line of sight to the galactic center, where it is about 150 (Pendleton *et al.* 1994). This suggests that the HAC mantles of interstellar grains must maintain a very narrow, constant, range of hydrogenation.

4. CONCLUSIONS

Our primary conclusions are: 1) HAC materials constitute a class of possible interstellar dust materials exhibiting a large range of physical properties. 2 The Tauc band gap is a useful characterizing parameter, being closely correlated with the PL efficiency and the $\tau(550\ \mathrm{nm})/\tau(3.4\ \mu\mathrm{m})$ ratio. 3) The observed ERE efficiency, the observed 3.4 μm band profile, the observed ratio $A_V/\tau(3.4\ \mu\mathrm{m})$, and the 3.4 μm band mass absorption coefficient can be matched by HAC with the fairly high ($E_g > 2.0$ eV) and constant band gap. 4) The PL band of HAC peaks at shorter wavelengths than the interstellar ERE. Impurities, especially the presence of Si, are likely to shift the PL peak to longer wavelengths.

References

Allamandola, L.J., Sandford, S.A., Tielens, A.G.G.M., and Herbst, T.M. 1992, *Ap. J.*, **399**, 134.

Duley, W.W. 1994, *Ap. J.*, **430**, L133.

Duley, W.W. 1995, *Ap. J.*, **445**, 240.

Duley, W.W., Jones, A.P., and Williams, D.A. 1989, *M. N. R. A. S.*, **236**, 709.

Furton, D.G. 1993, Ph.D. Thesis, University of Toledo.

Furton, D.G. and Witt, A.N. 1990, *Ap. J.*. **364**, L45.

Furton, D.G. and Witt, A.N. 1992, *Ap. J.***386**, 587.

Guhathakurta, P. and Tyson, J.A. 1989, *Ap. J.*, **346**, 773.

Jacob, W. and Unger, M. 1996, *Appl. Phys. Lett.*, **68**, 475.

Pendleton, Y.J., Sandford, S.A., Allamandola, L.J., Tielens, A.G.G.M. and Sellgren, K. 1994, *Ap. J.*, **437**, 683.

Perrin, J.-M., and Sivan, J.-P. 1992, *Astr. Ap.*, **255**, 271.

Perrin, J.-M., Darbon, S., and Sivan, J.-P. 1995, *Astr. Ap.*, **304**, L21.

Sandford, S.A., Allamandola, L.J., Tielens, A.G.G.M., Sellgren, K., Tapia, M., and Pendleton, Y.J. 1991, *Ap. J.*, **371**, 607.

Sandford, S.A., Pendleton, Y.J., and Allamandola, L.J., 1995, *Ap. J.*, **440**, 697.

Sofia, U.J., Cardelli, J.A., and Savage, B.D. 1994, *Ap. J.*, **430**, 650.

Sorrell, W.H., 1991, *M. N. R. A. S.*, **248**, 439.

Sussmann, R.S., and Ogden, R. 1981, Philos. Mag. B, 44, 137

Tauc, J. 1973, *Amorphous Semiconductors* ed. M.H. Brodsky, (New York: Plenum).

Tielens, A.G.G.M., Wooden, D.H., Allamandola, L.J., Bregman, J., and Witteborn, F.C. 1996, *Ap. J.*, **461**, 210.

Whittet, D.C.B. 1992, *Dust in the Galactic Environment* (London: IOP Publ. Ltd.)

Witt, A.N. and Boroson, T.A. 1990, *Ap. J.*, **355**, 182.

Witt, A.N. and Malin, D.F. 1989, *Ap. J.*, **347**, L25.

Witt, A.N. and Schild, R.E. 1988, *Ap. J.*, **325**, 837.

THE ROLE OF HYDROGEN IN SMALL AMORPHOUS CARBON GRAINS: THE IR SPECTRUM

V. MENNELLA *Osservatorio Astronomico Capodimonte, Napoli, IT*
L. COLANGELI *Osservatorio Astronomico Capodimonte, Napoli, IT*
C. CECCHI PESTELLINI *Osservatorio Astronomico Capodimonte, Napoli, IT*
E. PALOMBA *Osservatorio Astronomico Capodimonte, Napoli, IT*
P. PALUMBO *Istituto Universitario Navale, Napoli, IT*
A. ROTUNDI *Osservatorio Astronomico Capodimonte, Napoli, IT*
E. BUSSOLETTI *Istituto Universitario Navale, IT*

ABSTRACT. Preliminary results on the evolution of the IR spectrum of hydrogenated carbon grains as a function of heat treatment are presented. The trasformation of C-H and C-C bonding configurations is considered and the correlation with other properties of grains, such as their microstructure, is analyzed.

1. INTRODUCTION

The presence of carbon based materials has been detected by IR spectroscopy in the diffuse interstellar medium and in circumstellar environments. Organic spectral signatures have also been found in primitive solar system bodies such as comets and meteorites. The identification of the specific materials responsible for the observed absorption and/or emission is not complete and many points are still the subject of discussion.

Measurements on cosmic dust analogs can be useful in this framework. In particular, it is important to analyze the evolution of samples under various kinds of processes, which simulate those occuring in space. In this work we study the variations in the IR spectrum of hydrogenated carbon grains induced by thermal annealing. This process can be considerd, in a first approximation, a valid tool to understand grain processing in space. Moreover, IR spectroscopy allows us to extend the characterization of our grains, already performed in the UV-Vis spectral range, to the vibrational spectrum.

2. EXPERIMENT AND RESULTS

Hydrogenated amorphous carbon grains (ACH2) were produced by arc discharge in H_2 atmosphere (10 mbar) and collected on ZnSe substrates located 5 cm from the source. The samples are characterized by a chain-like structure of aggregates composed of three - five spherical grains with an average diameter of 11 nm.

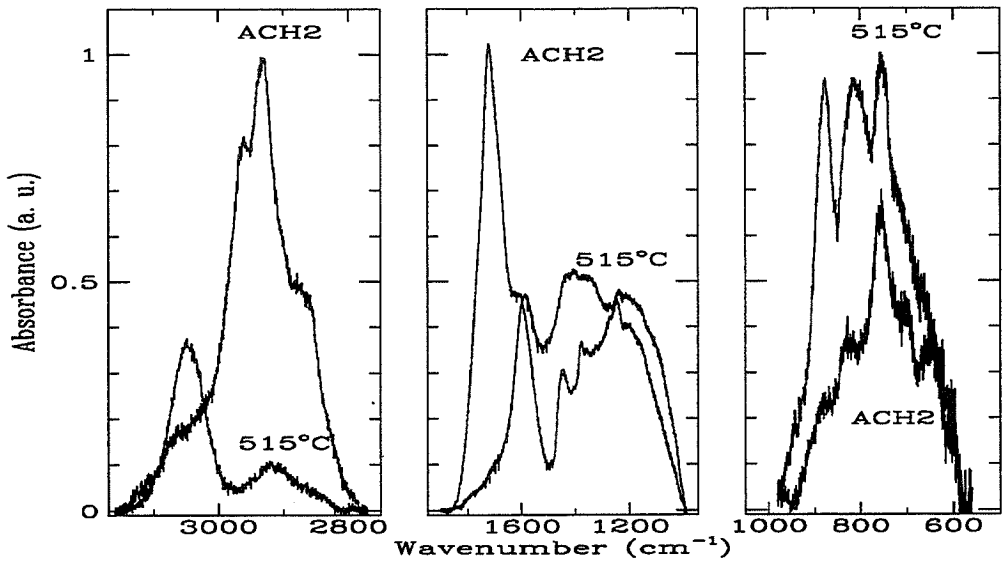

Figure 1. Evolution of IR bands in hydrogenated carbon grains as a function of annealing temperature.

Thermal annealing of ACH2 was carried out at a pressure less than 10^{-5} mbar for 3 hr at a fixed temperature, T_a, in the range 250 - 515 °C. Transmission measurements were performed on as produced and annealed samples in the range 4000 - 400 cm^{-1} with a resolution of 1 cm^{-1} by using a FTIR spectrophotometer (Bruker IFS 66v).

ACH2 samples are characterized by a hydrogen atomic concentration of 62 at. %, as measured by microcombustion calorimetry (MCC). The analysis of the C-H stretching region shows that: 1) the three atomic carbon hybridizations are present in the grains; 2) the sp^3 bonding configuration is dominant (Mennella et al. 1995a). The complete list of IR bands in ACH2 samples is reported by Colangeli et al. (1995).

Important spectral modification are induced by the heat treatment. The evolution of the IR bands as a function of T_a is shown in Fig. 1. The intensity of the stretching band corresponding to sp^3 $CH_{(2,3)}$ groups becomes less and less pronounced as T_a increases (see Fig. 1). Only a weak band at 2925 cm^{-1} remains at 515 °C. On the contrary, the aromatic C-H stretching mode at 3050 cm^{-1} becomes more intense as the temperature rises. The main intensity variations are observed for $T_a \geq 400$ °C.

The presence of C-C bonds in the as produced samples is testified by the band at 1600 cm^{-1} which appears as a shoulder of the prominent contamination feature at 1720 cm^{-1} due to C-O stretching. Moreover, the doublet at 1445 and 1375 cm^{-1} , assigned to deformation vibrations of CH_3 groups, is also present. For $T_a = 515$ °C, the peak at 1600 cm^{-1} , which now can be observed more clearly due to the disappearing of the contamination band, changes into a well defined and more intense band centred at 1580 cm^{-1} , while the doublet disappears. In the low frequency region, the spectrum of ACH2 grains is characterized by the presence of the C-H aromatic bending modes which become more intense after annealing (see Fig. 1).

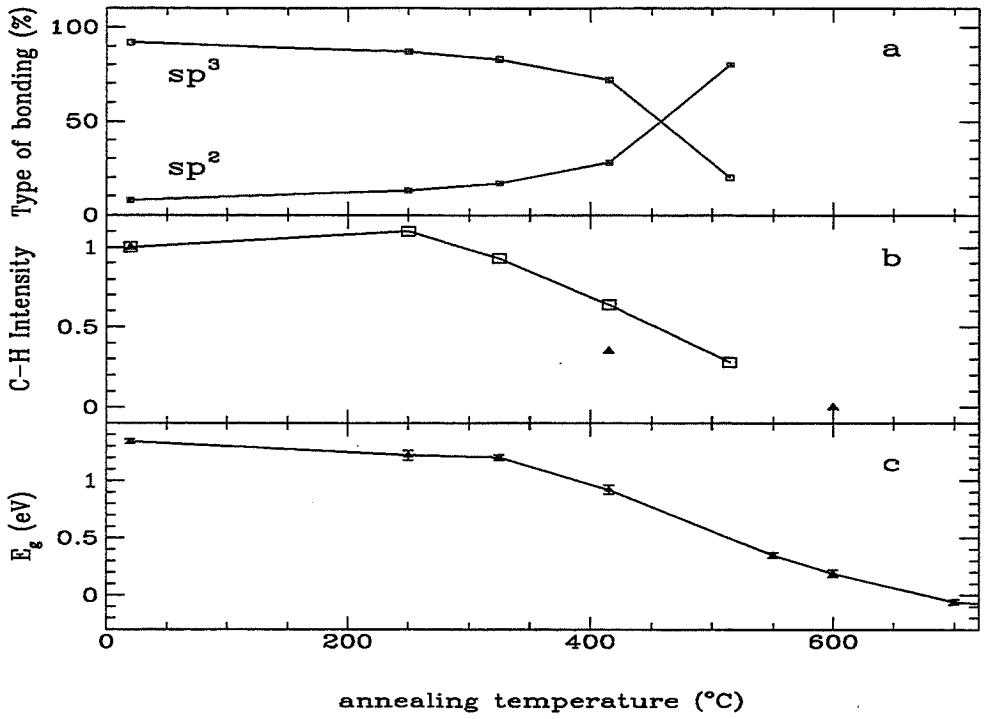

Figure 2. Physical parameters of carbon grains vs. annealing temperature: a) sp^2 and sp^3 site concentrations; b) Normalized C-H stretching intensity (the triangles represent the normalized H/C atom ratio, measured by means of MCC); c) Optical gap values from Mennella et al. (1995b).

3. DISCUSSION

The results reported in the previous section show that important changes take place in the IR spectrum of ACH2 grains because of heat treatment. They are caused by hydrogen effusion from the samples. In fact, the overall intensity of the C-H stretch absorption bands, an indicator of the hydrogen concentration in the samples, decreases as T_a increases. Only at 250 °C (Fig. 2b) the intensity increases due to the thermal conversion of weakly bonded hydrogen into normally bonded hydrogen (Dischler et al. 1983). The reduction of the hydrogen content is confirmed by the behavior of the H/C atom ratio, as determined by MCC technique (Fig 2b).

Hydrogen loss, however, induces significant rearrangements of the carbon bonding configuration. The as produced grains are dominated by sp^3 bonds, in agreement with the general result that hydrogen favors the sp^3 carbon hybridization and inhibits the growth of aromatic sp^2 clusters in carbons (Robertson 1986). Thermal annealing induces the breaking of sp^3 C-H bonds and tends to favour their transformation in sp^2 C sites (see Fig. 2a). At 515 °C, the remaining hydrogen atoms are mainly bonded to sp^2 sites in aromatic configurations, as testified by the intensity increase of the C-H stretching and bending modes. Moreover, the shift and the intensity increase of the C-C stretching band suggest not only an increase of the sp^2 site proportion, but also their better organization in graphitic clusters.

Although contributions of C-H bonds are still present at the highest considered temperature, the peak at 1580 cm^{-1} and the broad feature at about 1350 cm^{-1} are reminiscent of the graphitic features observed at the same frequencies in the Raman spectrum of disordered carbonaceous materials (e.g. Robertson 1986; Mennella et al. 1995b). This can be interpreted in terms of phononic density of states of the C-C skeleton structure of the graphitic clusters present in the samples.

In general, the bonded hydrogen concentration, or the corresponding proportions of sp^2 and sp^3 C sites, is not the most appropriate parameter for understanding the relations between the electronic properties and the microstructure in carbons. However, for our samples, a good correlation exsists between the increase of the optical gap, E_g, and the decrease of the sp^2 aromatic site concentration, as a function of T_a (see Fig. 2). We recall that the optical gap is determined by the π peak edges in the electronic density of states and it is correlated with the dimensions of the sp^2 aromatic clusters, with the larger clusters giving rise to the smaller optical gaps (Robertson 1986). Therefore, the observed decrease of E_g is an evidence of the growth in size of the graphitic islands during annealing. Thus, the bonding changes observed with IR spectroscopy are in agreement with the microstructural variations in our carbon grains, i.e. an increase of the sp^2 clustering degree as a function of annealing.

4. CONCLUSION

The analysis of the IR vibrational absorption spectrum allowed us to follow the changes in both C-H and C-C configurations in hydrogenated carbon grains due to thermal processing. We have found that the breaking of sp^3 C-H bonds upon annealing tends to favor the transformation of the carbon sites in a sp^2 aromatic configuration. The IR results are consistent with the scenario, outlined on the basis of complementary experimental techniques, for the microstructure thermal evolution of our carbon samples (Mennella et al. 1995a,b).

Acknowledgements. We thank S. Inarta, N. Staiano and E. Zona for their tecnhical assistance during measurements. This work has been supported by ASI, CNR and MURST research contracts.

References

Colangeli, L., Mennella, V., Palumbo, P., Rotundi, A., and Bussoletti, E., 1995, *Astr. Ap. Suppl. Ser.*, **113**, 561.

Dischler, B., Bubenzer, A., and Koidl, P. 1983, Solid State Comm. , 48, 105.

Mennella, V., Colangeli, L., Blanco, A., Bussoletti, E., Fonti, S., Palumbo, P., and Mertins, H. C. 1995a, *Ap. J.*, **444**, 288.

Mennella, V., Colangeli, L., Bussoletti, E., Monaco, G., Palumbo, P., and Rotundi, A. 1995b, *Ap. J. Suppl.*, **100**, 149.

Robertson, J. 1986, Adv. Phys., **35**, 317.

OBSERVATIONS OF TWO NON-STANDARD GRAIN COMPONENTS

R. F. SHIPMAN *Geophysics Directorate, Phillips Laboratory, Hanscom AFB*
SEAN J. CAREY *Geophysics Directorate, Phillips Laboratory, Hanscom AFB*
F. O. CLARK *Geophysics Directorate, Phillips Laboratory, Hanscom AFB*

ABSTRACT. We discuss evidence for two non-standard grain components: small conglomerates (Clark *et al.* 1995) and astronomical iron (Chlewicki & Laureijs 1988). The small conglomerates are small, temperature fluctuating grains made up of loosely bound 12 μm emitters (either PAHs or dielectrics). When these grains are exposed to strong UV radiation fields they break apart into smaller pieces. For high UV radiation regimes, such as H II regions, conglomerate grains best explain the reduction of 25 μm emission relative to 12 μm.

Astronomical iron was originally proposed for isolated cirrus clouds in order to account for the strength of the 60 μm emission. Within the diffuse ISM, these grains emit at a relatively high equilibrium temperature of 50 K. Our analysis of IRAS data shows the presence of a strong 60 μm emitter in the λ Orionis H II region and a component within the Rosette Nebula emitting primarily at 25 μm. Both of these observations can be accommodated by the presence of iron grains within the H II regions.

1. INTRODUCTION

Observations of the diffuse ISM in the mid to far infrared have provided a wealth of information about interstellar grains. Along with carriers of the UIR features, the diffuse ISM demonstrates stronger than expected emission at both 25 and 60 μm (see Puget and Léger 1989). The aim of our investigation has been to probe the nature of the carriers of the 25 and 60 μm emission.

Current models produce a portion (50%) of the 25 μm emission by PAH emission and the rest from very small, temperature spiking grains (VSG) (e.g. Désert, Boulanger and Puget 1988). In most models, the VSGs also provide half of the 60 μm emission with the other half due to the large classical grains. However, in one model, the 60 μm excess is due to equilibrium iron grains (Chlewicki and Laureijs 1988).

2. SMALL CONGLOMERATE MODEL

Figure 1 shows the radial profiles of IRAS color ratios for the Rosette Nebula. For comparison, we also show the results of the interstellar grain model of Désert,

Boulanger and Puget (1988, hereafter DBP) which correctly models the IRAS emission from quiescent clouds. To compare the model with the data, a distance of 1670 parsecs to the Rosette was assumed, and the emission at a given angular distance from HD 46223 (the earliest type star of the central cluster) was assumed to be due to grains at the corresponding linear distance from the star. The radiation field has been calculated using the model of Shipman (1994). Three models are presented in Figure 1: the full DBP grain model (dotted), the DBP model without PAHs (dash), and the DBP model without VSGs (dash-dot).

The 60/100 ratio shows heating of the large classical grain component towards the central cluster. However, relative to the 100 μm emission, the 12 μm emission declines with the increasing radiation field. A reasonable interpretation for this decline in 12 μm is that the carriers (PAHs in the DBP model) are destroyed by the harsh radiation field of the Rosette Nebula (Boulanger *et al.* 1988). The 12 μm image clearly demonstrates the lack of emission within the ionized region (Cox, Deharveng and Leene 1990).

Like the 60/100 ratio, the 25/100 ratio also increases with increasing radiation field. However, the value of the 25/100 ratio is three times lower than both the average diffuse ISM value (Laureijs 1989) and the DBP grain model at the greatest distances from the central cluster. This deficiency at 25 μm is also seen in the large 12/25 ratio beyond 40 arc minutes. Thus, the surrounding material outside of the Rosette Nebula appears to be deficient at 25 μm relative to the diffuse ISM (see Carey *et al.*, this volume).

Surprisingly, all three grain models overestimate the 25 μm emission in the outer regions of the Rosette Nebula. Separately, the removal of different components of the DBP grain model cannot match the observations. The only way to reconcile the grain models with the observations is to lower the abundance of both the PAHs and the VSGs for the outer regions.

However, this result implies that the VSGs are as easily destroyed as the PAHs, a result that is at odds with current destruction mechanisms (Guhathakurta and Draine 1989). In order to explain this result, Clark *et al.* (1995) proposed the conglomerate model. In this model, the VSGs are made up of loosely bound fragments of 12 μm emitters. In an enhanced radiation field, the conglomerates easily break apart and enhance the abundance of the 12 μm emitters. This scenario produces the low 25 μm emission and preserves enough 12 μm emitters in the outer regions to produce the observed 12/100 and 12/25 ratios. Further inside the H II regions, both 12 and 25 μm emitters are increasingly destroyed in this model.

3. ASTRONOMICAL IRON

The depletion of 25 μm carriers in the outer regions of the nebula implied by the models reduces the overall abundance of the emitters. The model, in this case, would significantly underestimate the emission within the ionized volume. In fact, if only global abundance variations are allowed, the DBP model is unable to simultaneously match the IRAS ratios in both the inner and outer regions of the Rosette Nebula. In order for the VSGs to produce the strength of the observed 25 μm emission in the core of the Rosette, these grains must increase in abundance within the nebula.

Perhaps, we are presented with a conglomerate model for the large classical grains:

where VSGs break off larger grains and replenish the overall abundance of the 25 μm emitters. However, for the λ Orionis H II region, observations indicate that the grains are larger than average ISM grains (Shipman and Carey 1996). Another alternative is the astronomical iron grain proposed by Chlewicki and Laureijs (1988) which would emit at a high equilibrium temperature and could potentially survive the harsh radiation fields of the Rosette and the λ Ori H II regions.

Within the Rosette, these grains would be hot enough to contribute at both 25 and 60 μm. COBE results for the λ Ori H II region also indicate a 60 μm excess (Wall *et al.* 1994) which could be explained by an iron grain component. However, we must point out that any material that emits at a significantly hotter temperature than classical grains and can survive in high UV environments could explain both the 25 and 60 μm emission within these H II regions.

Acknowledgements. This work was performed while S.J.C. held a National Research Council-USAF Research Associateship.

References

Boulanger, F., Beichman, C., Désert, X., Helou, G., Pérault, M., and Ryter, C. 1988, *Ap. J.*, **332**, 328.

Carey, S. J., Shipman, R. F., and Clark, F. O. 1996, this volume.

Chlewicki, G. and Laureijs, R. J. 1988, *Astr. Ap.*, **207**, L11.

Clark, F. O., Shipman, R. F., Assendorp, R., Kester, D., and Egan, M. P. 1995, P&SS, **43**, 1353.

Cox, P., Deharveng, L., and Leene A. 1990, *Astr. Ap.*, **230**, 181.

Désert, X., Boulanger F., and Puget J. L., 1990, *Astr. Ap.*, **237**, 215.

Guhathakurta, P., and Draine, B. T. 1989, *Ap. J.*, **345**, 230.

Puget, J. L., and Léger, A. 1989, *Ann. Rev. Astr. Ap.*, **27**, 161.

Shipman, R. F. 1994, PhD. Thesis, University of Wyoming.

Shipman, R. F., and Carey, S. J. 1996, in preparation.

Wall, W. F. *et al.* 1996, *Ap. J.*, **456**, 566.

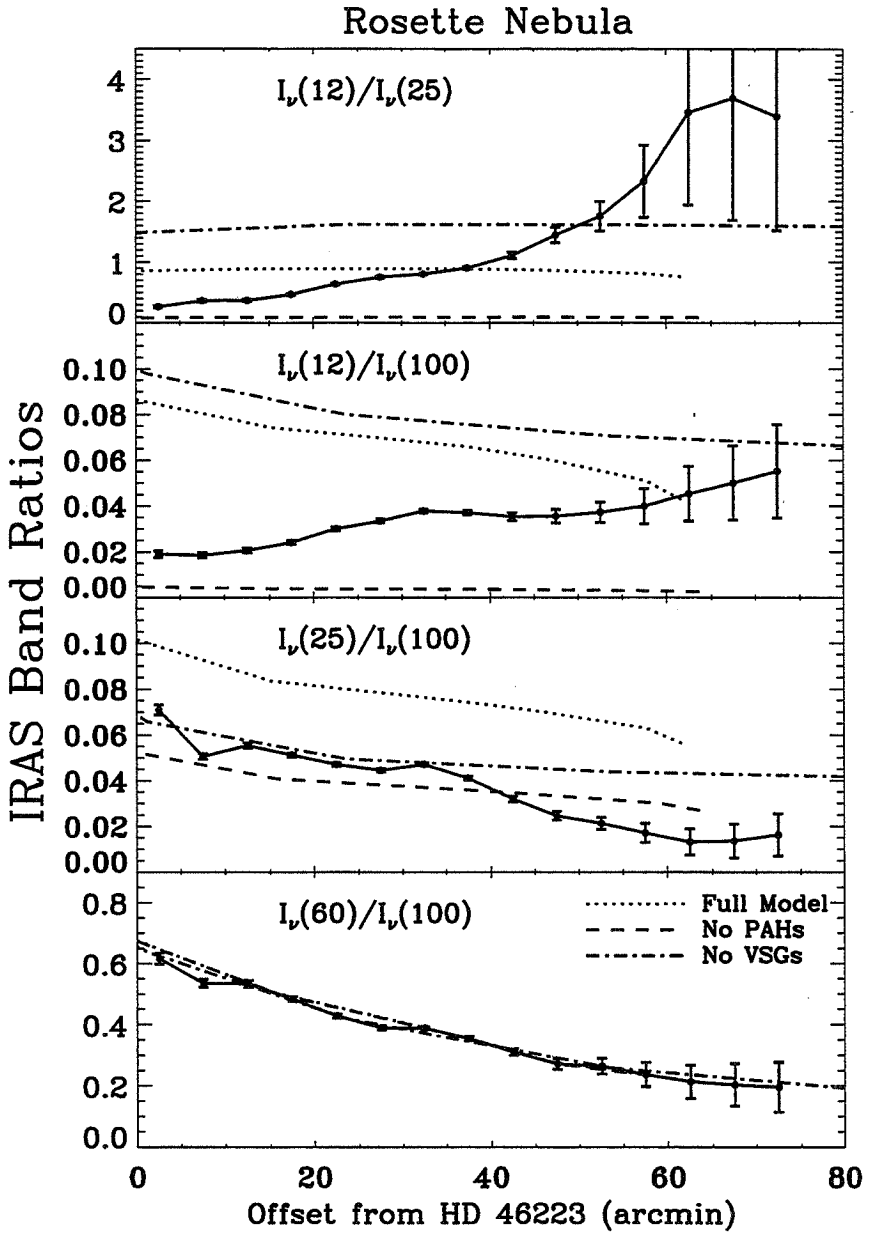

Figure 1. Band Ratios for the Rosette Nebula. Three models for the emission are presented from the O5 models of Désert, Boulanger and Puget (1990). The dotted line shows the complete DBP model. The dashed line shows the DBP model without the PAH grains. The dash-dotted line shows the DBP model without the VSGs.

IRAS COLORS OF THE PLEIADES

SEAN J. CAREY *Phillips Laboratory, Hanscom AFB, Massachusetts, USA*
R. F. SHIPMAN *Phillips Laboratory, Hanscom AFB, Massachusetts, USA*
F. O. CLARK *Phillips Laboratory, Hanscom AFB, Massachusetts, USA*

ABSTRACT. We present large scale images of the infrared emission of the region around the Pleiades using the ISSA data product from the IRAS mission. Residual Zodiacal background and a discontinuity in the image due to the scanning strategy of the satellite necessitated special background subtraction methods. The 60/100 color image clearly shows the heating of the ambient interstellar medium by the cluster. The 12/100 and 25/100 images peak on the cluster as expected for exposure of small dust grains to an enhanced UV radiation field; however, the 25/100 color declines to below the average interstellar value at the periphery of the cluster. Potential causes of the color deficit are discussed.

A new method of identifying dense molecular material through infrared emission properties is presented. The difference between the 100 μm flux density and the 60 μm flux density scaled by the average interstellar 60/100 color ratio (ΔI_{100}) is a sensitive diagnostic of material with embedded heating sources ($\Delta I_{100} < 0$) and cold, dense cores ($\Delta I_{100} > 0$). The dense cores of the Taurus cloud complex as well as Lynds 1457 are clearly identified by this method, while the IR bright but diffuse Pleiades molecular cloud is virtually indistinguishable from the nearby infrared cirrus.

1. INTRODUCTION

The wealth of observational information for the Pleiades makes the region ideal to study the effects of an increased radiation field on the dust emission properties of the diffuse interstellar medium. Optical (e. g. van Leeuwen *et al.* 1986) and UV (Andriesse *et al.* 1977) observations provide information on the ambient radiation field. The infrared emission has been previously studied by Castelaz, Sellgren and Werner (1987), who produced surface brightness maps at 12, 25, 60, and 100 μm and determined that the 40% of the infrared emission of the nebula is produced at 12 and 25 μm by a small, non-thermal grain component.

More recently, Shipman and Clark (1994) and Shipman (1994) have noted deficits in 12 and 25 μm emission with respect to 100 μm emission for the H II regions, S264 and the Rosette Nebula. We expand upon previous work by producing large format images of the Pleiades attempting to preserve the low-level emission at the edge of the cluster. The variations in infrared colors, particularly 12/100 and 25/100, as a function of radiation field are examined.

2. IMAGE PROCESSING

The 25° × 25° images presented in Figure 1 are mosaics of the ISSA images smoothed to a pixel size of 5 arcminutes. The image processing was complicated by two artifacts, the mission overlap discontinuity (MOD; Beichman *et al.* 1988) and residual Zodiacal emission. The MOD is the line along the in-scan direction dividing the 25 μm image (Figure 1a) in half and is a result of the scanning strategy of the instrument. The halves of the image were observed approximately six months apart and have very different levels of Zodiacal emission. The Zodiacal emission model subtracted from the data did not account for the Zodiacal bands (Wheelock *et al.* 1994) as evidenced by the horizontal striping in Figure 1a.

From the raw images at 12, 25, 60 and 100 μm, we subtracted a smooth background following the method of Laureijs (1989). Each image was rotated into Ecliptic coordinates and averaged into two slices in Ecliptic latitude on either side of the discontinuity. The averages consisted only of the diffuse cirrus emission as point sources, the Pleiades and IC 348 were not included in the averages. The averages at 12, 25, and 60 μm were fit by a function with the constraint that the average 12/100, 25/100 and 60/100 colors match those of Laureijs (1989). The function then represents the striping due to Zodiacal residuals. The 100 μm image was free of striping and needed no further processing. The fits were then applied to individual columns of the image (constant longitude slices) with a DC offset and small gain correction (of order unity). No correction was made for the MOD.

12/100, 25/100, 60/100 and 12/25 color maps were generated by direct ratioing of the images. Uncertainty maps were created by calculating an rms uncertainty in each of the flux images and then propagating the uncertainties in the ratio maps. Flux density, color ratio and uncertainty maps are available upon request.

3. IRAS COLORS OF THE PLEIADES

As expected for dust grains exposed to an increased radiation field (e. g. Désert *et al.* 1988), the 60/100 ratio (Figure 1d) increases towards the Pleiades rising from the average diffuse ISM value of 0.2 to > 0.5 near the exciting stars. The 12/100 color increases but more locally to the stars. The behavior of the 25/100 color (Figure 1c) is more complex. At the periphery of the cluster, the 25/100 color is below the diffuse ISM value, rising as the cluster is approached. The 12/25 color peaks on the periphery of the cluster reaching a value of ~ 1.5 before declining at the center.

The behavior of the 25/100 (and 12/25) color is similar to the variations identified for the H II regions and an isolated B4V star, HR 5336 (Carey *et al.* 1996). One possible explanation for the apparent deficiency of 25 μm emitters relative to both 100 μm emitters (large grains) and 12 μm emitters (PAHs) is a preferential destruction of small conglomerate grains contributing a significant fraction of the 25 μm emission (see Shipman *et al.* this volume and references therein). It is unlikely that the increased radiation field of the Pleiades is responsible for this grain destruction as the 25 μm decline is outside of the region of increased 60/100. One possible mechanism for the destruction of the 25 μm carriers is grain shattering by a mild shock due to the motion of the Pleiades through ISM (White and Bally 1993). Further study of conglomerate grain candidates is necessary to determine if the $\sim 18\,\mathrm{km\,s^{-1}}$ motion of the Pleiades through the ISM is sufficient to shatter grains.

4. IDENTIFICATION OF DENSE (MOLECULAR) REGIONS

A new method for identifying dense regions without heating sources is displayed in Figure 1b. The greyscale plot is of ΔI_{100} (Laureijs *et al.* 1991), where ΔI_{100} is

$$\Delta I_{100} = I_{100} - \frac{I_{60}}{\Theta}. \quad (1)$$

I_{100}, I_{60} are the flux densities at 100 and 60 μm and $\Theta = 0.21$, the average 60/100 value for the interstellar medium. Clouds with embedded heating sources will have $\Delta I_{100} < 0$, while dense clouds without heating sources will have $\Delta I_{100} > 0$ due to the attenuation of the interstellar radiation field by the cloud.

In Figure 1b, Lynds 1457 and the Taurus molecular cloud complex are clearly identified. Some of the molecular material around IC 348 is also visible indicating that star formation is not actively taking place in those condensations. Conspicuously absent is the Pleiades molecular cloud (south of the cluster; Federman and Wilson 1984). However, this cloud has a low density ($n \approx 300\,cm^{-3}$) and total visual extinction ($A_v = 3$) and should not be detected by the ΔI_{100} method. We are currently using this method to detect quiescent molecular material in the outer Galaxy.

Acknowledgements. This work was performed while S.J.C. held a National Research Council-USAF Research Associateship.

References

Andriesse, C. D., Piersma, Th. R., and Witt, A. N. 1977, *Astr. Ap.*, **54**, 841.

Beichman, C. A., Neugebauer, G., Habing, H. J., Clegg, P. E., and Chester, T. J. 1988, *IRAS Catalogs and Atlases: IRAS Explanatory Supplement*, (NASA reference publication: 1190).

Carey, S. J., Shipman, R. F., Clark, F. O., and Assendorp, R. 1996, *Ap. J.*, submitted.

Castelaz, M. W., Sellgren, K., and Werner, M. W. 1987, *Ap. J.*, **313**, 853.

Désert, X., Boulanger, F., and Puget, J. L. 1990, *Astr. Ap.*, **237**, 215.

Federman, S. R., and Wilson, R. F. 1984, *Ap. J.*, **283**, 626.

Laureijs, R. J. 1989, PhD. Thesis, University of Groningen.

Laureijs, R. J., Clark, F. O., and Prusti, T. 1991, *Ap. J.*, **372**, 185.

Shipman, R. F. 1994, PhD. Thesis, University of Wyoming.

Shipman, R. F., and Clark, F. O. 1994, *Ap. J.*, **422**, 153.

Shipman, R. F., Carey, S. J., and Clark, F. O. 1996, this volume.

van Leeuwen, F., Alphenaar, P., and Brand, J. 1986, *Astr. Ap. Suppl. Ser.*, **65**, 309.

Wheelock, S. L., *et al.*, 1994, *IRAS Sky Survey Atlas Explanatory Supplement*, JPL Publication 94-11 (Pasadena: JPL).

White, R. E., and Bally, J. 1993, *Ap. J.*, **409**, 234.

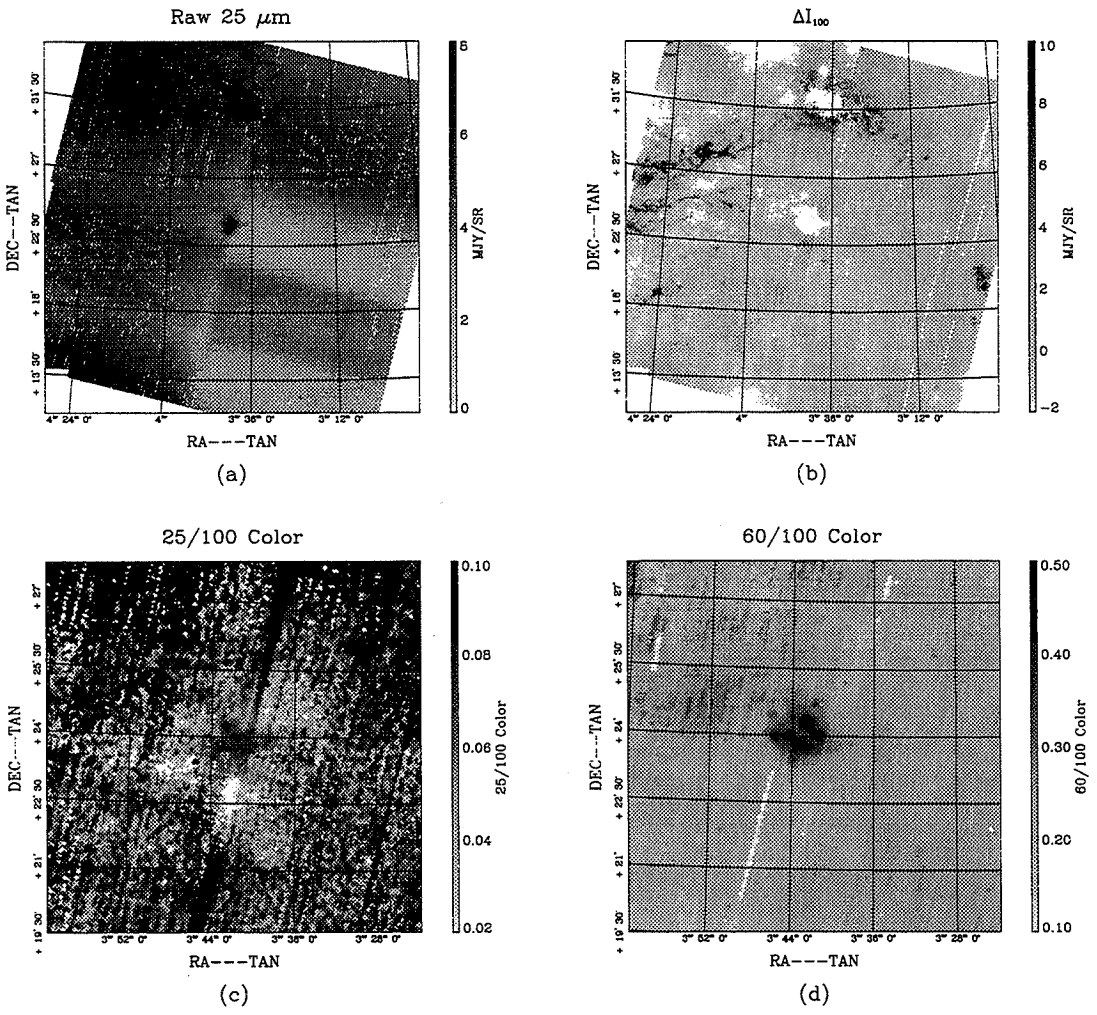

Figure 1. (a) Raw 25 μm image. Note the bands due to imperfect modelling of the Zodiacal light and the mission overlap discontinuity (line perpendicular to the residual bands). (b) ΔI_{100} image showing the location of cold dense molecular material, Lynds 1457 is to the right, the Taurus complex to the left. (c) 25/100 ratio map of the central 8 degrees. At the periphery of the cluster there is a deficiency of 25 μm emission. (d) 60/100 ratio map of the central 8 degrees. The background 60/100 value is nearly constant at 0.2.

PAH EMISSION IN THE ORION BAR

JESSE BREGMAN & G.C. SLOAN
NASA Ames Research Center, Moffett Field, CA

We have investigated the emission from polycyclic aromatic hydrocarbons (PAHs) in the Orion Bar region using a combination of narrow-band imaging and long-slit spectroscopy. Our goal is to study how the strength of the PAH bands vary with spatial position in this edge-on photo-dissociation region. Our specific focus here is how these variations constrain the carrier of the 3.4 μm band. The 3.29 μm band arises from a $v = 1 \rightarrow 0$ aromatic C–H stretch. The 3.40 μm band may arise from a $v = 2 \rightarrow 1$ aromatic C–H stretch (Barker et al. 1987), or an aliphatic C–H stretch in either attached methyl sidegroups (Joblin et al. 1996) or PAHs with more than one H atom attached to each C atom (H–PAHs; Bernstein et al. 1996a, 1996b).

Sloan et al. (1995) obtained narrow-band images of the Bar at 3.3 and 3.4 μm (Fig. 1) in order to compare the behavior of the 3.29 and 3.40 μm bands with distance from the ionization front. In a rectangle $\sim 16''$ across, both bands peak at the ionization front and then decrease exponentially into the neutral region. The 3.29 μm band has a 1/e scale height $\sim 9''$, but the 3.40 μm band shows an excess $\sim 10''$ behind the front. The positions of the H_2 and CO emission layers at $10''$ and $20''$ imply that the UV field decreases with a 1/e scale height of $3''$ (Tielens et al. 1993), a discrepancy which Giard et al. (1994) resolve by suggesting that the Bar has a very clumpy distribution. The PAH emission would occur in the regions between the clumps, and the longer attenuation distances would reflect the lower densities in these regions. The molecular emission would arise from shielded regions in and behind clumps where they are protected from the UV field. The higher opacities in the clumps would lead to different scale heights than in the interclump region.

Two PAH populations would explain the differences in the spatial behaviors of the 3.29 and 3.40 μm bands. Primitive unprocessed PAHs reside in and behind the clumps, while the PAHs in the interclump region have been processed by the UV field. In simple geometric models of these two distributions, in the primitive PAHs, the ratio of emission in the 3.40 μm band to the 3.29 μm band exceeds by more than a factor of two the limit of 0.17 for a $v = 2 \rightarrow 1$ transition set by Schutte et al. (1993). The energies required to produce a flux ratio higher than this limit would disrupt the C–H bond.

Sloan et al. (1996) obtained long-slit spectroscopy with the slit oriented perpendicular to the Bar, and showed that the 3.40 μm feature consists of two components. The main component (~ 3.395 μm) has a distribution similar to the 3.29 μm band, but the extra component (~ 3.405 μm) has a distribution very similar to the H_2 emission, peaking $\sim 10''$ behind the ionization front. They speculate that the extra component might arise from attached methyl sidegroups while the main component

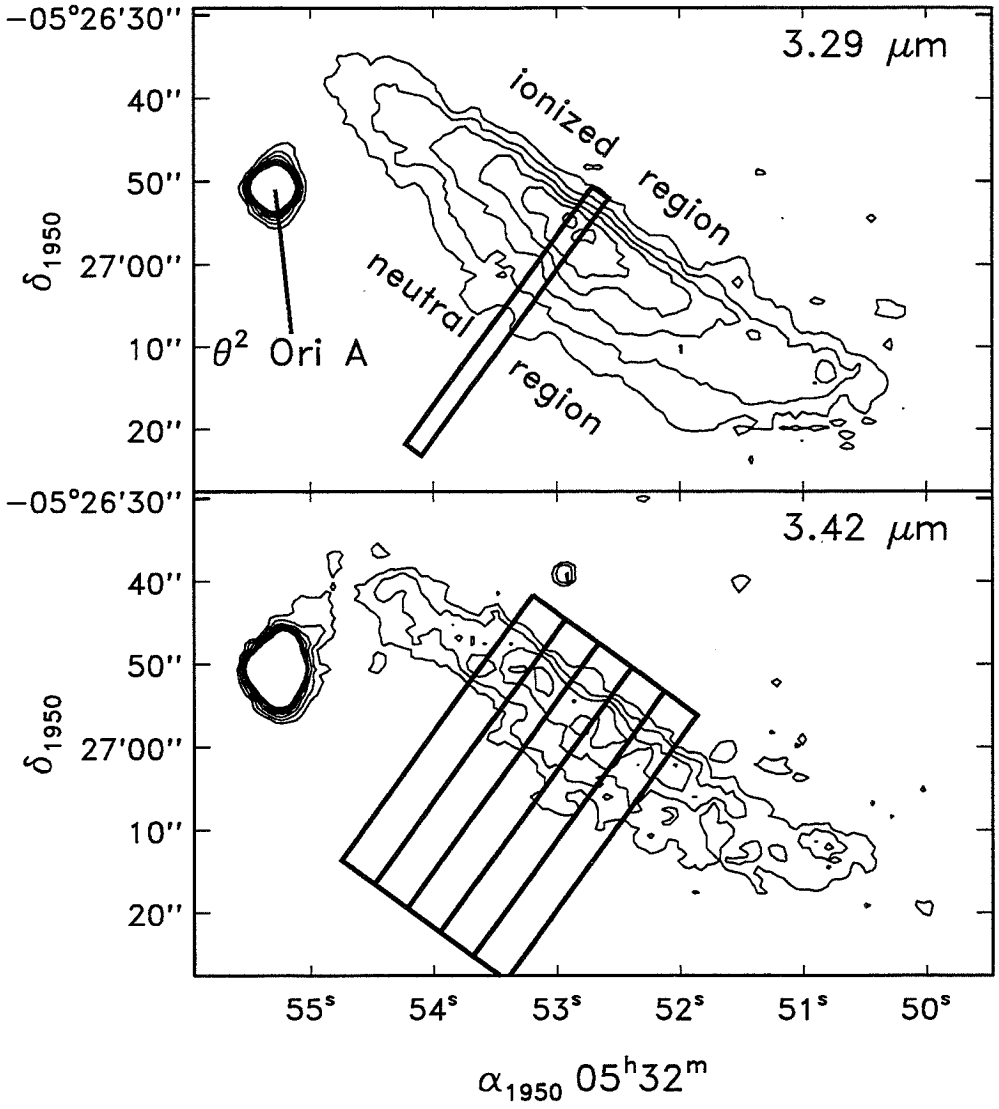

Figure 1. Contour plots of the 3.29 and 3.42 μm narrow-band images. The narrow rectangle in the 3.29 μm image depicts the position of the slit used for the spectroscopy. The five rectangles in the 3.40 μm image show the regions used to generate the profiles in Fig. 2.

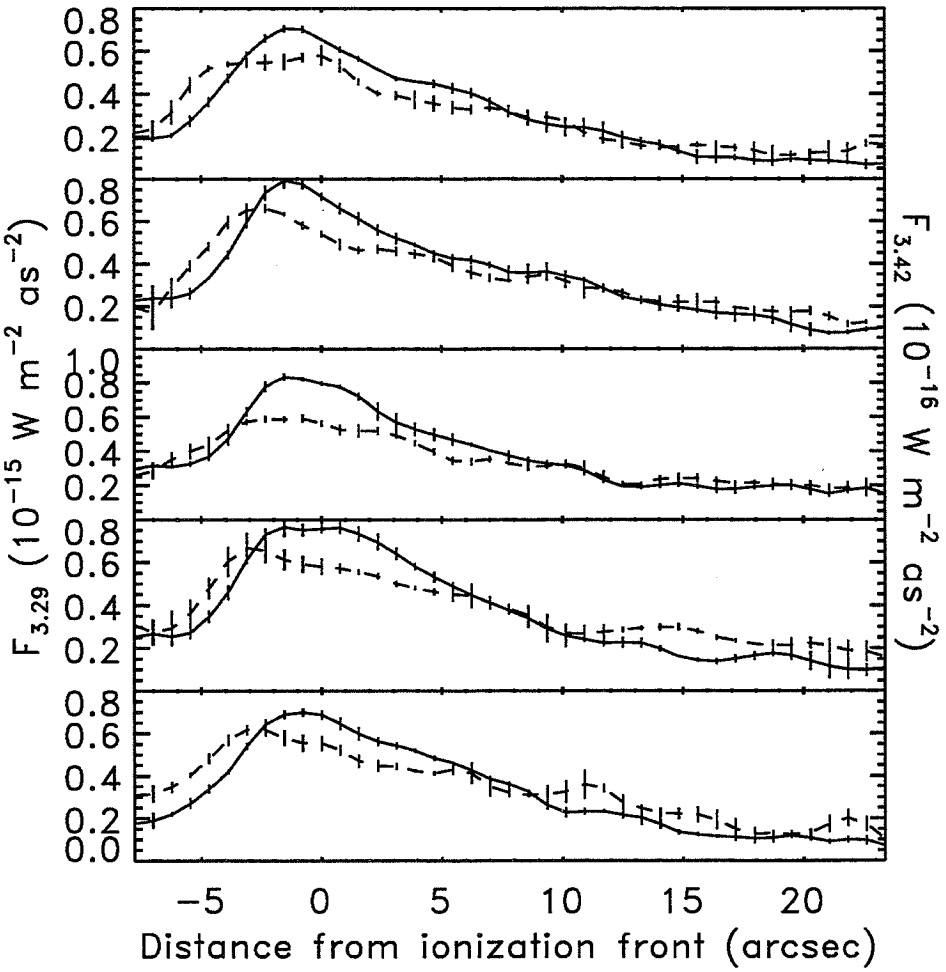

Figure 2. Profiles of the 3.29 and 3.40 μm emission features, extracted from the images in Fig. 1. The top panel corresponds to the east-most (or left-most) strip in Fig. 1; the bottom panel is the west-most profile. In each panel, the 3.29 μm profile is a solid line and the 3.40 μm profile is a dashed line. For clarity, the 3.40 μm profiles are plotted at ten times the scale of the 3.29 μm profiles.

arises from H–PAHs. Within the two-component PAH model, the methyl sidegroups would belong to the primitive PAHs, and the H–PAHs would be part of the processed PAHs.

We have modified our previous analysis of the narrow-band images of the Orion Bar by subdividing the Bar into five strips perpendicular to the ionization front, each five arcseconds across (Fig. 2). All of the strips show similar behaviors, but there are differences, primarily in the relative positions of the peaks of the 3.29 μm and 3.40 μm profiles, and also in secondary structures $\sim 10''$ behind the ionization front.

Our narrow-band imaging shows that the behavior of the 3.29 and 3.40 μm bands with distance from the ionization front varies along the Orion Bar. These differences point to the need to obtain additional long-slit spectroscopy of the Orion Bar with the slit in the perpendicular orientation. Such data would (1) test whether the results of Sloan et al. (1996) can be generalized along the Bar, and (2) exploit the inhomogeneities in the Bar to further disentangle the various spectral emission components.

References

Barker, J.R., Allamandola, L.J., & Tielens, A.G.G.M. 1987, *Ap. J.*, **315**, L61.

Bernstein, M.P., Sandford, S.A., & Allamandola, L.J. 1996a, this volume.

——. 1996b, *Ap. J.*, submitted.

Giard, M., Bernard, J.P., Lacombe, F., Normand, P., Rouan, D. 1994, *Astr. Ap.*, **291**, 239.

Joblin, C., Tielens, A.G.G.M., Allamandola, L.J., & Geballe, T.R. 1996, *Ap. J.*, **458**, 610.

Schutte, W.A., Tielens, A.G.G.M., & Allamandola, L.J. 1993, *Ap. J.*, **415**, 397.

Sloan, G.C., Bregman, J.D., Geballe, T.R., & Woodward, C.E. 1996, *Ap. J.*, in press.

Sloan, G.C., Bregman, J., Schultz, A.S.B., Temi, P., & Rank, D.M. 1995, in *The Role of Dust in the Formation of Stars*, ed. H.U. Käufl & R. Siebenmorgen (Springer Verlag).

Tielens, A.G.G.M., Meixner, M.M., van der Werf, P.P., Bregman, J., Tauber, J.A., Stutzki, J., & Rank., D. 1993, *Science*, **262**, 86.

LABORATORY EXPERIMENTS ON THE REACTIONS OF PAH CATIONS WITH MOLECULES AND ATOMS OF INTERSTELLAR INTEREST

V. LE PAGE *University of Colorado, Boulder, Co, USA*
H. S. LEE *University of Colorado, Boulder, Co, USA*
V. M. BIERBAUM *University of Colorado, Boulder, Co, USA*
T. P. SNOW *University of Colorado, Boulder, Co, USA*

ABSTRACT.

The $C_{10}H_8^+$ cation, and its dehydrogenated derivatives, $C_{10}H_7^+$ and $C_{10}H_6^+$, have been studied using a selected ion flow tube (SIFT). Reactions with molecules and atoms of interstellar interest show that $C_{10}H_8^+$ reacts with N and O to give neutral products HCN and CO, respectively. $C_{10}H_7^+$ and $C_{10}H_6^+$ are moderately reactive and reactions proceed through association with molecules. The implications of these results for the depletion of $C_{10}H_n{}^+$ in the interstellar medium are briefly discussed.

1. INTRODUCTION: THE PAH HYPOTHESIS

A series of interstellar and circumstellar infrared emission features was first noted by Gillet, Forrest, and Merrill (1973), and became known as the "unidentified infrared" features, or more simply the "UIRs". It was later noted by Duley and Williams (1981) that at least two of the more prominent UIRs (at 3.3 and 11.3 μm) coincided in wavelength with the positions of C-H stretching transitions in aromatic carbon molecules. Subsequently Léger and Puget (1984) and Allamandola, Tielens, and Barker (1985) proposed that the features are due to gas phase polycyclic aromatic hydrocarbons (PAHs), and this hypothesis has received broad support from both laboratory measurements and astronomical observations. The emission features are thought to be excited by absorption of UV photons in planetary nebulae, H II regions, and other regions where strong sources of UV flux are available. The presence of UIRs is correlated with carbon-rich environments (Cohen et al. 1986, 1989), which supports their identification with carbon-bearing species such as the PAHs. Further support arises from the great stability of the PAHs, a requirement imposed by the presence of the UIRs in the rather hostile environments near the stars. Today it is widely accepted among astrophysicists that PAHs are the carriers of the unidentified infrared emission features, and that these molecules represent an important constituent of the diffuse interstellar medium. While the dominant absorption bands of neutral PAHs lie in the UV (and in the visible for very large species which are probably not astrophysically important (Clar, 1964)), for the singly-ionized PAHs the absorption spectra are shifted into the visible regime. This fact led to the suggestion (Van der

Zwet and Allamandola 1985; Léger et d'Hendecourt 1985; Crawford et al. 1985) that ionized PAHs may be responsible for a well known but unidentified series of interstellar absorption features, known as the diffuse interstellar bands (DIBs). These features, of which about 200 are now known (Tielens and Snow 1995) have defied identification since their initial discovery over 70 years ago. The DIBs are significantly broader than atomic lines, having widths ranging from 0.8 to about 30 A. The widths are presumably due to unresolved rovibrational structure. Resolution of the strongest DIBs argues for large molecules as the carrier (Jenniskens et al. 1996; Ehrenfreund and Foing 1995). Recently, variation of the 8.6 and 11.3 m IR emission bands in reflection nebula in NGC 1333 was attributed to changes in the relative population of neutral and cationic PAHs (Joblin et al. 1996) showing evidence for PAH^+ in the interstellar medium (ISM). However the formation and destruction mechanisms of the PAH ions in the ISM are largely unknown. An understanding of the stability and chemical reactivities of these species is important for establishing their viability as carriers of the DIBs.

2. EXPERIMENTAL WORK

We have performed experiments in the gas phase on the chemistry of naphthalene cation $C_{10}H_8^+$ and its dehydrogenated derivatives ($C_{10}H_7^+$, $C_{10}H_6^+$), with H_2 , CO, NH_3 and H_2O. We have also carried out experiments on the reactions between $C_{10}H_8^+$ and N and O atoms, formed in a microwave discharge. The cations are produced in a selected ion flow tube source by reaction of neutral naphthalene with either He^+, produced by electron impact, or with argon metastable atoms, produced in a cold cathode discharge (Howorka 1978). After mass selection the ions are injected into a flow tube where they react with neutral gas. Monitoring the ion intensities versus distance from the neutral reactant inlet yields the rate constant and reaction products.

2.1. Formation of atoms

N atoms are produced by flowing nitrogen molecules (≈100 sccm) through a microwave discharge (power ≈30 Watt).

N density is measured using the well known titration reaction $N + NO > N_2 + O$ (Schiff 1964). When each N atom is replaced by an O atom the product ion counts reach a maximum. The measured NO flow at the endpoint gives the N and O density in the flow tube. Figure 1 shows a typical titration of N flow, using the appearance of the $C_9H_8^+$ ion, which is a main product of the reaction between $C_{10}H_8^+$ and O atoms.

3. RESULTS AND DISCUSSION

The results of astrophysical interest are summarized in Table 1.

$C_{10}H_8^+$ shows a small reactivity with O and N atoms and almost no reaction with neutral molecules ($k < 10^{-12}$ cm^3/s). This is attributed to delocalization of the radical cation throughout the aromatic system and to the small ionization potential of naphthalene (IP=8.14 eV). Indeed, the only fast reaction we found between $C_{10}H_8^+$ and a neutral molecule is the reaction with trimethylamine (IP=7.82 eV), which

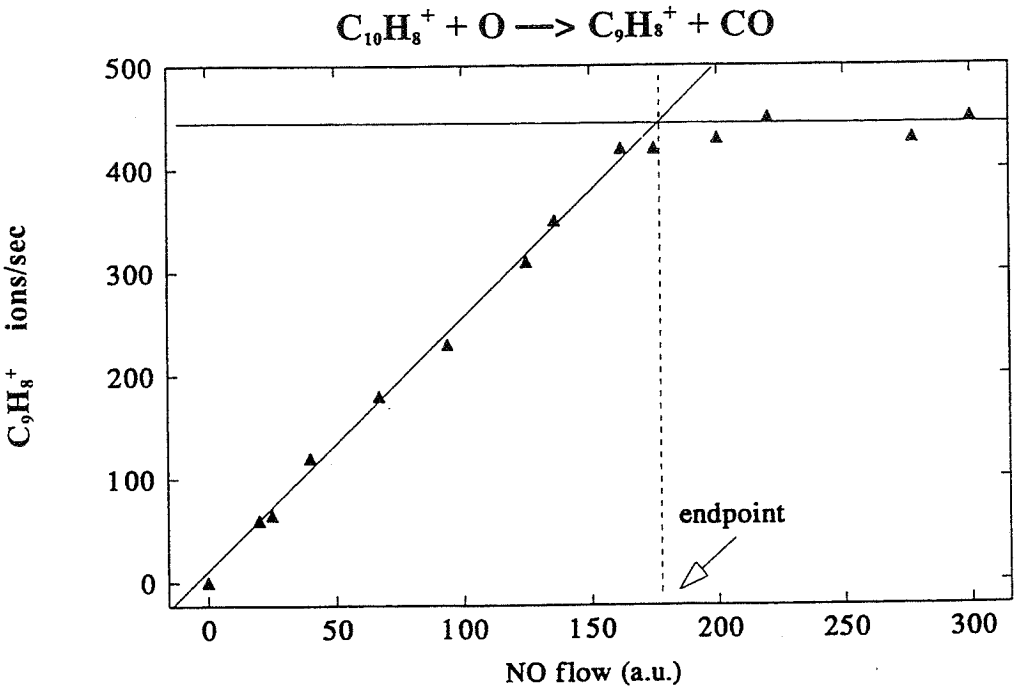

Figure 1. Calculation of the rate constant of the reaction between naphthalene cation and O atoms using the NO titration reaction. The endpoint gives the O density in the flow tube and the slope gives the reaction rate

proceeds near the collision rate (k = 1.0 10^{-9} cm^3/s). $C_{10}H_7^+$ is an even electron species with more localized charge, and this ion is found to be more reactive. However the only reaction channel is the association reaction, and pressure studies shows that these reactions, at least for H_2 , seem to be mostly saturated termolecular reactions. Thus, reaction between $C_{10}H_7^+$ and neutral molecules should not be an important $C_{10}H_7^+$ depletion channel in the ISM. Comparison with benzene suggests a similar behavior of naphthalene and benzene cations, and, also, of the phenylium cation $C_6H_5^+$ and $C_{10}H_7^+$. Identification of cyclic and acyclic isomers in Table 1 is suggested by this common behavior (ionization of $C_{10}H_8$ or C_6H_6 using He^+ leads in both case to the formation of at least two isomers for the dehydrogenated species (Ausloos 1989; Petrie et al. 1992)). $C_{10}H_6^+$ shows intermediate reactivity, lying between $C_{10}H_7^+$ and $C_{10}H_8^+$. This kind of behavior has been previously seen in the case of dehydrogenated pyrene cations $C_{16}H_8^+$ and was attributed to its odd electron character containing a localized charge and radical (Nourse et al. 1991). Reactions between $C_{10}H_8^+$ and atoms proceed through a C abstraction in the case of reaction with O and CH abstraction in the case of N atoms, leading to the formation of CO and HCN neutrals, respectively (see a mass spectrum of $C_{10}H_8^+$ + O reaction in Figure 2).

The main uncertainty in rate measurements involving atoms comes from the recombination of atoms on the wall of the reaction flow tube. This effect, if significant, could be the source of an underestimation of the rate constants. If the rate constant of the reaction between O atoms and naphthalene cations is as large as 10^{-10} cm^3/s this will lead to a lifetime of $C_{10}H_8^+$ in the ISM of about 10^5 years, which could be

Table 1. Rate constants of the reactions of $C_{10}H_n^+$ (n=6,7,8) with molecules and atoms

ion reactant *	molecule reactant	products	rate constant (cm^3/s) **
$C_{10}H_8^+$	H_2, CO, H_2O NH_3, N_2, O_2		no reaction
c-$C_{10}H_7^+$	H_2	$C_{10}H_9^+$	4.3 10-11
	CO	$C_{11}H_7O^+$	1.4 10-10
	H_2O	$C_{10}H_9O^+$	1.3 10-9
	NH_3	$C_{10}H_{10}N^+$	5.6 10-10
ac-$C_{10}H_7^+$	H_2,CO,H_2O NH_3	NH_4^+	no reaction 1.3 10-11
c-$C_{10}H_6^+$	H_2,CO,H_2O NH_3	$C_{10}H_9N^+$	no reaction 2.9 10-11
ac-$C_{10}H_6^+$	H_2,CO,H_2O NH_3	NH_4^+	no reaction 2.0 10-12
c-$C_{10}H_8^+$	N	$C_9H_7^+$ + HCN adduct	> 1.5 10-11
	O	$C_9H_8^+$ + CO adduct	> 2.2 10-11

* c represents the cyclic cation
ac represents the acyclic cation

** Helium pressure = 0.5 torr

too small to allow $C_{10}H_8^+$ to contribute to the DIBs. However it should be noted that we found that the reaction between benzene cations and atoms is considerably faster than reaction between $C_{10}H_8^+$ and atoms (almost one order of magnitude in the case of nitrogen atoms). This effect, if due to the delocalization of the radical cation throughout the aromatic rings, may favor larger PAHs and allow them to survive for a longer time in the ISM. Moreover, a matrix spectrum of compounds containing a five-carbon ring-like tetrahydrocyclopenta(a)pyrene fits the UIR features near 3.4 μm (Bernstein 1996) and products of reactions between large PAHs cations and O atoms cannot be ruled out as possible contributors of the DIBs, as reactions between PAH^+ and O atoms may produce five-carbon rings.

4. CONCLUSION

We have shown that $C_{10}H_8^+$ is a very stable ion. $C_{10}H_8^+$ does not react with most molecules which are abundant in the ISM but does react with O atoms. Further studies are in progress to refine the measurement of rate constants involving atoms. $C_{10}H_7^+$ and $C_{10}H_6^+$ are moderately reactive. The only product channel is association stabilized by He collisions, mainly a three-body process that cannot occur in interstel-

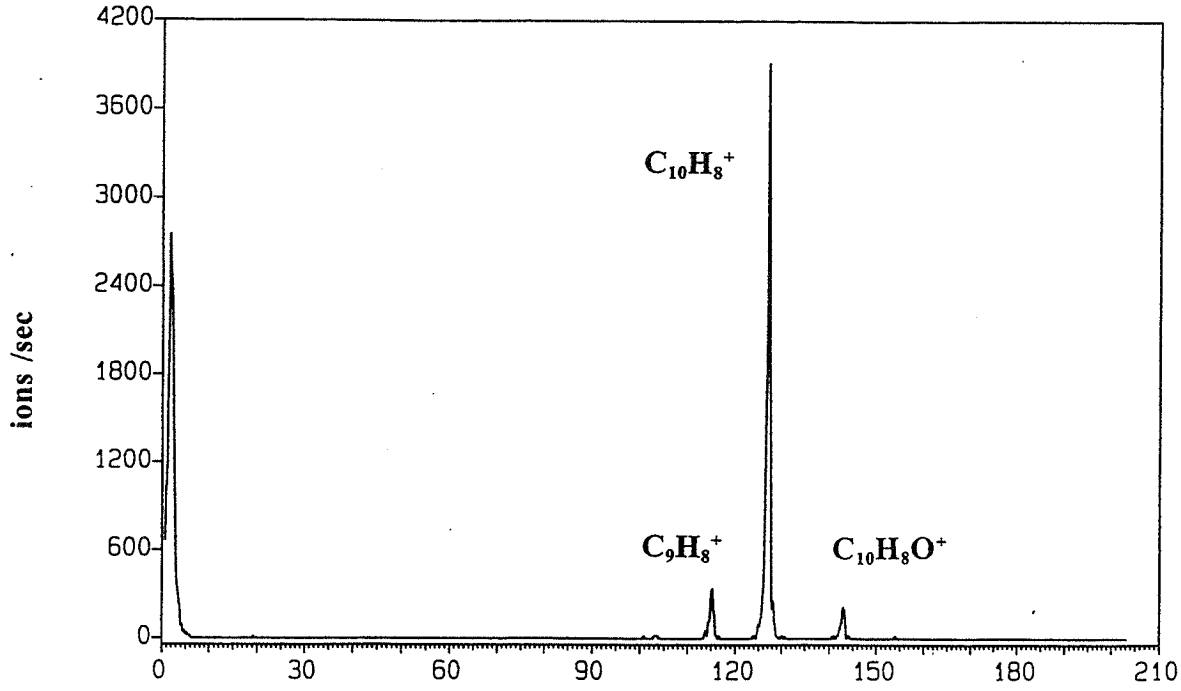

Figure 2. Products of the reaction between naphthalene cation and O atoms

lar clouds. Radiative association may also contribute and low pressure ICR studies are needed to measure the exact contribution of this channel. We have also shown that the chemistry of $C_{10}H_n^+$ is similar to that of benzene cations but with lower reactivity.

References

Allamandola, L. J., Tielens, A. G. G. M., and Barker, J. R. 1985, *Ap. J.*, **290**, L25.

Ausloos, P., Lias, S. G., Buckley, T. J., and Rogers, E. E. 1989, *Int. J. Mass. Spect. Ion Proc.*, **92**, 65.

Bernstein, M. P., private communication.

Cohen, M., Allamandola, L. J., Tielens, A. G. G. M., Bregman, J., Simpson, J. P., Witteborn, F. C., Wooden, D., and Rank, D. 1986, *Ap. J.*, **302**, 737.

Cohen, M., Tielens, A. G. G. M., Bregman, J., Witteborn, F. C., Rank, D., Allamandola, L. J., Wooden, D., and de Muizon, M. 1989, *Ap. J.*, **341**, 246.

Clar, E. 1964, in *Polycyclic Hydrocarbons*, (London: Academic Press).

Crawford, M. K., Tielens, A. G. G. M., Allamandola, L. J. 1985, *Ap. J. (Letters)*, **293**, L45.

Duley, W. W., and Williams, D. A. 1981, *M. N. R. A. S.*, **196**, 269.

Ehrenfreund, P., and Foing, B. H. 1996, *Astr. Ap.*, **307**, L25.

Gillet, F. C., Forrest, W. J., and Merrill, K. M. 1973, *Ap. J.*, **183**, 87.

Howorka, F. 1978, *J. Chem. Phys.*, **68**, 804.

Jenniskens, P., Porceddu, I., Benvenuti, P., and Desert, F.-X. 1996, *Astr. Ap., in press*

Joblin, C., Tielens, A. G. G. M., Geballe, T. R., and Wooden, D. H. 1996, *Ap. J.*, **460**, 119.

Léger, A., d'Hendecourt, L. and Boccara, N. 1987, in *Polycyclic Aromatic Hydrocarbons and Astrophysics*, (Dordrecht: D. Reidel Publishing Co.).

Léger, A., and Puget, J. 1984, *Astr. Ap.*, **137**, L5.

Nourse, B. D., Cox, K. A., and Cooks, R. G. 1991, in *Proceedings of the 39th ASMS Conference*, Nashville, TN, May 19 - 24.

Petrie, S., Javahery, G., and Bohme, D. K. 1992, *J. Am. Chem. Soc.*, **114**, 9205.

Schiff, H. I. 1964, *Ann. Geophys.*, **20**, 86.

Tielens, A. G. G. M., and Snow, T. P. 1995. *ıProc. Symp. Diffuse Interstellar Bands*, (Dordrecht: Kluwer).

Van der Zwet, G. P., and Allamandola, L. J. 1985, *Astr. Ap.*, **146**, 76.

PROCESSING OF ICY MANTLES IN PROTOSTELLAR ENVELOPES

J.E. CHIAR, D.C.B. WHITTET, & P.A. GERAKINES *Department of Physics, Applied Physics & Astronomy, Rensselaer Polytechnic Institute, Troy, NY 12180 USA*
A.C.A. BOOGERT *Kapteyn Laboratory, P.O. Box 800, 9700 AV, Groningen, NL*
A.J. ADAMSON *Centre for Astrophysics, University of Central Lancashire, Corporation Street, Preston PR1 2HE, UK*

1. INTRODUCTION

The 4.5–4.8 μm spectral region provides two potential diagnostics of radiative or thermal processing of interstellar ices in the environs of embedded stars in molecular clouds. A broad absorption feature centered at 4.62μm is seen in the spectra of several young stellar objects (YSOs) and attributed to C≡N bonds in a nitrile or isonitrile ("XCN"; see Tegler *et al.* 1995 and references therein). As CN-bearing solids in the laboratory are produced by energetic radiative processing of ices containing nitrogen, detection of this feature in YSOs is taken as evidence for (i) the presence of nitrogen in the unprocessed cloud ices, and (ii) evolution of the ice in the vicinity of the embedded source. The adjacent feature at 4.67 μm, identified with solid CO, provides not only quantitative information on CO itself but also indirect evidence for the presence of other species; its position and profile are sensitive to the molecular environment of the CO molecules in the ice mantle, and may be used to constrain both the composition and thermal/radiative history of the ice. One important example is the possibility to detect CO_2, which is produced easily in the laboratory by UV irradiation of CO-rich or CH_3OH-rich ices (e.g., Gerakines *et al.* 1996; Allamandola, *et al.* 1988). CO embedded in a CO_2 matrix gives a characteristic spectral signature (Sandford *et al.* 1988) distinct from other CO-bearing mixtures investigated to date. We have obtained CO absorption profiles of three young stellar objects in order to investigate their ice mantle composition.

2. OBSERVATIONS

All observations were carried out with the 256 × 256 InSb array of the cooled grating spectrometer CGS4 on the United Kingdom Infrared Telescope (UKIRT) on Mauna Kea. W33A was observed on 15 September 1995 with the spectropolarimetry module on CGS4 (see Chrysostomou *et al.* 1996). The spectra of R CrA-IRS2 and L1489-IRS were obtained on 18 May (via the UKIRTSERV program) and 31 October 1995, respectively. For these sources, the short focal length camera and the 75 lines/mm

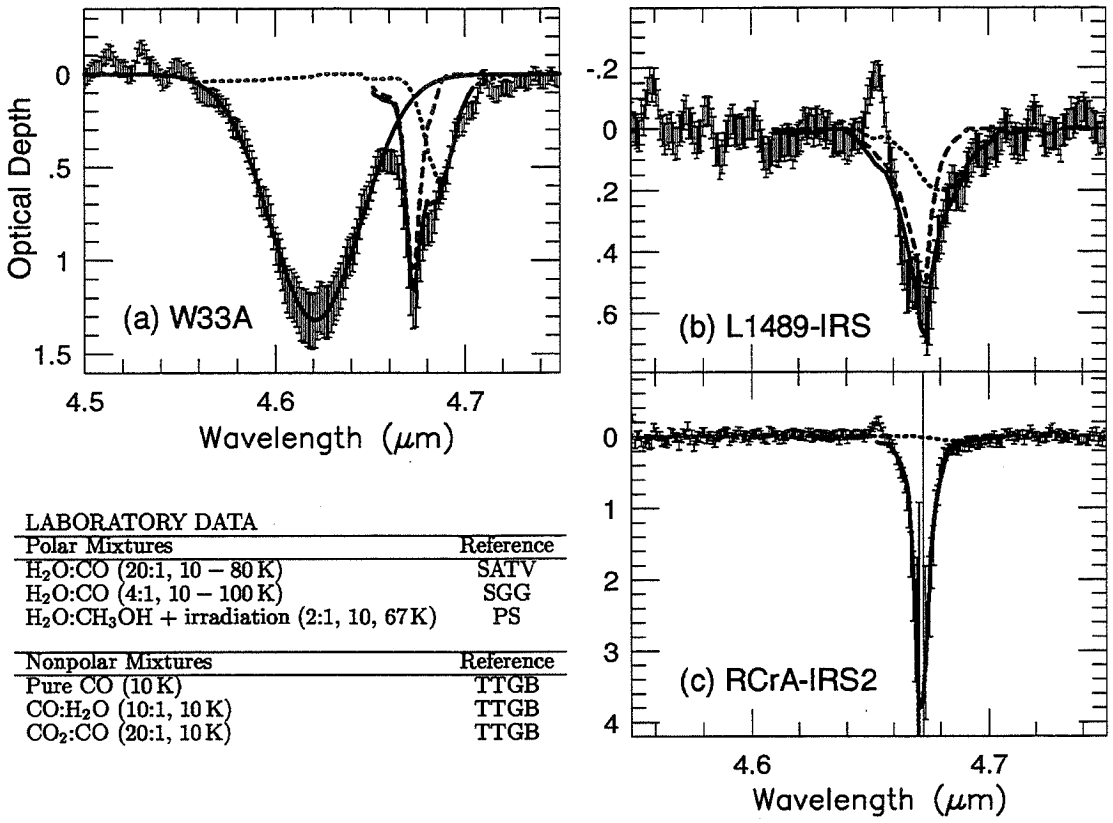

LABORATORY DATA

Polar Mixtures	Reference
H_2O:CO (20:1, 10 – 80 K)	SATV
H_2O:CO (4:1, 10 – 100 K)	SGG
H_2O:CH_3OH + irradiation (2:1, 10, 67 K)	PS

Nonpolar Mixtures	Reference
Pure CO (10 K)	TTGB
CO:H_2O (10:1, 10 K)	TTGB
CO_2:CO (20:1, 10 K)	TTGB

Figure 1. Spectra of protostellar objects showing absorption at 4.67 μm compared with the available laboratory spectra (listed above). Dotted and dashed lines represent the polar and nonpolar components, respectively. The solid lines represent the combination of broad and narrow components. [*a*] W33A. The 4.62 μm XCN feature is fitted with a Gaussian (solid line). [*b*] L1489-IRS. [*c*] R CrA-IRS2. See text for details.

grating were used. Wavelength calibration is relative to an argon lamp. Cancellation of atmospheric telluric features was achieved by ratioing with a standard star close in spectral type, observed at similar airmass (see Chiar *et al.* 1997 for details). Linear continua were fit to produce the optical depth spectra ($\tau(\lambda) = -\ln \frac{F_{obs}}{F_{cont}}$) shown in Fig. 1.

3. THE CO SPECTRA: EVIDENCE FOR PROCESSED GRAINS

Fits to the CO profile for all sources were carried out using the χ^2 minimization method described in Kerr *et al.* (1993) and Chiar *et al.* (1995). The available laboratory mixtures are listed in the table in Fig. 1 and the fits are shown in Figs. 1a – 1c. In the case of W33A, the XCN feature was "removed" before fits to the CO profile were done, by fitting a Gaussian (Fig. 1a) to the feature and subtracting it from the spectrum.

W33A is a highly luminous ($L \sim 10^5 L_\odot$) protostellar source deeply embedded ($A_V \sim 50-150$: Capps *et al.* 1978) in a dense molecular cloud. We find that two combina-

tions of mixtures each provide excellent fits to the CO profile (Fig. 1a) of W33A. The spectrum is best fit with either (a) CO:H_2O (10:1, 10 K: nonpolar component) and H_2O:CO (4:1, 100 K: polar component); or (b) (not shown) pure CO (nonpolar component) and the irradiated mixture of H_2O:CH_3OH (2:1, 10 K: polar component). The products, after irradiation, are: H_2O:CH_3OH:CO:CO_2 (100:10:1.5:4.6). These fits suggest that there are two different grain populations toward W33A: a cold component, located in the denser more shielded region of the W33 molecular cloud, and a processed component closer to the embedded object. Two scenarios may explain the type of processing: (1) In the first case, the mantles are thermally processed and there is a warm ($T \sim 100$ K) dust component. High resolution gas-phase CO observations have also shown two distinct temperature regimes along the line of sight, one at 23 K and one at 120 K (Mitchell *et al.* 1988). (2) The second fit is suggestive of a dust population that has been processed by irradiation, such as UV irradiation or ion bombardment. Both scenarios are consistent with the detection of the XCN feature at 4.62 μm which is thought to result from high energy processing of simple ices (§1).

L1489-IRS (IRAS 04016+2610) is a protostar embedded ($A_V \sim$ 29; Myers *et al.* 1987) in the L1489 dense core in the Taurus dark cloud. We present the first detection of solid CO in this object (Fig. 1b). The CO profile is similar to that of Elias 18, also embedded in the Taurus dark cloud (see Fig. 1e in Chiar *et al.* 1995). The spectra for these protostellar objects are broad with significant contributions from the polar component. The nonpolar components are best fit with CO_2:CO (20:1, 10 K). The polar component of L1489-IRS is best fit with an irradiated mixture of H_2O:CH_3OH (2:1, 10 K), although comparable fits are also provided by H_2O:CO (4:1) mixtures in the temperature range (10 – 50 K). The likely presence of CO_2 and the possible presence of XCN ($\tau < 0.03$) implies that we are sampling processed dust, in addition to a foreground dust component, around L1489-IRS.

The YSO R CrA-IRS2 is embedded ($A_V \sim$ 35) in the R CrA dark cloud, a region of recent star formation (Vrba *et al.* 1976). Wilking *et al.* (1986) have classified R CrA-IRS2 as a Class I protostar; the object is surrounded by dust at a wide range of temperatures and is still deeply embedded in its placental cloud. The CO absorption toward R CrA-IRS2, previously detected by Tanaka *et al.* (1994), is essentially "black" at the center of the feature. Our spectrum (Fig. 1c) has high S/N in the wings of the profile, thus a good estimate of the central optical depth can be made from the fitting procedure. We deduce an optical depth of $\tau_{4.67} = 3.81 \pm 0.04$. This relatively narrow profile is best fit with pure CO and H_2O:CO (4:1, 100 K) to the non-polar and polar components, respectively. The conspicuous weakness of the broad feature, in contrast to those of W33A and L1489-IRS, makes it difficult to constrain the composition of the polar mantle component. Nonpolar ices have low sublimation temperatures (15–20 K), thus a high abundance of pure CO (relative to H_2O-ice) in the line of sight to an embedded object seems surprising. It is probable we are sampling the more "quiescent" dust associated with the intracloud material in R CrA and/or the outermost dust region around R CrA-IRS2. The apparent absence of the XCN feature is thus not surprising.

4. DISCUSSION

Our ground-based studies of the CO profile (Chiar *et al.* 1995, 1997) provide strong indirect evidence for the presence of CO_2 ice in the molecular clouds associated with certain embedded young stellar objects. As yet, there is no evidence for CO_2 in

more quiescent material in lines of sight toward field stars. Recently, the Infrared Space Observatory (ISO) has achieved the first direct detection of solid CO_2 via the strong C=O resonance at 4.27 μm (de Graauw *et al.* 1996; Gürtler *et al.* 1996). The line of sight abundance of CO_2 is typically 10–20% of the H_2O abundance in sources studied to date. In some cases (GL2591, S140) CO_2 is seen in lines of sight that lack detectable CO, presumably because the grains in these lines of sight are irradiated and heated to such a degree that all CO is either evaporated or converted to other species. Elsewhere, in W33A and NGC 7538 IRS9, CO and CO_2 are both detected and presumably coexist in the same mantle layer, as we surmise to be the case towards L1489-IRS. Although ISO data are not yet available for the sources L1489-IRS and R CrA-IRS2 discussed in this paper, we predict the detection of CO_2 in (at least) L1489-IRS.

References

Allamandola, L.J., & Sandford, S.A. 1988, Dust in the Universe, ed. M.E., Bailey & D.A. Williams (Cambridge University Press), 229

Capps, R.W., Gillett, F.C., & Knacke, R.F. 1978, *Ap. J.*, **226**, 863

Chiar, J.E., Adamson, A.J., Kerr, T.H., & Whittet, D.C.B. 1995, *Ap. J.*, **455**, 234.

Chiar, J.E., *et al.* 1997, in preparation.

Chrysostomou, A., Hough, J.H., Whittet, D.C.B., Aitken, D.K., Roche, P.F., & Lazarian, A. 1996, *Ap. J. (Letters)*, **461**, L61

de Graauw, M.W.M., *et al.* 1996, *Astr. Ap.*, in press

Gerakines, P.A., Schutte, W.A., & Ehrenfreund, P. 1996, *Astr. Ap.*, **312**, 289

Gürtler, J., Henning, Th., Kömpe, C., Pfau, W., Krätschmer, W., Lemke, D. 1996, *Astr. Ap.*, in press

Kerr, T.H., Adamson, A.J., & Whittet, D.C.B. 1993, *M. N. R. A. S.*, **262**, 1047

Mitchell, G.F., Allen, M., & Maillard, J.-P. 1988, *Ap. J.*, **333**, 55

Myers, P.C., Fuller, G.A., Mathieu, R.D., Beichman, C.A., Benson, P.J., Schild, R.E., & Emerson, J.P. 1987, *Ap. J.*, **319**, 340

Palumbo, M. E., & Strazzulla, G. 1993, *Astr. Ap.*, **269**, 568 (PS)

Sandford, S.A., Allamandola, L.J., Tielens, A.G.G.M., & Valero, G.J. 1988, *Ap. J.*, **329**, 498 (SATV)

Schmitt, B., Greenberg, J. M., & Grim, R. J. A. 1989, *Ap. J. (Letters)*, **340**, L33 (SGG)

Tanaka, M., Nagata, T., Sato, S., & Yamamoto, T. 1994, *Ap. J.*, **430**, 779

Tegler, S.C., Weintraub, D.A., Rettig, T.W., Pendleton, Y.J., Whittet, D.C.B., & Kulesa, C.A. 1995, *Ap. J.*, **439**, 279

Tielens, A.G.G.M., Tokunaga, A.T., Geballe, T.R., & Baas, F. 1991, *Ap. J.*, **381**, 181

Vrba, F.J., Strom, S.E., & Strom, K.M, *A. J.*, **81**, 958

Wilking, B.A., Taylor, K.N.R., & Storey, J.W.V. 1986, *A. J.*, **92**, 103

THE ICE AND SILICATE SPECTRAL FEATURES FOR DUST AGGREGATES

A. E. ILIN *Pulkovo Observatory, Russian Academy of Sciences,*
65/1 Pulkovskoe shosse, 196140 St.Petersburg, Russia, alexei@ilin.spb.su

ABSTRACT. The optical properties of inhomogeneous aggregates of dust particles are calculated. The Discrete Dipole Approximation (DDA) is applied to the calculation of light scattering by the dust aggregates. The mixtures of ices and silicates are considered. The IR profiles near ice and silicate spectral features (3 μm and 10 μm) are constructed. The influence of grain topology, chemical composition and porosity have been investigated. The comparison of exact results for inhomogeneous aggregate and the effective medium theory (the rules of Maxwell-Garnett and of Bruggeman) is made.

1. INTRODUCTION

Last years fluffy and aggregate grains were often used as the dust models in the interstellar clouds (Mathis and Whiffen, 1989) and the protostellar environment (Krügel and Siebenmorgen, 1994). The optical properties of carbon-silicate aggregates were investigated in detail (see, for example, Bazell and Dwek, 1990, Stognienko *et al.*, 1995). However, the optical properties of ice-silicate aggregates (comet-like particles) are still far from complete understood.

2. MODEL

We use the Discrete Dipole Approximation (Draine, 1988) for computation of scattering by the single dust aggregate. It is flexible technique for computing scattering by dust particles of arbitrary geometry and complex structure. The application of the complex conjugate gradient algorithms and the fast fourier transform (Goodman *et al.*, 1991, Draine and Flatau, 1994) permits the study of scattering problems involving large number of small subgrains using modern scientific workstations.

The model of the dust particles is as follows: the spherical volume is filled with homogeneous ice and silicate spheres (subgrains). We consider three cases

- Model A (*"dipole"*): all silicate subgrains are grouped together in one hemisphere of a spherical volume, whereas the ice subgrains are aggregated in the opposite one. The light is incident on the aggregate parallel to the "equator";
- Model B (*core-mantle particle*): all silicate subgrains are grouped in a spherical volume (core) surrounded by the mantle of the ice subgrains;

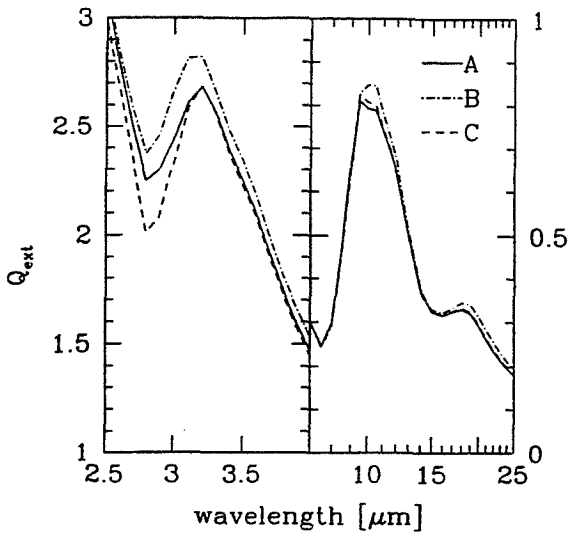

Figure 1. Influence of aggregate structure. The aggregate particle has effective radius $a = 1\mu m$

- Model C (*mixture*): the silicate and ice subgrains randomly fill the spherical volume of the aggregate.

We consider the rectangular lattice with the $N_x \times N_y \times N_z = 16 \times 16 \times 16 = 4096$ sites. This cube circumscribes our spherical aggregate so that only 2176 sites of cubic lattice are inside the sphere. The silicate and ice subgrains are arranged at these sites. In each model the number of silicate subgrains and the number of ice subgrains are equal ($N_{sil} = N_{ice}$).

We use in our calculation the refractive indexes of the astronomical silicate (Draine, 1985) and the "dirty" ice (Preibisch *et al.*, 1993) (the ice averages 10% of graphite inclusions). We compared also some our results with the effective medium theory (Maxwell-Garnett and Bruggeman rules (Bohren and Huffman, 1983)).

3. RESULTS

Figure 1 shows the effects of varying structure of the dust aggregate. The core-mantle model B gives more broad and strong bands both on 3 μm and 10 μm. The most distinctions are seen within the H_2O band. Most narrow bands are resulting for the model C (the quasiuniform mixture). In all, the figure demonstrates the clear distinctions in the IR band profiles depending on the dust aggregate structure or, more precisely, depending on the degree of the different subgrains mixing.

We have found also that the Maxwell-Garnett and the Bruggeman rules produce results coinciding very closely with the band profiles for the model C derived from the DDA. Therefore the effective medium theory is unacceptable for highly ununiform dust aggregates.

Figure 2 illustrates the effects of varying composition of randomly mixed aggregate (model C) for effective radii 0.1 and 1 μm. We have considered three cases of the

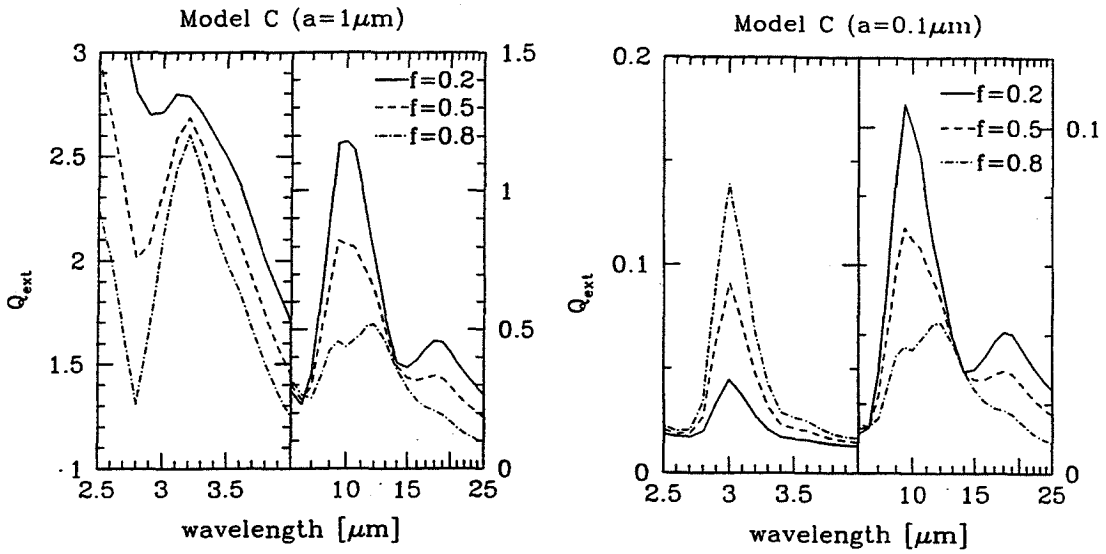

Figure 2. Influence of aggregate composition. The dust aggregate (Model C) has effective radius $a = 1\mu m$ (a) and $= 0.1\mu m$ (b). The volume concentration of ice equals 0.2 (solid line), 0.5 (short-dashed line) and 0.8 (dot-dashed line).

relative volume fraction of ice subgrains (0.2, 0.5 and 0.8). The half-width of 10 μm band is increasing when the relative volume fraction of ice is decreasing. This owes to the existence of the 12 μm ice band that modifies the profile of 10 μm silicate feature. One can see also that there are no distinctions in the silicate profiles behavior for two effective radii of the dust aggregate, because we are working within the Rayleigh limit even if the effective radius of dust aggregate equals 1 μm. The influence of aggregate composition on the H_2O band profile for $a = 1\mu m$ is more interesting. A decrease of the band strength keeps pace with the continuum level increase when we reduce the relative volume fraction of the ice.

We have investigated also the effects of fluffiness on the polarization profiles across the ice and silicate spectral features (Figure 3). We have considered a prolate spheroidal aggregate ($N_x = N_y = 8, N_z = 16$) with the randomly mixing ice and silicate subgrains ($N_{sil} = N_{ice}$). The number of porosity is the fraction of unoccupied sites in the lattice. Henning and Stognienko, 1983 and Ilin, 1995 have found that the increase of the porosity shifts the 10 μm and the 18 μm peak positions to longer wavelengths and raises the relative strength of the 18 μm band. This effect is seen on Figure 3, where we show also the evolution of the H_2O band profile.

Our preliminary results may be useful for the interpretations of numerous IR observations of protostars.

Acknowledgements. I thank Drs. B.T. Draine and P.J.Flatau for making the DDA code available as shareware.

References

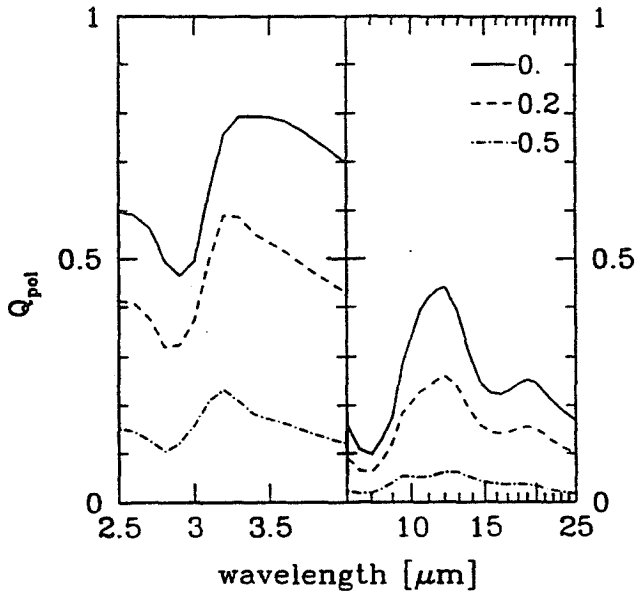

Figure 3. Influence of aggregate fluffiness on the polarization. The randomly mixed aggregate (prolate spheroid ($N_x = N_y = 8, N_z = 16$)) has effective radius 1 μm. The number of porosity equals 0 (solid line), 0.2 (short-dashed line) and 0.5 (dot-dashed line).

Bazell, D., and Dwek, E. 1990, *Ap. J.*, **360**, 142.

Bohren, C.F., and Huffman, D.R. 1983, *Absorption and Scattering of Light by Small Particles* (New York: Wiley).

Draine, B. T. 1985, *Ap. J. Suppl.*, **57**, 585.

Draine, B. T. 1988, *Ap. J.*, **333**, 848.

Draine, B. T., and Flatau, P.J. 1994, *J. Opt. Soc. Am. A.*, **11**, 1491.

Goodman, J.J., Draine, B.T., Flatau, P.J. 1991, *Opt. Lett.*, **16**, 1198.

Henning, Th., and Stognienko, R. 1993, *Astr. Ap.*, **280**, 609.

Ilin, A.E. 1995, *Ap. Space Sci.*, **224**, 233.

Krügel, E., and Siebenmorgen, R. 1994, *Astr. Ap.*, **288**, 929.

Mathis, J.S., and Whiffen, G. 1989, *Ap. J.*, **341**, 808.

Preibisch, T., Ossenkopf, V., Yorke, H.W., and Henning, Th., 1993, *Astr. Ap.*, **279**, 577.

Stognienko, R., Henning, Th., and Ossenkopf, V. 1995, *Astr. Ap.*, **296**, 797.

EVIDENCE FOR THE EVOLUTION OF GRAIN PROPERTIES IN THE NGC 2024 STAR FORMING RIDGE

C. J. CHANDLER *Mullard Radio Astronomy Observatory, University of Cambridge, UK*
J. E. CARLSTROM *Department of Astronomy and Astrophysics, University of Chicago, USA*
J. S. RICHER, A. VISSER, AND R. PADMAN *Mullard Radio Astronomy Observatory, University of Cambridge, UK*

ABSTRACT. High-resolution images of the NGC 2024 molecular ridge in CS(2–1) and 3 mm continuum emission have been obtained using the Owens Valley millimeter array. The data are used to determine the temperature and dynamics of the ridge, and to ascertain the evolutionary state of the embedded protostars FIR2–7. Dust continuum emission is detected from all six FIR sources. The CS(2–1) follows the ridge closely, but does not always coincide with the FIR sources. Direct comparison of column density estimates derived from the CS and the dust emission in the ridge shows that for all FIR sources except FIR5 both methods are in agreement to within a factor of two, assuming a dust opacity $\kappa_{3\mathrm{mm}} = 0.01$ cm^2 g^{-1}. However, away from the FIR sources strong CS(1–0) emission is observed in several compact clumps which, with the above dust opacity, should have been detected in 3 mm dust continuum. The brightness temperature of the CS, $\sim$ 40 K, rules out the possibility that the high line-to-continuum ratio is due to low gas temperatures; the discrepancy can be resolved if $\kappa_{3\mathrm{mm}}$ is a factor of 10 lower away from the FIR sources. A new high-resolution image of the 450-μm dust continuum emission obtained using the James Clerk Maxwell Telescope supports this hypothesis. These results suggest an evolution in the physical properties of the dust grains, possibly grain size, between quiescent regions in the ridge and the sites of active star formation.

1. INTRODUCTION

When written in the usual long-wavelength form, the dust opacity $\kappa_\nu = \kappa_0(\nu/\nu_0)^\beta$ is observed to have β in the range 0 to 1 in T Tauri disks rather than the theoretical limit for small grains of $\beta = 2$ (Beckwith & Sargent 1991; Mannings & Emerson 1994). This has been interpreted as an evolution of the dust properties, perhaps an increase in grain size, in T Tauri disks compared to the interstellar medium. To ascertain whether the change in β occurs only during the later phases of T Tauri disk evolution, or whether similarly low values for β are observed in the high-density circumstellar material of more embedded sources, we have studied the NGC 2024 star forming ridge in both dust emission and molecular line emission. The FIR sources in

the NGC 2024 cloud were identified through their mm continuum emission by Mezger *et al.* (1988, 1992). Three of the sources, FIR4, FIR5 and FIR6 are associated with molecular outflow, and so contain embedded protostars (Chandler & Carlstrom 1996; Richer *et al.* 1989; Richer 1990). The other FIR sources may be younger, even pre-protostellar.

2. OBSERVATIONS

Using the Owens Valley mm array three fields covering FIR2–7 in the NGC 2024 ridge were observed in 98 GHz continuum and CS(2–1) emission, with a synthesized beam $\theta_b = 4.5 \times 3.6''$ (1900 × 1500 AU). Also presented is an image of the 450-μm dust continuum obtained using the 15-m James Clerk Maxwell Telescope, with $\theta_b = 8''$ (3300 AU).

3. CONTINUUM EMISSION

We detect 3-mm continuum emission from all the FIR sources covered by our observations (Figure 1a). Ridges of free-free emission oriented east-west are also detected, and are locations where the foreground HII region is ionization-bounded by the molecular cloud (Gaume *et al.* 1992). The spectral indices of all the FIR sources except FIR4 are consistent with dust emission (Chandler & Carlstrom 1996). At FIR4 a flatter spectral component is also needed, which may be due to confusion with the nearby ridge of ionized gas.

4. CS AND DUST AS TRACERS OF $N(H_2)$

The CS(2–1) is represented as a greyscale in Figure 1b. By making some assumptions about the temperature, the CS abundance, and the dust opacity, both the dust and the integrated CS(2–1) emission can be used to estimate the column density of molecular hydrogen in the ridge. For the dust we use $T_d = 30$ K, $\kappa_0 = 0.1$ cm^2 g^{-1} at $\nu_0 = 10^{12}$ Hz (*cf.* Hildebrand 1983; Beckwith *et al.* 1990), and $\beta = 1$, *i.e.*, the value commonly observed in T Tauri disks rather than the interstellar medium. For the CS we use an abundance relative to molecular hydrogen of 2.5×10^{-9} (as found for the Orion ridge: Blake *et al.* 1987), $T_{ex} = 40$ K, and $\tau_{21} = 1$. We find good correspondence (within a factor of 2) between the column densities derived using both methods at all the FIR sources apart from FIR5. However, there is a striking anti-correlation between the CS and the dust at FIR5 and in the CS condensations to the east of FIR5/6.

5. CS/DUST DISCREPANCIES AT FIR5/6

Close to FIR6, spectra of the CS(2–1) emission are dominated by the compact molecular outflow from that source (see Chandler & Carlstrom 1996). The condensations close to FIR5, however, appear to be quiescent, with Gaussian line profiles and no sign of star formation. At these locations there is a serious discrepancy between the

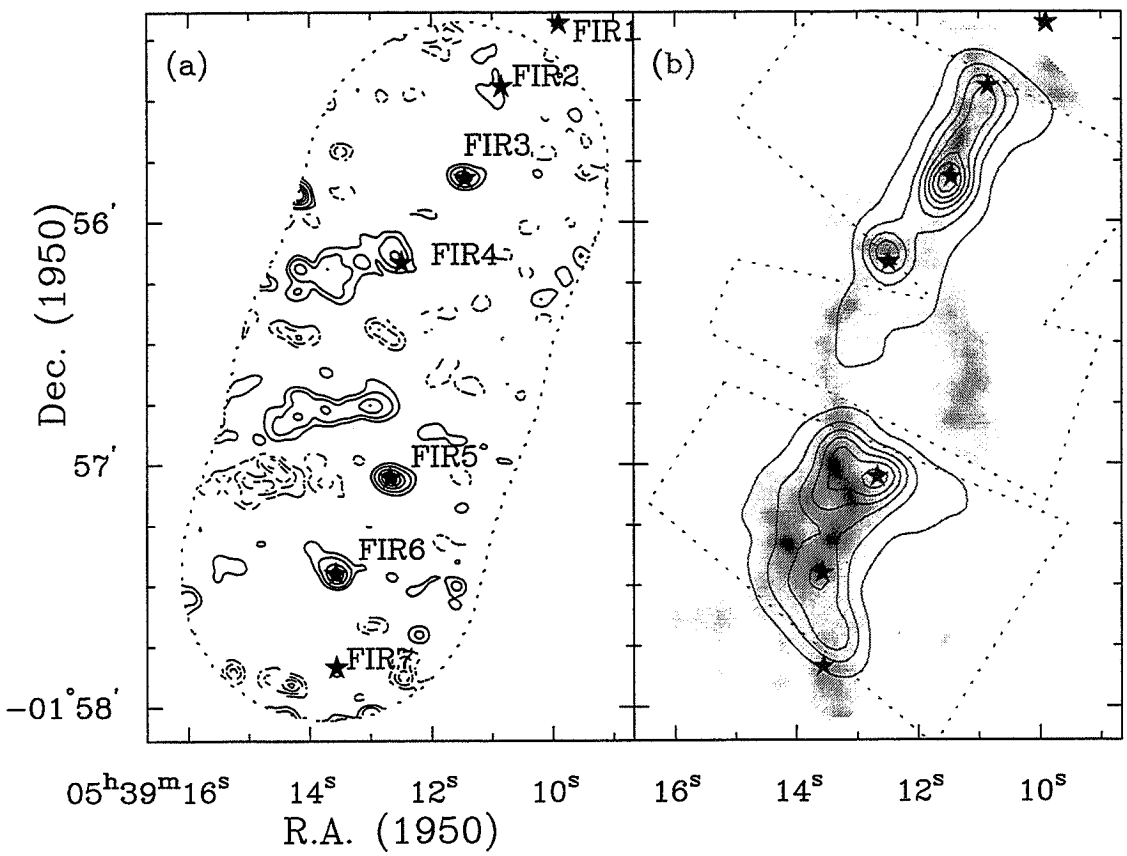

Figure 1. (a) 3-mm continuum image of NGC 2024. Stars indicate the positions of FIR1–7. The outline gives the 50% response level of the region imaged. (b) contours of the 450-μm continuum emission overlaid on a greyscale of integrated CS(2–1) emission. The outline gives the area of the 450-μm map.

column density derived from CS compared to the dust. The most plausible explanations for the discrepancies both at FIR5, where $N(\mathrm{H_2})_{\mathrm{dust}}/N(\mathrm{H_2})_{\mathrm{CS}} \sim 10$, and in the CS condensations, where $N(\mathrm{H_2})_{\mathrm{dust}}/N(\mathrm{H_2})_{\mathrm{CS}} \sim 0.15$, are given below.

FIR5: Since $\tau_{\mathrm{CS}(2-1)} \propto N(\mathrm{H_2})/T_{\mathrm{ex}}^2$ while $\tau_{\mathrm{dust}} \propto N(\mathrm{H_2})$, an increase in the temperature of the gas and dust to $T \gtrsim 100$ K can resolve the discrepancy without invoking depletion of CS or anomalous dust properties. A dust temperature of 100 K leads to a source luminosity of 700 $\mathrm{L_\odot}$. However, because no high-resolution 50–100 μm measurements of FIR5 exist, there is no good constraint on the dust temperature in this source. It is therefore also possible that the depletion of CS in low temperature, high density gas at FIR5, can explain our observations.

CS condensations: The brightness temperature of the CS lines is $T_{\mathrm{b}} \approx 40$ K, and so should have been detected in continuum emission if the dust properties were the same as those in the FIR sources. $\kappa_{3\mathrm{mm}}$ must therefore be lower in the CS condensations than in the FIR sources, either due to a decrease in κ_0 or an increase in β. Below we show that the latter is most likely to be the case.

6. β IN THE CS CONDENSATIONS AND FIR SOURCES

In Figure 1b we overlay the 450-μm continuum emission from the ridge on the integrated CS(2–1). At this shorter wavelength strong dust emission is also associated with the CS condensations, showing that the spectral index at those locations is considerably steeper than in the FIR sources. To estimate the value of β we have subtracted the extended emission from the 450-μm map and compared it with the 3-mm continuum. After applying a Rayleigh-Jeans correction and an opacity correction to the 450-μm data we find for the protostars FIR5 and FIR6 a value for β of 1.2 ± 0.2 and 0.9 ± 0.2 respectively. At the CS condensation east of FIR5 on the other hand we obtain $\beta > 1.7$. For FIR3, which is younger than FIR5 and FIR6, $\beta = 1.6 \pm 0.2$. Thus a variation of β with protostellar age is suggested, even in these very early phases of star formation. It is possible that this evolution of β corresponds to an increase in grain size in dense interstellar environments.

Acknowledgements. JSR acknowledges the support of the Royal Society and of Queens' College, Cambridge. JC acknowledges support from a NSF-YI award and the David and Lucile Packard Foundation. Research at the Owens Valley Radio Observatory is supported by NSF grant AST 93-14079. The James Clerk Maxwell Telescope is operated by The Joint Astronomy Centre on behalf of the Particle Physics and Astronomy Research Council of the United Kingdom (PPARC), the Netherlands Organisation for Scientific Research, and the National Research Council of Canada. CJC was funded by a PPARC Advanced Fellowship during part of this work.

References

Beckwith, S. V. W., & Sargent, A. I. 1991, *Ap. J.*, **381**, 250.

Beckwith, S. V. W., Sargent, A. I., Chini, R. S., & Güsten, R. 1990, *A. J.*, **99**, 924.

Blake, G. A., Sutton, E. C., Masson, C. R., & Phillips, T. G. 1987, *Ap. J.*, **315**, 621.

Chandler, C. J., & Carlstrom, J. E. 1996, *Ap. J.*, in press.

Gaume, R. A., Johnston, K. J., & Wilson, T. L. 1992, *Ap. J.*, **388**, 489.

Hildebrand, R. H. 1983, *Quart. J. R. A. S.*, **24**, 267.

Mannings, V., & Emerson, J. P. 1994, *M. N. R. A. S.*, **267**, 361.

Mezger, P. G., Chini, R., Kreysa, E., Wink, J. E., & Salter, C. J. 1988, *Astr. Ap.*, **191**, 44.

Mezger, P. G., Sievers, A. W., Haslam, C. G. T., Kreysa, E., Lemke, R., Mauersberger, R., & Wilson, T. L. 1992, *Astr. Ap.*, **256**, 631.

Richer, J. S. 1990, *M. N. R. A. S.*, **245**, 24P.

Richer, J. S., Hills, R. E., Padman, R., & Russell, A. P. G. 1989, *M. N. R. A. S.*, **241**, 231.

Sanders, D. B. & Willner, S. P. 1985, *Ap. J.*, **293**, L39.

THE ABUNDANCES OF CHARGED PARTICLES IN PROTOSTELLAR CORES

STEVEN J. DESCH *University of Illinois, Urbana-Champaign, Illinois, USA*

ABSTRACT. We investigate the abundances of charged particles in very dense ($10^5\,\mathrm{cm}^{-3} \lesssim n_{H_2} \lesssim 10^{14}\,\mathrm{cm}^{-3}$) molecular cloud (protostellar) cores. We focus on the dust grains, which are the dominant charge carriers for high densities. Previous studies have investigated the abundances of charged grains in the case that the grain radii follow an MRN distribution. We account for the transfer of charge between grains of different size, an effect that was ignored in previous calculations, but which is significant in determining the total abundance of charged grains. The consequences for star formation are considered.

1. INTRODUCTION

The abundances of charged particles in protostellar cores are crucial inputs to the determination of the conductivity of the gas and the degree of coupling between the gas and the magnetic field. In very dense cloud cores ($n_{H_2} \gtrsim 10^{12}\,\mathrm{cm}^{-3}$), grains are the dominant charge carriers; in addition, they provide the surface area on which most recombinations of ions and electrons take place. The processes which affect grains fundamentally impact on the charge state of dense cores.

Previous calculations (Elmegreen 1979; Nishi et al. 1991) have recognized the sensitivity of the charge state to the size distribution of the grains. A preponderance of small grains, such as is found in the MRN distribution (Mathis et al. 1977), leads to a greater surface area on which electrons and ions recombine, and lower abundances of electrons and ions. What previous calculations have ignored is the possible effect of different mechanisms of charge transfer between grains of different size.

In this paper, the effect of varying the details of grain charge transfer is investigated. The abundances of charged particles are found by solving a network of chemical reactions which are initiated by the ionizations of H_2 molecules. A simple physical model of the protostellar core environment is described, based on recent numerical calculations by Fiedler & Mouschovias (1993). It is found that the details of grain charge transfer are significant in setting the total abundance of charged grains, and especially the abundance of small charged grains.

2. BACKGROUND

2.1. Physical Model

The abundances of charged particles in a protostellar core are sensitive to the physical conditions in the core, particularly the temperature and ionization rate. Both of these

quantities depend on the column density of gas from the core to the exterior of the cloud. Column densities can only be specified within the context of a physical model.

We base our physical model on recent calculations by Fiedler & Mouschovias (1993) which show that the column density to the core is approximately 7 g cm^{-2} at a central density of $n_{H_2} = 1 \times 10^9\,\mathrm{cm}^{-3}$ (near the end of their runs). The collapse becomes spherically symmetric in the center at densities higher than this, so we rouhgly model the column density as $\sigma \propto n^{2/3}$. Based on these column densities, the core is expected to become opaque to its own infrared emission for $n_{H_2} \gtrsim 3 \times 10^9\,\mathrm{cm}^{-3}$, using the opacities of Ossenkopf & Henning (1994). Below this density, the temperature in the core is assumed to be $T \approx 10\,\mathrm{K}$; above this density the temperature is assumed to rise adiabatically.

The column density also sets the level of ionization. According to Umebayashi & Nakano (1983), the ionization rate ζ per H_2 molecule is given by

$$\zeta = \zeta_{\mathrm{R}} + \zeta_{\mathrm{CR}} \exp(-\sigma / 96\,\mathrm{g\ cm}^{-2}), \tag{1}$$

where $\zeta_{\mathrm{R}} = 6.9 \times 10^{-23}\,\mathrm{s}^{-1}$ is the ionization rate due to radioactivities such as ^{40}K. The ionization rate due to cosmic rays, ζ_{CR}, is assumed to be $5 \times 10^{-17}\,\mathrm{s}^{-1}$ (Sptizer 1978). The cosmic rays that ionize the gas are shielded by column densities on the order of 10^2 g cm^{-2}, corresponding to central densities of $n_{H_2} \gtrsim 10^{12}\,\mathrm{cm}^{-3}$.

2.2. Chemical Network

The ionization of H_2 molecules leads to the production of ions, electrons, and charged grains, via a network of chemical reactions. The ionization of H_2 results rapidly in the production of HCO^+ ions and free electrons. Charge is transfered from the molecular ion HCO^+ to free atomic species, leading to atomic ions (a^+) such as Mg^+ and Na^+. At very high temperatures ($T \gtrsim 1000\,\mathrm{K}$), potassium is thermally ionized. Each ion above can recombine in the gas phase with electrons. The collision of an electron or an ion with a neutral grain results in a charged grain. An ion colliding with a negative grain, or an electron colliding with a positive grain, results in a neutral grain.

Grains can also collide with other grains, according to the following reactions:

$$g^{\pm} + g^0 \rightarrow g^0 + g^{\pm} \tag{2}$$

$$g^+ + g^- \rightarrow g^0 + g^0. \tag{3}$$

The last reaction is very significant, as is it the means by which most charge is neutralized for densities $n_{H_2} \gtrsim 10^8\,\mathrm{cm}^{-3}$. The first two reactions are only relevant when grains differ from each other, for example, by size. Their presence here is directly due to the consideration of a size distribution of grains. In that case, it may be that when a charged grain and a neutral grain collide, the larger grain always retains the charge. The details of charge transfer between grains of different size are therefore potentially significant.

2.3. Grain Charge Transfer

In order to quantify the effects of grain charge transfer, we must adopt a physically plausible model for it. In the collision $g_1^{\pm} + g_2^0$, the probability that grain 1 retains the charge when the grains separate is:

$$P_1 = \frac{\sigma_1 4\pi a_1^2}{\sigma_1 4\pi a_1^2 + \sigma_2 4\pi a_2^2}, \tag{4}$$

where σ represents the average charge density over each grain's surface area.

If charge randomly wanders over the combined grain surface area while the grains are colliding, then $\sigma_1 = \sigma_2$, and $P_1 = [1 + (a_2/a_1)^2]^{-1}$. On the other hand, if the electrostatic potentials on both grains are equal, then $\sigma \propto 1/a$, and $P_1 = [1 + (a_2/a_1)^1]^{-1}$. We adopt the following parameterization: $P_1 = [1 + (a_2/a_1)^m]^{-1}$. We consider the two cases above, as well as two extremes: $m = +4$ (large grains hoard charge); and $m = -4$ (small grains always retain the charge). These reactions are entered into the chemical network by binning the grains into five possible grain radii, and considering each grain size bin as a distinct species.

3. RESULTS

The abundances of charged particles as a function of central density are displayed in Figure 1 for the case $m = +1$. Other values of m yield nearly identical graphs, except in the number of charged grains during the very dense stages ($n_{H_2} \gtrsim 10^{13}\,\mathrm{cm}^{-3}$), in which cosmic rays are shielded. Between the cases $m = +1$ and $m = +2$, the total abundance of charged grains differs by 30%, while between the cases $m = +4$ and $m = -4$ it differs by a factor of 2.5 (for $n_{H_2} \gtrsim 10^{13}\,\mathrm{cm}^{-3}$).

Also calculated were the fraction of grains charged as a function of grain size for various values of m. Between the physically relevant cases $m = +1$ and $m = +2$, it was found that 5 times as many small ($a \lesssim 0.01\mu\mathrm{m}$) grains are charged for the case $m = +1$, compared to $m = +2$. It can be shown that in the very dense stages of protostellar collapse, the conductivity of the gas may be due primarily to small grains. The degree of coupling between the magnetic field and gas, (e.g., given by the magnetic Reynolds number), is proportional to this quantity. Significant uncertainties in the degree of coupling between the magnetic field and gas (factors of at least 5) will arise unless the details of charge transfer between grains of different radii are specified.

References

Ciolek, G. E., & Mouschovias, T. Ch. 1993a, *Ap. J.*, 418, 774

Ciolek, G. E., & Mouschovias, T. Ch. 1993b, *Ap. J.*, 425, 142

Draine, B. T., & Sutin, Brian 1987, *Ap. J.*, 320, 803

Elmegreen, Bruce, G. 1979, *Ap. J.*, 232, 729

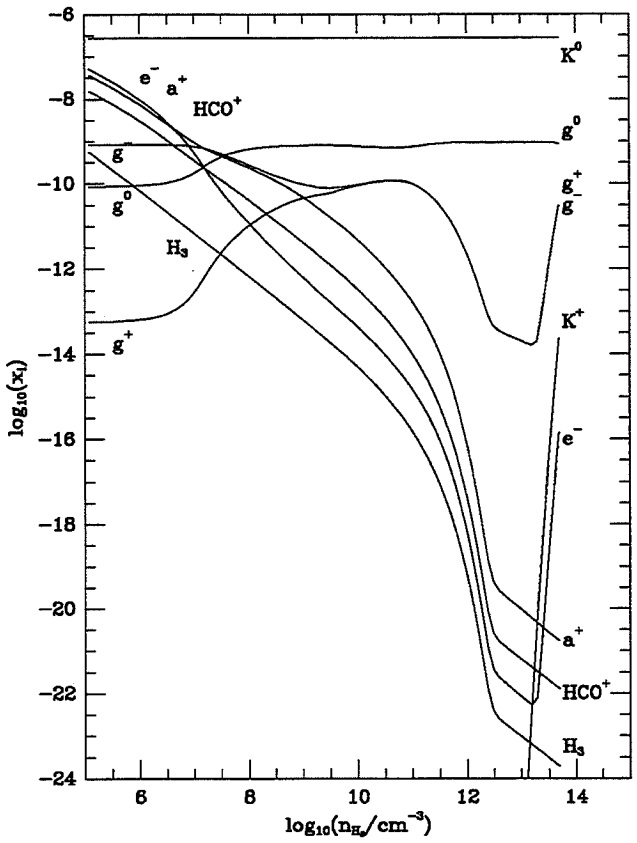

Figure 1. Abundances of charged particles as a function of central density.

Fiedler, R. A., & Mouschovias, T. Ch. 1992, *Ap. J.*, 391, 199

Fiedler, R. A., & Mouschovias, T. Ch. 1993, *Ap. J.*, 415, 680

Mathis, J. S., Rumpl, W., & Nordsieck, K. H. 1977, *Ap. J.*217, 425

Nakano, T., & Umebayashi, T. 1986a, *M. N. R. A. S.*, 218, 663

Nakano, T., & Umebayashi, T. 1986b, *M. N. R. A. S.*, 221, 319

Nishi, R., Nakano, T., & Umebayashi, T. 1991, *Ap. J.*, 368, 181

Ossenkopf, V. & Henning, Th. 1994, *Astr. Ap.*, 291, 943

Spitzer, L. 1978, *Physical Processes in the Interstellar Medium*, (New York Wiley-Interscience: New York)

Umebayashi, T., & Nakano, T. 1981, P.A.S.J., 33, 617

Whittet, D. C. B. 1992, *Dust in the Galactic Environment*, (Institute of Physics: London)

THE PROTOSOLAR NEBULA

CATALYSIS BY DUST GRAINS IN THE SOLAR NEBULA

MONIKA E. KRESS *Rensselaer Polytechnic Institute, Troy, New York; and NASA Ames Research Center, Moffett Field, California USA*
ALEXANDER G. G. M. TIELENS *NASA Ames Research Center, Moffett Field, California, USA*

ABSTRACT. In order to determine whether grain-catalyzed reactions played an important role in the chemistry of the solar nebula, we have applied our time-dependent model of methane formation via Fischer-Tropsch catalysis to pressures from 10^{-5} to 1 bar and temperatures from 450 to 650 K. Under these physical conditions, the reaction $3H_2 + CO \longrightarrow CH_4 + H_2O$ is readily catalyzed by an iron or nickel surface, whereas the same reaction is kinetically inhibited in the gas phase. Our model results indicate that under certain nebular conditions, conversion of CO to methane could be extremely efficient in the presence of iron-nickel dust grains over timescales very short compared to the lifetime of the solar nebula.

1. INTRODUCTION

In the molecular cloud from which our solar system condensed, CO was by far the most abundant carbon-bearing molecule in the gas. Because gas-phase reactions converting CO to CH_4 are exceedingly slow, there was insufficient time within the Jovian subnebula and the solar nebula (of which a chemical memory may be retained by comets and some meteorites) to account for the large amount of organics thought to be present there, when only gas phase reactions are considered. Catalysis by FeNi grains, which are found in many primitive meteorites and interplanetary dust particles today, is a process which could account for the conversion of CO to organics within nebular timescales. In this study, our goal is to see whether the assumption that CO is converted to methane via Fischer-Tropsch catalysis (invoked in nebula chemistry models, for example, see Engel et al., 1990) is valid under the most ideal conditions, i.e., that iron and nickel are present in metallic form, providing the surface on which Fischer-Tropsch synthesis may take place.

Since the turn of the century, Fischer-Tropsch reactions have been widely used in industry to produce alkanes, alkenes, and alcohols from CO and H_2 using transition metal catalysts. When using iron and nickel, methane is the primary product, and smaller amounts of higher hydrocarbons (both saturated and unsaturated) are also formed. Alcohols and other oxygen-containing molecules besides water and CO_2 are not produced with these catalyst materials. Therefore, we expect methane to be the most abundant molecule formed primarily via a surface-catalyzed process in the solar nebula.

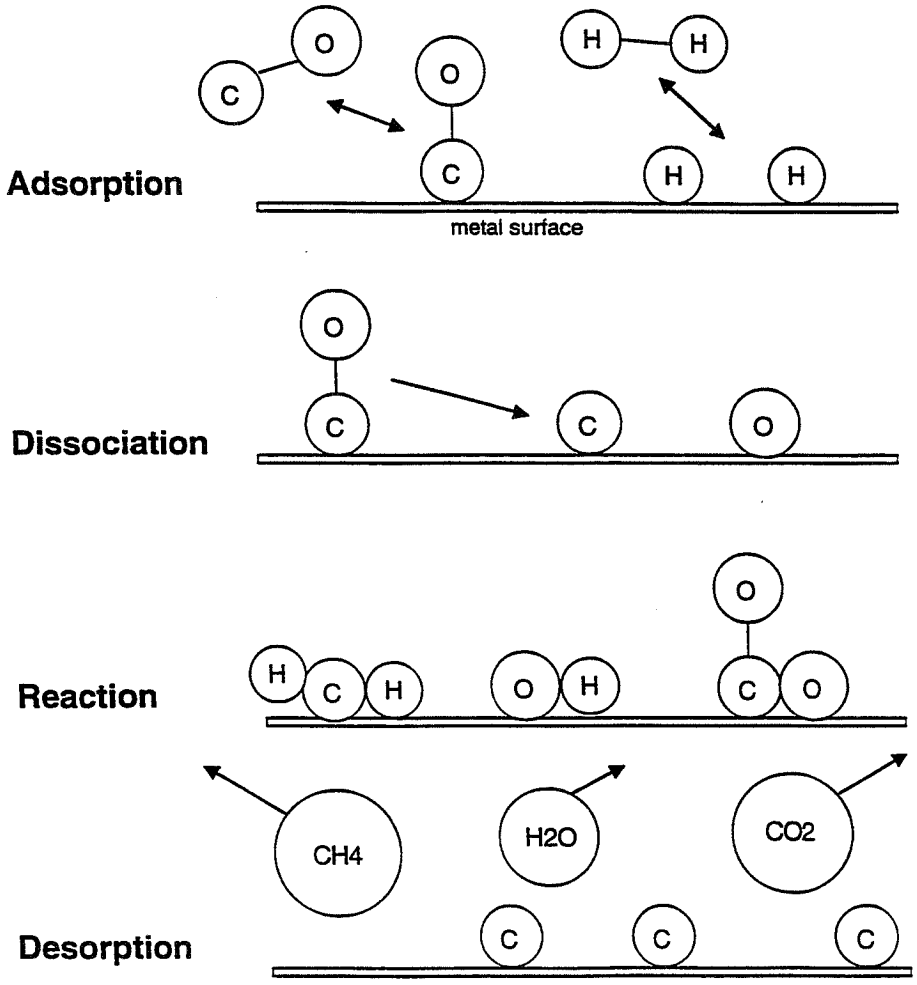

Figure 1. Steps involved in CH_4 formation from H_2 and CO. A carbon adlayer is established on the surface because there is a significant energy barrier to hydrogenating C. Oxygen is not an abundant surface species because the barriers to removing it as either water or CO_2 are relatively low.

Figure 1 shows the steps involved in converting CO to methane. CO adsorbs to the surface via the carbon atom and forms a strong metal-CO bond. This strong bond allows the CO to reside on the surface long enough to dissociate. This ability to dissociate CO and other diatomic molecules is the hallmark of a good catalyst and is unique to the transition metals, because the metal-CO interaction is is strong enough to dissociate the molecule, but the individual metal-C and metal-O bonds are not so strong that these atoms cannot then be removed as products. Continuing through figure 1, we see that carbon forms an adlayer because there is a high energy barrier to hydrogenation due to the strong metal-C bond. Oxygen is rapidly removed as either H_2O or CO_2 and does not tend to form an adlayer. Once the carbon is out of CO and into CH_4, the formation of other organics may proceed in the gas phase and also by subsequent processing on planets.

2. MODEL RESULTS

Using a kinetic surface chemical model (Kress & Tielens, 1996) based on experimental data (see Sault & Goodman, 1989, and references therein), the methane formation rate and the timescale for converting 10% of the CO to CH_4 ($\tau_{10\%}$) were calculated for the following physical conditions: T = 450 to 650 K (the range of maximum efficiency for this reaction) and total pressures from 10^{-5} to 1 bar, at a CO/H_2 ratio of 3.5×10^{-4}. In this range of pressure and temperature, the thermochemical equilibrium values for the CH_4/CO ratio are ≥ 0.1.

In their nebula chemistry models, Prinn and Fegley (1989) used an empirical expression based on experimental data for methanation rate via catalysis by iron with a "site density" n_s of 10^6 sites per cm^3 in the nebula. A "site" is a location on a grain where one molecule can adsorb and catalysis take place; usually, a site is defined as one surface atom. There are about 10^6 sites per 0.1 μm radius grain. n_s is thus a measure of the surface area available for catalysis per unit volume. In our model, we used Prinn and Fegley's value of $n_s = 10^6$ cm^{-3} and kept it constant for gas pressures from 10^{-5} to 1 bar, essentially increasing the number of H_2 molecules per site, n_{H_2}/n_s. Figure 2 shows our model results for $\tau_{10\%}$, the timescale for converting 10% of the CO to CH_4, as a function of n_{H_2}/n_s for several temperatures. The pressure scale for a temperature of 550 K is shown to illustrate how $\tau_{10\%}$ behaves as the gas pressure on a grain increases, which is essentially a measure of the H_2 flux that the grain experiences.

In figure 2, the independent variable is n_{H_2}/n_s, the number of H_2 molecules per site. In the discussion to follow, this quantity can also be thought of as gas pressure (for a given temperature and surface area) and as flux of H_2 molecules to the surface.

$\tau_{10\%}$ increases with decreasing temperature (at constant pressure, n_{H_2}/n_s or flux) because the reaction is slower at low temperatures, requiring more time to convert CO to CH_4. This timescale remains constant at low n_{H_2}/n_s because the reaction rate scales with pressure just as gas-phase reactions do. At higher n_{H_2}/n_s, $\tau_{10\%}$ departs from its constant value, *increasing* as the pressure increases, indicating that it takes *more* time to convert greater quantities (i.e., pressures) of CO to CH_4 as the pressure increases. This behavior occurs when the reaction rate no longer scales with pressure; a maximum conversion rate is reached when the catalyst surface becomes saturated with hydrogen and further increase in pressure cannot drive the reaction faster. This behavior is not typical of gas-phase reactions, but is very typical of heterogeneous

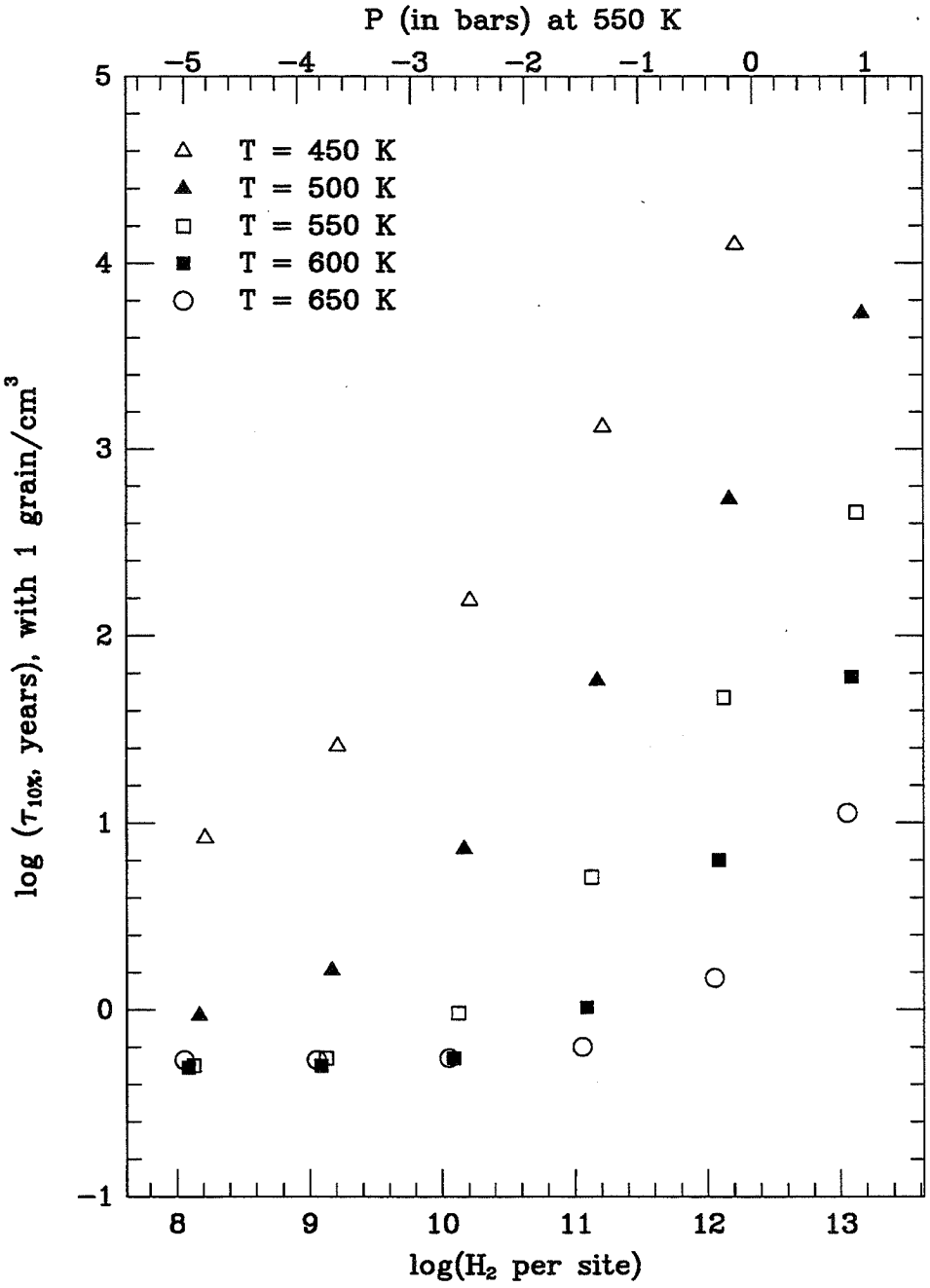

Figure 2. Timescale for conversion of 10% of the CO to CH_4 in the presence of one 0.1 μm radius FeNi grain per cm^3 (corresponding to $n_s = 10^6$ cm^{-3}) as a function of H_2 per site, for a range of temperatures.

(e.g., surface-catalyzed) ones. This maximum conversion rate is reached at increasingly lower pressures as the temperature decreases, because at lower temperatures, the surface becomes saturated at lower pressures.

The very short timescales shown in Figure 2 do not imply that there would have been total conversion of CO into methane over the lifetime of the solar nebula, because catalysts can only make a reaction reach equilibrium faster; they do not increase the amount of product obtained at equilibrium. In fact, real catalysts often cannot completely equilibrate a mixture of gases because the catalyst can be chemically altered during the course of the reaction, rendering it less active, if not completely inactive. Even under carefully controlled laboratory conditions, iron and nickel catalysts are usually rendered inactive before the reaction reaches equilibrium because iron or nickel surface carbide is an unavoidable by-product of this reaction.

3. CONCLUSIONS

For temperatures of 450 to 650 K, pressures of 10^{-5} to 1 bar, and a solar CO/H_2 abundance, catalytic formation of methane from CO and H_2 is extremely efficient in the presence of a grain population providing 10^6 surface sites cm^{-3} of FeNi metal. A peculiar conclusion that we draw from this work is that in lower pressure regions of the solar nebula, shorter timescales are required to reach $CH_4/CO = 0.1$ than in high pressure regions. This result is in contrast to work done by Prinn and Fegley (1989), who noted that laboratory studies of this reaction indicated that high pressures meant a faster reaction rate and hence more efficient conversion of CO to CH_4. However, at best this would mean it took *as much time*, not less, to reach a certain CH_4/CO ratio as it would to reach that ratio at lower pressures. At worst, it would actually take *more* time to reach that ratio at high pressure because rates of surface reactions do not increase indefinitely with pressure as rates of gas-phase reactions do.

The critical quantity in determining the methane formation rate, and hence $\tau_{10\%}$, is not the absolute gas pressure, but the ratio of H_2 to surface sites for catalysis, n_{H_2}/n_s. If conditions are ideal for catalysis, i.e., iron and nickel are in the form of small (0.1 μm radius) metallic grains which provide lots of surface area per H_2 molecule (high n_s), n_{H_2}/n_s is small and $\tau_{10\%}$ is short. If there is actually less area for catalysis to take place, n_{H_2}/n_s is larger and $\tau_{10\%}$ is longer.

Since we have determined that catalysis is very efficient under these conditions of pressure, temperature, and site density, the next question which needs to be addressed is this: what is n_{H_2}/n_s (or an upper limit for n_{H_2}/n_s) in the solar nebula once we take into consideration the factors which reduce the surface area available for catalysis? First, not all of the iron and nickel atoms in the solar nebula will be in the form of metallic grains, although there should be some because they are found in meteorites and IDPs. Second, these grains are subject to poisoning (loss of active sites) by graphite and sulfur. Third, coagulation of grains in denser regions will also result in a loss of surface area. All of these factors ultimately reduce n_{H_2}/n_s. Could catalysis still be a viable means of making methane out of CO, thus initiating the formation of organics? Our results show that $\tau_{10\%}$ can be very short even at larger values of n_{H_2}/n_s, particularly at higher temperatures, so these additional considerations will reduce but not eliminate the efficiency of catalysis in the nebula.

Future work will entail studying the effects of these three factors to place some constraints on n_{H_2}/n_s so that we can get a better idea of how efficient catalysis really could have been in the solar nebula. Also, there is another reaction which

is worthwhile to study: $N_2 + 3\ H_2 \longrightarrow 2\ NH_3$, which is also catalyzed by iron and has been suggested as a possible route to form ammonia in the same context as methane (Prinn & Fegley, 1989). These simple, well-studied reactions provide promising insight into grain surface chemical processes in general, which we believe are extremely significant in the chemistry of all regions of space which can harbor stardust.

References

Engel, S., Lunine, J. I., and Lewis, J. S. 1990, *Icarus*, **85**, 380.

Kress, M. E., and Tielens, A. G. G. M. 1996, preprint.

Prinn, R. G., and Fegley, B. 1989, in *Origin and Evolution of Planetary and Satellite Atmospheres*, eds. S. K. Atreya, J. B. Pollack, and M. S. Matthews, (University of Arizona), p. 78.

Sault, A. G., and Goodman, D. W. (1989), in *Advances in Physical Chemistry, Vol. LXXVI: Molecule Surface Interactions*, ed. K. P. Lawley, (Wiley-Interscience), p. 153.

RESTRUCTURING OF DUST AGGREGATES IN THE SOLAR NEBULA

C. DOMINIK *Sterrewacht Leiden, PO Box 9513, 2300 RA Leiden, The Netherlands*
A.G.G.M. TIELENS *NASA Ames Research Center, Mail-Stop 245-3, Moffett Field, CA 95035, USA*

ABSTRACT.

We discuss the results of a recent effort to analyze the mechanical stability of dust aggregates with a detailed model of the physical properties of a contact between grains. This model contains both elastic repulsion forces and attractive van der Waals/dipole/metallic forces along with a description of the energy dissipation due to rolling, sliding, and breaking of contacts. We find that (1) aggregates formed from single sized grains via Particle-Cluster-Aggregation remain fluffy, (2) collisions with other aggregates and with large grains may lead to compaction (3) the velocities of small grains and aggregates in the early solar nebula are too small to produce marked compaction as long as the aggregates are small, and (4) internal restructuring of aggregates is a potentially large sink of energy which could enable the sticking of large bodies even at collision velocities of the order of several hundred cm/s.

1. INTRODUCTION

It is now recognized that coagulation is the only process contributing to the growth from sub-micron sized grains all the way to bodies with diameters in excess of a few 100m (Weidenschilling, this conference). Gravitation only takes over for the subsequent growth of these planetesimals to earth-like planets or to the cores of gas giants. The aggregates which form in this process are expected to first be fluffy (i.e. they contain a large amount of vacuum) and possibly fractal, depending on the details of the formation process. However, somewhere along the growth process the aggregates need to become non-fractal ("fractal dimension $D = 3$") and eventually compact. This compaction requires energy and will occur in collisions with sufficient impact energy. In order to estimate the energy associated with that compaction, a detailed model of a contact between dust grains and the involved forces and energy dissipation terms is required. Such a model has recently been developed (Chokshi *et al.*, 1993, Dominik and Tielens 1995, 1996a, 1996b) and is based largely on results obtained in Tribology and the theory of elasticity (see Singer and Pollock, 1992 for an overview.). We will briefly describe this model and some consequences which arise with respect to the compaction of dust aggregates in the solar nebula.

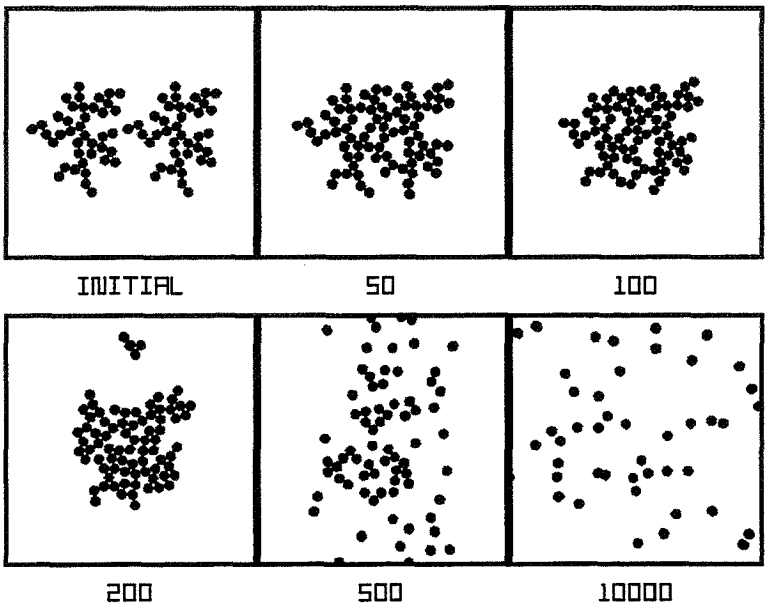

Figure 1. Outcome of collisions between two identical aggregates made from $r = 10^{-5}$cm silicate grains. The impact velocity in cm/s is noted below each panel.

2. MODEL OF THE CONTACT

In our description of the contact between two dust grains we view the grains as elastic spheres which are attracted by a material dependent force (van der Waals forces in the case of silicate and carbonaceous grains, hydrogen bonds in the case of icy grains and metallic forces for iron grains). The mutual attraction deforms the grains near the contact point until the attractive force is balanced by an elastic repulsion force. The force needed to separate two grains is given by $F_c = 3\pi\gamma R$ where γ is the surface energy and describes the attractive forces. $R = 1/(R_1^{-1} + 1/R_2^{-1})$ is the reduced radius of the two grains. Typical forces for sub-micron grains are of the order of a few hundreds of a dyne. The energy needed to break a contact is given by $E_{\rm break} = 2.3F_c\delta_c$ where δ_c is the separation of the grains at which the contact actually breaks, typically a few Ångstroem (Dominik and Tielens 1996b).

Tangential forces try to move to contact over the surface of the grains. An analysis of the involved forces shows, that it is very difficult to slide two grains over each other. The resistance to sliding is due to surface irregularities and dissipation processes in the atomic grids of the grains. It turns out that the energy required to slide a contact for only a few Ångstroem is already comparable to $E_{\rm break}$ so that any attempt to slide will actually break the contact (Dominik and Tielens 1996a). On the other hand, the resistance to rolling is much smaller. An energy comparable to the break-up energy $E_{\rm break}$ is enough to move a contact over a distance $\approx \pi R$ (Dominik and Tielens 1995). The application of a steadily pressing force as is arises in collisions between two aggregates (but not in collisions between an aggregate and a small grain) may therefore lead to the efficient compaction of the aggregate without destroying it.

3. AN EXAMPLE CALCULATION

We have incorporated the interaction between grains as sketched above into an 2D N–particle code which can be used to model collisions. Figure 1 shows as an example the result of collisions of two silicate aggregates at different speeds. At small velocities, the aggregates suffer some local compaction near the impact point and stick. At higher velocities, the compaction becomes more marked. At still higher velocities the aggregates are broken into several fragments and eventually into single grains. However, the relative velocities of small grains and aggregates in the early solar nebula are typically smaller than 1cm/s (Weidenschilling and Cuzzi 1993). This shows that the formation of aggregates early in the solar nebula will not lead to effective restructuring or compaction. The first aggregates were fluffy.

4. RESTRUCTURING AS A WAY DISSIPATING IMPACT ENERGY

However, later in the growth process, the relative velocities increase. In fact, it has been a matter of large concern for some time to understand how larger bodies can stick in a collision. Chokshi *et al.*(1993) showed that sticking of meter sized solid silicate spheres would require relative velocities of less than 1 mm/s, which is unrealistic. Gravitational binding becomes only important when the bodies become about a kilometer in size (Weidenschilling 1996). However, since the bodies are made by coagulation from small grains, they are not solid spheres but aggregates. This internal structure has to be considered when studying sticking of such bodies. Meakin and Donn (1988) considered the inter-penetration of fractal grains as one way to account for increased stickiness. Another possibility is the dissipation of kinetic collision energy in internal degrees of freedom (the contacts between grains).

The discussion above give us the opportunity to estimate the energy needed to compress an aggregate. If we consider making a compact aggregate out of linear chain of dust grains, it is clear that folding this chain to a compact object requires some shifting of contacts by rolling or sliding. If the folding could be done in a perfectly organized way (like an inch rule), we would have to move only very few contacts and the energy to do that is negligible. However, in a collision, forces are not applied in this very organized way to only a few contacts. Under the forces arising due to a collision, many contacts will move at the same time. On average every contact will then have to be moved over a distance of the order of πR before the grain will have made enough contacts with other grains in order to fix its position in the resulting, more compact structure.

Thus we can see that the compaction of an originally fluffy aggregate to a compact body will require an energy of the order of

$$E_{\rm comp} = n_c E_{\rm roll}(\pi R) \approx n_c E_{\rm break} \qquad (1)$$

where n_c is the number of contacts in the aggregate. For open aggregate structures, this is equal to the number of grains in the aggregates and thus, for a given size distribution of grains, proportional to the total mass. The impact energy for a given velocity, is also proportional to the involved masses. This implies that the critical velocities for sticking of two aggregates of similar size is independent of the aggregate size. Thus, the critical velocity derived from Fig. 1 applies as well to much larger

aggregates. Internal restructuring may thus be a large sink of energy which can be used to dissipate collision energy and achieve sticking.

In a collision between bodies of different size, the critical velocity will be even higher due to the fact that the impact energy is determined by the smaller of the two colliding masses while the number of contacts available for restructuring is determined by the larger of the two bodies.

5. CONCLUSIONS

We conclude that coagulation of dust grains in the early solar nebula will first lead to open and fractal structures. Compaction of these structures in subsequent collisions of larger bodies introduces a large energy sink which will allow sticking of equal sized silicate bodies at velocities in excess of 100cm/s.

Acknowledgements. CD acknowledges a fellowship of the National Research Council during which much of the work described here was performed.

References

Chokshi, A. and Tielens, A.G.G.M. and Hollenbach, D. 1993, *Ap. J.* **407**, 806

Dominik, C. and A.G.G.M. Tielens 1995, Phil. Mag. A, **72**, 783

Dominik, C. and A.G.G.M. Tielens 1996a, Phil. Mag. A, **73**, 1279

Dominik, C. and A.G.G.M. Tielens 1996b, *Ap. J.*, in preparation

Meakin, P. and Donn, B. 1988, *Ap. J. (Letters)* **329**, L39

Singer, I.L. and Pollock, H.M. 1992. *Fundamentals of Friction: Macroscopic and Microscopic Processes*, NATO ASI Series, Dordrecht

Weidenschilling, S.J. 1996, in *From Stardust to Planetesimals*

Weidenschilling, S.J., and Cuzzi, J.N. 1993, in *Protostars and Planets III*, University of Arizona Press, Tuscon

EFFECT OF DUST COAGULATION DYNAMICS ON THE GEOMETRY OF AGGREGATES

R. NAKAMURA *Information Processing Center, Kobe University, JAPAN*

ABSTRACT. Master equation gives a more fundamental description of stochastic coagulation processes rather than popular Smoluchowski's equation. In order to examine the effect of the dynamics on the geometry of resulting aggregates, we study Master equation with a rigorous Monte Carlo algorithm. It is found that Cluster-Cluster aggregation model is a good approximation of orderly growth and the aggregates have fluffy structures with a fractal dimension ~ 2. A scaling analysis of Smoluchowski's equation also supports this conclusion.

1. SCALING THEORY OF THE DYNAMICS

Smoluchowski's "Coagulation Equation" has been widely used to describe the evolution of dust particle or planetesimal size distributions, i.e.,

$$\frac{dn_k}{dt} = \sum_{i+j=k} K_{ij} n_i n_j - n_k \sum_{i=1}^{\infty} K_{ki} n_i \tag{1}$$

where n_k denotes the number density of k-mer (the particle of mass k) and K_{ij} is the collision kernel between i-mer and j-mer. In order to simplify this complex set of differential equations, we consider collision kernels having scaling properties, such as $K_{ai,aj} \sim a^{\lambda} K_{ij}$ and $K_{ij} \sim i^{\mu} j^{\nu}$ $(i \ll j)$. In addition, we assume that the cluster size distributions normalized by "mean cluster size" $S(t)$ tend towards an invariant form $\Phi(k/S(t)) = (S^2(t)/M_0)n_k$ where $M_p = \sum_{k=1}^{\infty} k^p n_k$ and $S(t)$ is given by M_2/M_1. The dynamics of coagulation processes can be predicted quantitatively by these exponents μ, ν and λ as shown below (van Dongen and Ernst, 1985). Substituting scaling kernels in eq.(1), we obtain a equation which determines the static shape of the scaling function Φ, i.e.,

$$-w[x\Phi'(x)+2\Phi(x)] = \lim_{\varepsilon \downarrow 0} \frac{1}{2} \int_{\varepsilon x}^{(1-\varepsilon)x} dy\, K(y, x-y)\Phi(y)\Phi(x-y) - \Phi(x) \int_{\varepsilon x}^{\infty} dy\, K(x,y)\Phi(y) \tag{2}$$

On the other hand, the dynamics is described by the evolution of $S(t)$. Since $\dot{S}(t) = wS^{\lambda}$, it becomes power-law $(\sim t^{1/(1-\lambda)})$ for $\lambda < 1$ and exponential for $\lambda = 1$, respectively. Besides, Hendriks et al. (1983) has proved that gelation, which

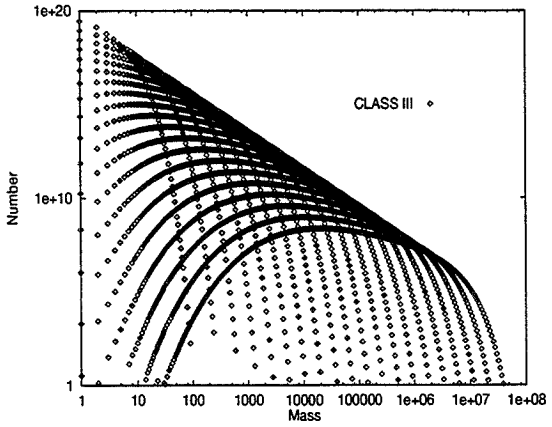

Figure 1. Evolution of the size distribution for class III test kernel

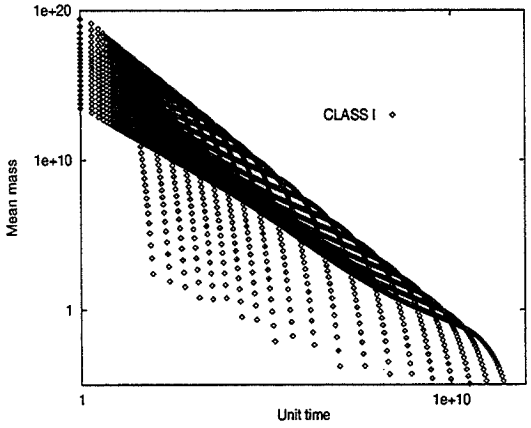

Figure 2. Same as fig.1, but for class I test kernel

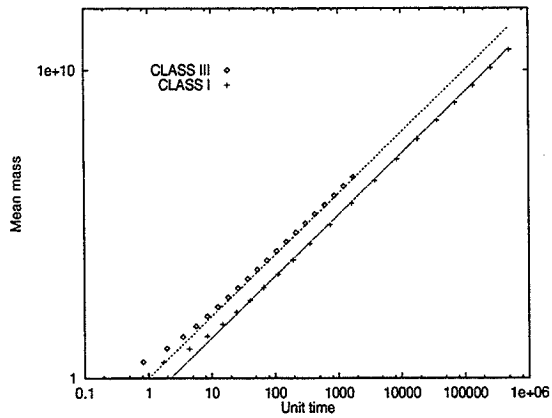

Figure 3. Time development of the mean cluster size for the same epochs as figures 1 and 2

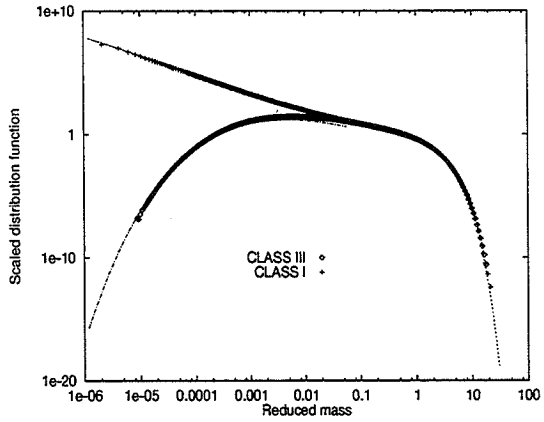

Figure 4. Normalized size distribuions. Fitted curves are derived from the analysis of eq.(2).

is known as "runaway growth" in the filed of planetary sciences, occurs when λ exceeds 1. It seems natural that runaway growth corresponds to simple Particle-Cluster aggregation model. In this article, we investigate the shape of the aggregates produced in a certain non-gelling coagulation process.

We divide non-gelling coagulation equations into three classes with the value of μ. Class I, II and III corresponds to the case for $\mu > 0$, $\mu = 0$ and $\mu < 0$, respectively. While class III kernels give bell-shaped size distributions, class I kernels yield power-law at the lower end of the size distribution (Leyvraz, 1986). Although the general behavior of class II kernels are more complex, they also become power-law if $\mu = 0$ and $\nu = \lambda = 1$. This is an important case because the exactly solvable sum kernel ($K_{ij} = i + j$) belongs to this subclass. Figures 1 and 2 show the evolution of the size distribution with $K_{ij} = (ij)^{1/4}$ and $i^{-1/4}j^{3/4} + j^{-1/4}i^{3/4}$. Each curve is drawn when the total cluster number becomes half of the previous epoch. The mean size increase in the same way ($\sim t^2$) as shown in figure 3 because they have a common exponent $\lambda = 1/2$. In figure 4, the normalized size distribution functions Φ, derived from numerical calculations, are compared with the prediction based on scaling theory. Our numerical calculations seem to confirm the scaling assumption on both figures.

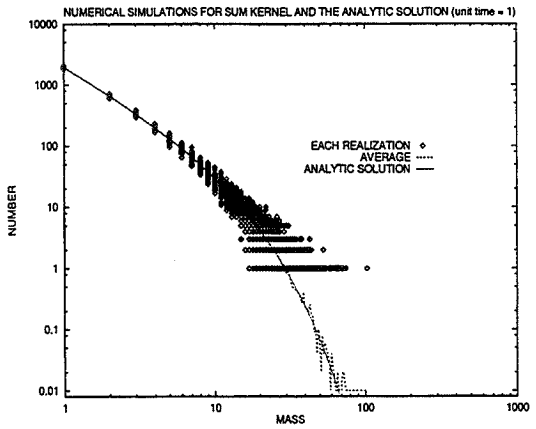

Figure 5. Results of 100 numerical calculations for sum kernel

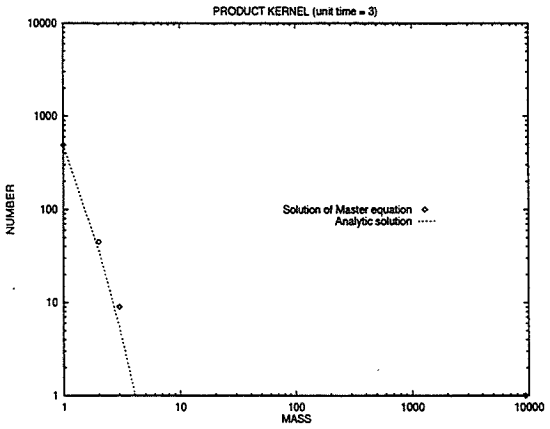

Figure 6. Size distribution for product kernel

Intuitively, it is expected that bell-shaped size distributions with class III kernels generate aggregates similar to Cluster-Cluster aggregation model. However, it is somewhat uncertain what kind of aggregates are generated by power-law size distributions.

2. MASTER EQUATION

A random coagulation process with M monomers is formulated as

$$\dot{P}(\mathbf{m},\mathbf{t}) \;=\; \mathbf{2M^{-1}} \sum_{\mathbf{(i,j)}} \mathbf{K_{ij}P(m^{+}_{ij},t)(m_i+1)(m_j+1-\delta_{ij})} \;-\; \mathbf{P(m,t)\; m_i\; (m_j\; -\; \delta_{ij})} \tag{3}$$

where $\mathbf{m} = \{m_l\}$ represents a cluster distribution: m_1 monomers, m_2 dimers, m_3 trimers, $\cdots$ etc. Also, $\mathbf{m}^{+}_{ij} = \{m_l + \delta_{il} + \delta_{jl} - \delta_{i+j,\,l}\}$ represents a similar distribution containing an extra i-mer and j-mer and one less (i+j)-mer. $P(\mathbf{m},\mathbf{t})$ is the probability that the cluster distribution at time t is $\mathbf{m}$. For example, $P(\mathbf{m},\mathbf{t}) = \mathbf{1}$ if $\mathbf{m} = \{\mathbf{M},\mathbf{0},\mathbf{0},...,\}$ and 0 for other states with a monodisperse initial condition. This equation provides a realistic picture of stochastic coagulation processes with intrinsic fluctuations. Many authors have proved that coagulation equation (1) derives physical validity as the limit of this equation (e. g. Spouge, 1985). Moreover, we can investigate the geometry of resulting aggregates with this approach because a sample path of eq.(3) provides a complete collision sequence in the system. Among several numerical schemes proposed to simulate the evolution of eq.(3) (Liffmann, 1992), we employed the most efficient and rigorous algorithm developed by Gillespie (1975). Total particle number in the system is 10^4 throughout this article.

Figure 5 indicates the results of our calculations for sum kernel $K_{ij} = i + j$ at the unit time t = 1. As we have mentioned in the previous section, this kernel belongs to a special subclass of class II and yields power-law size distributions. One can see excellent agreement between the average of numerical calculations and the

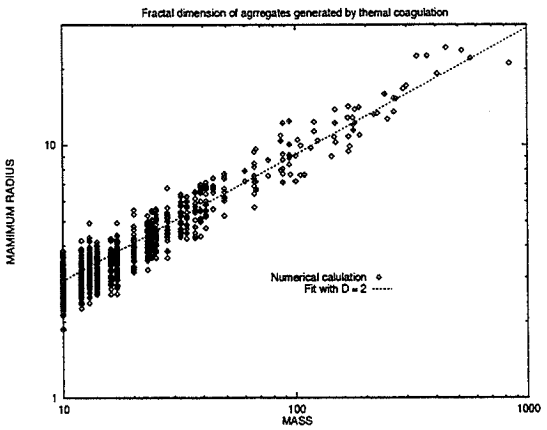

Figure 7. Relation between the maximum radius and mass of the aggregates produced by the thermal coagulation kernel

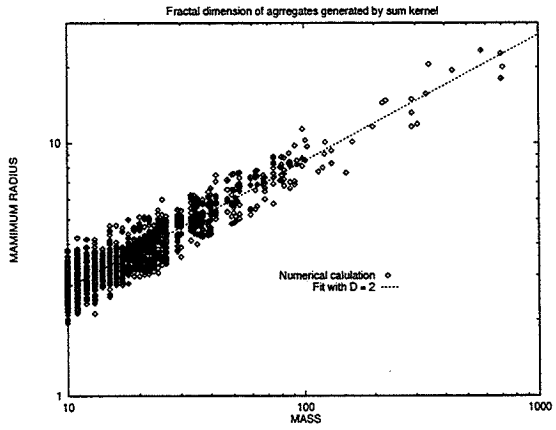

Figure 8. Same as the previous figure, but for sum kernel

corresponding analytic solution of eq.(1). It should be noted that the fluctuation in each sample path is not a numerical artifact, but a intrinsic property of the stochastic system. In addition, this code can treat runaway growth as demonstrated in figure 6. The size distribution for product kernel (K_{ij} = ij) is drawn at the unit time t = 3. A runaway body, which has appeared at t = 1, is absorbing the swarm of small particles as Particle-Cluster aggregation model assumes.

Next, we have performed numerical calculations for sum kernel and the kernel for thermal coagulation ($K_{ij} = (i^{1/3} + j^{1/3})^2(1/i + 1/j)^{1/2}$). In contrast to the power-law for sum kernel, thermal coagulation belongs to class III and gives bell-shaped distribution. It is found from figures 7 and 8 that the fractal dimension can be approximated by 2 for both cases. This fact can be explained in terms of scaling theory as follows. As long as runaway growth doesn't occur, we obtain $\dot{S}(t) \sim K_{S,S}$ independent of their class. It means that the the variation of the mean cluster size is dominated by the collisions between the clusters of mean size. In power-law size distributions, mass gradually cascades from smaller size to the upper end of the size distribution. As a result, the aggregates are generated by piling up smaller aggregates like Cluster-Cluster aggregation model. In conclusion, scale-invariance of the dynamics produces spatially scale-invariant (= fractal) aggregates universally.

References

Gillespie, D. T. 1975, *J. Atmos. Sci.*, **32**, 600.

Hendriks,E.M.,Ernst,M.H and Ziff,R.M. 1983, *J.Stat.Phys.*, **31**, 519.

Leyvraz,F. 1986, in *On Growth and Form* , eds. E. Stanley and N. Ostrowsky, (Martinus Nijhoff Publisher), p. 136.

Liffman,K. 1992, *J. Comput. Phys.*, **100**, 116.

van Dongen, P. G. J. and Ernst, M. H. 1985, *Phys. Rev. Letters*, **54**, 1396.

Spouge,J.L. 1985, *J. Col. Int. Sci.*, **107**, 38.

SELF–CONSISTENT SIMULATION OF THE BROWNIAN STAGE OF DUST GROWTH

S. KEMPF, S. PFALZNER AND TH. HENNING *Max Planck Society, Research Unit "Dust in Star–forming Regions", D-07745 Jena, Germany*

ABSTRACT. It is a widely accepted view that in proto-planetary accretion disks the collision and following sticking of dust particles embedded in the gas eventually leads to the formation of planetesimals (coagulation). For the smallest dust grains, Brownian motion is assumed to be the dominant source of their relative velocities leading to collisions between these dust grains. As the dust grains grow they eventually couple to the turbulent motion of the gas which then drives the coagulation much more efficiently. Many numerical coagulation simulations have been carried out to calculate the fractal dimension of the aggregates, which determines the duration of the ineffective Brownian stage of growth. Predominantly on-lattice and off-lattice methods were used. However, both methods require simplification of the astrophysical conditions. The aggregates found by those methods had a fractal dimension of approximately 2 which is equivalent to a constant, mass-independent friction time. If this value were valid for the conditions in an accretion disk, this would mean that the coagulation process would finally "freeze out" and the growth of a planetesimal would be impossible within the lifetime of an accretion disk.
In order to investigate whether this fractal dimension is model independent, we simulate self–consistently the Brownian stage of the coagulation by an N–particle code. This method has the advantage that no further assumptions about homogeneity of the dust have to be made. In our model, the dust grains are considered as aggregates built up of spheres. The equation of motion of the dust grains is based on the probability density for the diffusive transport within the gas atmosphere. Because of the very low number density of the dust grains, only 2–body–collisions have to be considered. As the Brownian stage of growth is very inefficient, the system is to be simulated over long periods of time. In order to find close particle pairs of the system which are most likely to undergo a collision, we use a particle–in–cell (PIC) method for the early stages of the simulation where the system is still very homogeneous and a tree method later when the particles are more clustered.

1. INTRODUCTION

In the solar nebula, a population of dust particles is embedded in the dilute nebula gas. It is widely believed that within the lifetime of the pre-solar accretion disk of a few million years the initial sub–micron dust grains grow to kilometer–sized planetesimals which are regarded as the building bricks for the planets. Although there exists a general idea of the genesis from stardust to planetesimals some crucial points do not fit together. Recent investigations by Weidenschilling showed that the growth (coagulation) is due to collisional sticking regardless of particle size. The important

feature for this process is a relative velocity between the grains. Due to the small size of the grains they are initially strongly coupled to the global gas motion. In this stage the dominant source of relative velocity between the grains is the thermal (Brownian) motion of the dust. This Brownian motion is a very ineffective growth mechanism because of the $1/\sqrt{m}$ mass dependence of the relative velocities. Therefore, there are two possible limiting cases – either the grains are able to loosen their coupling to the Brownian motion or the growth 'freezes out' eventually.
The coupling strength is the typical time a particle needs to dissipate its kinetic energy of a relative motion to the gas expressed by the friction time τ_f. The deceleration of the particle will depend on the resistance offered by the surrounding gas. For convex particles, which are small compared with the mean free path of the gas , τ_f is proportional to the mass–surface ratio, $S = m/\sigma$, (Epstein, 1923). In an accretion disk the assumption of convex aggregates is not really justified, because due to the collisional sticking the growing grains become very fluffy and irregularly shaped. However, it is widely assumed that the linear dependence of S holds for the entire coagulation process, anyway.
Because of the S-dependence of τ_f, the important point for the duration of the Brownian stage is the structure of the aggregates produced by the growth process. The increase of the particle mass m with respect of a typical radius R is a characteristic scaling property of any growth regime and can be expressed by a fractal dimension D_f: $m(\lambda R) = \lambda^{D_f} m(R)$. Using this, the friction time of a growing aggregate can be written as $\tau_f \sim R^{D_f-2}$. For $D_f \sim 2$, τ_f remains constant for all particle sizes. So we have the situation of an increasing particle mass although τ_f remains constant and consequently, the growth process will never overcome the Brownian stage but 'freeze out'. This is the limiting case of the 'cluster cluster aggregation' (CCA), where impacts between clusters of similar size form very fluffy aggregates. The opposite case of $D_f \sim 3$ is governed by collisions of aggregates with single particles, building up quite compact structures.
During the last twenty years many numerical simulations of the coagulation have been carried out (for an overview see Meakin, 1988). Using on-lattice and off–lattice methods, the authors found a fractal dimension of $D_f \sim 2$ for Brownian growth. As mentioned above such a value would inhibit the formation of planetesimals within the lifetime of the disk. One way to get rid of this contradiction would be the assumption of a compaction of the aggregates due to mutual grain collisions. However, at least for thermal impact velocities, experimental investigation of grain collisions did not confirm any compaction (Blum, 1996). Another reason for obtaining such a low fractal dimension could be the applied numerical methods themselfs. The off-lattice methods allows only the nodes of a lattice as particle sites and the diffusive particle motion is described by jumps between the nodes. The result has to be renormalized by comparison with known analytical expressions introducing a large uncertainty. The disadvantage of on–lattice simulations is that they require a homogeneous spatial particle size distribution, which is only valid during the early stages of particle coagulation. In our model, we investigate the Brownian growth by a direct simulation of the N-particle system. This way we avoid the problems of renormalization and restriction to homogeneous spatial particle distribution.

2. METHOD

Our simulation starts with N spherical particles of a given size distribution randomly positioned in a periodic cubic box. In order to treat the Brownian growth self-consistently, we simulate the diffusive path of each aggregate i, having a mass m_i

and a diffusivity $D_i = \tau_{f_i} kT/m_i$. Due to the stochastic nature of the diffusion, only the probability $p(r)$ for a particle position r or velocity u is known. For a particle undergoing a diffusive motion the time evolution of its probability density p_{OF} is given by the Ornstein-Führt relation (Uhlenbeck and Ornstein, 1930):

$$p_{OF}(r;\tau)dr = \exp\left[-\left\{r - u(0)\tau_f\left(1-e^{-\hat{\tau}}\right)\right\}^2/2\sigma(\tau)\right]/\sqrt{2\pi\sigma(\tau)}\,dr, \qquad (1)$$

where $\hat{\tau} = \tau/\tau_f$ and $\sigma(\tau) = D\tau_f(2\hat{\tau} - 3 + 4e^{-\hat{\tau}} - e^{-2\hat{\tau}})$ are the dimensionless time and the dispersion of p_{OF}, respectively. As a consequence of p_{OF} being a Gaussian, we simulate the diffusive path applying normally distributed random numbers ξ ($\langle\xi\rangle = 0\,, \langle\xi^2\rangle = 1$):

$$\begin{aligned} r(\tau) &= r(0) + \sqrt{\sigma(\tau)}\,\xi + u(0)\tau_f\left(1-e^{-\hat{\tau}}\right) \\ u(\tau) &= \sqrt{kT/m}\sqrt{1-e^{-2\hat{\tau}}}\,\xi + u(0)e^{-\hat{\tau}}. \end{aligned} \qquad (2)$$

The trajectories of colliding particles are semi–ballistic, because the collision time $\tau_{coll} \ll \tau_f$. The timestep has to be chosen accordingly, $\Delta\tau \ll \tau_f$, to resolve the semi-ballistic segments of the diffusive paths. Expanding eq. (2) in Taylor series of the order $\mathcal{O}(\hat{\tau}^2)$ we yield the "semi-ballistic equation of motion" for a Brownian particle ($\tau \ll \tau_f$):

$$\begin{aligned} r(\tau) &= r(0) + u(0)\tau + \mathcal{O}(\hat{\tau}^2) \\ u(\tau) &= u(0)(1-\hat{\tau}) + \sqrt{kT/m}\sqrt{2\hat{\tau}}(1-\hat{\tau}/2)\,\xi + \mathcal{O}(\hat{\tau}^2). \end{aligned} \qquad (3)$$

As a consequence of the low particle number densities in the solar nebula ($n_d \sim 1\mathrm{cm}^{-3}$) many–body–collisions are unlikely. There is only a significant probability for an intersection during $\Delta\tau$ for a relative small number of particles closer than a critical separation r_c. Consequently, in order to reduce computation time, the N-particle system is searched for pairs closer than r_c and a multiple timestep scheme is used, in which the high time resolution $\Delta\tau$ is only applied for particles closer than a few r_c. After testing the critical pairs for collision, the new positions and velocities of the aggregates are updated according to eq. (3).
The most time-consuming component of the simulation is the nearest neighbor search. The CPU-time required to examine the N-particle system using a standard direct method scales as $\mathcal{O}(N^2)$. For a reasonable N of about $\sim 10^5$ particles, the numerical cost for the application of such a method would be too high. In order to minimize the expense, we use the particle–in–cell method (PIC), scaling as $\mathcal{O}(N)$ in the beginning of the simulation and a tree–method, scaling as $\mathcal{O}(N\log N)$ during later stages. In the PIC-algorithm the space is subdivided in $n_c = N/N_c$ cells of the same size accommodating N_c particles on the average. For each cell, the near neighbor pairs are searched by a direct method, requiring a mean numerical cost $C_c \sim N_c^2$. As C_c is independent of the particle number, the total numerical expense is $C_{tot} = n_c C_c \sim N$. However, if the distribution is not spatially homogeneous and particles concentrated in some parts of the space, the PIC method scales as $\mathcal{O}(N^2)$ again. Therefore the

tree–method, which is insensitive to inhomogeneities, is used during the later stages of the simulation. Here, the particles are sorted in a hierarchical structure of cells like a tree (see Pfalzner and Gibbon, 1996). As mentioned before, the tree building and near neighbor search in this algorithm costs of the order $\mathcal{O}(N \log N)$. Both methods, PIC and tree algorithm, can be vectorized efficiently.

3. CONCLUSIONS

We developed a model that should allow us to simulate the Brownian growth phase of the dust coagulation process by a direct simulation of the N-particle system. Our model avoids the problems on–lattice and off-lattice simulations have and should therefore be able to settle the discussion whether the obtained fractal dimension of $D_f \sim 2$ is realistic or caused by the applied method.

Acknowledgements. The authors appreciate helpful and stimulating discussions with R. Mucha, J. Blum and H. Klahr. The support of S. Kempf's contribution to this research by the DFG grant He1935 within the special programme "Physics of Starformation" is gratefully acknowledged. The numerical simulations were mostly carried out at the supercomputing center Juelich, Germany and we wish to thank for generous allocation of computing time.

References

Blum, J. 1996, in *From Stardust to Planetesimals*

Gardiner, C. W. 1990, *Stochastic Methods*, (Springer-Verlag).

Epstein, P. 1923, *Phys. Rev.*, **22**, 710–723.

Kempf, S., Pfalzner, S. & Henning, Th., in preparation.

Meakin, P. 1988, in *Phase Transitions*, (Academic Press), chapter 3.

Pfalzner, S. and Gibbon, P. 1996 *Many-Body Tree Methods in Physics* (Cambridge University Press).

Uhlenbeck, G. E. and Ornstein, L. S. 1930, *Phys. Rev.*, **38**, 823–841.

Weidenschilling, S. J. 1980, *Icarus*, **44**, 172–189.

DUST COAGULATION IN PROTOPLANETARY ACCRETION DISKS

W. SCHMITT, TH. HENNING, AND R. MUCHA *Max Planck Society, Research Unit "Dust in Star-forming Regions", D-07745 Jena, Germany*

ABSTRACT. The time evolution of dust particles in circumstellar disk-like structures around protostars and young stellar objects is discussed. In particular, we consider the coagulation of grains due to collisional aggregation. The coagulation of the particles is calculated by solving numerically the non-linear Smoluchowski equation. The different physical processes leading to relative velocities between the grains are investigated. The relative velocities may be induced by Brownian motion, turbulence, and drift motion. Starting from different regimes which can be identified during the grain growth, we also discuss the evolution of dust opacities. These opacities are important for both the derivation of the circumstellar dust mass from submillimetre/millimetre continuum observations and the dynamical behaviour of the disks. We present results of our numerical studies of the coagulation of dust grains in a turbulent protoplanetary accretion disk described by a time-dependent one-dimensional (radial) α–model. For several periods and disk radii, mass distributions of coagulated grains have been calculated. From these mass spectra, we determined the corresponding Rosseland mean dust opacities. The influence of grain opacity changes due to dust coagulation on the dynamical evolution of a protostellar disk is considered. Significant changes in the thermal structure of the protoplanetary nebula are observed. A "gap" in the accretion disk forms at the very frontier of the coagulation, i.e., behind the sublimation boundary in the region between 1 and 5 AU.

1. INTRODUCTION

The understanding of the dust component evolution in a protoplanetary nebula is crucial for explaining the formation of planetary systems. Safronov (1969) and Goldreich and Ward (1973) suggested a gravitational instability of a thin midplane dust layer leading to the formation of planetesimals. The protoplanetary disk is expected to be turbulent at least at the beginning of its evolution. Even weak turbulence is sufficient to prevent the dusty layer from becoming gravitationally unstable (Weidenschilling, 1988). Cuzzi *et al.* (1993) showed that the Goldreich-Ward instability is unlikely to occur until objects have already accreted by some other proceses to the mass of the largest known meteorite samples, if at all. This supports the coagulation scenario (e. g. Mizuno *et al.*, 1988), combined with grain and vapour transport processes. However, all the time, the grains were assumed to be spheres – an assumption which is not longer justified, if the coagulation process gets ahead. Various authors pointed out that the internal structure of the dust grains influences the opacities significantly (e. g. Preibisch *et al.*, 1993, Ossenkopf and Henning, 1994, Henning and Stognienko, 1996). Calculations on the coagulation of dust particles having a fluffy

structure were performed by Ossenkopf (1993) for the cores of cold molecular clouds. The investigations resulted in constraints on the dust size spectrum and its influence on the opacity.

In this contribution, we investigate the dust coagulation in a protoplanetary accretion disk. At the first time, in contrast to other studies, we couple the dust evolution directly to the evolution of the disk and follow the influence of opacity changes due to collisional aggregation on the dynamics of the disk.

2. COUPLING OF DISK EVOLUTION AND DUST COAGULATION

Since in protoplanetary disks dust grains dominate the opacity and the opacity again influences the disk evolution, we have created a model coupling disk and dust evolution (see for more details Schmitt *et al.*, 1996). The basic idea behind that is to use the disk structure to calculate the mass distribution of dust grains due to collisional aggregation and then to determine the corresponding Rosseland mean dust opacities from these dust spectra for the evolving protoplanetary disk.

For the description of the structure of a geometrically thin protoplanetary accretion disk, we use the hydrodynamical equations of a viscous fluid (e. g. Ruden and Pollack, 1991).

The mathematical formulation of the coagulation process is given by the Smoluchowski equation

$$\frac{\partial f(V,t)}{\partial t} = -f(V,t)\int_{V_{min}}^{V_{max}} dV'\, f(V',t)\, R(V,V')$$

$$+\frac{1}{2}\int_{V_{min}}^{V_{max}} dV' \int_{V_{min}}^{V_{max}} dV'' f(V',t)\, f(V'',t) R(V',V'')\, \delta(V-(V'+V'')), \quad (1)$$

where $R(V,V') = Q_{coll}(V,V')\, S(V,V')\, v_{rel}(V,V')$ is the coagulation rate between the dust grains with compact volumes V and V', with Q_{coll}, S, and v_{rel} being the collisional cross section, the sticking efficiency and mean relative velocity of two dust grains, respectively. The sticking efficiency for small particles is practically unit (Blum *et al.*, 1996). The sources of the relative velocity are Brownian, turbulent and drift motions. The collisional cross section is calculated from the model of Ossenkopf (1993) for the PCA's, i.e., aggregates grown by the particle-cluster agglomeration process.

The optical properties of the coagulated grains were calculated by an effective medium theory combined with a core-mantle approach (see e. g. Ossenkopf, 1993).

3. CONCLUSIONS

We observe three characteristical evolutionary stages during the coagulation of the dust particles:

- **Starting phase:** The first phase of the coagulation is characterised by the fast disappearance of the smallest particles. The total mass (volume) is spread over a relatively small particle size interval (see Figs. 1-2).

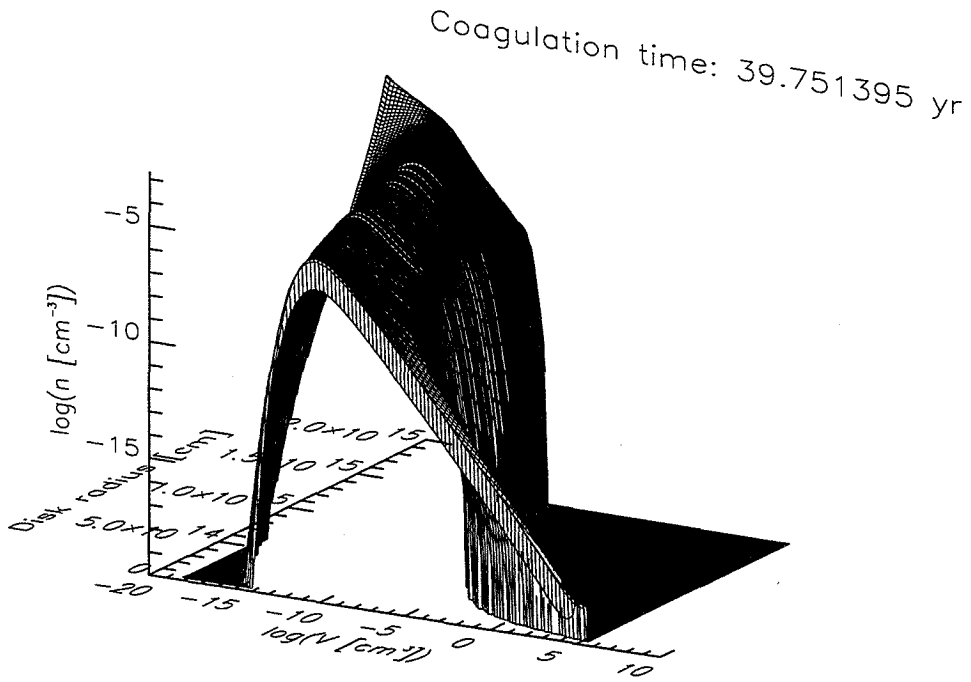

Figure 1. Size distributions of dust grains after a period of $\sim$ 40 yr at different radii of the protoplanetary accretion disk.

- **Phase of self-similar growth:** During the second evolutionary stage, a significant part of the distribution can be described by scaling laws. The self-similar parts in the dust distribution become larger as the coagulation proceeds. The total mass is dispersed slightly more than in the first phase (see Figs. 1-2).

- **Transition phase:** In the last phase of the evolution (observed only for regions below 5 AU), a wide part of the distribution shows a scaling behaviour (see Fig. 1). The most massive particles begin to decouple from the gas motion and drift motions become an important source of relative velocities.

The different characteristical times for the coagulation at different places result in the restructuring of the dust region of the protoplanetary disks: Due to the faster growth of the dust grains in the inner part of the disk, the opacity drops faster here. As a consequence, a "gap" in thermal and optical characteristics of the nebula appears in the region between 1 and 5 AU and the spectral luminosity curve shows a shallow double hump feature (see Fig. 2).

Acknowledgements. The authors would like to thank S. Kempf, H. Klahr, J. Blum, and V. Ossenkopf for their fruitful discussions.

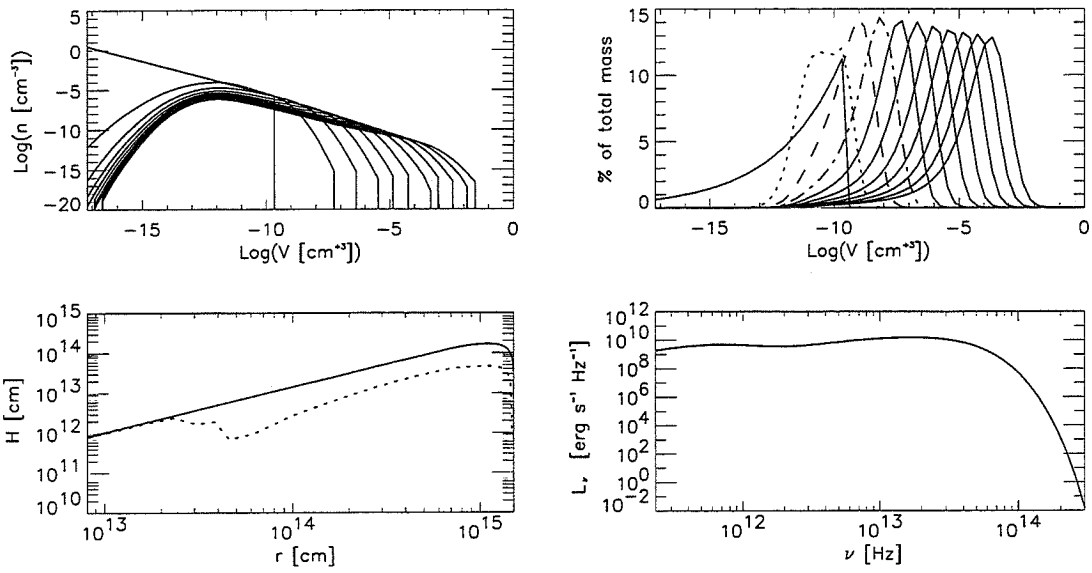

Figure 2. Evolution of the size distribution of dust grains (upper left figure) and of the relative mass fraction in particular sizes of the dust grains (upper right figure) over a period of 100 yr at a disk radius of 30 AU. Photosphere height of the disk (lower left figure) at the beginning (upper curve) and after 100 yr (lower curve). Spectral luminosity of the entire accretion disk L_ν after 100 yr of coagulation (lower right figure).

References

Blum, J., Wurm, G., Kempf, S., Henning, Th. 1996, *Icarus*, in press

Cuzzi, J. N., Dobrovolskis, A. R., Champney, J. M. 1993, *Icarus*, **106**, 102

Henning, Th., Stognienko, R. 1996, *A & A*, **311**, 291

Goldreich, P., Ward, W. R. 1973, *Ap. J.*, **183**, 1051

Mizuno, H., Markiewicz, W. J., Völk, H. J. 1988, *A & A*, **195**, 183

Ossenkopf, V. 1993, *A & A*, **280**, 617

Ossenkopf, V., Henning, Th. 1994, *A & A*, **291**, 943

Preibisch, T., Ossenkopf, V., Yorke, H. W., Henning, Th. 1993, *A & A* , **279**, 577

Ruden, S. P., Pollack, J. B. 1991, *Ap. J.*, **375**, 740

Safronov, V. S. 1969, *Evolution of the Protoplanetary Cloud and Formation of the Earth and the Planets* (Moscow: Nauka)

Schmitt, W., Henning, Th., Mucha, R. 1996, in preparation

Weidenschilling, S. J. 1988, in *Meteorites and the Early Solar System*, eds. J. F. Kerridge and M. S. Matthews (Tuscon: Univ. Arizona Press), p. 348

SIZE SEGREGATION AND NUMBER DENSITY ENHANCEMENT OF PARTICLES IN ACCRETION DISK EDDIES

H. H. KLAHR AND TH. HENNING *Max Planck Society, Research Unit "Dust in Star-forming Regions", D-07745 Jena, Germany*

ABSTRACT. We investigate the conditions for trapping solid dust particles in eddies and discuss the behavior of particles in a non-laminar protoplanetary accretion disk. We considered particle sizes from small dust grains to larger objects, 10^{-4}cm $< a_p < 10^2$cm. Independent of the source of turbulence, one can expect eddies to exist in the gas flow of a accretion disk, in the form of randomly occurring turbulent features or as convective cells. Due to the centrifugal force, solid particles are driven out of an eddy. It will be shown that this process is inhibited by the gravitational force induced by the protostar. Because of the mass dependence of the friction time, a given eddy becomes a trap for particles of a characteristic size and causes a local change in the dust density. Thus, the size distribution of the grains is no longer spatially homogeneous on small scales. Our general estimates do not depend on special turbulence or convection models. We calculate the maximal inhomogeneity due to this process. The strongest effect was observed for mm-sized particles, which can be concentrated by a factor of 100 within only 100 years.

1. INTRODUCTION

The theory of planet formation predicts that planetesimals form in a protoplanetary accretion disk by accumulation of presolar particles or nebula condensates (cf. review by Lissauer, 1993). In order to understand the time-scales and mechanisms of this growth process, one has to investigate the dynamical behavior of objects, embedded in a dilute gas. The motion of micron–sized particles is dominated by the gas drag, while meter–sized objects decouple efficiently from the gas and move on Keplerian orbits. But there exists a transition regime of particle sizes, where the influence of the gas drag, the gravity of the central object, and the inertia forces of the particles are of the same order of magnitude.

Adachi (1976) and Weidenschilling (1977) assumed a laminar rotating accretion disk. They discovered that the general behavior of the particles is to settle towards the mid-plane and drift radially to the central object. However, the protoplanetary accretion disk is generally assumed to be turbulent. Völk *et al.*(1980), Cuzzi *et al.*(1993), and Dubrulle *et al.*(1995) showed that small particles will not be able to concentrate in the mid–plane as they are stirred up by a turbulent–driven diffusion.

The above calculations were performed with the assumption of a homogeneous particle distribution. Squires and Eaton (1991) showed for the first time turbulent concentration of particles related to their aerodynamical stopping time (reviewed by Eaton

and Fessler, 1994). Dobrovolskis *et al.*(1993) calculated this particle concentration for the scenario of a protoplanetary accretion disk. But even in this work, only small eddies have been considered.
In our work (Klahr and Henning, 1996), we found that for large eddies, e. g.convective rolls, there is no tendency to collect grains between the eddies but, on the contrary, within their interior.

2. PARTICLE MOTION IN EDDIES

The motion of a particle in an accretion disk is determined by the gravitational field of a central object and the gas drag $\vec{F}_{\rm d} = -m(\vec{v} - \vec{V}_{\rm g})/\tau_{\rm f}$, where $\tau_{\rm f}$ is the friction time, giving the coupling of a particle to the gas. We solved a simplified set of differential equations for obtaining analytical results and the full set of equations using numerical integration schemes.
For the analytical treatment we used the simplified gravitational acceleration $g_{\rm z} = -\Omega^2 z$, where Ω is the Keplerian frequency. This harmonical potential is the key in understanding the particle concentration.
In the standard framework of particle transport via a turbulent flow, eddies are always zones with a smaller particle density than in any other flow feature. Particles cannot follow a curved streamline but they spiral away from the center of the vortex due to centrifugal forces. Only in convergence zones, particles are concentrated by the same mechanism.
However in the accretion disk, the gradient of the gravitational acceleration $-\Omega^2$ leads to a stronger settling of the dust in the upper half of the circle than in the lower part. If the gradient is strong enough in comparison to the rotational frequency ω of the eddy, then the particles will spiral inwards.
The general particle motion is described by a circulation with an increasing or decreasing radius $a = a_0 \exp(\tau_{\rm f}\ c\ t)$ where c depends on the Stokes number ${\rm St} = \omega\tau_{\rm f}$

$$c = \begin{cases} \omega^2 - \frac{1}{2}\Omega^2 & : \quad \omega\tau_{\rm f} \leq \frac{1}{\sqrt{2}} \\ \left(\frac{\omega^2}{4\tau_{\rm f}^4}\right)^{\frac{1}{3}} - \frac{1}{2}\Omega^2 & : \quad \omega\tau_{\rm f} \gg \frac{1}{\sqrt{2}} \end{cases} \tag{1}$$

The smaller the rotational frequency of the eddy is, the stronger is the concentration capability. As long as $\Omega \gg \omega$ the drift velocity towards the equilibrium point is $\sim \tau_{\rm f}$. The effect is independent of $\tau_{\rm f}$ until we enter the critical regime, where $\tau_{\rm f}$ is of the same size as the eddy period ω^{-1}.
We consider typical eddies in a protoplanetary accretion disk, in order to find scenarios for particle concentration. In the simplest case, there are large convective rolls rotating with a quite moderate frequency. Our 2D hydrodynamical calculations showed that these frequencies are 40 times smaller than the Keplerian frequency. That means that dust grains will be collected and concentrated in these huge eddies.

3. EFFICIENCY OF PARTICLE CONCENTRATION

The concentration of particles is limited by three mechanisms. These are the limited lifespan of the eddies, turbulent diffusion, and radial drift of the particles towards the central object.

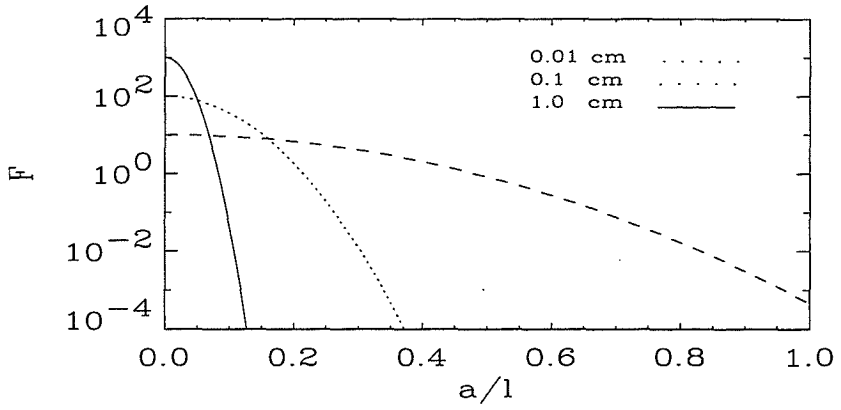

Figure 1. Maximal possible number density enhancement for different particle sizes. The local concentration factors for 0.01, 0.1 and 1cm grains are plotted over the radius of the eddy, thus showing the increase of concentration towards the equilibrium point, or in this case the center of the eddy. Millimetre-sized particles are concentrated by a factor of up to 100. At radii larger than 25 percent of the eddy size the particle density is strongly depleted. Thus about 90 percent of the eddy volume are free of mm-sized particles. Centimetre particles would be concentrated even stronger, but their concentration is limited by other effects than diffusion.

Turbulence on smaller length scales than the eddy will drive a diffusion process. We derived a maximal concentration which will be obtained after the mechanisms of diffusing and advecting have come to an equilibrium (Klahr and Henning, 1996). The solution is a distribution around the center of the particle circulation in the form of a Gaussian function (Fig. 1). D denotes the diffusivity due to turbulence on sub-eddy scales. The maximal concentration is

$$\rho_{\max} = \rho_{\mathrm{ini}} \frac{\tau_{\mathrm{f}}\,(-c)\,l^2}{2D\left(1-\exp\left(-\frac{\tau_{\mathrm{f}}(-c)}{2D}\,l^2\right)\right)}, \tag{2}$$

where ρ_{ini} denotes the initially homogeneous distribution and $\rho_{\max}$ the maximal achievable concentration in the center of the distribution. The concentration factor increases with τ_{f} and c.
If one considers only the largest eddies, where $l = H_{\mathrm{D}}$ and $\omega = \alpha\Omega$, Eq. 2 simplifies to

$$F = \frac{\rho_{\max}}{\rho_{\mathrm{ini}}} = \frac{\epsilon^2}{4}\frac{\tau_{\mathrm{f}}\Omega}{\alpha}. \tag{3}$$

Here, ϵ is the relation between the typical time for particle concentration and diffusion. The radial drift towards the protostar becomes important for compact particles in the size of centimetres at 1AU(cf. Weidenschilling, 1977), thus they get lost for the concentration process.

4. CONCLUSIONS

We have shown that there is a very effective mechanism for concentrating particles in a non-laminar accretion disk:

1. Particles can not only be concentrated by settling, thus, forming a particle sub-disk in the mid-plane of the accretion disk. They can also collect in eddies far above the mid-plane. By this mechanism, convective regions of the protoplanetary accretion disk become very interesting places for particle processing.
2. The concentration capability increases exponentially with τ_f up to a critical value, where the radial drift and/or the settling velocity exceed the velocity of the non-laminar flow. Thus the concentration is strongly size segregating, which leads to a narrow size distribution in convective cells.
3. While on small scales, the particles behave like in laboratory-observed turbulence (i. e.particles tend to leave the eddy and concentrate in convergence zones), this behavior is diminished and reversed with increasing scales.

The implications for the solar nebula are given by:
1. **Grain Growth:** The number density enhancement by a factor of 100 will strongly influence the time-scales of coagulation.
2. **Chondrule Formation:** Only grains in the size of chondrules (or with an equivalent friction time) concentrate in convective zones.
3. **Charge Separation:** If grains of a different size have distinct charges, the size segregation can lead to strong electric fields. In this case, the charge separation is not driven by sedimentation but by convection, thus the energy provided for this process is much larger.

Acknowledgements. We want to thank P. Artymovicz, K.R. Bell, J. Blum, J.N. Cuzzi, A. Heines, S. Kempf, R. Mucha and S. Pfalzner for supporting us with their specific knowledge and their merciless criticism. A part of the numerical calculations has been performed at the computing center of the Friedrich Schiller University Jena and at the super computer center HLRZ Jülich. We acknowledge support by the DFG program "Physik der Sternentstehung". The participation of H.K. at the Stardust Conference was made possible by a financial assistance offered through the conference.

References

Adachi, I.C., Hayashi, C., and Nakazawa, K. 1976, *Prog. Theor. Phys.*, **56**, 1756

Cuzzi, J.N., Dobrovolskis, A.R., and Champney, J.M. 1993, *Icarus*, **106**, 102

Dobrovolskis, A.R., Cuzzi, J.N., and Hogan, R.C. 1993, *Bull. Amer. Astron. Soc.*, **25**, 1122

Dubrulle, B., Morfill, G., and Sterzik, M. 1995, *Icarus*, **114**, 237

Eaton, J.K., and Fessler, J.R. 1994, *Int. J. Multiphase. Flow.*, **209**, 168

Klahr, H.H., and Henning, Th. 1996, in preparation

Lissauer, J.J. 1993, *Ann. Rev. Astr. Ap.*, **31**, 129

Squires, K.D., and Eaton, J.K. 1991, *Phys. Fluids A3*, **5**, 1169

Völk, H.J., Jones, F.C., Morfill, G.E., and Röser, S. 1980, *A&A*, **85**, 316

Weidenschilling, S.J. 1977, *M. N. R. A. S.*, **180**, 57

FROM CHONDRULES TO PLANETESIMALS: SOLIDS AND TURBULENCE IN THE SOLAR NEBULA

ANTHONY R. DOBROVOLSKIS *U. C. Santa Cruz*
JENNIFER S. DACLES-MARIANI *U. C. Davis*
JEFFREY N. CUZZI *NASA Ames Research Center*

ABSTRACT. The usual theory of planetesimal formation is untenable because turbulence inhibits gravitational instability. However, turbulence can actually concentrate chondrule-sized particles by factors up to a million near stagnation points. The implications for accretion may be profound.

1. THE EKMAN LAYER

According to conventional theory (Goldreich and Ward, 1973), dusty aggregates settle into a thin disk at the midplane of the preplanetary nebula until the local density of particles there exceeds the threshold for gravitational instability. At this point Goldreich and Ward (1973) claim that the solids in the subdisk collapse directly into first-generation planetesimals. However, Weidenschilling (1980) has raised a serious objection to their theory. The particle-rich subdisk rotates at nearly the Keplerian speed, but the surrounding gas-rich nebula rotates slightly slower because it is partly supported by a radial pressure gradient. The resulting velocity shear generates turbulence which stirs the particles away from the midplane and prevents gravitational instability (Weidenschilling, 1980). Our earlier work confirmed this with a simple numerical model (Cuzzi *et al.*, 1993; Champney *et al.*, 1995). Our recent results show that including damping of turbulence by particle drag increases the particle density at the midplane somewhat, but still inhibits gravitational instability.

The general outline of the physics may be stated as follows. The velocity difference ΔV between the particle-rich subdisk and the surrounding nebula sets up a turbulent boundary layer of the Ekman type, familiar from oceanography and meteorology. This Ekman layer has a characteristic thickness

$$L_E = \sqrt{\nu_T/\Omega}, \tag{1}$$

where ν_T is the kinematic viscosity due to turbulence and Ω is the Keplerian rotation rate of the nebula. In turn, the eddy viscosity can be estimated as

$$\nu_T \approx L_E \Delta V / Re_*, \tag{2}$$

where Re_* is a dimensionless parameter known as the critical Reynolds number, estimated on the order of 100. Solving eqs. (1) and (2) above gives

$$L_E \approx \frac{\Delta V}{\Omega Re_*} \text{ and } \nu_T \approx \frac{\Delta V^2}{\Omega Re_*^2}. \tag{3}$$

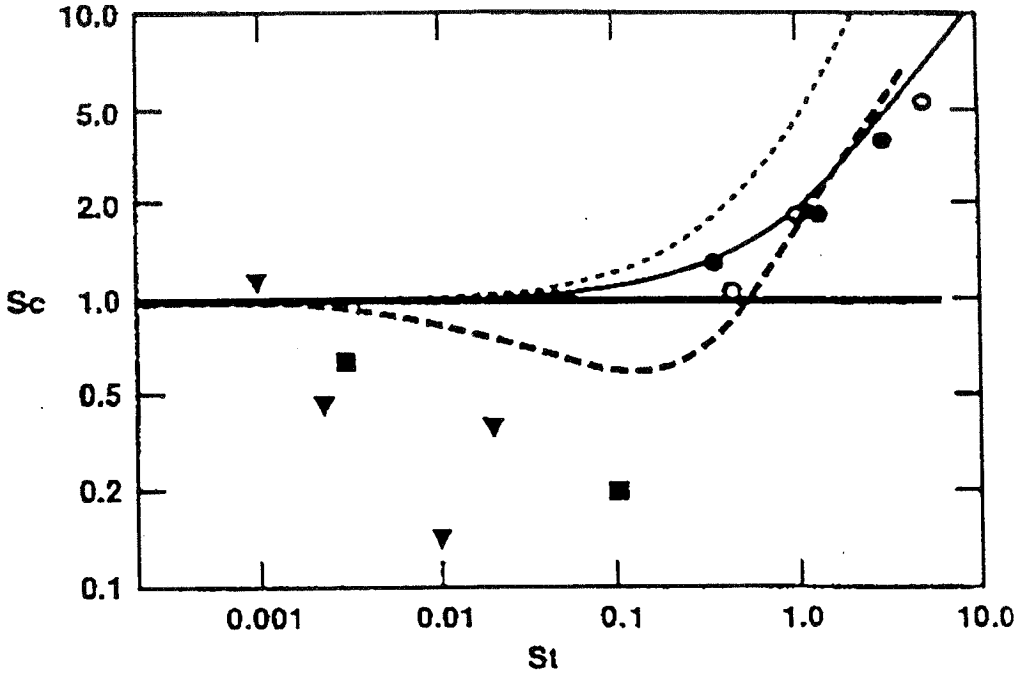

Figure 1. Particle diffusivity *vs.* Stokes number (size).

Inserting values of $\Omega = 2 \times 10^{-7}$ s^{-1} and $\Delta V \approx 50$ m/s thought appropriate to the terrestrial zone of the Solar nebula gives $L_E \approx 3000$ km and $\nu_T \approx 10^6$ m^2/s, in rough agreement with our simulations.

2. PARTICLE CONCENTRATION BY TURBULENCE

In order to simulate the distribution of solids in the Solar nebula, we assume that particles diffuse along their gradient of concentration, with a characteristic diffusivity D proportional to the eddy viscosity:

$$D = \nu_T / Sc. \tag{4}$$

Here Sc is a dimensionless parameter known as the Schmidt number. In turn, Sc is a function of the Stokes number St: the ratio of the particle drag time constant to the mean eddy turnover time. St is proportional to the radius and density of a particle.

Very small, light particles ($St << 1$) are locked to the gas, so $D = \nu_T$ and $Sc = 1$. On the contrary, large, heavy particles hardly respond to the turbulence, so $D << \nu_T$ and $St >> 1$. This is illustrated in Figure 1. The various points are experimental data, taken from Crowe *et al.* (1985), and the dashed curve is their

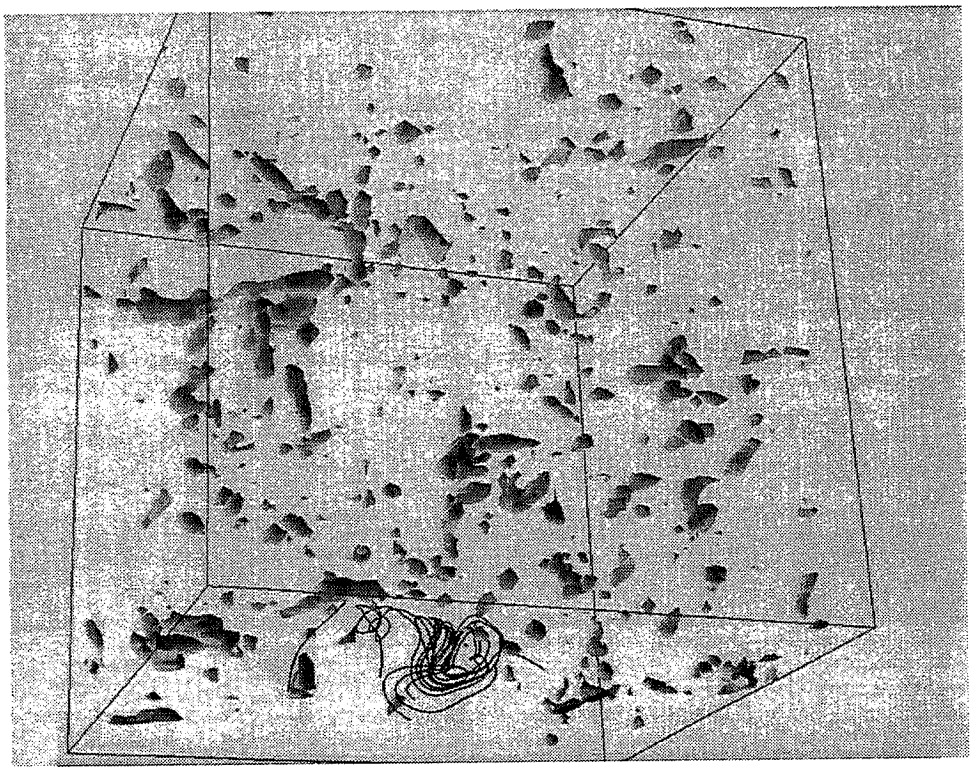

Figure 2. Regions of high particle concentration in our simulations.

numerical simulation. The dotted curve represents Safronov's (1969) assumption

$$Sc = (1 + St)^2, \tag{5}$$

while the solid curve plots our result

$$Sc \approx 1 + St. \tag{6}$$

The latter appears to be best for the largest particles, such as those near the midplane.

Note, however, the interesting middle range of St where the particles actually diffuse *faster* than the gas. This effect is most pronounced for particles whose drag time constants are comparable to the turnover times of the *smallest* eddies. Furthermore, it has been discovered within the last decade that differential motion between such particles and the gas causes the particles to "unmix" from the fluid and become concentrated near stagnation points (e. g. Squires and Eaton, 1990, 1991; Eaton and Fessler, 1994). The mechanism for both these phenomena appears to be as follows (Crowe *et al.*, 1988): Small particles remain entrained in eddies, while large ones pass right through. Particles of intermediate size couple weakly to the gas are scattered by the turbulence. Such particles tend to be flung out of vortices by "centifugal force", but linger in regions of high strain rate near stagnation points.

We have reproduced these results by direct numerical simulation of particles in isotropic turbulence. Starting from an initial uniform distribution of about a million particles, we find that they concentrate near stagnation points within a few mean eddy turnover times. The solid contours in Figure 2 delimit regions where the particle concentration is over 15 times the initial value. The peak concentration factor increases with Reynolds number. (The tracer particle at the top of the simulation volume is atypical in lingering near the same vortex).

Conditions in the Solar nebula depend on location and on the alpha parameter, thought to lie between 10^{-4} and 10^{-2} (note $Re \approx 10^{12}\alpha$); but in general, the most concentrated particles have radii of a fraction of a millimeter. Note that this spans the size range of chondrules, which show signs of aerodynamic sorting. We strongly suspect that chondrules have undergone the process of preferential concentration by turbulence. The high Reynolds numbers corresponding to nebular alphas cannot be simulated for the foreseeable future. However, by pushing the state of the art, we have developed scaling laws which imply that chondrule-sized particles in the Solar nebula may be concentrated by factors up to a million (Cuzzi *et al.*, 1996). Such particle clouds would still not reach solid densities, but would be thousands of times denser than the gas phase. We suspect that the feedback of these clouds on the gas flow may perpetuate their existence. The implications of these phenomena for turbulence damping, the rate of interparticle collisions, accretion, and radiative transfer are just beginning to be explored.

References

Champney, J. M., Dobrovolskis, A. R., and Cuzzi, J. N. 1995, *Physics of Fluids* **7**, 1703–1711.

Crowe, C. T., Gore, R. A., and Troutt T. R. 1985, *Particulate Science and Technology* **3**, 149–159.

Crowe, C. T., Chung, J. N., and Troutt, T. R. 1988, *Prog. Energy Combust. Sci* **14**, 171–194.

Cuzzi, J. N., Dobrovolskis, A. R., and Champney, J. M. 1993, *Icarus* **106**, 102–134.

Cuzzi, J. N., Dobrovolskis, A. R., and Hogan, R. C. 1996, Accepted for *Chondrules and the Protoplanetary Disk*, eds. R. H. Hewins, R. H. Jones, and E. R. D. Scott, (Cambridge University Press).

Eaton, J. K., and Fessler, J. R. 1994, *Int. J. Multiphase Flow* **20**, 169–209.

Goldreich, P., and Ward, W. R. 1973, *Ap. J.* **183**, 1051–1061.

Safronov, V. S. (1969). *Evolution of the Protoplanetary Cloud and Formation of the Earth and Planets*, (Akademiya Nauk SSSR).

Squires, K. D., and Eaton, J. K. 1990, *Physics of Fluids* **A 2**, 1991–1203.

Squires, K. D., and Eaton, J. K. 1991, *Physics of Fluids* **A 3**, 1169–1178.

Weidenschilling, S. J. 1980, *Icarus* **44**, 172–189.

VORTICES AND PLANETESIMALS

P. BARGE *Laboratoire d'Astronomie Spatiale, Marseille, France*
J. SOMMERIA *Ecole Normale Supérieure de Lyon, dpt. de Physique, Lyon*

ABSTRACT. How planetesimals form in a turbulent nebula is a key question for planetary formation. This paper investigates the interaction of the solid particles with the giant vortices, suspected to survive during many rotation periods in the protoplanetary disks. Such vortices could have an origin similar to that of the coherent structures of the 2D turbulence. It is found that these vortices can capture and concentrate large amounts of the solid particles. The strong efficiency of this mechanism make them the most favourable places where to form the planetesimals. A conclusion which holds even if their lifetime is assumed much shorter than expected.

1. INTRODUCTION

Long-lived vortices may be maintained by specific instability mechanism (Dubrulle, 1993), but more generally emerge from random turbulence in rotating shear flows. While 3D eddies are quickly damped by energy cascade toward small scales, 2D turbulence persists without energy dissipation, forming instead larger and larger vortices until a steady solitary vortex is formed. Striking examples are the persistent atmospheric vortices in the giant planets, like Jupiter's great Red Spot. This phenomenon can be reproduced in laboratory experiments, and explained in terms of statistical mechanics of 2D turbulence (Sommeria et *al.* 1991). Observations of accretion-disks around black holes (Abramowicz et *al.* 1992) or T-tauri stars could also indicate the presence of such organized vortices. Using the classical α-prescription for a turbulent accretion disk (with $\alpha \simeq 10^{-3}$, the decay time of the vortices is approximately 500 rotation periods.

2. A SIMPLE VORTEX MODEL

Neglecting pressure forces, Barge and Sommeria (1995) developed a simple model of a persistent gaseous vortex which is consistent with a Keplerian flow. This simple modeling of the gas velocity field is sufficient to explore the dynamics of the solid particles and to bring some conclusions on the capture efficiency. Far from the vortex the flow can be approximated by a set of circular orbits with Keplerian azimuthal velocity. On the other hand a set of Keplerian ellipses with the same semi-major axis but different eccentricities, corresponding to concentric epicycles, is also a steady solution of the fluid equations with uniform pressure and can describe, to the lowest order, the vortex flow (this correspondence was used first by Von Weizsäcker in 1944). We have chosen a cartesian frame of reference in which x and y stand for the azimuthal position and the radial displacement, respectively, rotating around the sun at the

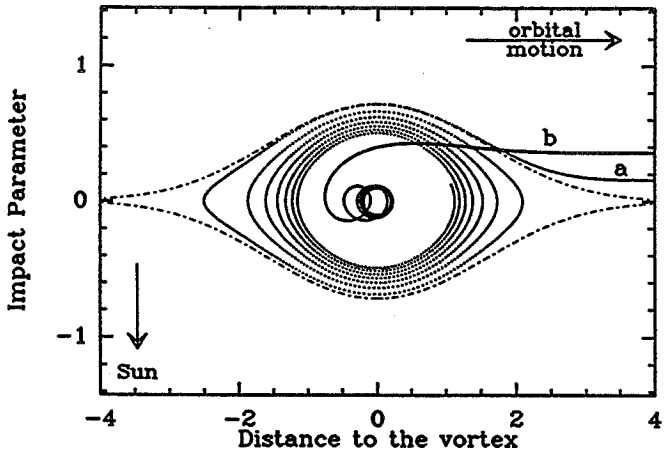

Figure 1. Trajectories of the the particles captured into a gaseous vortex, sketched by the separatrix (dashed line) between open and closed streamlines. The particles tend to reach purely epicyclic motions with a transient behaviour strongly dependant on the friction parameter: light particles ($\tau_s \simeq 0.05$ in case (a)) remain near the edge of the vortex whereas heavy ones ($\tau_s \simeq 3$ in case (b)) first sink deeply into the inner regions. For clarity the ordinates have been expanded by a factor of 2.

Keplerian angular velocity $\Omega = \Omega_o r^{-3/2}$ (Ω_o is the Earth's velocity for $r = 1$ in astronomical unit, AU). Assuming a simple matching of the "epicyclic flow" with the azimuthal Keplerian flow at large distances the velocity field is (see Fig.1):

$$\begin{cases} V_x = -\frac{3}{2}\Omega y - \frac{1}{2}\Omega y \; e^{-\frac{x^2+y^2}{2R^2}} \\ V_y = \frac{1}{2}\Omega x \; e^{-\frac{x^2+y^2}{2R^2}} \end{cases}$$

In which R is the characteristic size (or "radius") of the vortex and is limited to the thickness H of the nebula. In a standard model of nebula, the surface densities (both for gas and for particles) and the temperature are decreasing power laws $r^{-3/2}$ and $r^{-1/2}$, respectively; consequently, H ($\simeq$ R), increases as $r^{-5/4}$ (H$\simeq$ 0.04 AU near Earth's orbit).

3. PARTICLE TRAJECTORIES AND CAPTURE RATE

The particles embedded in the gas of the Nebula are submitted to a friction drag whose expression depends on the mean-free-path of the gas molecules relative to the particle size. For decimetric particles (and beyond 2 AU from the sun), mean-free-path exceeds particles size and the drag reaches the Epstein regime. The motions equations of the particles submitted to the Sun attraction, Coriolis force and friction drag, then reads:

$$\begin{cases} \frac{dv_x}{dt} = -2\Omega v_y - \frac{1}{t_S}(v_x - V_x) \\ \frac{dv_y}{dt} = 3\Omega^2 y + 2\Omega v_x - \frac{1}{t_S}(v_y - V_y) \end{cases},$$

where $t_S = \rho_d s/(\rho_{gas} C_S)$ is the stopping-time for a spherical particle with radius s and density ρ_d in a gas with density ρ_{gas}. The dynamical evolution depends on the

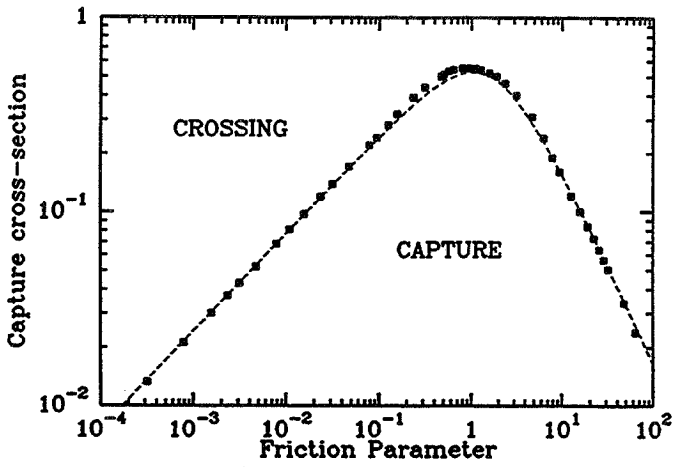

Figure 2. Non dimensional capture cross-section of the vortex as a function of the friction parameter ($tau_s = \Omega t_s$). Filled squares represent the values obtained by successive numerical integrations. The dashed line is a function of $f(\tau_s) = A\tau_s^{1/2}/(\tau_s^{3/2} + B)$ fitting at best the dependance $\eta_c(\tau_s)/R$; it distinguishes between a capture by the vortex and a simple crossing.

single non-dimensional friction parameter $\tau_S = \Omega t_S$, that is on the particle mass/area ratio: (i) the lightest particles ($\tau_S << 1$) come at rest rapidly with the gas and travel with the local flow; (ii) the heaviest particles ($\tau_S >> 1$) cross the vortex with a keplerian motion nearly unaffected by the friction drag. In the intermediate range of τ_s, a numerical integration of the equations shows that a particle can be captured by the vortex if its impact parameter (initial distance to the x axis) is sufficiently small (Fig.1); otherwise it is dragged by the flow. The corresponding critical impact parameter η_c can be fitted by the function (see Fig.2)

$$f(\tau_S) = \frac{\eta_c}{R} = \frac{A\ \tau_S^{1/2}}{\tau_S^{3/2} + B} \ ,$$

where $A \simeq 2.4$ and $B \simeq 2.2$. This function reaches a maximum when $\tau_S \simeq 1$, and reduces to the power laws $\tau_S^{1/2}$ and τ_S^{-1}, in the limits of the light and heavy particles, respectively. As the approach velocity ($3\eta\Omega/2$) only depends on the impact parameter, the mass capture rate is straightforwardly:

$$\frac{dM_{capt}}{dt} = \frac{3}{2}\sigma R^2 \Omega f^2(\tau_S)$$

where σ is the mean surface density of nebular solid material. The mass collected (at constant rate) reaches typical planetary values ($\simeq 16 M_\oplus$ at 5 AU) after a time corresponding to 500 revolutions of the vortex. This calculation implicitly assumes that the particles are continuously renewed near the vortex orbit. The renewal is maintained by the inward drift under the systematic drag associated with the velocity difference between gas and particles (the gas is pressure supported, not the particles).

4. DISCUSSIONS AND CONCLUSIONS

Our two dimensional capture mechanism adds to the vertical settling toward the nebula midplane, which is known to form a particle sublayer whose typical thickness is H_p. It results, inside the vortices, in an increasing surface density σ_{vort} and in an stronger volume density σ_{vort}/H_p which may reach much more easily the Roche threshold for gravitational instability. In the absence of any surface density enhancement, the velocity threshold for the gravitational instability is very low and is easily exceeded by any residual turbulence. By contrast inside the vortices, the surface density is increased by several order of magnitude in some ten rotation periods, so that gravitational instabilities become much easier and could gather rapidly the material into planetesimals.

In summary, after the decays of 3D turbulence, 2D turbulence could persist and organizes into long-lived vortices able to concentrate the solid material. We propose that the planetesimals form inside the vortices, either through gravitational instabilities or enhanced aggregation. This capture in vortex mechanism bring also new solutions to other major problems of planetary formation such as rapid formation of the giant planet cores and chemical segregation (cf. Barge and Sommeria, 1995). Of course the existence and structure of our long-lived vortices would require further justifications. However it must be stressed that our capture mechanism is insensitive to the choice of the starting assumptions, (i.e) nebula model and constant particle size, and, moreover, remains very efficient even if the vortex lifetime is assumed much shorter. For example, with a 5 rotation period lifetime (instead of 500), the surface density of the particles inside the vortex is still greater, locally, by a factor of several units than outside the vortex. This is the reason why, in our opinion, this way to form planetesimals can be considered as a possible alternative to the classical scenario. The capture in vortex mechanism was recognized important for planetary formation by Barge and Sommeria (1994, 1995) and is being studied (Fuente and Barge, 1996).

Acknowledgements. One of the authors (P.B.) wants to thank GDR "Mécanique des Fluides Astrophysiques et Géophysiques" for supporting his stay in Santa Clara during the symposium.

References

Abramowiccz,M.A., Lanza, A., Spiegel, E., Szuszkiewicz, E. 1992, *Nature*, **356**, 41.

Barge, P., Sommeria, J. 1994, in *Circumstellar Dust Disks and Planet Formation*, Proceedings of the 10th IAP Astrophysics Meeting, eds. R. Ferlet and A. Vidal-Madjar, (éditions frontières), p. 295.

Barge, P., Sommeria, J. 1995, *Astr. Ap.*, **295**, L1.

Dubrulle, B. 1993, *Icarus*, **106**, 59.

Fuente Marcos (de la), C., Barge, P. 1996, (in preparation).

Sommeria, J., Nore, C., Dumont, T., Robert, R., 1991, C.R. Acad. Sci. (Paris), **312**, II, 999.

Weizsäcker, C.F. von 1944, *Zeit. für Astrophys.* **22**, 319.

THE ROLE OF VORTICES IN THE FORMATION OF THE SOLAR SYSTEM

ANAND V. MEHTA *Massachusetts Institute of Technology, Cambridge, MA, USA*
GLENN R. FLIERL *Massachusetts Institute of Technology, Cambridge, MA, USA*

ABSTRACT. To show that robust vortices can exist in the solar nebula, a pseudo-spectral model has been developed to examine the evolution of the vortex in a Keplerian shear. Calculations show that a vortex can exist for $10^4 yr$ at Jupiter's radius.

1. INTRODUCTION

To understand the role that vortices in the gaseous solar nebula disk played in the formation of grains from dust, three questions need to be answered: how would a large vortex form; what are the characteristics, such as size, strength, and aspect ratio, of a long-lived vortex; and how does it affect the flow of dust. This poster presentation focuses on the second question.

It has been shown analytically that persistent vortices can exist in a constant background shear field (Moore and Saffmann, 1971). Since the Keplerian velocity of the disk results in a radially varying shear, the characteristics of these vortices must be studied numerically.

A pseudo-spectral model has been developed to track numerically the evolution of a vorticity field in a simple, two-dimensional system, using the conservation of vorticity equation.

2. THE VORTICITY EQUATION

To determine the conditions for the existance long-lived, robust vortices, the conservation of vorticity equation is derived by taking the curl of the Navier-Stokes equation (Landau and Lifschitz, 1987, §10). The vorticity equation can be non-dimensionalized using length $L[AU]$; time $T[yr]$; angular velocity and vorticity $\Omega_0 = 1/T[yr^{-1}]$; and velocity $U = L/T[AUyr^{-1}]$. The horizontal velocity, streamfunction, and vorticity are related by

$$\begin{aligned} \vec{v}_{x,y} &= \hat{z} \times \vec{\nabla}\psi, \\ q &= \hat{z} \cdot (\vec{\nabla} \times \vec{v}) = \nabla^2 \psi. \end{aligned} \tag{1}$$

The z-component of the vorticity equation can be written in a streamfunction-vorticity form,

$$\frac{\partial q}{\partial t} - \frac{\partial \psi}{\partial x}\frac{\partial q}{\partial y} + \frac{\partial \psi}{\partial y}\frac{\partial q}{\partial x} = \frac{1}{Re}\nabla^2 q \tag{2}$$

where $Re = LU/\nu$ is the Reynolds number, and ν is the viscosity.

The derivation uses the assumptions that

- the flow is incompressible, $\frac{D\rho}{Dt} = 0$,
- the flow is two dimensional, $w = 0$ and $\frac{\partial \cdot}{\partial z} = 0$,
- the fluid is barotropic, $\vec{\nabla}\rho \times \vec{\nabla}p = 0$, and
- the coordinate system is rotating with $\Omega = \hat{z}\Omega_c$,

where ρ is the fluid density, p is the pressure, and w is the z-component of the velocity.

3. NUMERICAL MODEL

To track the evolution of a vortex, the coordinate system needs to be specified and the background flow can be separated from the vortex flow.

A set of curvilinear coordinates, $\vec{x} = \vec{x}(x, y, z)$, are used to map a fraction of an annulus (with M sections in the whole ring). These relate to cylindrical coordinates, $\vec{r} = \vec{r}(r, \theta, Z)$, by

$$\begin{array}{rclcrcl} r &=& e^{y/M} & & x &=& 2\pi - M\theta \\ \theta &=& \frac{1}{M}(2\pi - x) & & y &=& M\ln(r) \end{array} \qquad Z = z \tag{3}$$

In a rotating coordinate frame, the cylindrical coordinate values for the background Keplerian flow are

$$\begin{aligned} \bar{v} &= \hat{\theta}2\pi\left[r^{-1/2} - r r_c^{-3/2}\right], \\ \bar{\psi} &= 2\pi\left[2r^{1/2} - \tfrac{1}{2}r^2 r_c^{-3/2}\right], \\ \bar{q} &= 2\pi\left[\tfrac{1}{2}r^{-3/2} - 2r_c^{-3/2}\right], \end{aligned} \tag{4}$$

where r_c is the radius at the center of the vortex. Separating the background values from the vortex flow values, the vorticity equation in curvilinear coordinates is

$$(e^{2y/M}q')_t = [(\bar{\psi}_y + \psi'_y)q']_x - (\psi'_x\bar{q}_y) - (\psi'_x q')_y + \frac{1}{Re}(q'_{xx} + q'_{yy}). \tag{5}$$

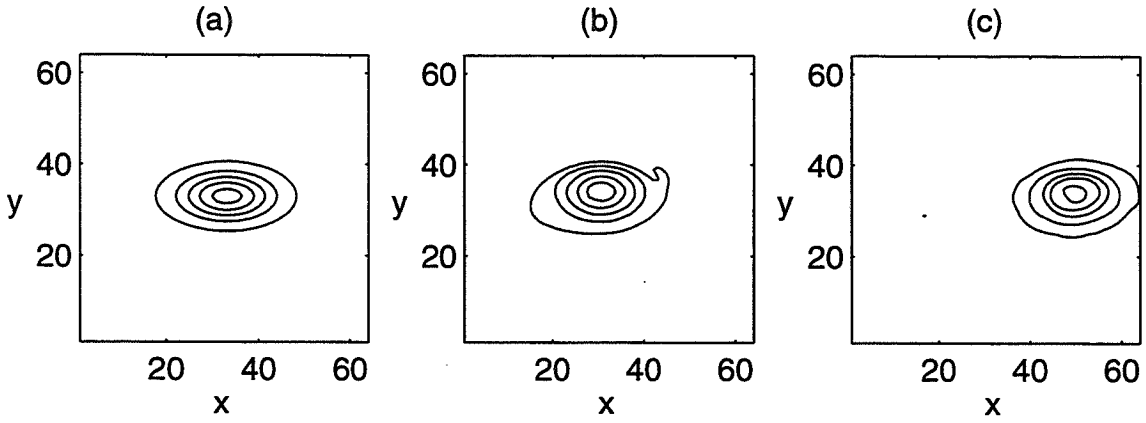

Figure 1. The evolution of a robust vortex: (a) the initial vorticity field, (b) the vorticity after a short time ($t = 50T_c$), and (c) the vorticity after $1500T_c$

4. NUMERICAL EXPERIMENTS

The vorticity equation is evolved using a pseudo-spectral method (Fox and Orszag, 1973). The right hand side of equation (5) is Fourier transformed into frequency space to perform the spatial derivatives and inverse transformed into real space to perform the products. The transform is a sine transform in y and an exponential transform in x since the data is periodic and real in x and is zero at the y boundaries (Press, *et al.*, 1993, §12.2–4). Since there are then no derivatives to be performed, this gives an ordinary differential equation, which can be integrated with a 4th-order Runge-Kutta scheme. The time step is governed by the Courant-Friedrichs-Lewy (CFL) stability criterion (Press, §19.1).

For the initial conditions needed for these calculations, vortices with a Gaussian vorticity distribution are used, with varying sizes, aspect ratios, and amplitudes. Calculations can also be performed with multiple vortices in the field.

5. RESULTS OF EXPERIMENTS

The overriding condition for long-lived vortices is that the vortex be oriented prograde relative to the shear. Since the vorticity of the background flow is negative around $r = r_c$, the robust vortex also has a negative vorticity. The vortex with a positive vorticity, in contrast, is torn apart almost immediately, in a few rotation periods. The vortex is also stable if the minor axis of an elliptical vortex is aligned along the shear, in this case radially. If the major axis is aligned radially, then the vortex is pulled apart into a series of smaller vortices which are elliptical and oriented angularly.

The strength of the vortex—the amplitude of the Gaussian—directly affects the aspect ratio of the robust vortex with weaker vortices being stretched relative to stronger vortices. The size of the vortex also affects the aspect ratio, but not as strongly. Figure 1 shows the evolution of a robust vortex. After a short time, the vortex has evolved into a steady state, which is largely unchanged after $t = 1.5^3 T_c$, where T_c is the period of the flow at the radius of the vortex. Figure 2 shows a similar vortex, with one-tenth the strength of the vortex in figure 1. After $t = 150T_c$, the vortex is stretched compared to the stronger vortex.

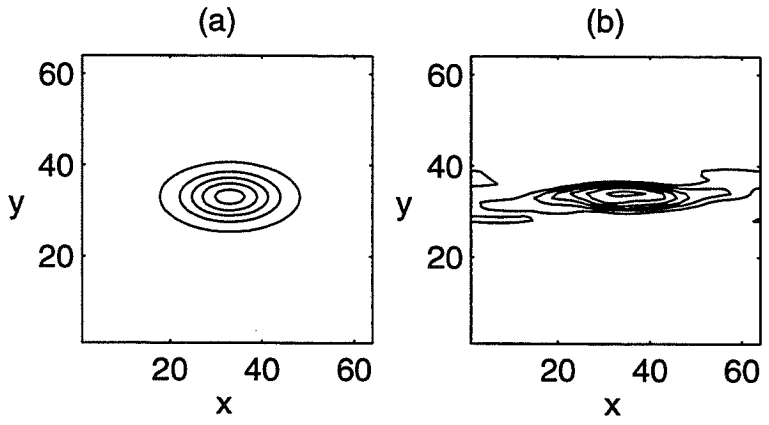

Figure 2. The evolution of a weaker vortex: (a) the initial vorticity field, (b) the vorticity after a short time ($t = 150T_c$)

6. CONCLUSIONS AND FUTURE WORK

Robust, long-lived vortices can exist for timescales of order 10^3 orbits, which is long enough to affect the conditions under which grain formation occurs.

Further work on the gas flow includes determining the effects of multiple vortices in the field and examining the evolution of a random assortment of vortices of different size, strength, aspect ratio, and orientation.

In addition, the effect of the vortex on the motion of dust particles will to be explored.

References

Canuto, C., Hussaini, M. Y., Quarteroni, A., and Zang, T. A. 1988, *Spectral Methods in Fluid Dynamics*, (Springer-Verlag).

Fox, D. G., and Orszag, S. A. 1973, *J. Comp. Phys.*, **11**, 612.

Goldreich, P., and Ward, W. R. 1973, *Ap. J.*, **183**, 1051.

Landau, L. D., and Lifschitz, E. M. 1987, *Fluid Mechanics, 2nd ed.*, (Pergamon Press).

Meacham, S. P., Flierl, G. R., and Send, U. 1990, *Dynamics of Atmospheres and Oceans*, **14**, 333.

Moore, D. W., and Saffman, P. G. 1971, in *Aircraft Wake Turbulence and its Detection*, eds. J. H. Olsen, A. Goldburg, and M. Rogers, (Plenum), p. 339.

Press, W. H., Teukolsky, S. A., Vetterling, W. T., and Flannery, B. P. 1993, *Numerical Recipes in C, 2nd Ed.*, (Cambridge University Press).

Weidenschilling, S. J. 1980, *Icarus*, **44**, 172.

Weidenschilling, S. J. 1984, *Icarus*, **60**, 553.

THE GLOBAL PERSPECTIVE ON THE EVOLUTION OF SOLIDS IN A PROTOPLANETARY DISK

T. F. STEPINSKI *Lunar and Planetary Institute, 3600 Bay Area Blvd., Houston, TX 77058, USA*
P. VALAGEAS *Service de Physique Théorique, CEN Saclay, 91191 Gif-sur-Yvette, France*

ABSTRACT. It is currently thought that planets around solar-type stars form by the accumulation of solid matter entrained in a gaseous, turbulent protoplanetary disk. We have developed a model designed to simulate the part of this process that starts from small particles suspended in the gaseous disk at the end of the formation stage, and ends up with most of the solid material aggregated into 1-10-km planetesimals. The major novelty of our approach is its emphasis on the global, comprehensive treatment of the problem, as our model simultaneously keeps track of the evolution of gas and solid particles due to gas-solid coupling, coagulation, sedimentation, and evaporation/condensation. The result of our calculations is the radial distribution of solid material circumnavigating a star in the form of a planetesimal swarm. Such a distribution should well approximate the radial apportionment of condensed components of the planets spread over the radial extent of the mature planetary system. Therefore we view our calculations as an attempt to predict the large-scale architecture of planetary systems and to assess their potential diversity. In particular, we have found that some initial conditions lead to all solids being lost to the star, but we can also identify initial conditions leading to a radial distribution of solid material quite reminiscent of what is found in our solar system.

1. INTRODUCTION

Recently, with the identification of several solar-like stars showing evidence of planet-sized companions circling around them (Marcy and Butler, 1996a,b) , our interest in understanding the formation of planetary systems on their largest scale has intensified and widened beyond the long-standing question of the origin of the solar system. The increasingly well-characterized properties of the formation process of solar-like stars, as well as the character of the solar system, which is thought to be typical, give us growing confidence that planets around such stars form by the accumulation of solid matter entrained in gaseous disks surrounding those stars. It is therefore timely to develop a model, built from an evolutionary perspective and based on the global outlook, capable of predicting the overall architecture of planetary systems.

After the disk forms out of a collapsing molecular cloud fragment, the subsequent evolution of solids within it can be divided into several consecutive stages set apart by the physical processes dominating each of them. First, the disk goes through a dissipative stage evolving in such a manner as to feed material to the star while

spreading out. It is during this stage that solid particles coagulate, settle toward the midplane, are advected toward the star, and can condense or evaporate in the changing gaseous environment. Thus, from the solids point of view, this stage is the age of major transformation. At the end of the dissipative stage surviving solids are deposited into planetesimals and the spatial distribution of solid matter around the star has little resemblance to that at the onset of this stage. During the next, accumulation stage, the backbone of the planetary system actually forms via the growth of planetesimals into solid protoplanets. The accumulation process apparently proceeds with only minimum radial displacement. Thus the distribution of solids on the scale of say 1 AU, as opposed to the scale of say 10^5 km, is about the same before and after the final accumulation. Once planets form, they can migrate due to tidal interaction with a gaseous disk (Ward and Hourigan, 1989), interactions with unaccreted planetesimals (Fernandez and Ip, 1984), and the general instability of the solar system on the timescale of 10^9 yr (Laskar, 1994). Yet, these migrations tend to be relatively small, and are not expected to rearrange the overall architecture of the planetary system. Thus, it seems that given a certain initial conditions at the end of the formation stage of the disk, the global evolution of solids during the dissipative stage plays a crucial role in determining the ultimate large-scale character of a planetary system.

On this basis we have developed a model that simultaneously keeps track of the evolution of the gas and the evolution of solid particles due to gas-solid coupling (Stepinski and Valageas, 1996a), as well as coagulation, sedimentation, and evaporation/condensation (Stepinski and Valageas, 1996b). This model takes the radial distribution of a dust surface density at the end of the disk formation as the input, and gives the radial distribution of the surface density of the solid material aggregated into planetesimals as the output.

2. COMPUTATIONAL MODELS

We applied our model to initial conditions sometimes considered fiducial by modelers of gaseous disks. The $1M_\odot$ star is surrounded by a viscously evolving disk characterized by dimensional viscosity $\alpha = 0.01$ with an initial gas surface density given by

$$\Sigma(r, t_o) = 8540\left[1 + (r/15\mathrm{AU})^2\right]^{-3.78} \quad \mathrm{g\ cm^{-2}} \tag{1}$$

Thus, the initial distribution of the gas is practically constant, equal to about 8540 g cm^{-2}, between the inner radius assumed to be at 0.036 A.U. and the radius of about 15 AU. At larger distances there is practically no gas. The total mass of the gaseous disk is equal to 0.245 $M_\odot$ and angular momentum is equal to 5.6×10^{52} g cm^2 s^{-1}. Solid particles, assumed to be made up solely of water-ice, have initially all the same size, $s = 10^{-3}$ cm, and the surface density of the solid material constitutes 1% of the gas surface density to account for cosmic abundance. *The most important result of this, "high-mass model", calculation is that such a model leads to a complete loss of all solids into the star* (see Fig. 1).

We have also considered a scenario where the $1M_\odot$ star is surrounded by a viscously evolving disk characterized by $\alpha = 0.001$ with an initial surface density of the gas given by

$$\Sigma(r, t_o) = 2\left[1 + (r/200\mathrm{AU})^2\right]^{-3.78} + 600(r/1\mathrm{AU})^{-1.5} \quad \mathrm{g\ cm^{-2}} \tag{2}$$

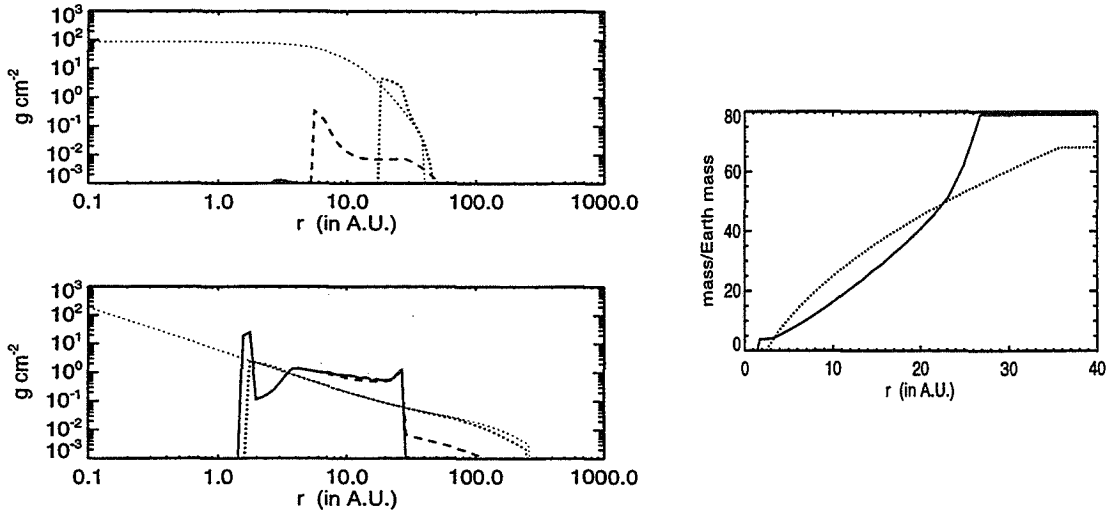

Figure 1. The two panels on the left side show the radial distribution of surface density of icy solids at selected times: $t = 10^4$ yr (dotted line), $t = 3.2 \times 10^5$ yr (dashed line), and $t = 3.2 \times 10^6$ yr (solid line). The light dotted line indicates the surface density of solids at the end of the formation stage. The upper panel shows the evolution of the high-mass disk, all solids are lost to the star. The lower panel shows the evolution of the low-mass disk, the surface density of solids converges when all solids are deposited into planetesimals. The sharp inner boundary of the distribution is located at the evaporation radius. The panel on the right side is a plot of the disk's mass interior to a given radius versus the radius. The dotted line represents the mass of icy planetesimals in the solar nebula "reproduced" by means of the minimum-mass concept (Hayashi et al. 1985) and the solid line depicts the mass of icy planetesimals predicted by our low-mass model.

The first term ensures that there is some mass up to very large distances from the star. The second term corresponds to the central concentration of the mass and sets the location of the evaporation radius. The total mass of the gaseous disk is equal to 0.023 $M_\odot$ and an angular momentum is equal to 1.8×10^{52} g cm^2 s^{-1}. The solid constituent is prescribed as in the high-mass model. *The most important result of this, "low-mass model" calculation is that such a model leads to the survival of solid material* (see Fig. 1).

3. CONCLUSIONS

Planetary systems diversity. We have found that the shape of the distribution of gas and dust around the star at the end of the formation stage indeed makes a big difference in the ultimate location and the character of the planetesimal swarm. In particular, a disk evolving from the initial state characterized by a relatively large amount of gas concentrated relatively close to the star does not lead to the formation of planetesimals. On the other hand, solids in a disk evolving from the initial state characterized by a relatively small amount of gas extended over relatively large distances from the star develop into planetesimals.

Character of planetary systems. We have shown that the number density of planetesimals has an abrupt outer limit resulting from advectional compression. This leads to the prediction that planetary systems end abruptly. This is certainly true of

our solar system, where the mass of all objects in the Kuiper belt is estimated to be only a fraction of Earth's mass (Jewitt & Luu 1995). It also appears that the final mass of solid material locked into planetesimals is about equal to the initial mass of solids at the end of the formation stage.

Recovering the solar system architecture. Among several models starting from the low-mass, extended initial mass distribution, the one characterized by dimensionless viscosity $\alpha = 10^{-3}$ yields the mass distribution in the planetesimal swarm that can lead to a planetary system like our own. Assume that four giant planets in the solar system have cores of $M_{\rm J} = 20M_{\oplus}$, $M_{\rm S} = 20M_{\oplus}$, $M_{\rm U} = 10M_{\oplus}$, and $M_{\rm N} = 10M_{\oplus}$ respectively. According to the minimum-mass concept the giant planets have locations $r_{\rm J} = 4.7$AU, $r_{\rm S} = 11.8$AU, $r_{\rm U} = 19.6$AU, and $r_{\rm N} = 26$AU. Applying this same mass apportionment formula for our model yields $r_{\rm J} = 4.05$AU, $r_{\rm S} = 15$AU, $r_{\rm U} = 21$AU, and $r_{\rm N} = 23.6$AU, which in these qualitative terms is not much different from the actual locations. The most important difference is the excess of mass near the outer limit of the mass distribution. This causes "Neptune" to be too close to "Uranus." The excess of mass at 20–30 AU may account for the mass lost from the plane of the ecliptic due to gravitational scattering of unaccreted planetesimals by planets that have already attained their final masses (Duncan et al. 1987).

Acknowledgements. This research was done while the authors were supported by the Lunar and Planetary Institute, which is operated by USRA under contract No. NASW-4574 with NASA. This is Lunar and Planetary Institute Contribution No. 891.

References

Marcy, G. W., and Butler, R.P. 1996a, *Ap. J. (Letters)*, **464**, L147.

Marcy, G. W., and Butler, R.P. 1996b, *Ap. J. (Letters)*, **464**, L153.

Duncan, M., Quinn, T., and Tremaine, S. 1987, *A. J.*, **94**, 1330.

Fernandez, J. A., and Ip, W.-H. 1984, *Icarus*, **58**, 109.

Hayashi, C., Nakazawa, K., and Nakagawa, Y. 1985, in *Protostars & Planets II*, eds. D.C. Black and M.S. Matthews (Univ. of Arizona Press, Tucson), p. 1100.

Jewitt, D. C., and Luu, J. X., 1995, *A. J.*, **109**, 1867.

Laskar, J. 1994, in *Circumstellar dust disks and planet formation*, eds. R. Ferlet and A. Vidal-Madjar (Editions Frontieres), p. 257.

Stepinski, T. F., and Valageas, P., 1996a, *Astr. Ap.*, **309**, 301.

Stepinski, T. F., and Valageas, P., 1996b, submitted to *Astr. Ap.*

Ward, W. R., and Hourigan, K., 1989, *Ap. J.*, **347**, 490.

TOWARD AN ASTROPHYSICAL THEORY OF CHONDRITES

HSIEN SHANG *Astronomy Department, University of California, Berkeley, CA 94720-3411, USA*
FRANK H. SHU *Astronomy Department, University of California, Berkeley, CA 94720-3411, USA*
TYPHOON LEE *Institute of Earth Science, Academia Sinica, Taipei 115, TAIWAN*

ABSTRACT. Sunlike stars are born with disks. Based on our recently developed model to understand how a magnetized new star interacts with its surrounding accretion disk, we advanced an astrophysical theory for the early solar system. The aerodynamic drag of a magnetocentrifugally driven wind out of the inner edge of a shaded disk could expose solid bodies lifted into the heat of direct sunlight, when material is still accreting onto the protosun. Chondrules, calcium-aluminum-rich inclusions (CAIs), and rims could form along the flight for typical self-consistent parameters of the outflow in different stages of star formation. The process gives a natural sorting mechanism that explains the size distribution of CAIs and chondrules, as well as their associated rims. Chondritic bodies then subsequently form by compaction of the processed solids with the ambient nebular dust comprising the matrices after their reentry at great distances from the original launch radius.

1. INTRODUCTION

Chondrules and CAIs are major components of chondrites which are thought to preserve the information from when the solar system formed. It has been a puzzle for many years that the chondrules and CAIs show evidence of transient heating events which could not be explained by any conventional astrophysical models of solar nebula at 2.5 AU where the parent bodies of the chondritic meteorites are from. Judging from the mass fraction contained in chondrules and CAIs, one can infer that the process of forming them must be one that solids in the solar system must undergo in the evolution.

2. MAGNETOCENTRIFUGALLY DRIVEN WINDS AND FUNNEL FLOWS

We have recently developed a model (X-Wind Model) to explain the outflow phenomenon based on the star-disk interaction of a young star born with a disk. The disk interacts with the rotating magnetosphere of the young star with an unperturbed dipole. With star mass M_*, radius R_*, magnetic dipole moment μ_*,

and the disk mass accretion rate $\dot{M}_D$, the disk is truncated at an inner radius $R_x \approx \left(\mu_*^4/GM_*\dot{M}_D^2\right)^{1/7}$. Stellar spin rate is regulated to co-rotate with the inner disk edge at $\Omega_* = (GM_*/R_x^3)^{1/2}$.

The disk inflow $\dot{M}_D$ will divide at R_x into the wind which carries off excess angular momentum and the funnel flow which accrets gas and dust onto the newborn star. When the funnel flow impacts the star, the gravitational energy will be released at the hot spots, which contributes to most of the stellar luminosity in the embedded phase. The stellar luminosity of a T-Tauri star comes from gravitational contraction, and accretion and deuterium burning contribute as corrections. We can also estimate disk temperature at base of flow for an optically thick, purely absorptive, completely flattened portion of a disk at R_x from the star, when it is exposed to oblique rays. The calculated base temperatures are $T_x \approx$ 800K to 1200 K from the embedded to revealed phase.

3. GAS-SOLID COUPLING AND AERODYNAMIC SIZE-SORTING

Small solid bodies of density ρ_c and radius R_c are lifted out of the disk by the outflowing wind through aerodynamic drag with the drag coupling constant:

$$\alpha \equiv \frac{3C_D\dot{M}_w}{16\pi\Omega_* R_x^2 \rho_c R_c},$$

and may be exposed to the radiation of proto-Sun.

Particles with $\alpha \gg 1$ are well coupled to the outflowing wind and will be thrown to interstellar space, whereas large and dense particles with $\alpha \ll 1$ decouple early from the wind and fall back to the disk not much farther from the original launch location. Particles of appropriate size are thrown to large, but not infinite, distances before reentering the disk. For example, in our calculation, particles of $\alpha = 0.4$ which fly to very large distance correspond to 3mm and 0.2mm in diameter for $C_D = 1$ and $\rho_c = 3$ gcm^{-3}, in the embedded phase and revealed phase, respectively. They will then be processed and carried back to the inner region with the general disk accretion inflows. *Our model predicts that chondrules and CAIs should be sprayed over the entire solar system and should be found among sufficiently primitive solid materials at all distances from the Sun.*

4. PEAK TEMPERATURE

Surface-averaged radiative-equilibrium temperature of those solids being lifted can be estimated by adding the contributions from the unocculted starlight of the proto-sun, the energy density of the diffuse radiation field in the flow and the drag heating. Gently lifting the particle into the wind changes the optical depth from the star to the particle basically from $\tau_* = \infty$ to ~ 0. Surface-averaged peak temperature will be reached for spherical particles whose rotational period is shorter than radiative-conduction time and whose spin axis change randomly on time scale rapid compared with 1 s. $\bar{T}_{\rm peak} =$ 1800 K to 1300 K from the embedded to the revealed phase.

For fluffy aggregates whose heat conduction time and spin period are longer than the radiation deposition time, the fractal heating and conductive cooling will apply

and the subsolar temperature

$$T_{\rm subsolar} \approx \sqrt{2} T_{\rm peak}$$

can be reached.

X-wind could provide an environment of high fugacity because the ultraviolet light from the hot spot can photodissociate H_2O, liberating oxygen even in the relatively abundant presence of hydrogen. If H_2O is totally dissociated, the partial pressure of O would exceed 3×10^{-10} atm for dimensionless time $t < 1.5$ in the fiducial embedded case. The retention of volatile Na under high temperatures in chondrules is aided by high oxygen fugacity. High oxygen fugacity may also explain the enhanced loss from CAIs of W and Mo, whose oxides evaporate much more readily than their highly refractory metallic states.

5. CAIS, CHONDRULES AND THEIR RIMS

CAIs contain the most refractory inclusions $\bar{T}_{\rm peak} \sim 1800$K. They form by the mean cooling mechanism of dropping surface-averaged temperature of an unshielded particles from $\bar{T}_{\rm peak}$ to values below it. The mean mechanism will characterize an exposure time scale $\sim 2\Omega_*^{-1}$ to full sunlight. According to our model, CAIs form in the embedded phase of protostellar evolution.

Chondrules form during a later phase (embedded or revealed) than the CAIs when the base and surface-averaged peak temperatures are lower and when the temperatures are enough to vaporize the moderately volatile substances on a time scale short compared to an hour, but not to vaporize silicate rocks. Molten bodies of the appropriate sizes move quickly into the shade provided by the small dust grains entrained in the upwelling gas of the bipolar outflow, and cool down much more quickly than simply moving away from the sun. Fractal heating of dustballs may provide another effective melting conditions for only tens of minutes, beyond which the compact protochondrule is cooled radiatively and conductively from $\bar{T}_{\rm peak} \sim 1300$ K to much lower values on a time scale of days. Dustballs carried by every wind streamline can experience the fractal heating during the revealed phase of protostellar evolution. The chondrules thus formed will be small; they will acquire only thin coarse-grained rims that are easily destroyed when these objects reenter the disk. The chondrules in CO3 meteorites have mean sizes of 0.15 mm, and only $\sim 1\%$ of them possess coarse-grained rims. Formed in an earlier phase, the chondrules in CV3 meteorites have mean sizes of 1.0 mm, and $\sim 50\%$ of them possess coarse-grained rims, which shows an interesting contrast.

Chondrules show coarse rims of grains of roughly 10 μm diameter. Their sizes and the devolatized compositions chemically similar to the body of the chondrule can be explained by the remelting of the chondrule mantle by the deposited energy of collision with fast moving 10 μm grains followed by local recrystallization. The cumulative energy deposited per unit area into the mantle is proportional to the integral of ρw^3 along the trajectory times the mass fraction $X_{\rm si}$ contained in silicate grains. We get the fractional thickness $\Delta R_{\rm coarse}/2R_{\rm c} \approx 10\%$ during both phases.

Recondensed material from the less refractory silicates that evaporate upon launch will form the fine-grained rims on CAIs as the wind expands and cools appreciably below a temperature of ~ 1700 K. Observed CAI rims often display layers of sequentially lower condensation temperatures as one moves radially outward from the center

of the CAIs, which is consistent with our scenarios. If condensation of silicates begins immediately after launch, $\Sigma \equiv \int_0^t \rho \sup(w, v_t)\, dt$ gives the column density of swept-up condensing gas or small grains along the trajectories of flight and the fractional thickness of the rim accquired is

$$\frac{\Delta R}{R_c} = \frac{X_{si} \Delta \Sigma \alpha}{3 C_D}.$$

If the x-wind is turbulent and $\Delta\Sigma$ = 80-160, we get $\Delta R_{fine}/2R_c \approx$ 2-4%. Extremely thick examples of fine-grained rims may require multiple coatings from several launches. The fine-grained rims on top of coarse-grained rims are acquired by this process.

Reentry of CAIs and chondrules will add fragments and broken rim material to matrix, which are essentially "compacted nebular dust" by the gradual interlocking and compaction of many cm-sized, porous, "dustballs". We can get an erosion of about 7% of the object's radius for standard values of X_{si} and C_D. For weaker rocks, the reentering CAI or chondrule would be eroded to about half of its former size. Chondrites then subsequently form with the matrix made from this mix of primitive nebular dust and processed fragments.

6. CONCLUSIONS

We have proposed a theory of the early solar system when solid materials are being processed by the bipolar outflow. Unlike other conventional models seeking for chondrule formation at 2.5 AU, we have a location of formation in the inner edge of the solar nebula: 0.06 AU. We have also explained the following facts about CAIs and chondrules: size ranges, compositions, temperatures, efficiencies and the the paleomagnetism in the meteoritic materials since magnetic field is a basic component underlying our model. Our scenario can unify not only the facts of chondrites but also the chronology of the formation events under a framework of star formation.

References

See Shu, F.H., Shang, H., & Lee, T. 1996, *Science*, **271**, 1545 and the references therein.

PLANETESIMAL FORMATION IN THE OUTER SOLAR NEBULA

K. D. SUPULVER *University of California, Santa Cruz, California, USA*

ABSTRACT. A numerical investigation of the orbital trajectories of individual particles in the turbulent outer solar nebula has been performed. The (spherical) particle consists of an unchanging mm-sized "dust" core surrounded by an H_2O ice mantle; the density of both core and mantle is 0.5 g cm^{-3}. The simulations include the effects of H_2O condensation from the gas phase, H_2O sublimation from the particle surface, and collisional growth via particle collisions with a background distribution of small H_2O grains. The model nebula is an azimuthally symmetric minimum-mass nebula of solar composition with a vertical (and radial) temperature gradient. Particle evolution follows a pattern. A particle starting out in a cool region grows via condensation and collisional accretion until it is large enough (decimeter- to meter-sized) to decouple somewhat from the turbulence. (This growth occurs on a timescale of several thousand years at 10 AU; at 30 AU, the timescale is $\approx 10^4$ years.) The particle then moves rapidly inward toward the sun due to secular gas drag forces, sublimates much of its icy mantle, and slows its inward migration as it gets caught up in the turbulence again (due to its now-smaller size) at the "sublimation boundary", where the ambient gas temperature is ≈ 150 K. Such a process could, on a short timescale (*i.e.*, a timescale much shorter than the nebular gas lifetime of $\sim 10^6$ yr), generate a population of decimeter- to meter-sized bodies which would then collisionally accrete to form planetesimals.

1. INTRODUCTION

Current theories hold that the planets formed from a disk of gas and dust orbiting the sun (*e.g.*, Cameron 1995). Such disks have been observed around other stars, and these disks are thought to be very commonplace around young stars with masses similar to that of the sun (Beckwith and Sargent 1993). Recent detections of planets around other solar-type stars (*e.g.*, Mayor and Queloz 1995) suggest that planet formation may be a ubiquitous process.

According to current theories of the formation of our solar system, terrestrial planets and outer planet cores with sizes $\sim 10^4$ km must form somehow from the population of μm-sized grains that condense out of the cooling solar nebula. Gas drag forces played a significant role in determining the motions of small particles orbiting in the early solar nebula. If no gas were present, a particle would simply execute a Keplerian orbit about the sun. In a laminar solar nebula, it would spiral into the sun in a relatively short time; the precise timescale depends on the particle's size and density (Adachi *et al.* 1976, Weidenschilling 1977). The solar nebula was very likely turbulent, however, and many workers have investigated the problem of

particle motion and growth in such an environment (*e.g.*, Weidenschilling 1984, Cuzzi *et al.* 1993, Weidenschilling and Cuzzi 1993, Dubrulle *et al.* 1995, Sterzik *et al.* 1995). This paper considers the effect of sublimation and condensation processes, as well as growth via collisions with μm-sized grains, on an icy particle's orbital trajectory in the turbulent outer solar nebula.

2. TURBULENT STRUCTURE OF THE NEBULA

Turbulence is imposed on the laminar solar nebula to model a complex structure consisting of turbulent cells with sizes l_i ranging from about 80% of the scale height down to the viscous scale. Random time-dependent convective velocities drawn from a Kolmogorov spectrum are imposed on the nebular gas in the radial (r) and vertical (z) directions:

$$v_r = -\frac{1}{10}\Omega(r)H(r)\sum_{i=0}^{7}\left(\frac{l_i}{H(r)}\right)^{1/3}\cos(\theta_{r,i}(t))\sin(\theta_{z,i}(t)); \quad (1)$$

$$v_z = \frac{1}{10}\Omega(r)H(r)\sum_{i=0}^{7}\left(\frac{l_i}{H(r)}\right)^{1/3}\sin(\theta_{r,i}(t))\cos(\theta_{z,i}(t)). \quad (2)$$

The convective velocity at any given position (r, z) is the sum of individual contributions from cells spanning eight orders of magnitude in size. Thus, the turbulent gas

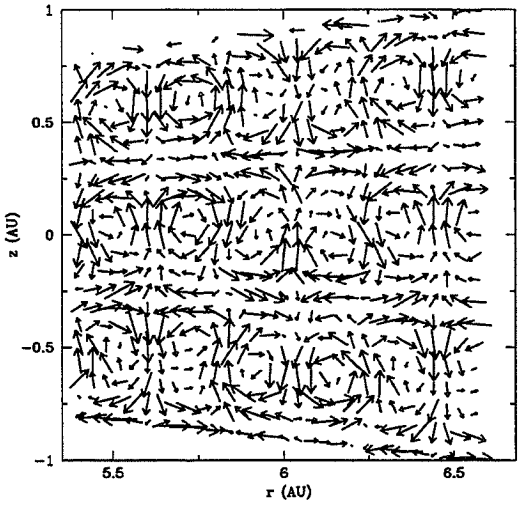

Figure 1. "Kolmogorov" convective structure imposed on the laminar solar nebula.

motion (Fig. 1) is generated by eight grids of evenly-spaced cells superimposed upon one another. Figure 1 shows turbulence near 6 AU; the same cell structure is present near 10 AU, where the simulation described in Sec. 4. was done. The relative radial and vertical phases of the grids change randomly with time; this change in phase is responsible for the time-dependence of the velocities. Maximum convective velocities are approximately 10% of the sound speed. The timescale for convective overturn of the largest eddies is roughly the orbital timescale at a given nebular radius.

3. SUBLIMATION, CONDENSATION, AND GROWTH PROCESSES

The sublimation and condensation rates used in the model, E_{exp} and C_{exp}, respectively, are as follows (Haynes *et al.* 1992):

$$E_{exp} = \gamma E_{max} = (0.63)\ P_p(2\pi mkT_p)^{-1/2}; \tag{3}$$

$$C_{exp} = \alpha C_{max} = (1.04 - T_p/500)\ P_v(2\pi mkT_g)^{-1/2}. \tag{4}$$

The evaporation and condensation coefficients, γ and α, are experimentally determined factors multiplying the theoretical maximum rates, E_{max} and C_{max}. P_p is the H_2O vapor pressure above an ice surface of temperature T_p; P_v is the H_2O vapor pressure of the ambient gas at temperature T_g. The quantity m is the mass of an H_2O molecule. The particle temperature is determined by the net energy flux (radiative plus latent heat fluxes) at the particle surface.

The collisional growth rate, assuming perfect sticking, for a spherical particle of radius r_p and mass m_p moving with speed v_{rel} relative to a smooth background distribution of icy grains with density ρ_{grains} is

$$\frac{\Delta m_p}{\Delta t} = \rho_{grains}\ v_{rel}\ \pi r_p^2. \tag{5}$$

The grain density is assumed to be proportional to the gas density.

4. ORBITAL TRAJECTORY OF A PARTICLE

Figure 2 shows the results of a complete simulation, including sublimation, condensation, and collisional growth processes. The particle started at $r_0 = 10$ AU on a circular orbit in the midplane of a turbulent nebula. The total run time was 600 orbital times. The particle began as a mm-sized core of density 0.5 g cm^{-3}. In the cold (120–140 K) environment at 10 AU, H_2O condensed on the particle as it circled the large convective cell centered near 10 AU. Collisional growth and sublimation also took place, but at rates roughly one order of magnitude less. When the particle radius r_p reached $\approx$ 25 cm, secular gas drag began to dominate, and it moved inward rapidly (in $\sim 10^{10}$ s), sublimating some of its ice mantle as it entered warmer (130–150 K) regions. It then became trapped for the duration of the run in a large convective cell centered near 8.8 AU. The net H_2O mass gain or loss varied as the particle moved back and forth across the (warmer) midplane, and the particle radius r_p fluctuated accordingly. Condensation and sublimation rates were roughly equal at this point (the collisional growth rate was an order of magnitude lower), and the particle never again grew large enough for secular gas drag to dominate and force it inward to even warmer regions.

5. CONCLUSIONS

Numerical integrations of particle orbital trajectories in a turbulent outer solar nebula show that sublimation and condensation processes are very important in determining the trajectories of small icy particles. Such particles can grow rapidly to decimeter sizes. These bodies might then serve as the seed population for the collisional growth

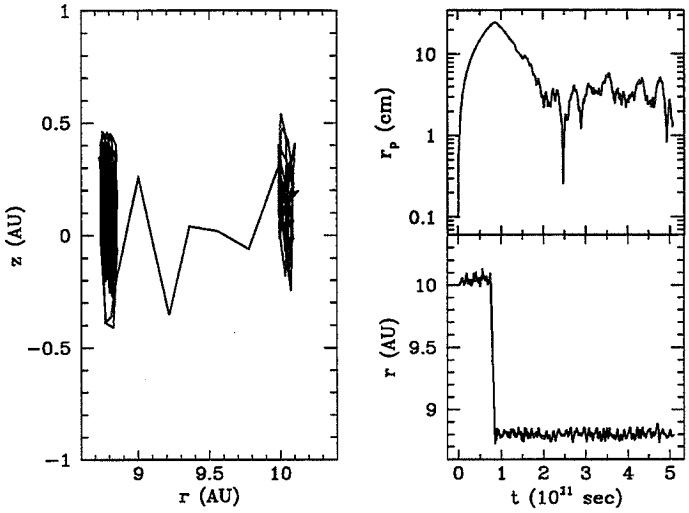

Figure 2. The orbital trajectory of a particle projected on the r–z plane. Particle radius r_p and orbital radius r as a function of time for that trajectory.

of km-sized planetesimals. If such a body survived long enough against collisions with other particles, it could be trapped near the sublimation boundary; a concentration of particles there could enhance the collisional growth rate at that radius.

References

Adachi, I., Hayashi, C., and Nakazawa, K., 1976, *Prog. Theor. Phys.*, **56**, 1756.

Beckwith, S. V. W., and Sargent, A. I., 1993, in *Protostars and Planets III*, eds. E. H. Levy and J. I. Lunine, (Univ. Arizona Press), p. 521.

Cameron, A. G. W., 1995, *Meteoritics*, **30**, 133.

Cuzzi, J. N., Dobrovolskis, A. R., and Champney, J. M., 1993, *Icarus*, **106**, 102.

Dubrulle, B., Morfill, G., and Sterzik, M., 1995, *Icarus*, **114**, 237.

Haynes, D. R., Tro, N. J., and George, S. M., 1992, *J. Phys. Chem.*, **96**, 8502.

Mayor, M., and Queloz, D., 1995, *Nature*, **378**, 355.

Sterzik, M. F., Morfill, G. E., and Dubrulle, B., 1995, *Ap. Space Sci.*, **224**, 567.

Weidenschilling, S. J., 1977, *M. N. R. A. S.*, **180**, 57.

Weidenschilling, S. J., 1984, *Icarus*, **60**, 553.

Weidenschilling, S. J., and Cuzzi, J. N., 1993, in *Protostars and Planets III*, eds. E. H. Levy and J. I. Lunine, (Univ. Arizona Press), p. 1031.

PLANETESIMALS AND COMETS

THE MASS OF LARGE IMPACTORS

M. G. PARISI *Facultad de Ciencias Astronómicas y Geofísicas, Universidad Nacional de La Plata, La Plata, Argentina*
A. BRUNINI *Facultad de Ciencias Astronómicas y Geofísicas, Universidad Nacional de La Plata, La Plata, Argentina*

ABSTRACT. By means of a simplified dynamical model, we have computed the eccentricity change in the orbit of each giant planet, caused by a single, large impact at the end of the accretion process. In order to set an upper bound on this eccentricity change, we have considered the giant planets' present eccentricities as primordial ones. By means of this procedure, we were able to obtain an implicit relation for the impactor masses and maximum velocities. We have estimated by this method, the maximum allowed mass to impact Jupiter, to be $\sim 1.136 \times 10^{-1}$, being in the case of Neptune, $\sim 3.99 \times 10^{-2}$ (expressed in units of each planet final mass). Due to the similar present eccentricities of Saturn, Uranus and Jupiter, the constraint masses and velocities of the bodies to impact them (in units of each planet final mass and velocity respectively), are almost the same for the three planets. These results are in good agreement with those obtained by Lissauer and Safronov (1991). These bounds might be used to derive the mass distribution of planetesimals in the early solar system.

1. INTRODUCTION

Planets in the Solar System have accreted mass mainly via collisions with solid planetesimals. Within this scenario, giant impacts are currently believed to be events that have played a significant role in the formation of the planets. For example, the rotation axes of the planets were tilted from the direction perpendicular to the orbital plane by stochastic, off-center impacts (Lissauer and Safronov, 1991; Safronov, 1972; Brunini, 1993). Specially, the large obliquity of Uranus (98°) suggests that it may have suffered an oblique impact by a large body during its formation (Koricansky et al., 1990; Parisi and Brunini, 1996). The random component of the spin angular momentum of a planet has been computed as a function of the size and velocity distribution of the planetesimals from which it accreted (Lissauer and Safronov, 1991; Parisi and Brunini, 1996). Using the present observed rotation periods and obliquities of the planets as constraints, the sizes of the largest bodies which impacted each planet and the upper limit to the continuous power law distribution of planetesimals were obtained.

In the present work, through a different approach than those described above, we set upper bounds on the masses and orbital velocities of the outer planets' impactors. For this purpose, we have considered the present orbital eccentricity of the giant

planets as primordial, since the large planets motion seems to be very regular during their history. Nevertheless, this treatment cannot be employed for the inner planets, since their eccentricities and obliquities have probably experienced large scale chaotic behavior during their history (Laskar, 1990; Laskar and Robutel, 1993).

2. DYNAMICAL METHOD AND RESULTS

We study how the impulse imparted by a single large impact would have affected the orbital eccentricity of each giant planet at the end of its accretion phase. Gauss form of Lagrange's planetary equations predicts that if the eccentricity of the planet is negligibly small before the collision, due to the impact, the orbit of the planet acquires the following eccentricity:

$$(\Delta e)^2 = \frac{1}{V_{orbp}^2}[\Delta V_r^2 \sin^2 l + 4\Delta V_t^2 \cos^2 l + 4\Delta V_r \Delta V_t \sin l \cos l], \tag{1}$$

where l is the mean longitude of the original circular orbit of the planet, V_{orbp} is its original orbital velocity (both measured when the impactor entered the sphere of influence of the planet), and ΔV_r and ΔV_t are the orbital velocity changes that suffers the planet due to the collision in the direction perpendicular and parallel to V_{orbp} respectively. The velocities and angular coordinates considered in this work are all measured from the barycenter of the three-body system (Sun-planet-impactor). It will be noticed that the orbital velocities and coordinates of bodies in heliocentric orbits are usually referred to the center of the Sun. Nevertheless, on account of the small relative mass of the planets and impactors, the results are very nearly the same if we refer those quantities to the barycenter. Since the impactor enter the sphere of influence of the planet, the perturbation of the Sun is neglected and a two-body approximation is used, being the following equation fullfiled:

$$m_p \vec{V}_{orbp} + m_i \vec{V}_{orbi} = (m_p + m_i)\vec{V}_{cm}, \tag{2}$$

where $\vec{V}_{orbi}$ was the orbital velocity that had the impactor when entered the sphere of influence, and m_i and m_p are the masses of the impactor and the planet respectively. It is worth noting, that $\vec{V}_{orbi}$ and $\vec{V}_{orbp}$ are measured when the impactor and the planet are at infinite each other, since we are considering they are just begining to feel their mutual gravitation when the impactor entered the sphere of influence. An inelastic collision for the planet and the impactor is assumed and consequently, the final orbital velocity of the planet after collision is the velocity of the center of mass of the two bodies, $\vec{V}_{cm}$, being $(m_p + m_i)$ its final mass. Therefore, due to the collision, the orbital velocity of the planet changes in:

$$\Delta\vec{V} = \vec{V}_{cm} - \vec{V}_{orbp}. \tag{3}$$

It is possible to determine the radial and tangential components of $\Delta\vec{V}$ (ΔV_r and ΔV_t respectively) as functions of ΔV, l, θ and ϕ, being θ and ϕ the angular coordinates of $\Delta\vec{V}$. Through Eqs.(2) and (3), and with the help of some vectorial diagrams, we

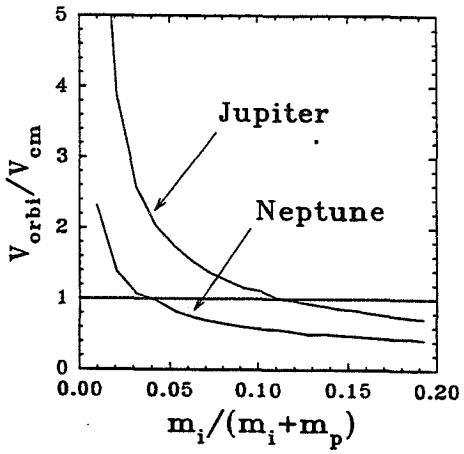

Figure 1. These curves display the most probable maximum allowed value of the impactor orbital velocity V_{orbi} (in units of the planet final orbital velocity V_{cm}), as a function of its mass m_i (in units of the planet final mass $(m_p + m_i)$). The results are displayed for Jupiter and Neptune. The curves for Saturn and Uranus are not displayed, since they are almost identical to that of Jupiter. In the probable case, where the impactor would have belonged to a zone similar to the planet's final one ($V_{orbi}/V_{cm} = 1$), the maximun allowed value for the impactor mass is given by the intersection of the dashed line with the solid lines.

have been able to obtain analytical relations for ΔV and V_{orbp} as functions of V_{orbi}, V_{cm}, ψ, and $m_i/(m_p + mi)$, where the angle ψ verifies: $\cos\psi = \cos(\phi - (\frac{\pi}{2} + l))\sin\theta$.

In order to estimate the maximum allowed $V_{orbi}(m_i)$ of the impactors, we have followed the above description to obtain, from Eq.(1): $(\Delta e)^2 = (\Delta e)^2(V_{orbi}, V_{cm}, m_i/(m_p + m_i), l, \theta, \phi)$. The value of $(\Delta e)^2$ is constrained being less than, or equal to the present square of the eccentricity e^2 of the planet, $(\Delta e)^2 \leq e^2$. In principle, this relation was employed to obtain an implicit equation for the maximum allowed orbital velocity of the impactor, where e, V_{cm} and $(m_p + m_i)$ are fixed parameters for each giant planet and l, θ and ϕ are variables. The spatial average in l, θ and ϕ has been computed numerically to obtain by this way, the most probable value of the maximum allowed V_{orbi} as a function of m_i. This result is displayed in Figure 1 for Neptune and Jupiter. In the probable case in which the impactor would have belonged to a zone similar to the planet's final one, the most probable impactor orbital velocity would be $V_{orbi} \sim V_{cm}$. This allows us to determine the maximum allowed value of the impactor mass in units of the final mass of the planet. In the case of Neptune this value is $\sim 3.99 \times 10^{-2}$, and for Jupiter $\sim 1.136 \times 10^{-1}$ (see Figure 1). The values of the maximum mass and orbital velocity allowed for Saturn and Uranus are almost the same than the ones obtained for Jupiter, due to the similar present eccentricities of these planets.

3. CONCLUSIONS

Giant impacts have played an important role in planetary formation. Consequently, these impacts must be constrained by the present physical properties of the planets. Therefore, in the present work, we have used the present eccentricities of the giant

planets to set bounds on the masses and orbital velocities of large impactors. Considering an unique, inelastic impact, the upper limit on the impactor orbital velocity as a function of its mass was obtained (see Figure 1), being the maximum allowed mass to impact Jupiter, $\sim 1.136 \times 10^{-1}$, and in the case of Neptune, $\sim 3.99 \times 10^{-2}$ (in units of the final mass of each planet). The results for Saturn and Uranus are similar to that of Jupiter.

Our estimates of the largest allowed masses which impacted the outer planets are in good agreement with those obtained by Lissauer and Safronov (1991) through a very different method. Nevertheless they considered different cases, which are not exactly the same case we have considered in the present work. It is worth noting however, that in the case of Neptune and Saturn, our maximum allowed mass for a single impact fall just in same cases, on the upper constraint obtained by Lissauer and Safronov (1991). It should also be mentioned that the linear impulse received by a planet from large, discrete collisions has been computed through a somewhat different method, where it was found that the orbital eccentricities and inclinations of the planets apparently demand much smaller values of the mass ratio than the ones here obtained (Harris and Ward, 1982).

Some improvements are being examined, since we have simplified a three-body problem. It should also be noted, that in Eq.(1) we could have constrained $(\Delta e) \leq e$ intead of $(\Delta e)^2 \leq e^2$, since both relations are the same for a single impact. The effect caused by the distribution of planetesimals to impact the planets is being considered in the final version of this work which is in preparation to be submitted for publication. In this case, we have to constrain the dispersion in eccentricity $\langle (\Delta e)^2 \rangle \leq e^2$ caused by all the possible impacts.

Acknowledgements. We acknowledge the financial support of PROFOEG, CONICET, Argentina. M.G.P. kindly appreciate the collaboration of Dr. O. G. Benvenuto and she thanks the fellowship of the Universidad Nacional de La Plata, Argentina.

References

Brunini, A. 1993, *Plan. Space Sci.*, **41**, 747.

Harris, A. W., and Ward, W. R. 1982, *Annu. Rev. Earth Planet. Sci.*, **10**, 61.

Koricansky, D. G., Bodenheimer, P., Cassen, P., and Pollack, J. B. 1990, *Icarus*, **84**, 528.

Laskar, J. 1990, *Icarus*, **88**, 266.

Laskar, J., and Robutel, P. 1993, *Nature*, **361**, 608.

Lissauer, J. J., and Safronov, V. S. 1991, *Icarus*, **93**, 288.

Parisi, M. G., and Brunini, A. 1996, *Plan. Space Sci.*, in press.

Safronov, V. S. 1972, in *Evolution of the Protoplanetary Cloud and Formation of the Earth and the Planets, NASA TTF*, 677.

TIDAL BREAKUP OF ASTEROIDS BY THE EARTH AND MOON

DEREK C. RICHARDSON *Canadian Institute for Theoretical Astrophysics, Toronto, CANADA*
WILLIAM F. BOTTKE, JR. *Division of Geological and Planetary Sciences, California Institute of Technology, USA*

ABSTRACT. We report on preliminary results from simulations of the tidal breakup of "rubble pile" asteroids by the Earth and Moon. We find that both bodies can disrupt 2 g cm^{-3} asteroids and the outcome depends on various adjustable factors, including the encounter distance and velocity. The results of the completed study will have implications for the origins of such geological features as crater chains.

1. INTRODUCTION

The spectacular breakup of comet P/Shoemaker-Levy 9 by Jupiter's tidal forces in 1992 has fueled speculation that many small (few km) bodies in our solar system may be "rubble piles": loose collections of smaller component material held together by self-gravity (Asphaug and Benz, 1996). This idea is supported by Harris (1996), who found that none of the 107 small asteroids he examined rotate fast enough to be in a state of tension. Other evidence for rubble piles was found by Bottke and Melosh (1996), whose Monte Carlo simulations showed that fast rotating rubble pile asteroids encountering the Earth could be split into multiple co-orbiting components by tidal forces. By showing that this mechanism could produce binary asteroids, they were able to reproduce the observed fraction of doublet craters on the Earth, Venus, and Mars. We propose to extend this model by incorporating results from direct N-body simulations of the breakup process (code details in Richardson 1995). Our results should place important constraints on formation scenarios for doublet craters, binary asteroids, and crater chains.

2. INITIAL CONDITIONS

In the simulations, several hundred self-gravitating spherical particles are arranged in an elongated pile on an orbit that closely approaches the target body (either the Earth or the Moon). The encounter geometry for a typical run is illustrated in figure 1. A closeup of the disruption process in this example is shown in figure 2.

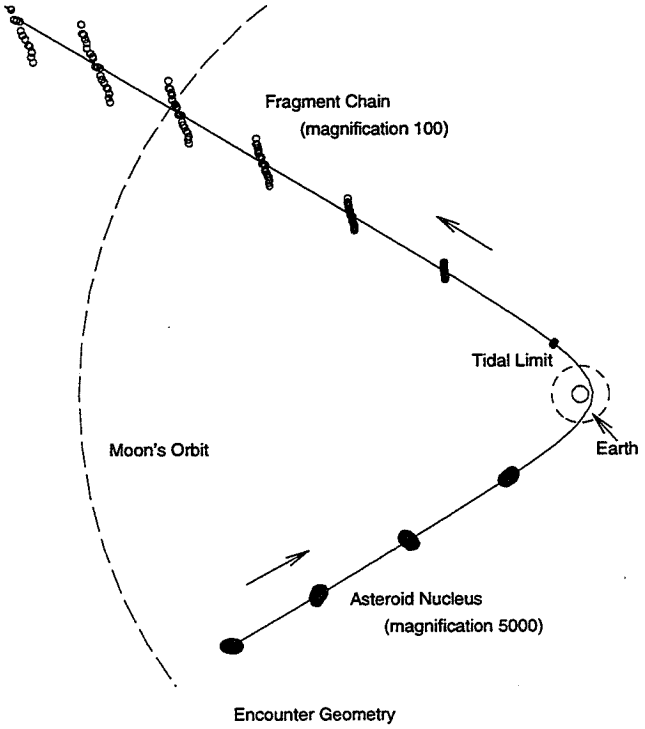

Figure 1. Orbit geometry of an asteroid encountering the Earth with periapsis $q = 1.5R_{\oplus}$ and velocity $v_{\infty} = 3$ km s^{-1}. The nucleus has a 6 h rotation. The orbit shown begins at a distance of 15 Roche radii from the Earth and takes 70 h to complete.

3. ENCOUNTER OUTCOMES

Figure 3 summarizes the possible encounter outcomes as a function of close approach distance and velocity for the asteroid shown in the previous figures. Other critical parameters that frequently determine the encounter outcome are the asteroid's shape, rotation period, obliquity, bulk density, and encounter orientation. Post-encounter statistics collected from the runs include the number of stable clumps formed, the mass and spin of each clump, and the osculating elements of the clumps and fragments with respect to the largest clump (usually near the train mass centre).

4. CONCLUSIONS

Both the Earth and the Moon can tidally disrupt rubble pile asteroids, resulting in reshaping, mass stripping, or catastrophic breakup, depending on the encounter parameters. One application of this study is a determination of the relative probability of crater chains occuring on the Earth and Moon. Early indications are that crater chains can occur on the Moon much more readily than on the Earth (Bottke, Richardson & Love, *Science*, in preparation).

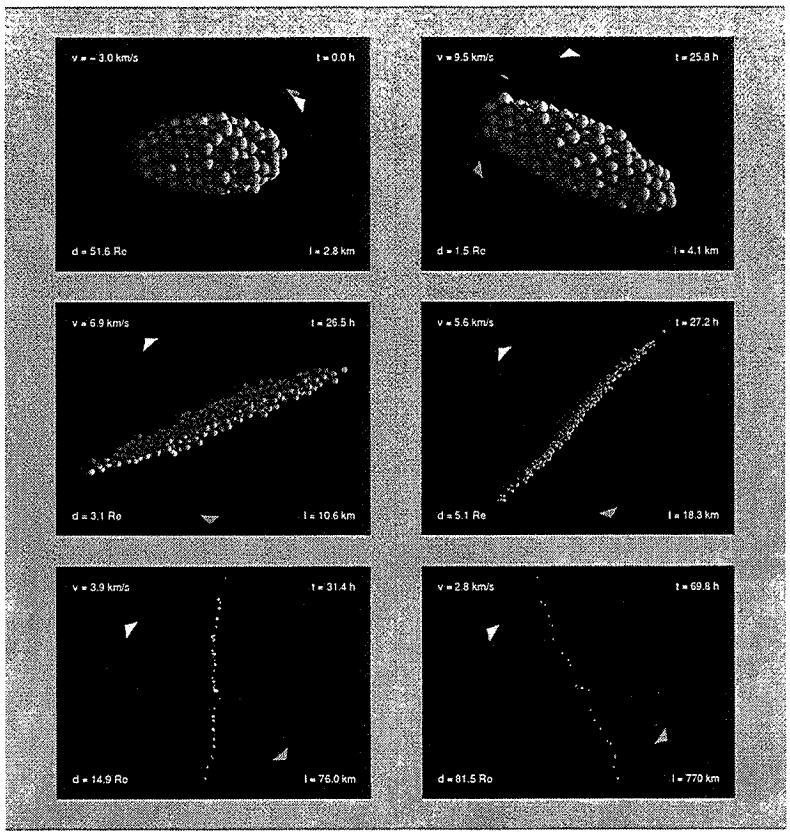

Figure 2. Time sequence showing the encounter of the $P = 6$, $q = 1.5$, $v_\infty = 3$ asteroid (previous figure) with the Earth. Axis ratios of 1.8:1.1:1.0 were adopted since most ECAs are elongated rather than spherical. The asteroid has a bulk density of 2 g cm^{-3} and is composed of 247 uniform spheres of radius 130 m and restitution coefficient 0.8. The bright triangle in each frame points in the direction of motion of the asteroid centre of mass; the dark triangle points to the Earth (in the plane of the orbit). In the annotations: v is the relative velocity with respect to the Earth (negative velocity indicates approach); t is the time since the start of the simulation; d is the distance to the Earth; and l is the length of the asteroid or fragment chain. The model shown undergoes SL9-type disruption into a "string of pearls".

References

Asphaug, E., and Benz, W. 1996, *Icarus*, **121**, 225.

Bottke, W. F., and Melosh, H. J. 1996, *Nature*, **381**, 51.

Harris, A. W. 1996, *LPSC*, **27**, 493.

Richardson, D. C. 1995, *Icarus*, **115**, 320.

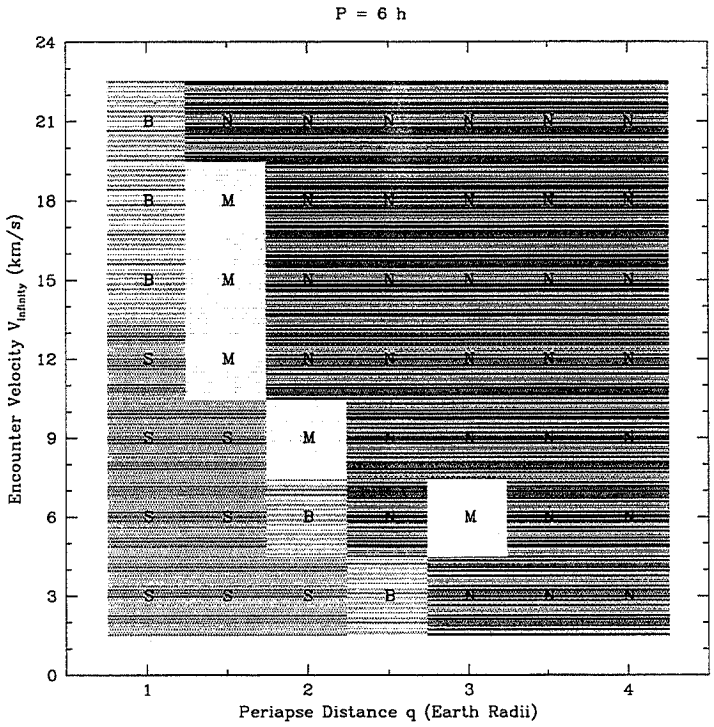

Figure 3. The q-v_∞ parameter space for the asteroid in the previous figures encountering the Earth. Outcomes for 49 runs are shown here: "S" indicates a catastrophic SL9-type disruption (formation of roughly equal size clumps into a "string of pearls" with the primary containing no more than 50% of the mass); "B" indicates significant mass shedding of clumps and/or particles (between 50% and 90% of mass left in progenitor); "M" indicates mild mass shedding of small fragments (at least 90% of mass left in progenitor); and "N" indicates reshaping of progenitor accompanied by spin-up or spin-down, or no effect (no mass loss). For faster spins the "S" region is larger; for slower spins it is smaller. For the Moon, SL9-type disruptions are restricted to a significantly smaller region ($\sim$ 50%) of q-v_∞ space compared to the Earth.

ON THE DYNAMICS OF THE ZODIACAL DUST CLOUD CLOSE TO THE SUN

K. SCHERER *Jet Propulsion Laboratory, Pasadena, California, USA*

I. MANN *Max-Planck-Institut für Aeronomie, Katlenburg-Lindau, Germany*

G. REAVES *University of Southern California, Los Angeles, USA*

ABSTRACT. We study the interplanetary dust cloud near the Sun – inside Mercury's orbit – with particular emphasis on the clouds out-of-ecliptic distribution. In addition to the Poynting-Robertson effect, we discuss the Lorentz force, the relativistic advance of the perihelion, and the perturbation of the gravitational potential due to the rotation of the Sun, and planetary perturbations.

1. INTRODUCTION

The observed over-all structure of the Zodiacal Dust cloud (ZD) between about 0.3 and 1.3 AU can be explained by the electromagnetic Poynting-Robertson (PR) effect which is caused by the radially symmetric solar radiation and explains the radial inward increase of dust density. The amplitude of the perturbation introduced by the plasma PR effect depends on the inclination, but does not cause a migration of the inclination (Banaszkiewicz et al. 1994, BFS). Assuming that the ZD is continuously refilled from the asteroid belt, the distribution of inclinations should be independent of the solar distance (Kneißel and Mann 1991). However, the spherical shape of the solar F-corona is inconsistent with the flat structure of the ZD and indicates, that there is a significant dust component above the solar poles. We study dynamically effects which can change the inclination of dust orbits in the solar vicinity. The perturbation of the inner Zodiacal Dust Particles (DP's) by PR effect as well as that by Mercury were discussed in Mann and Scherer (1995,1996). Close to the Sun the relativistic advances of the perihelion (RA) and internal oblateness of the Sun may become important. Furthermore, the Lorentz force (LF) acting on the DP can influence the motions of DP of sizes larger than 1 μm, because the number of revolutions between the magnetic field reversals of an 11-year solar cycle is large. We remark that because of the large mass of Jupiter, its perturbations inside 0.2 AU are larger than that of Mercury.

2. THE FORCES

In the following we give a short description of the different forces, which perturb the orbit of a DP. The PR forces are discussed elsewhere (e.g., BFS). The total force $\vec{F}_{tot}$

acting on a DP is the sum of the individual forces:

$$\vec{F}_{tot} = \vec{F}_K + \vec{F}_J + \vec{F}_M + \vec{F}_P + \vec{F}_R + \vec{F}_O + \vec{F}_L + \ldots \tag{1}$$

where the indices $\{K, J, M, P, R, O, L\}$ stand for the Kepler-force (two body problem), the perturbations of Jupiter and Mercury, PR effects, RA, oblateness of the Sun, and LF. The integration of the orbital equations was done by a vectorial method described in Scherer and Neutsch 1996, Neutsch and Scherer 1992.

2.1. The Poynting-Robertson forces

The action of the PR forces is to perturb the orbit of a DP in such a way that it spirals into the Sun:

$$\left\langle \frac{da}{dt} \right\rangle = -\frac{c_1}{a(1-\epsilon^2)^{3/2}} \left[c_2 + c_3\epsilon^2 + c_4 \, sin^2\imath \left(1 + \frac{3}{4}\epsilon^2 - \frac{1}{2}\epsilon \, cos\,\omega \right) + \ldots \right] \tag{2}$$

$$\left\langle \frac{d\epsilon}{dt} \right\rangle = -\frac{c_1\epsilon}{a^2(1-\epsilon^2)^{1/2}} \left[c_5 + c_4 \, sin^2\imath \left(\frac{7}{8} - \frac{1}{4} cos^2\omega \right) + \ldots \right] \tag{3}$$

$$\left\langle \frac{d\omega}{dt} \right\rangle = \frac{c_1 \, sin\,\omega \, \cos\,\omega}{4a^2(1-\epsilon^2)^{1/2}} \left[c_4 \, sin^2\imath + \ldots \right] \tag{4}$$

with the semimajor axis a, the eccentricity ϵ and the argument of the perihelion ω. The coefficients $c_i, i = 1, ..., 5$ are constants (for details see BFS). The inclination and the ascending node do not change under these forces. The time for a DP with radius s to spiral into the Sun - called the PR lifetime τ - is:

$$\tau = 7.04 \cdot 10^3 [years] \, \frac{a^2[AU^2] \, s\,[10\mu m]}{S\,[S_0]} \tag{5}$$

where S is the irradiation of the DP is measured in units of the solar constant S_0.

2.2. The Lorentz force

The solar dipole magnetic field imprinted in the solar wind propagates like a spiral and reverses its polarity after each 11 year solar cycle. The gradient of the perturbation depends on the polarity of the solar magnetic field and hence also changes sign after each solar cycle. It turns out that the magnetic drift is negligible for DP greater than $5\,\mu m$ orbiting the Sun with semimajor axis between $0.5\,AU$ and $5\,AU$, but becomes important for semimajor axis less than $0.1\,AU$. For a spiral magnetic field the perturbation equation can be written as (Scherer and Mann 1996):

$$\left\langle \frac{da}{dt} \right\rangle = 2 \, \frac{\omega_g \nu_\otimes r_0^2}{an} \, cos\,\imath \tag{6}$$

$$\left\langle \frac{d\epsilon}{dt} \right\rangle = \frac{\omega_g \nu_\otimes r_0^2}{a v_{sw}} \frac{1-\epsilon^2}{\epsilon} \cos i \tag{7}$$

$$\left\langle \frac{di}{dt} \right\rangle = \frac{\omega_g \nu_\otimes r_0^2}{a^2 \epsilon^2 n v_{sw}} \sin i \left[v_{sw}(1-\epsilon^2) \cos 2\omega - 2an\sqrt{1-\epsilon^2} \sin 2\omega \right] \tag{8}$$

$$\left\langle \frac{d\Omega}{dt} \right\rangle = -4 \frac{\omega_g r_0^2}{a^2\sqrt{1-\epsilon^2}} sig(\sin i) - \left\langle \frac{di}{dt} \right\rangle \tag{9}$$

$$\left\langle \frac{d\omega}{dt} \right\rangle = \left\langle \frac{d\Omega}{dt} \right\rangle (1 - \cos i) \tag{10}$$

where ω_g is the gyrofrequency of the DP, and $\nu_\otimes$ is the frequency of the solar rotation. The LF changes the inclination of the DP. But the magnetic field reverses the sign after one solar cycle, so that the inclination drift also changes direction. (The sign is hidden in the gyrofrequency.) The semimajor axis and the eccentricity do not change significantly. If the semimajor axis becomes so small, that the lifetime τ is less than the time between polarity changes, the evolution of the DP depends on the polarity, i.e. the motion of the perihelion is reversed.

2.3. The relativistic advance of perihelion

The gravitational potential of the Sun perturbs the argument of the perihelion. The General Relativistic treatment of this effect gives:

$$\left\langle \frac{d\omega}{dt} \right\rangle = \frac{6\pi GMn}{c^2 a(1-\epsilon^2)} = \frac{6\pi R_s}{a(1-\epsilon^2)} \tag{11}$$

where R_S is the solar Schwartzschild radius. Close to the Sun the changes of the perihelion becomes large during lifetime τ which affects the PR- and LF-forces, because they are functions of ω. Thus the RA is important in its indirect influence on other forces, but it does not change the inclination.

2.4. The oblateness of the Sun

Because the Sun is a gaseous ball and most of its mass (about 90%) is in the inner 10% of its radius, the dynamical flattening of the Sun cannot be determined by measuring the flattening of the visible solar disk. With the methods of helioseismography and with satellite observations one can determine the dynamical form factor as $J_2 = 7.710^{-6}$ (Hill et al. 1982). Moreover, the oblateness effects only:

$$\left\langle \frac{d\omega}{dt} \right\rangle = \frac{3}{2} J_2 \frac{nR^2}{a^2(1-\epsilon^2)^2} \left(3\cos^2 i - 1\right) \tag{12}$$

$$\left\langle \frac{d\Omega}{dt} \right\rangle = -\frac{3}{2} J_2 \frac{nR^2}{a^2(1-\epsilon^2)^2} \tag{13}$$

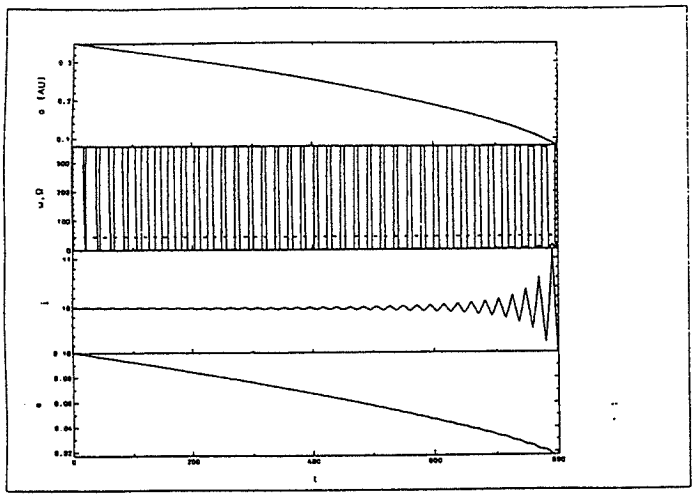

Figure 1. The evolution of a dust particle from top to bottom: The semimajor, the argument of the perihelion and the ascendig node, the inclination, and the eccentricity. The time is in years. The initial values are: $a = 0.35\,AU$, $e = 0.1, i = 10°, \omega = 45°, \Omega = 0°, s = 10\mu m$

where R is the solar radius. Hence, like the RA, it interacts also indirectly with other forces. Because the amplitude of the perturbation is proportional to R^2/a^2 which is < 1 the effects are insignificant; in our calculations they are neglected.

3. DISCUSSION AND CONCLUSION

The combinations of the planetary perturbations by Jupiter, Mercury, the Poynting-Roberston effect, the Lorentz force, the relativistic advance of the perihelion and the solar oblatness are discussed. We find that these perturbations cannot change an initial flat distribution of intra-Mercurial dust particle orbits into the observed spherical distribution. The most likely explanation of the spherical distribution of the DP orbits is thus not an asteroidal but a cometary source. If this is indeed correct, then further study of the properties of the DP's would give us inside into the frequency and properties of comets in polar orbits.

References

Banaszkiewicz, M., Fahr, H.J., Scherer K. 1994, *Icarus*, **107**, 358.

Kneißel, B., Mann, I. 1991, in *Origin and Evolution of Interplanetary Dust*, eds. A. C. Levasseur-Regourd and H. Hasegawa, (Dordrecht: Kluwer) p. 139.

Hill, H.A., Bos, R.J., Goode, P.R. 1982, ApJ **49**, 1794

Mann, I., Scherer, K. 1995, Eos Trans. AGU, 76 (46), Fall Meet. Suppl., F338.

Mann, I., Scherer, K. 1996, Eos Trans. AGU, 77 (17), Spring Meet. Suppl., S218.

Neutsch, W., Scherer, K. 1992, Celestial Mechanics, Bibliographisches Institut, Mannheim

Scherer, K., Mann, I. 1996, submitted to JGR.

Scherer, K., Neutsch, W. 1996, in: Completing the Inventory of the Solar System, ed.: T. Rettig in press

DUST AND SPUTTERED PARTICLE STREAMS IN COMETARY ATMOSPHERE

STANISLAV B. SVIRSCHEVSKY *Moscow State Aviation Institute-Technical University 4 Volokolamskoye shosse, Moscow, 125871, Russia*

ABSTRACT. Dynamics of dust particles in a comet atmosphere was investigated using Monte - Carlo simulation method taking into account radiation and gravitational forces applied to the particles. The model distribution function found out in VEGA experiments was chosen for calculations. Dust particles with masses more then 10^{-10} g were considered. The delay effect for the big mass particles is shown. In this paper the boundary distribution function for sputtered particles drifting off the surface was determined using Nochilla's model. General dependences for the normal component of the relative mass velocity of sputtered particles are given as the function of particle energy normalized by Tomas-Fermi energy.

1. INTRODUCTION

Some of the sources of a space dust are comets, asteroids and other small celestial structures. Knowledge of the dust particle distribution function over the masses allows to formulate strict mathematical definition for the calculation of the space dust particle streams.

Investigation of the comet P/Halley allowed to receive the data of dust distribution over the comet nucleus (Rijov *et al.*, 1989). As follows from FOTON experiments, the values of distribution function measured on the space station's trajectory can defer from mean values defined for whole dust atmosphere of the comet. This phenomena could be explained by delay effect of the heavy particles. The effect persist because the mean motion time of particles from comet nucleus till cross point with VEGA has the same order as the characteristic time of the comet activity. Calculations show that time interval between particle emission and registration on a craft trajectory increases with increasing of particle masses.

2. MODELING OF DUST STREAMS IN COMETARY ATMOSPHERE

Let us consider dust particles leaving the comet nucleus. The particle moves with velocity V_*, directed with angle θ (figure 1 a). Two forces are applied along the axis O1Y1: the gravitation to the Sun F_s and the Sun pressure F_p. After a time t a particle will be situated at the distance: $X1 = t*V_**sin(\theta)$, $Y1 = t*V_**cos(\theta) - gt^2/2$, where g is the resulting acceleration. Then one could find: $Y1_{max}(\theta) = V_*^2 cos^2(\theta)/2g$. It is known that $Y1_{max}(\theta = 0) = V_*^2/2g = 4.5\times10^4$ km (Rijov *et al.*, 1989). Consequently, the maximal value of angle θ_*, with which a particle starts from the nucleus and

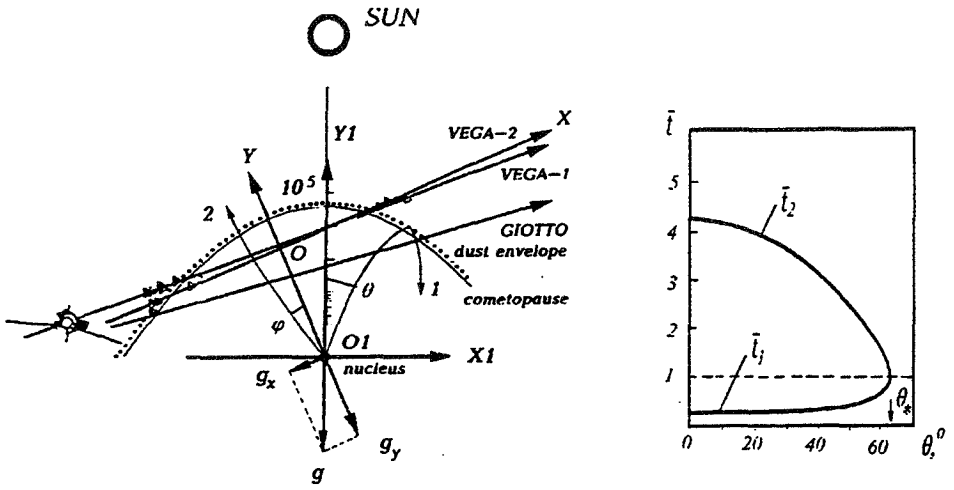

Figure 1. Parameters for dust stream calculations: a) model of the dust particles motion, b) normalized time of particle movement as a function of particle's start angle

reaches the spacecraft trajectory is equal to 63° 20′ (VEGA-1) and 65°(VEGA-2). From motion equation follows that the boundary of dust envelope from the axis O1X1, is situated at the distance equal to $X1_{max} = V_*^2 cos(\theta) sin(\theta)/g$ (3.57×10^4 km for VEGA-1 and 3.45×10^4 km for VEGA-2). For definition the motion time for particle of class a_* (a_* is the radius of particle) let us consider equation for $Y1$ and found, that $L_* = cos(\theta) \pm (cos^2(\theta) - Y1_0/Y1_a)^{1/2}$. Here:$L_* = V_* t/2Y1_a$; $Y1_0/Y1_a$ = 0.198, because $Y1 = Y1_0$ at $Y1_0 = R_0$ (R_0 = 8912 km (VEGA-1)); $Y1 = Y1_a$ at $Y1_a = (V_*^2/2g) = 4.5{*}10^4$ km. This expression shows, that particles (in the angle range from 0 till θ_*) crosses the spacecraft trajectory twice, being under overcoming action of F_p. Its motion time can be defined from the expression:

$$t_i = 2Y1_a L_{*i}/V_* = t' L_{*i},\ [day],$$

here i=1,2; V_* =1081 / $(\rho * a_*)$ cm/sec; $\rho \simeq$ 1 g/cm^3; t′ = 12.96 for biggest particles fixed by FOTON-1 with the mass $m_* = 2.51\times10^{-5}$ g and t′ = 3.15 for smallest particles with mass 5.15×10^{-9} g. The computational results for different θ are shown at figure 1 b in form of $\bar{t} = t_i(\theta)/t_i(\theta_*)$ for pointed values of mass. Calculations show strong delay (from 1 to 24 days) for particles with big masses. Real measurements confirm numerical results, because at minimal flight distance from the comet nucleus the only particles with small masses were registered.

Numerical modeling of dust particle streams with $m_* \geq 10^{-10}$ g was based on the Monte Carlo method. The dust leaves the comet nucleus (point-source) with fixed particle distribution $f_* = A_*(R) a_*^{-u}$. The sign of resulting acceleration of particles depends of relation F_p/F_s. If a_* is small (light particles) and $F_p > F_s$ then these particles cross the craft trajectory twice ($g > 0$, see trajectory 1 on figure 1 a). Heavy particles cross the trajectory once and move to the Sun ($g < 0$, see trajectory 2 on figure 1 a).

As follows from the motion equation of a particle leaving the nucleus with angle

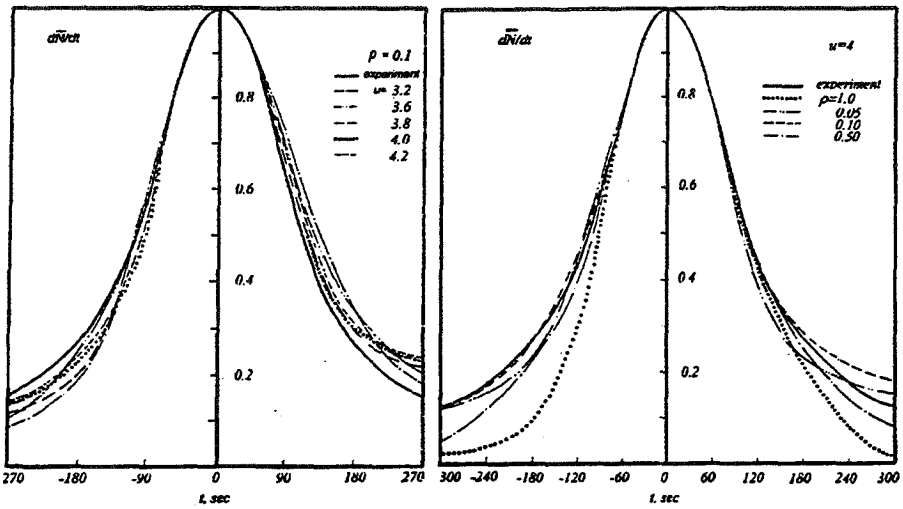

Figure 2. Comparison of the experimental and modeled dust fluxes

ϕ the coordinates of such particle is:

$$X = -tV_* \sin(\phi) - g_x t^2/2,\ Y = tV_* \cos(\phi) - g_y t^2/2.$$

Coordinates X,Y could be calculated using time interval (between start and crossing the craft trajectory) $t_{1,2} = (V_* \cos(\phi) \pm (V_*^2 cos^2(\phi) - 2R_0 g_y)^{1/2})/g_y$. The craft trajectory was devided into 60 sections in order to calculate particle distribution along this trajectory. The probability of present the particle of a_* class in the dust stream for chosen f_* is defined as follows:

$$\eta = \frac{M_*(a, a+da)}{M_*(a_{min}, a_{max})} = \frac{a_{j+1}^{-u+3.5} - a_j^{-u+3.5}}{a_{max}^{-u+3.5} - a_{min}^{-u+3.5}},\ M_* = \frac{8}{3} 1081 \pi^2 \rho^{1/2} A_*(R) R^2 \frac{a_{max}^{-u+3.5} - a_{min}^{-u+3.5}}{-u+3.5},$$

here: $a_{min} = 6{\times}10^{-4}$ cm; $a_{max} = 3{\times}10^{-2}$ cm. The part of particles from chosen interval of particle radia from a_j till $a_{j+1} = a_j + da$ was defined as $N_{a_j, a_{j+1}} = \eta N$, where N is total number of particles involved into statistical modeling. The relative error of modeling at N=10000 does not exceed $\pm$ 2.5 - 5 %.

Normalized dependencies $d\bar{N}/dt$ are shown on the figure 2 as function of time. Line 'experiment' corresponds to average flux of particles $d\bar{N}/dt$ from the flight experiment FOTON. Numerical simulation satisfied them at ρ = 0.1 - 0.5. Some other experiments show that particles with $m_* > 10^{-12}$ g are the particles with low density and complex structure. Figure 2 shows that results numerical calculations are close to experimental distribution of flux of particles with u close to 4. Average value of u is 3.58 for the whole fly trajectory of VEGA-1.

3. BOUNDARY DISTRIBUTION FUNCTION OF SPUTTERED PARTICLES

Sputtering particle fluxes could be calculated if corresponding moment of the boundary distribution function is found. The important astrophysical task is a definition of

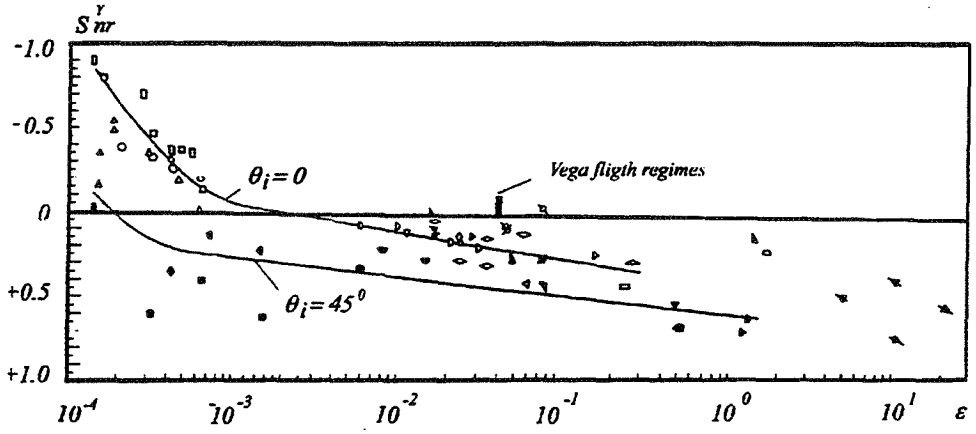

Figure 3. Normal component of relative speed of sputtered particles as a function of the reduced energy

the boundary distribution function of particles during the sputtering process. One of the perspective direction for restoring of the parameters of such interaction is application of the modeling functions and experimental data for indices of the sputtered mass fluxes. The boundary distribution function for sputtered particles drifting off the surface was determined using Nochilla's model $f_N = n_N \pi^{-3/2} \beta_n^{-3} exp[-(\xi_r - U_N)^2 \beta_N^{-2}]$ (Svirschevsky, 1993). Here: $n_N; \beta_N = (2RT_N)^{1/2}; S_N = U_N/\beta_N; \theta_N = (\bar{U}_N; \bar{n})$ are four parameters characterizing the concentration, temperature, value and direction of the velocity of sputtered particles. These parameters could be found from conservation law on the boundary. The particles fluxes conservation law allows to defined the coefficient of sputtering Y. The experiments show that this coefficient depends from the relative energy for different atom-target combinations (Rijov *et al.*, 1989) $\epsilon = E_i/E_{TF}$. The normal component of sputtered particles $S^Y_{nr} = S_N \sin\theta_N$ and angle of start θ_N could be defined as a function of relative energy. These values were defined by processing of experimental indices of mass fluxes. The sputtering of materials with different mass from Pb till C were considered Different incoming ions were used (from H till Hg). As the result the general expression for the normal component of relative mass velocity of sputtered particles was determined as a function of relative energy and angle of incidence θ_i. Such parameters allows to defined final expression for distribution function of sputtered particles.

The research was made possible in part by Grant N 2V300 from the ISF.

References

Rijov Yu.A., Svirschevsky S.B. and Kuzovkin K.N. 1989, in *Rarefied Gas Dynamics: Space-Related Studies*, eds. by E.P. Muntz *et. al.*. Progress in Asronautics and Aeronautics, **116**, AIAA, Inc., p. 23.

Svirschevsky S.B. *et al.*, 1993, *Aerohydrodynamics.* (Mashinostroenie, Moscow), p. 452.

PRELIMINARY RESULTS OF OBSERVATIONS OF COMETS DE VICO AND HYAKUTAKE BY THE ULYSSES COMET WATCH NETWORK

C.C. PETERSEN, J.C. BRANDT, Y. YI *Laboratory for Atmospheric and Space Physics University of Colorado, Boulder, CO, USA*

Cometary interactions with the solar wind allow us to use comets as probes of the inner regions of the heliosphere. During their close passage to the Sun, comets are exposed to different environments depending on their latitude (Brandt, Petersen and Yi, 1996). Until recently, characterizing these environments has been difficult because most spacecraft studying the sun have been confined to studying its mid-latitudes.

A valuable source of information about the differing regimes of the solar wind is the joint ESA/NASA ULYSSES mission, which is the first spacecraft to explore the polar regions of the heliosphere. In 1995, ULYSSES' orbit covered a range of solar latitudes from -80 degrees to +80 degrees – an interval referred to as the 'fast latitude scan' (Smith and Marsden, 1995.)

The Ulysses Comet Watch incorporates in-situ measurements during these periods by the ULYSSES spacecraft with images contributed by a world-wide network of observers (both amateur and professional). Bright comets whose paths come within 20 degrees solar latitude of the spacecraft are considered especially good targets for correlation between spacecraft data and plasma tail activity.

Ulysses findings of interest to cometary plasma research are:

Verification of global differences in solar wind properties (speed and density) at different solar latitudes. At polar latitudes – ranging from roughly ±30 degrees to ±80 degrees – the solar wind speed is about 750 kilometers/sec, and has a proton density (1 AU) around 3 cm^{-3}. Changes in properties are small and the heliospheric current sheet (HCS) is not seen.

In the equatorial latitudes (roughly +30 to -30 degrees), the average solar wind speed is about 450 kilometers/sec, with an average proton density (at 1 AU) around 9 cm^{-3}. The HCS is seen and changes in properties can be large. An object, spacecraft or comet, at a given latitude, can be entirely in the polar, entirely in the equatorial, or can experience both – sort of a transition region.

1. COMETS AND THE SOLAR WIND

Comets have often been described as 'natural' solar wind probes, due to the nature of their interaction with the solar wind. The plasma tails act as "wind socks", giving

observers information on the conditions of the solar wind at the location of the comet. Plasma (or ion) tails are composed of an electron/ molecular ion plasma, threaded by a magnetic field. The comet's interaction with the solar wind captures the magnetic field from the wind by "loading" the field lines with heavy ions. The loaded field lines near the comet slow down, while the field lines from the comet continue to travel away from the sun at a typical solar-wind speed (equatorial) of approximately 450 kilometers/sec. The lines form a roughly hair-pin shaped magnetic structure around the comet. Ionized molecules trapped on the field lines fluoresce sunlight, revealing the plasma tail.

Cometary plasma tails change constantly due to their interactions with the solar wind. The most dramatic changes in plasma tails are called disconnection events (DEs) – when the tail attachment to the comet's ionosphere is severed. The entire plasma tail comes off and drifts away. A new tail forms immediately. The probable cause for the disruption is magnetic reconnection occurring on the sunward side of the comet when it crosses the HCS (where the polarity of the solar-wind magnetic field reverses). It is important to note that we would expect DEs only in the equatorial or transition regions of the solar wind.

2. COMET DE VICO (P/122)

The Ulysses Comet Watch is correlating network images of Comet de Vico with ULYSSES solar wind data. Because of its relatively high-inclination orbit (i=85.3 degrees), de Vico sampled a wide range of solar latitudes, and its plasma tail showed a variety of effects. At least three disconnection events were observed on or around September 27, October 1 and October 5, 1995, and these dates correspond quite well with the dates of the comet crossings of the heliospheric current sheet.

The appearance of the comet's plasma tail shows differences with latitude. On 1 October 1995, the comet was at +0.1 degrees latitude, and on October 5, it appeared at +10.3 degrees latitude. Streamers and ray structures are easily seen.

At high heliocentric latitude on 18 September 1995 (at -29.3 degrees), and on 10 October, 1995 (at +23.1 degrees), the plasma tail of the comet, while showing some activity, does not display the streamers or fine structure normally associated with the active plasma tail in the mid-latitudes. More images are being correlated with solar wind data to confirm these findings.

3. COMET HYAKUTAKE

Comet Hyakutake (1996 B2) provided the network with an extended period of observations of a bright comet. Hyakutake, like the ULYSSES spacecraft and comet de Vico, follows a high-inclination orbit (i=124.9 degrees), and also sampled a wide variety of solar wind regimes. More than 100 images have been received. The comet showed a highly-active plasma tail, and a spectacular disconnection event was clearly seen on March 25.3. Continued study of these and additional images should provide further confirmation of the connection between plasma tail activity and position of the comet in the various regimes of the solar wind.

4. ULYSSES COMET WATCH NETWORK

In 1992, the Ulysses Comet Watch network was initiated as a way to gather comet images suitable for correlation with Ulysses' in-situ measurements of the solar wind, particularly when the spacecraft was at high solar latitudes. If successful, comets could be used as calibrators of high-latitude solar winds, as well as the mid-latitudes.

Currently observers are kept informed of upcoming comets through email exploder lists, a printed newsletter, and messages on the Internet and CompuServe astronomy-related areas.

The Network's approach to date has been to gather data on appropriate comets and correlate that data with available solar wind information from a variety of sources, including the ULYSSES spacecraft data.

Observers wishing to contribute images to the network should contact the authors at the addresses below:

Ulysses Comet Watch
Laboratory for Atmospheric and Space Physics
Campus Box 392
University of Colorado
Boulder, CO 80309

email: brandt@orion.colorado.edu
petersen@orion.colorado.edu

References

Brandt, J.C., Petersen, C.C., and Yi, Y. 1996, Comet de Vico (P/122) and Latitude Variations of Plasma Phenomena, presented at Asteroids, Comets, Meteors, Versailles, France.

Brandt, J.C., Randall, C.E., Yi, Y., Snow, M. Initial Overview of Disconnection Events in Halley's Comet 1986, in *Asteroids, Comets Meteors*, ed. A. Harris, T. Bowell, (Houston, LPI), pp. 93-96.

Smith, E.J., Marsden, R.G. 1995, Ulysses Observations from pole-to-pole: An introduction, *Geophys. Res. Lett.*, **22, No. 23.**

Yi, Y., Walker, R.J., Ogino, T., Brandt, J. C., 1996, Global Magnetohydrodynamic Simulation of a Comet Crossing a Heliospheric Current Sheet, *J. Geophys. Res. - Space Physics*, in press.

Yi, Y., Caputo, F.M., Brandt, J.C. 1994, Disconnection Events (DEs) and Sector Boundaries: The Evidence from Comet Halley 1985-1986, *Planet. Space Sci.*, **42**, 705-720.

(Sources of Ulysses material: The Ulysses Mission Bulletin No. 6, August 1995; The Ulysses Home Page: http://ulysses.jpl.nasa.gov)

POROSITY AND PERMEABILITY OF CHONDRITIC MATERIALS

MICHAEL E. ZOLENSKY *NASA Johnson Space Center, Houston, TX 77058 USA*
CATHERINE M. CORRIGAN *Lunar and Planetary Institute, Houston, TX 77058 USA*
JASON DAHL *Bemidji State University, Bemidji, MN 56601 USA*
MICHAEL LONG *Core Laboratories, Houston, TX 77040 USA*

ABSTRACT. We have investigated the porosity of a large number of chondritic interplanetary dust particles and meteorites by three techniques: standard liquid/gas flow techniques, a new, non-invasive ultrasonic technique, and image processing of backscattered images . The latter technique is obviously best suited to sub-kg sized samples. We have also measured the gas and liquid permeabilities of some chondrites by two techniques: standard liquid/gas flow techniques, and a new, non-destructive pressure release techn ique. We find that chondritic IDPs have a somewhat bimodal porosity distribution. Peaks are present at 0 and 4% porosity; a tail then extends to 53%. These values suggest IDP bulk densities of 1.1 to 3.3 g/cc. Type 1-3 chondrite matrix porosities ra nge up to 30%, with a peak at 2%. The bulk porosities for type 1-3 chondrites have the same approximate range as exhibited by matrix, indicating that other components of the bulk meteorites (including chondrules and aggregates) have the same average porosity as matrix. These results reveal that the porosity of primitive materials at scales ranging from nanogram to kilogram are similar, implying similar accretion dynamics operated through 12 orders of size magnitude. Permeabilities of the investiga ted chondrites vary by several orders of magnitude, and there appears to be no simple dependence of permeability with degre

1. INTRODUCTION

Interplanetary dust particles (IDPs) and chondritic meteorites of low petrologic grade (1-3) are believed to derive from within or just below the regoliths of comets and undifferentiated asteroids, and carry important records of such processes as grain ac cretion, regolith compaction, aqueous alteration and freeze-thaw cycles. Integral to the study of these diverse processes are the concepts of porosity and permeability.

IDPs constitute an extremely important source pool of extraterrestrial material for study, especially since they provide a broader sampling of material than meteorites, having accreted at such a wide range of distances from the sun, as well as being less biased (with respect to source) than conventional meteorite samples (Brownlee, 1994). Consequently, IDPs represent the only samples we have of comets and Kuiper Belt objects, and, theoretically, sample all asteroids. Chondritic meteorites, though provi

ding a biased sample of asteroids, are available in large specimens of more convenient size and possibly provide a more representative sampling of the few asteroids from which they derive.

There are a number of time-proven methods for determining porosity in a bulk sample, and actual physical liquid/gas flow measurements work quite well in samples large enough to test in this manner. These techniques have been applied to numerous ordinary chondrites, irons and a few carbonaceous chondrites (see Corrigan et al., 1997, for references). However, these techniques are not applicable to IDPs or to the extremely small samples obtainable from most meteorites, and cannot be applied to components o f meteorites like matrix, chondrules or dark inclusions. Thus, up to this point, there has been no reliable method for accurately determining porosity in IDPs, and expected porosity values have been largely estimated. It has been suggested that the poro us, anhydrous chondritic IDPs have porosities which are much higher than those seen in meteorites, and that typically exhibit porosities of 20

By utilizing scanning electron microscope images and computer image processing, we have developed a method by which sample porosity may be determined both efficiently and accurately for nanogram-sized samples, and have applied this technique to chondritic interplanetary dust particles (IDPs), and the matrix and other components of carbonaceous chondrites and unequilibrated ordinary chondrites.

We have also investigated the porosity of a large number of chondritic meteorites by new, non-invasive ultrasonic techniques as well as two by standard liquid/gas flow techniques. Finally, we have measured the gas and liquid permeabilities of some chond rites by a new, non-destructive technique.

With these new data we hope to provide new constraints of the critical processes of grain accretion, regolith compaction, aqueous alteration in the early Solar System.

2. ANALYTICAL PROCEDURE

The chondrites involved in this project included a full range of carbonaceous (CV's, CM's, CI's and CR's) and ordinary chondrites. These were collected all over the world as finds or falls, many coming from Antarctica. In sampling these, we took portion s from matrix, rims and dark inclusions to obtain information on diverse types of material generally composing a chondritic meteorite. The IDP's used in this project were collected in the stratosphere using aircraft equipped with special collector surfac es, and are curated at NASA's Johnson Space Center. A standard was developed using the Allende meteorite using conventional liquid/gas flow techniques; we used this standard in all of the following procedures of measuring porosity and permeability as de scribed below.

We note here that we performed multiple analyses of each sample by every technique applied, and that only average values are presented in the tables, figures and discussion.

The CV chondrite Allende and CM2 chondrite Murchison (available in large samples) were investigated using standard liquid/gas flow techniques at CORE Labs. For this analysis, 2.5 cm diameter core samples were taken, using liquid nitrogen as the cooling agent. The cores were then immersed in mercury and various gases depending upon the analysis being performed. The core of Murchison broke during extraction (probably owing to the presence of numerous fine cracks, which would be expected

from the dessi cation of such a "wet" chondrite), which prevented analysis of permeability in this case. However, we successfully obtained high quality porosity data for both meteorites, and permeability data for Allende. A fine-grained rock sample with consistent, independently well-determined porosity (Berea Sandstone, 23% porosity) was also obtained from Core Laboratories, and used as a standard to test our methods. Measurement of the porosity of this material by all of the other techniques we used showed relative errors of 15% or less. Therefore, we are confident that all of the various methods we used to measure porosity work well.

For determining porosity of IDP's and small pieces of meteorites, the following procedure was developed and used. The samples, ranging in size from 10 to 100 microns, were mounted on epoxy blocks and impregnated with EMBED-812 low viscosity epoxy and cu red in an oven after which thin sections were sliced away using an ultramicrotome with a diamond knife. The remaining polished, planar surfaces of the samples were then available for our examination. We assume that the sample is fairly homogeneous, and t hat slicing through a random plane will allow us to obtain a sample well-representative of the entire meteorite. After preparing the samples, a JEOL 35-CF scanning electron microscope (SEM) was used to collect backscattered electron (BSE) images of each particle at 13 kV. We determined this to be the optimum voltage to minimize the interference of epoxy below the sample, which, when visible, reduced pore space. Next, these images were taken to the Video Digital Analysis Systems (VDAS) laboratory and dig itized. This image was then processed using the NIH Image image processing program to compute porosity, where porosity corresponds to the percentage of black pixels within the selected area. Complete details of this procedure are given in Corrigan et a l. (1997).

For larger samples, we used a new technique, the PSP (porosity sonic profile) 300 instrument, developed by Core Laboratories. This procedure, developed for the petroleum industry, involves sending microsonic waves through the sample and is completely non -destructive. No sample preparation is necessary. The process involves 2 probes, one a transmitter and one a receiver, which are placed 6.2 cm apart on the sample. A microsonic signal is sent through the sample between the probes, and the arrival times of the compressional and shear waves are measured. We used a glass standard to calibrate the porosity data. We were unable to obtain any useful data for CM chondrites; we believe this to be due to the fact that there are ubiquitous cracks (caused by de ssication). This result was consistent with the previous experience of Core Lab employees.

Permeabilities of bulk meteorites were also measured using another of Core Lab's instruments, the Pressure-Decay Profile Permeameter (PDPK-200). This technique is also non-destructive, but requires the presence of a flat surface. In this analysis, a s mall (approximately 1 cm) O-ring connected to a nitrogen gas line descended from the instrument. A seal with the o-ring is made, and an aliquot of nitrogen gas fills the line under a set pressure. The nitrogen then bleeds away through the sample, and th e rate of loss determines the permeability of the meteorite. We used the standard Allende sample to verify that this technique was operating correctly.

3. POROSITY MEASUREMENTS OF CHONDRITIC IDPS

The results of our measurements 33 different chondritic IDPs are somewhat surprising. When compared to porosity in carbonaceous and ordinary chondrite meteorites, IDPs do not seem to show the significantly higher porosities that had been expected. As sh own in Figure 1, chondritic IDPs have a somewhat bimodal porosity distribution.

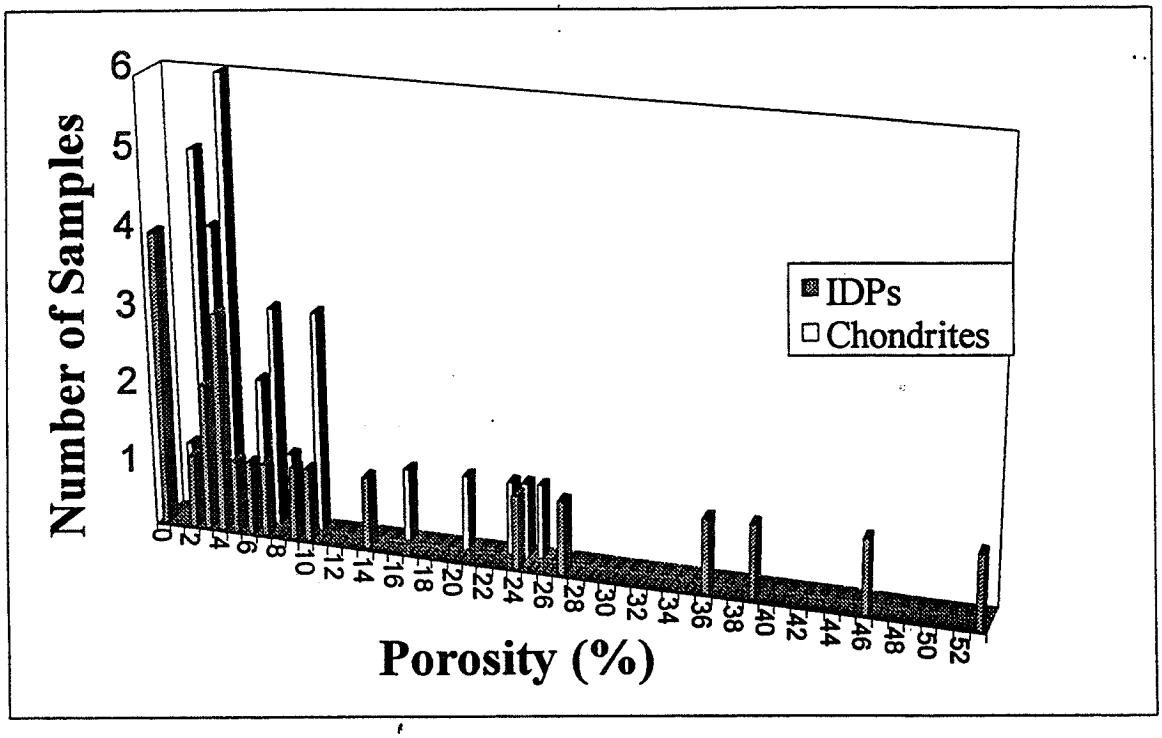

Figure 1. Porosities of Chondritic IDPs and Chondrite Meteorites

Peaks are present at 0 and 4% porosity; a tail then extends to 53%. In fact, these results appear to basically overlap with chondrite meteorite porosities, as measured by bulk analysis methods (C = 1-26%, H = 2-18%, L = 3-20%, LL = 7-16%) (Corrigan et al., 1997; this paper). However, until further investigation our measured porosities should be considered lower estimates, since some IDPs should have broken along large pore walls during stratospheric capture, yielding smaller apparent measured porosities for the resultant pieces. Relatively few IDPs have been examined, therefore, a great deal of work remains. These values suggest IDP bulk densities of 1.1 to 3.3 g/ cc.

4. POROSITY MEASUREMENTS OF CHONDRITE MATRIX

Matrix porosities for ordinary chondrites range from 2 to 10%. Within the carbonaceous chondrites, CV3 chondrite matrix ranges (6 meteorites) from 1 to 30%. CR2 chondrite matrices (2 meteorites) have porosities ranging from 2 to 14%, with a modal val ue of 3%. Matrices of CM2 chondrites (7 meteorites) range between 2 and 25%, with a modal value of 2%, and CI1 (2 meteorites) chondrite matrices have porosites ranging from 4 to 5%. The porosity measurements for UOC's are reasonable when compared wi th literature values, and similar to those for carbonaceous chondrites. In summary, type 1-3 chondrite matrix porosities range up to 30%, with a peak at 2%. By comparison, IDP porosities range from 0-53% and the mode is at 4%.

5. POROSITY MEASUREMENTS OF BULK CHONDRITES

Bulk porosities for CV3 chondrite (6 meteorites) from 2 to 24%. The one bulk CM2 chondrite we analyzed (Murchison) has a value of 23%. The one bulk CO3 chondrite we analyzed (Isna) has a value of 4%. In general, these bulk values have the same range as exhibited by matrix, indicating that other components of the bulk meteorites (including chondrules and aggregates) have the same average porosity as matrix, which could explain the widespread alteration observed in these chondrite components. Most of the bulk porosity values are at values less than 10%, similar to chondritic IDPs and chondrite matrix.

6. PERMEABILITY MEASUREMENTS OF BULK CHONDRITES

Permeabilities of the investigated chondrites vary by several orders of magnitude, from 0.001 to 2 mdarcies. There appears to be no simple dependence of permeability with degree of aqueous alteration, or chondrite type. For example, the least permeable chondrites are those that show a low but significant degree of aqueous alteration.

7. CONCLUSIONS

We have discovered that the porosities of the most primitive chondrites (CO3 and reduced CV3: Isna, Leoville, Vigarano and Efremovka, see Brearley 1993; Krot et al., 1995) are in the range 1-7e for chondritic IDPs (see figure 1). This means that the porosity of primitive materials at scales ranging from nanogram to kilogram are similar, implying similar accretion dynamics operated through 12 orders of size magnitude.

With the data now collected for IDP's, carbonaceous and ordinary chondrites, we can better conduct 3-D numerical modeling of the fluid flow and attendant alteration that occurred within the hydrous parent asteroids, also permitting the determination of ra tes and temperatures of alteration. We can also follow how fluid flow affected the porosity and permeability of the body, alternately increasing it by dissolution or decreasing it by deposition.

We know that the chondrite meteorites originated at 5 AU from the Sun, and can measure the constituent grain size distribution. With this information in hand porosity data should ultimately shed new light on processes occurring as dust settled to the so lar mid-plane and began to clump into the seeds of planetesimals.

Acknowledgements. Glenn MacPherson, Linda Schramm (both NMNH), Michael Weisberg, Marty Prinz (both AMNH), and Tomoki Nakamura provided critical samples. This research was supported by the Origins of Solar Systems Program.

References

Brearley, A.J. 1993, in *Geochimica et Cosmochimica Acta*, **57**, p. 1521.

Brownlee, D. 1994, in *Analysis of Interplanetary Dust Particles. AIP Conference Proceedings 310*, eds. Zolensky, M.E., Wilson, T.L., Rietmeijer, F. and Flynn, G., (AIP), p. 5.

Corrigan, C.C., Zolensky, M.E., Dahl, J., Long, M., Weir, J. and Sapp, C. 1997, in *Meteoritics and Planetary Science*, **32**, in press.

Krot, A.N., Scott, E.R.D. and Zolensky, M.E. 1995, in *Meteoritics*, **30**, p. 748.

RAMAN SPECTRUM OF QUENCHED CARBONACEOUS COMPOSITE

S. WADA *University of Electro-Communications, Chofu-shi, Tokyo, Japan*
S. HAYASHI *University of Kobe, Kobe-shi, Hyogo, Japan*
H. MIYAOKA *University of Electro-Communications, Chofu-shi, Tokyo, Japan*
A. T. TOKUNAGA *Institute for Astronomy, Univ. of Hawaii, Honolulu, HI, USA*

ABSTRACT. Quenched Carbonaceous Composites (QCCs) are products from the ejecta of a hydrocarbon plasma. Two types of QCC, dark QCC and thermally-altered (heated) filmy QCC, have been shown to have a 220 nm absorption feature similar to that seen in the interstellar extinction curve (Sakata *et al.* 1994). We present here Raman spectra of the QCCs and compare them with various carbonaceous materials to better understand the structure QCC. We find that structure of QCC is different from that of graphite and more similar to carbonaceous material found in some interplanetary dust particles and chondritic meteorites.

1. INTRODUCTION

Quenched Carbonaceous Composites (QCCs) are carbonaceous materials which we believe are good laboratory analogs to the carbonaceous interstellar dust particles. QCCs are produced in low-pressure methane gas which is heated to a high temperature with a microwave generator. A small amount of plasma is ejected into a vacuum through a small orifice and the plasma is quenched onto a room temperature substrate. "Granular QCC" forms at the center of the beam of the plasma, and "dark QCC" mixed with "filmy QCC" on the outside edge of the granular QCC. Dark QCC has a brown-black color, and it has a 220 nm absorption similar to that seen in the interstellar extinction curve. Filmy QCC is light yellow brown in color and is found on the walls of the apparatus surrounding the room temperature substrate. It also shows a broad 220 nm absorption after thermal-alteration by heating to a high temperature (Sakata *et al.* 1994). We present here Raman spectra of QCCs and compare them with those of various carbonaceous materials to better understand their structure and to clarify the origin of the 220 nm absorption.

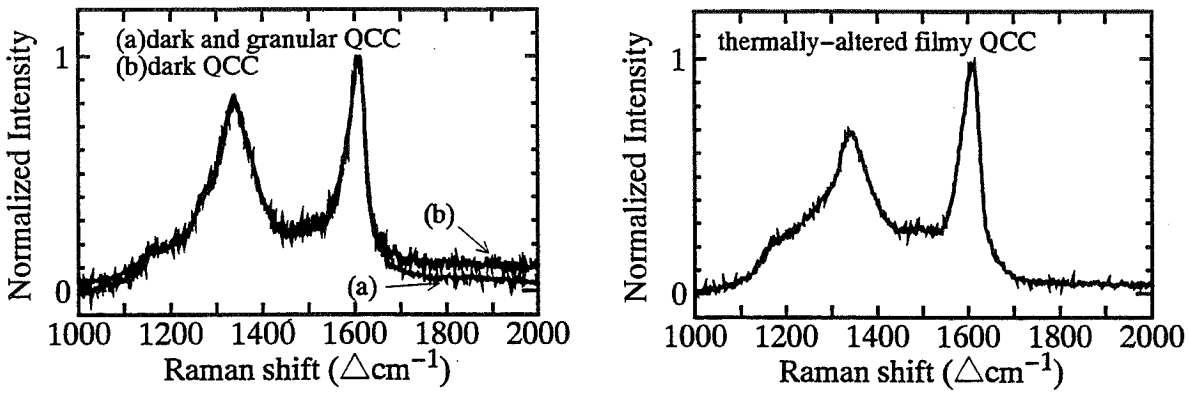

Figure 1. Raman spectra of dark QCCs and filmy QCC heated at 600 C in a vacuum.

2. EXPERIMENTAL DETAILS

We showed the experimental setup for QCC formation in a previous paper (Sakata *et al.* 1994). After washing with acetone to remove the filmy QCC, we measured the uv spectrum and the Raman spectra of the QCCs at two locations of the substrate: (a) The location where the granular QCC and dark QCC were deposited, and (b) The location where the dark QCC was deposited. We also heated the filmy QCC at 600 C in a vacuum cell for 20 min, and we measured its Raman spectrum after cooling it to room temperature. The heating causes the loss of volatile components of the filmy QCC and its structure is thermally altered.

The Raman spectra of QCCs were obtained with a Spex 1877E Triplemate spectrometer that was equipped with a CCD camera. The 514.5 nm line of Ar-ion laser with a power of less than 30 mW was used to excite the samples. The laser beam was spread out by a cylindrical lens to 0.5 by 15 mm in size to illuminate the sample.

3. RESULTS AND DISCUSSION

3.1. UV-Vis spectra

The dark QCC, at the location of (b), shows a peak absorbance at 221 nm. The mixture of both dark QCC and granular QCC, at the location (a) shows a peak absorbance at 224 nm that is broader. Sakata *et al.* (1994) found that the filmy QCC became thermally-altered at the temperature of 500–700 C, and it showed a broad 220 nm absorbance feature.

3.2. Raman spectra

The Raman spectra at locations (a) and (b) are very similar to each other (Fig. 1, left). Each spectrum has two sharp peaks. One is located at 1609–1616 cm^{-1} (g-peak). The other peak is located at 1338–1348 cm^{-1} (d-peak). A small feature is seen around 1160 cm^{-1}. The Raman spectrum of thermally-altered filmy QCC (Fig.

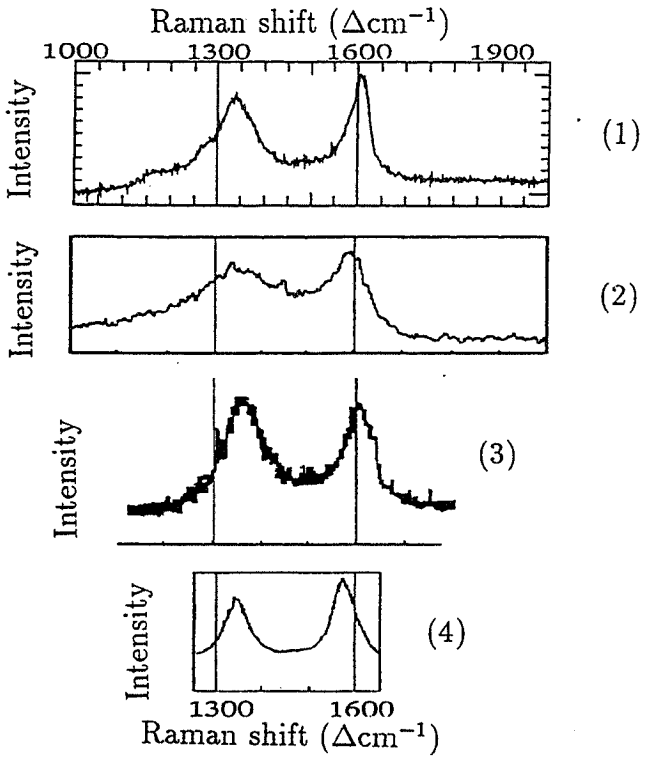

Figure 2. Comparison of Raman spectra of dark QCC to astronomical carbonaceous materials. (1) dark QCC, (2) interplanetary dust particle "Essex" (Allamandola *et al.* 1987), (3) carbon in chondrule rim of Tieschitz H3 chondrite (Michel-Levy and Lautie, 1981), (4) carbon in glass inclusion of Allende meteorite (Makjanić *et al.* 1989). The carbon in (4) is graphitic.

1, right) also shows two peaks having similar wavenumbers to those of dark QCCs. The g-peak is located at 1605–1609 cm^{-1} and the d-peak is located at 1342–1344 cm^{-1}. A small peak around 1160 cm^{-1} is also seen in the spectrum. The ratio of d-peak/g-peak is smaller in the thermally-altered filmy QCC.

By comparison, the Raman spectra of graphite and diamond show a sharp peak at 1580 cm^{-1} and at 1333 cm^{-1}, respectively. Small crystalline graphite shows two peaks at 1580 cm^{-1} (g-peak) and at 1360 cm^{-1} (d-peak). It is reported that the peak height ratio of d-peak/g-peak changes depending on the crystal size (Tuinstra and Koenig, 1970).

When carbonaceous materials are formed from hydrocarbons with heating, the peaks appear at 1600 cm^{-1} and 1350 cm^{-1} and their shapes and their intensity ratios are changed with heating. These are caused by the increase of size of the condensed aromatic ring structures (Ohnishi, 1987). In general, as hydrocarbons are thermally altered by heating (carbonization), hydrogen is expelled, the concentrations of sp and sp^3 sites decrease, and plane clusters of sp^2 sites grow larger in size (Papoular *et al.* 1996).

We compare the Raman spectra of dark QCC to those of astronomical carbonaceous materials in Fig. 2. The g-peak of Raman spectra of the dark QCC is located

in the highest wavenumber region among them. In addition, the shapes of the g- and d-peaks of QCCs are sharp. The ring structure is more developed in thermally-altered filmy QCC because it has a smaller d-peak/g-peak ratio.

Electron micrographs of QCCs indicates that some of the crystalline structure was formed in the center of the granular QCC region and in the dark QCC close to the center. From the Raman peak location, this crystallinity is not caused by micro-graphite, because the Raman peaks do not match up with graphite as mentioned above. Most likely the QCCs have condensed ringed structure with sp^2 bonds because of the similarity of the peak wavenumber of the g-peak of carbonaceous materials formed by heating of hydrocarbons. In addition, in the QCCs these condensed rings are linked chemically with sp^3 bonds because the QCCs are not soluble in organic solvents.

4. CONCLUSIONS

Raman spectra of dark QCC and thermally-altered filmy QCC show distinct peaks at 1340 and 1610 cm^{-1}. The peaks are not characteristic of graphite. Instead, there is a close correspondence to the peaks found in carbonaceous material in some interplanetary dust particles and meteorites. We suggest that QCC materials are a good laboratory analog to the interstellar carbonaceous dust particles because of the close correspondence of the Raman spectrum peaks to extraterrestrial carbonaceous material as well as the correspondence to interstellar infrared emission features, uv absorption, and visible fluorescence (Sakata *et al.* 1984, 1987, 1990, 1992, 1994).

References

Allamandola, L. J., Sandford, S. A., and Wopenka, B. 1987, *Science*, **237**, 56.

Makjanić, J., Touret, J. L. R., Vis, R. D., and Verheul, H. 1989, *Meteoritics*, **24**, 49.

Michel-Levy, M. C., and Lautie, A. 1981, *Nature*, **292**, 321.

Ohnishi, T. 1987, Tanso, **1987**, 81.

Papoular, R., Conard, J., Guillois, O., Nenner, I., Reynaud, C., and Rouzaud, J. -N. *Astr. Ap.*, 1996 in press.

Sakata, A., Wada, S., Tanabe, T., and Onaka, T. 1984, *Ap. J.*, **287**, L51.

Sakata, A., Wada, S., Onaka, T., and Tokunaga, A. T. 1987, *Ap. J.*, **320**, L63.

Sakata, A., Wada, S., Onaka, T., and Tokunaga, A. T. 1990, *Ap. J.*, **353**, 543.

Sakata, A., Wada, S., Narisawa, T., Asano, Y., Iijima, Y., Onaka, T., and Tokunaga, A. T. 1992, *Ap. J.*, **393**, L83.

Sakata, A., Wada, S., Tokunaga, A. T., Narisawa, T., Nakagawa, H., and Ono, H. 1994, *Ap. J.*, **430**, 311.

Tuinstra, F., and Koenig, J. L. 1970, *J. Chem. Phys.*, **53**, 1126.

AUTHOR INDEX

Adamson, A.J. 101, 131
Ageorges, N. 3
Akeson, R. 45
Anderson, C.M. 93

Barge, P. 179
Barlow, M.J. 9, 23, 61
Bierbaum, V.M. 125
Bjorkman, K.S. 27
Blanco, A. 69
Bloemhof, E.E. 81
Boogert, A.C.A. 131
Bottke, W.J. 205
Brandt, J.C. 217
Bregman, J. 41, 121
Brunini, A. 201
Bussoletti, E. 109
Butner, H.M. 13

Carey, S.J. 113, 117
Carlstrom, J. 45, 139
Cecchi Pestellini, C. 109
Chandler, C.J. 139
Chiar, J.E. 131
Clark, F.O. 113, 117
Clayton, G.C. 93
Colangeli, L. 109
Corrigan, C.M. 221
Cuzzi, J.N. 175

Dacles-Mariani, J.S. 175
Dahl, J. 221
Danen, R.M. 81
Desch, S.J. 143
de Winter, D. 33
Dobrovolskis, A.R. 175
Dominik, C. 155
Dunkin, S.K. 23
Duschl, R.J. 3

Egan, M.P. 73

Fischer, O. 37
Flierl, G.R. 183
Fonti, S. 69
Furton, D.G. 105

Gerakines, P.A. 131
Grady, C.A. 19, 27
Gwinn, C.R. 81

Hanner, M.S. 19
Hayashi, H. 227
Henning, Th. 163, 167, 171
Holbrook, J.C. 41
Hollenbach, D.J. 55

Ilin, A.E. 135
Il'in, V.B. 37

Johnstone, D. 55

Kempf, S. 163
Kim, S.H. 93
Klahr, H.H. 171
Krivova, N.A. 37
Kress, M.E. 149
Krüger, D. 77

Larson, K.A. 97
Lee, H.S. 97
Lee, T. 191
LePage, V. 125
Little-Marenin, I.R. 65
Long, M. 221
Lynch, D.K. 19

Mann, I. 209
Martin, P.G. 93
Mehta, A.V. 183
Mennella, V. 109
Miyaoka, H. 227
Mucha, R. 167
Muci, A.M. 69

Nakamura, R. 159

Orofino, V. 69

Padman, R. 139
Palomba, E. 109
Palumbo, P. 109
Parisi, M.G. 201
Pérez, M.R. 27
Petersen, C.C. 217

Pfalzner, S. 163
Price, S.D. 65

Rank, D. 41
Rawlings, M.G. 101
Reaves, G. 209
Richardson, D.C. 205
Richer, J.S. 139
Rotundi, A. 109
Russell, R.W. 19
Ryan, S.G. 23
Ryutov, D. 195

Scherer, K. 209
Schmitt, W. 167
Sedlmayer, E. 77
Shang, H. 191
Shipman, R.F. 73, 113, 117
Shu, F. 55, 191
Siebenmorgen, R. 49
Sitko, M.L. 19
Skinner, C.J. 9, 61
Sloan, G.C. 65, 121
Snow, T.P. 87, 125
Sommeria, J. 179
Speck, A.K. 61
Stepinski, T.F. 187
Supulver, K.D. 195
Svirschevsky, S.B. 213
Sylvester, R.J. 9

Thé, P.S. 33
Temi, P. 37
Tielens, A.G.G.M. 149, 155
Tokunaga, A.T. 227

Valageas, P. 187
van den Ancker, M.E. 33
Visser, A. 139

Wada, S. 227
Walker, H.J. 13
Whittet, D.C.B. 97, 101, 131
Witt, A.N. 87, 105
Wittebron, F.J. 13
Wolff, M.J. 93
Wooden, D.H. 13

Yi, Y. 217

Zolensky, M.E. 221

SUBJECT INDEX

abundances, cosmic 89
accretion 21, 25, 27, 35
AeBe stars 15, 20, 24, 27, 29, 33, 37, 83
AGB stars 67
agglomorates see: fluffy grains
alumina 67
albedo 40, 42
alignment 48, 95
amorphous carbon (HAC, α: C-H) 62, 63, 68, 69, 105, 109, 227
asteroids 205

band gap 106, 111
bipolar outflows 46
λ Bootis stars 24

catalysis 149
chondrules 174, 178, 193, 229
circumstellar disk 4, 9, 13 see also: disk
circumstellar dust 4, 29, 39, 61ff, 73ff, 77ff, 83
circumstellar gas 24, 28
clumps 5, 6, 30, 38, 140
coagulation 98, 155, 159, 163, 168
comets 14, 15, 206, 212, 213, 217
C stars 62, 68, 73, 78

depletion 25, 87, 88
disk 4, 9, 13, 35
disk, model 6, 56, 57, 188
disk, temperature 5
disk, mass 10
disk, mass loss rate 55, 139
dust, charge 144, 174
dust, collisions 144, 156, 164, 197
dust, cometary 212, 213
dust, composition 90
dust, formation 73ff, 77ff, 83
dust, mass 10, 53
dust, models 90
dust, processing 133
dust, rims 193
dust, size 15, 49ff, 77, 79, 83, 94, 98, 157, 159, 163, 170, 173, 177, see also: size sorting
dust, stream 213
dust, temperature 5, 35
dust, velocities 165, 172, 177, 180, 211
dust, zodiacal 209

elemental abundances 89
ERE 105
(Extended Red Emission)
extinction 34, 42, 53, 70, 98, 102, 107, 136, 139
extinction, 3.4μm band 102, 107, 110
extinction, UV 99
extinction, UV bump 69ff, 93, 228

Fischer-Tropsch 149
fluffy grains 40, 49, 113, 118, 135, 155, 160, 164, 168, 192, 207, 221

HII regions 56, 114, 115, 118
high lattitude clouds 97

ice 42, 49, 132, 136, 193, 196
IDP 223, 229
(interplanetary dust particle)
ionization 144, 174
ion-molecule reactions 126ff
imaging, submillimeter 46, 140
imaging, infrared 4, 13, 43, 83, 86ff, 114, 118, 122
IR emission features 10, 15, 20, 121
IR emission, models 9, 50
iron 114, 149

lines CaIIK 24
NaID 24, 35
luminescence 106, see also: ERE

magnetic fields 45, 47
material see: alumina, amorphous carbon, ice, iron, olivine, organic dust, PAHs, SiC, silicate, solid CO
meteorites 69, 193, 224, 229
miras 67

olivine 20, 21, 29
organic dust 29, 101
outflow 43, 46, 56, 192

PAHs 94, 114, 118, 121, 125
PAHs, dehydrogenation 127
PAHs, hydrogenation 124
PAHs, methyl side groups 124
PAHs, reactions 125ff
PAH emission see IR emission features
PDR 56, 57, 121
(photodissociation regions)
β Pic-like stars see: Vega-like stars
planetesimals 21, 30
planetesimal, collisions 202, 205
planetesimal, formation 179, 187, 189, 195

plasma 216, 218
polarization 38, 39, 41, 46, 93ff, 98, 137
porosity 223, see also: fluffy grains
Poynting Robertson force 210

radiation pressure 58, 74, 77, 210
reactions 125ff, 144, 149
reflection nebula 42

scattering 34, 38, 42ff
SiC 61ff, 67, 68
silicate 10, 14, 19, 29, 65
silicate, feature 10, 14, 19, 20, 21, 65, 102, 137
size sorting 173, 176, 180, 192
Smoluchowski equation 159, 168
solar nebula, models 157, 165, 168, 172, 175, 180, 185, 188
solid CO 132
spectral energy distribution 11, 12, 35, 38, 51, 52, 83, 170
stardust 63
(in meteorites)

T-Tauri stars 3, 139
turbulence 173, 175, 179, 183, 196

UIR bands
see IR emission features

variability 3, 21, 27, 33, 39
Vega-like stars, models 9, 13
very small grains 114
vortex 172, 175, 177, 179, 183

Object Index

AB Aur 20

β Cas 15
O Ceti 87
comet de Vico 217
comet Halley 14, 15
comet Hyakutake 212
R CrA IRS 2 132

GL 2136 41
GL 3068 63

HD 35187 24, 26
HD 38238 33
HD 45677 20
HD 98800 10
HD 100546 20, 21, 27, 28
HD 123160 10
HD 139614 25
HD 141569 10
HD 142666 15
HD 144432 10, 15, 24, 26
HD 147933 94
HD 169142 25
HD 188037 15
HD 197770 95
HD 210121 99
HH 100 50

IRAS 02408+1720 63
IRAS 16293-2422 47

Juggler nebula 41

LkHα 101 83
L1489 IRS 132

NGC 1333 46
NGC 2024 140

51 Oph 15, 24
ρ Oph 93
BF Ori 39
UX Ori 20, 39
λ Ori 115
Orion bar 122
Orion KL 47

β Pic 13
Pleiades 118
α PsA 15

Rosette nebula 114

SAO 140789 10
SAO 158350 10
SAO179815 10
SAO 184124 10
α Sco 83

CQ Tau 39

V536 Aql 3
V351 Ori 33
WW Vul 39

W33A 132

ADDRESSES OF PARTICIPANTS

Nancy Ageorges
ESO
Karl Schwarzschildstrasse 2
85748 Garching b. Muenchen
Germany
nageorge@eso.org

Emma Bakes
NASA Ames Research Center
MS 245-3
Moffett Field CA 94035-1000
bakes@dusty.arc.nasa.gov

Rachel Akeson
Caltech
MS-105-24
Pasadena CA 91125
rla@astro.caltech.edu

Betty Baldwin
NASA Ames Research Center
Mail Stop 245-6
Moffett Field CA 94035-1000
baldwin@ssa1.arc.nasa.gov

Anthony Allen
University of California at Berkeley
Cambell Hall
Berkeley CA 94720
allen@amoeba.berkeley.edu

Jorge Ballester
Department of Physics
Emporia State University
Emporia
KS 66801
ballestj@esumail.emporia.edu

Dana E. Backman
Franklin and Marshall College
Physics and Astronomy Dept.
P.O. Box 3003
Lancaster, PA 17604
Dana@astro.fandm.edu

Pierre Barge
C.N.R.S. Laboratoire D'Astronomie Spatiale
BP8 - Traverse du Siphon
13376 Marseille Cedex 12
France
barge@astrsp-mrs.fr

Thomas G. Barnes
McDonald Observatory
University of Texas
Austin
TX 78712
tgb@astro.as.utexas.edu

David Blake
MS 239-4
Nasa Ames Research Center
Moffett Field CA 94035-1000
dblake@mail.arc.nasa.gov

Luann Becker
4826 Lamont Street
San Diego CA 92093
lbecker@ucsd.edu

Armando Blanco
Dipartimento di Fisica
Universita di Lecce
C.P. 193
73100-Lecce Italy
blanco@le.infn.it

Luther Beegle
University of Alabama at Birmingham / Dept. of Physics
310 Campbell Hall
1300 University Blvd.
Birmingham AL 35294-1170
beegle@phy.uab.edu

Dr. Jane Blizard
827 16th St.
Boulder Co 80302

Tom Bernatowicz
Washington University
Campus Box 1105
One Brookings Dr.
St Louis MO 63130-4899
tom@howdy.wustl.edu

Eric Bloemhof
Caltech 105-24
Pasadena CA 91125
eeb@astro.caltech.edu

Max Bernstein
NASA Ames Research Center
Mail Stop 245-6
Moffett Field CA 94035
maxb@ssa1.arc.nasa.gov

Jürgen Blum
Max Planck Society
Research Unit " Dust in Star Forming Regions "
Schiller gasschen 3
D-07745 Jena Germany
blum@astro.uni-jena.de

Peter Bodenheimer
Lick Observatory
University of California
Santa Cruz CA 95064
peter@ucolick.org

Don Brownlee
University of Washington
Astronomy Dept.
Seattle Washington 98195
browmlee@astro.washington.edu

John Bradley
MVA Inc.
5500 Oakbrook Pkwy #200
Norcross GA 30093
jbrad@mindspring.com

Harold Butner
Carnegie Institute
Dept. of Terrestrial Magnetism
5241 Broad Branch Rd.
Washington DC 20015
butner@dtm.ciw.edu

Jesse Bregman
NASA Ames Research Center
Mail Stop 245-6
Moffett Field CA 94035
bregman@ssa1.arc.nasa.gov

Sean Carey
Phillips Laboratory
29 Randolph Road
Hanscom MA 01731
carey@pldac.plh.af.mil

Geoff Briggs
NASA Ames Research Center
Mail Stop 245-1
Moffett Field CA 94035
gbriggs@mail.arc.nasa.gov

Bruce Carney
Department of Physics
University of North Carolina
Chapel Hill NC 27599-3255
bruce@sloth.astro.unc.edu

Ron Brown
6630 Newcastle Ave.
Reseda CA 91335
Ronny@ix.netcom.com

Pat Cassen
NASA Ames Research Center
Mail Stop 245-3
Moffett Field CA 94035
cassen@cosmic.arc.nasa.gov

Claire Chandler
MRAO Cavendish Lab
Madingley Road
Cambridge CB3 OHE
UK
cjc@mrao.cam.ac.uk

Hiram Clawson
107 Meadow Road
Santa Cruz CA 95060
hiram@sco.com

Sherwood Chang
NASA Ames Research Center
Mail Stop 239-4
Moffett Field CA 94035
schang@mail.arc.nasa.gov

Geoffrey C. Clayton
Dept. of Physics & Astronomy
Louisiana State University
Baton Rouge LA 70803
gclayton@rouge.phys.lsu.edu

Connie Chang
Harvard University
002 Quincy Mail Center
Cambridge MA 02138-6609
changcon@cco.caltech.edu

Simon Clemett
Dept. of Physics
Stanford University
Stanford CA 94305-4055
simon@brackett.stanford.edu

Jean Chiar
Physics Dept.
Rensselaer Polytechnic Institute
110 Eighth Street
Troy NY 12180
chiar@charon.phys.rpi.edu

George Cooper
NASA Ames Research Center
Mail Stop 239-4
Moffett Field CA 94035
gcooper@mail.arc.nasa.gov

Rolf Chini
MPI für Radioastronomie
AUF DEM HüGEL 69
D-53121 Bonn
Germany
rchini@mpifr-bonn.mpg.de

Nancy Cox
1065 S. Van Ness #305
San Francisco CA 94110

Dale Cruikshank
NASA Ames Research Center
Mail Stop 245-6
Moffett Field CA 94035
dale@ssa1.arc.nasa.gov

Tony Dobrovolskis
NASA Ames Research Center
245-3
Moffett Field, CA 94035
dobro@cloud9.arc.nasa.gov

Jeff Cuzzi
NASA Ames Research Center
Mail Stop 245-3
Moffett Field CA 94035
cuzzi@cloud9.arc.nasa.gov

Carsten Dominik
Sterrewatch
P.O. Box 9513
NL-2300 RA Leiden
The Netherlands
carsten_dominik@strw.leidenuniv.nl

Louis d'Hendecourt
Baitment + 121
University of Paris
91405 Orsay
Cedex France
ldh@iaslab.ias.fr

Luke Dones
NASA Ames Research Center
Mail Stop 245-3
Moffett Field CA 94035
luke@boombox.arc.nasa.gov

Emmanuel Dartois
Batiment + 121
University of Paris
91405 Orsay
Cedex France
dartois@ias.fr

Sarah Dunkin
Dept. of Physics and Astronomy
University College London
Gower St.
London WC1E 6BT England
skd@star.ucl.ac.uk

Steve Desch
University of Illinios
1011 S. Anderson Street
Urbana IL 61801
desch@astro.uiuc.edu

Michael Egan
Phillips Laboratory
Geophysics Directorate
29 Randolf Rd.
Hanscom AFB MA 01731-3010
egan@pldac.plh.af.mil

Jamie Elsila
Kalamazoo College
BOX 392
Hicks Center
Kalamazoo MI 49001
KO86952@hobbes.kzoo.edu

Marina Fomenkova
Center for Astrophysics and Space Sciences,0111
University of California San Diego
Lajolla CA 92093-0111
mfomenko@ucsd.edu

J.P. Emerson
Dept. of Physics
Queen Mary & Westfield College
Miles End Road
London E1 4NS England
j.p.emerson@qmw.ac.uk

Mark Fonda
NASA Ames Research Center
Mail Stop 239-12
Moffett Field CA 94035
mfonda@mail.arc.nasa.gov

Pantin Eric
Service d' Astrophysique
Ce Saclay
91 191 Gif sur Yvette
France
pantin@sapvxg.saclay.cea.fr

Michael Frenklach
Dept of Mechanical Engineering
University of CA at Berkeley
Berkeley CA 94720-1740
myf@euler.berkeley.edu

Ed Erickson
NASA Ames Research Center
Mail Stop 245-6
Moffett Field CA 94035
erickson@cygnus.arc.nasa.gov

Roy H. Garstang
JILA
University of Colorado
Boulder CO 80309-0440
garstang@aip.org

Sheila Faraco
Av.Celso Garcia Cid
479 Apto 302
CEP 86010-440
Londrina Pr Brasil
sheila%brfuel.bitnet@ubvm.cc.buffalo.edu

Tom Geballe
Joint Astronomy Center
660 N. A'ohoku Place
University Park
Hilo HI 96720
tom@jach.hawaii.edu

Carol A. Grady
Eureka Scientific
9554 Canterbury Riding
Laurel, MD 20723
cgrady@mtolympus.ari.net

Donald Hall
CSU Sacramento
3235 Via Grande
Sacramento CA

John Graham
Carnegie Inst./ Dept. of Terrestrial Magnetism
5241 Broad Branch Rd
Washington, D.C. 20015
graham@jag.ciw.edu

Heather Hauser
Department of Physics and Astronomy
San Francisco State University
1600 Hollaway Ave
San Francisco CA 94132
hhauser@stars.sfsu.edu

Jamison Gray
Millikin University
Dept. of Physics & Astronomy
1184 West Main St.
Decatur IL 62522
JDgray@gnn.com

Thomas Henning
Max Planck Society
Research Unit " Dust in Star Forming Regions "
Schillergaesscheu 2-3
D-07745 Jena Germany
henning@astro.uni-jena.de

Mayo Greenberg
Univ. of Leiden
Huygens Astrophys. Lab
PO Box 9504
2300 RA Leiden The Netherlands
mayo@rulhl1.LeidenUniv.nl

Jarita Holbrook
Univ. of Calif. Santa Cruz
Astronomy Dept.
Santa Cruz CA 95064
charm@ucolick.org

Mike Haas
NASA Ames Research Center
M/S 245-6
Moffett Field
CA 94035
hass@cygnus.arc.nasa.gov

David Hollenbach
NASA Ames Research Center
Mail Stop 245-3
Moffett Field CA 94035
hollenba@warped.arc.nasa.gov

Olenka Hubickyj
NASA/Ames Research Center
M.S. 245-3
Moffett Field, CA 94035
hubickyj@cosmic.arc.nasa.gov

William Irvine
University of Massachusetts
619 Lederle Graduate Res. Ctr.
Amherst, MA 01003
irvine@fcrao1.phast.umass.edu

Doug Hudgins
Chemistry Dept.
Adrian College
Peelle Hall
Adrian Michigan 49221
dhudgins@adrian.adrian.edu

Peter Jenniskens
NASA Ames Research Center
M/S 239-4
Moffett Field
CA 94035
peter@max.arc.nasa.gov

Reggie L. Hudson
Department of Chemistry
Eckerd College
St. Peterburg, FL 33712
hudson@eckerd.edu

Elmar Jessberger
Max Planck Institute
Postfach 103980
D-69029 Heidelberg
Germany
ekj@vampi.mpi-hd.mpg.de

Truell Hyde
Dept. of Physics
P.O. Box 97316
Baylor University
Waco TX 76798-7316
Truell_Hyde@Baylor.edu

David Jewitt
Institute for Astronomy
2680 Woodlawn Drive
Honolulu HI 96822
jewitt@murk.ifa.hawaii.edu

Alexei E. Ilin
Pulkovo Observatory
65/1 Pulkovskoe shosse
St. Petersburg 196140
Russia
alexei@ilin.spb.su

Christine Joblin
CESR
BP 4346
9, Av. du Colonel Roche
31029 Toulouse Cedex FRANCE
christine.joblin@cesr.cnes.fr

Ant Jones
Institute d' Astrophysique Spatiale
Universite` Paris XI- Batiment 121
91405 Orsay Cedex
France
ant@ias.u-psud.fr

Mr. Sascha Kempf
Max-Plank Society
Jenaisome Strasse 7-2
Jena 07747 Germany
kempf@astro.uni-jena.de

Dan Judnick
5702 Calpine Dr.
San Jose, CA 95123-3616

John F. Kerridge
334 El Amigo
Del Mar CA 92014
jkerridge@ucsd.edu

Kay Justtanont
SRON
P.O. Box 800
9700 AV Groningen
The Netherlands
kay@sron.rug.nl

Sang-Hee Kim
Korea Astronomy Observatory
San 36-1, Whaam dong, Yuseong gu
Daejeon, 305-348
South Korea
shkim@hanul.issa.re.kr

Helen L. Kahler
2485 Shoreline Dr.
Apt. 206
Alameda CA 94501
HELEN@mcm.com

Hubert Klahr
c/o MPG-AG "Staub in Sternentstehungsgebieten"
Schillergaesschen 3
D-07745 Jena
Germany
klahr@astro.uni-jena.de

James B. Kaler
Dept. of Astronomy at University of Illinois
103 Astronomy Bldg.
1002 W. Green St.
Urbana, IL 61801
kaler@astro.uiuc.edu

Dave Koch
NASA Ames Research Center
Mail Stop 245-6
Moffett Field CA 94035
koch@icthus.arc.nasa.gov

Monika Kress
NASA Ames Research Center
Mail Stop 245-3
Moffett Field CA 94035
kress@dusty.arc.nasa.gov

Pierre-Olivier Lagage
Service d'Astrophysique, CE Saclay
F-91191 Gif-sur-Yvette
France
lagage@sapvxa.saclay.cea.fr

Natalia Krivova
Astronomical Institute
St. Petersberg University
Stary Peterhof
198904 St. Petersberg Russia
krivov@celest.aispbu.spb.su

Jeff Lannin
Penn State Univeristy
Department of Physics
634 W. Fairmont
State College PA 16801
jsl@phys.psu.edu

Daniel Krüger
Institut fur Astronomie und Astrophysik
PN 8-1
Hardenbergstr. 36
12103 Berlin Germany
D.Krueger@physik.TU-berlin.DE

Kristen Larson
Dept. Physics, Applied Physics, and Astronomy
Rensselaer Polytechnic Institute

Troy NY 12180
kal@charon.phys.rpi.edu

E. Kuehrt
DLR-WS
Rudower Chaussee 5
12489 Berlin
Germany
kuehrt@kuehrt.ws.ba.dlr.de

William Latter
NASA-Ames Research Center
Space Sciences Division
MS 245-3
Moffett Field, CA 94035
latter@dusty.arc.nasa.gov

John Kulander
P.O. Box 70415
Sunnyvale CA 94086

Oliver Lay
1097 Blanche Street #117
Pasadena CA 91106
opl@astro.caltech.edu

Valery Le Page
Campus Box 215
Dept. of Chemistry and Biochemistry
University of Colorado
Boulder CO 80309
vlepage@cuchem.colorado

Vincent Mannings
Dept. of Astronomy
Caltech
MS 105-24
Pasedena CA 91125
vgm@astro.caltech.edu

Jack Lissauer
NASA Ames Research Center
M/S 245-3
Moffett Field CA 94035
jlissauer@cloud9.arc.nasa.gov

Jerry Manweiler
Dept. of Physics & Astronomy
University of Kansas
Lawrence, KS 66045
manweiler@kuphsx.phsx.ukans.edu

Jonathan Lunine
University of Arizona
Lunar and Planetary Lab
Tucson AZ 85721
jlunine@lpl.arizona.edu

Aaron Martin
Physical Science Dept.
Guilford Technical Community College
P.O. Box 309
Jamestown NC 27282
martina@gtcc.cc.nc.us

I. Mann
MPI für Aeronomie
Post Box 20
D 37189 Katlenburg-Lindau
Germany

John Mathis
University of Wisconsin
Dept. of Astronomy
475 N. Charter St.
Madison WI 53706-1582
mathis@madraf.astro.wisc.edu

Vincent Mannings
University College London
Dept. of Physics and Astronomy
Gower St.
London WC1E 6BT England
vgm@astro.caltech.edu

Mark McCaughrean
Max-Plank-Institute for Astronomy
Konigstuhl 17
69117 Heidelberg
Germany
mjm@wpia-hd.mpg.de

Christopher McKay
NASA Ames Research Center
Mail Stop 245-3
Moffett Field CA 94035
mckay@gal.arc.nasa.gov

Allan W. Meyer
M / S 244-30
NASA Ames Research Center
Moffett Field CA 94035
meyer@cygnus.arc.nasa.gov

Anand Mehta
MIT
Room 6-110
77 Massachusetts Ave
Cambridge MA 02139
amehta@mit.edu

John Mihalov
NASA Ames Research Center
Mail Stop 245-3
Moffett Field CA 94035
jmihalov@windee.arc.nasa.gov

Vito Mennella
Observatorio Astonomico di Capodimonte
via Moiariello, 16
80131 Napoli
mennella@astma.na.astro.it

Darrel Moon
Oxnard Comm. College
2610 S. Harbor Blvd. Box 2
Oxnard CA 93035
tomoon@worldnet.att.net

Scott Messenger
Washington University
Campus Box 1105
One Brookings Road
St. Louis MO 63130-4899
scott@ionprobe.wustl.edu

Dave Morrison
NASA Ames Research Center
Mail Stop 200-1
Moffett Field CA 94035
dmorrison@mail.arc.nasa.gov

Michael Meyer
NASA HEADQUARTERS
CODE SL
WASHINGTON D.C. 20546
MMEYER@SL.MS.OSSA.HQ.NASA.GOV

Soma Mukherjee
Physics and Applied Mathematics
Indian Statistical Institute
203, Barrackpore Trunk Road
Calcutta 700 035 India
soma@isical.ernet.in

Michael Mumma
NASA Goddard Space Flight Ctr.
Lab. for Extraterrest. Phys.
Code 693
Greenbelt MD 20771
mmumma@lepvax.gsfc.nasa.gov

Fritz Osell
Leeward Community College- Astronomy Dept.
Pearl City HI 96785
fritz@hawaii.edu

Ryosuke Nakamura
Dept. of Earth & Planetary Sciences
Faculty of Science
Kobe University
Kobe 657 Japan
ryosuke@komadori.earth.s.kobe-u.ac.jp

Tobias Owen
University of Hawaii
3030 Pualei Circle
Honolulu HI 96815
owen@hubble.ifa.hawaii.edu

Doug O'Handley
NASA Ames Research Center
Mail Stop 245-1
Moffett Field CA 94035
dohandley@mail.arc.nasa.gov

Julie Paque
NASA Ames Research Center
Mail Stop 244-11
Moffett Field CA 94035
jpaque@mail.arc.nasa.gov

L. Robert Ochs
The Norwich Free Academy
305 Broadway
Norwich CT 06360
lrochs@snet.net

Mirta Gabriela Parisi
Observatorio Asrtonomico
Paseo Del Bosque S/N
1900 La Plata
Argentina
gparisi@fcaglp.fcaglp.unlp.edu.ar

Elizabeth M. Orosz
Dept. of Physics & Astronomy
University of South Carolina
Columbia SC 29208
eorosz@sc.edu

James G. Peters
Physics and Astronomy Department
San Francisco State University
1600 Holloway Avenue
San Francisco CA 94132
pjpeters@earthlink.net

Pendleton Yvonne
NASA Ames Research Center
M/S 245-3
Moffett Field CA 94035
pendleton@galileo.arc.nasa.gov

Sun Hong Rhie
IGPP/LLNL, L-413
Livermore CA 94550
sunhong@igpp.llnl.gov

Carolyn Petersen
Ulysses Comet Watch
Laboratory for Atmospheric and Space Physics
University of Colorado
Boulder CO 80309
petersen@lyrae.colorado.edu

Derek C. Richardson
CITA, McLennan Labs
University of Toronto
Toronto, ON M5S 3H8
Canada
richards@cita.utoronto.ca

Elisha Polomski
Astronomy Dept.
University of Florida, mSSRB-211
Gainesville, FL 32611
elwood@astro.ufl.edu

Michael Robinson
University of Alabama at Birmingham / Dept. of Physics
310 Campbell Hall
1300 University Blvd.
Birmingham AL 35249-1170
mrobin@phy.uab.edu

Mark G. Rawlings
The Centre for Astrophysics
University of Central Lancashire
Preston
Lancashire PR1 2HE U.K.
m.g.rawlings@uclan.ac.uk

Mars A. Rodrigus
P.O. Box 105
Los Altos CA 94023
MarsARS@aol.com

Gibson Reaves
Department of Physics and Astronomy, MC 1342
University of Southern California
Los Angeles CA 90089-1342
reaves@mizar.usc.edu

Thomas Roellig
NASA Ames Research Center
Mail Stop 245-6
Moffett Field CA 94035
roellig@ssa1.arc.nasa.gov

C.F. Rogers
Desert Research Institute
P.O. Box 60220
Reno NV 89506
fredr@sage.dri.edu

Klaus Scherer
Jet Propulsion Laboratory
MS 301/230
4800 Oak Grove Drive
Pasadena CA 91109
scherer@lism.usc.edu

Farid Salama
NASA Ames Research Center
Mail Stop 245-6
Moffett Field CA 94035
salama@ssa1.arc.nasa.gov

Wolfgang Schmitt
Max Planck Society
Research Unit " Dust In Star Forming Regions "
Schiller gasschen 2-3
07745 Jena Germany
schmitt@astro.uni-jena.de

Scott Sandford
NASA Ames Research Center
Mail Stop 245-6
Moffett Field CA 94035
sandford@ssa1.arc.nasa.gov

Hsien Shang
University of California Berkeley
601 Campell Hall
Berkeley CA 94720-3411
shang@minerva.berkeley.edu

Anneila Sargent
California Institute of Tech.
Dept. of Astronomy
105-24
Pasedena CA 91125
afs@astro.caltech.edu

Russell Shipman
Phillips Laboratory
8 Brook Lane
Sudbury MA 01776

Jeff Scargle
NASA Ames Research Center
Mail Stop 245-3
Moffett Field CA 94305
jeffrey@sunshine.arc.nasa.gov

Ralph Shuping
Box 389
University of Colorado
Boulder, CO 80309
shuping@casa.colorado.edu

Ralph Siebenmorgen
ESA-Villafranca del Castillo
Satellite Tracking Station
P.O. Box 50727
E-28080 Madrid
rsiebenm@iso.vilspa.esa.es

Ted Snow
University of Colorado
CASA- Campus Box 389
Boulder CO 80309
tsnow@casa.colorado.edu

Janet Simpson
NASA Ames Research Center
Mail Stop 245-6
Moffett Field CA 94035
simpson@cygnus.arc.nasa.gov

Angela Speck
University College London
International Hall
Brunswick Square
London WCIN AS England
aks@star.ucl.ac.uk

Michael Sitko
University of Cincinnati
Dept. of Physics, M.L. #011
400 Geology/Physics Bldg.
Cincinnati, OH 45221-0011
sitko@dusty.phy.uc.edu

Tomasz Stepinski
Lunar & Planetary Institute
3600 Bay Area Blvd.
Houston, TX 77058
tom@lpis54.jsc.nasa.gov

Greg Sloan
NASA Ames Research Center
M/S 245-6
Moffett Field
CA 94035
sloan@ssa1.arc.nasa.gov

Sarah T. Stewart
Division of Geological and Planetary Sciences
Caltech 170-25
Pasadena, CA 91125
sstewart@kepler.gps.caltech.edu

Bruce Smith
NASA-Ames Research Center
Theoretical Studies Branch
MS 245-3
Moffett Field, CA 94035-1000
bsmith@warped.arc.gov

Gianni Strazzulla
Osservatorio Astrofisico
Citta Universitaria
I-95125 Catania Italy
gianni@alpha4.ct.astro.it

Kim Supulver
University of California
Lick Observatory
Santa Cruz, CA 95064
supulver@ucolick.org

Alexander Tielens
NASA Ames Research Center
Mail Stop 245-3
Moffett Field CA 94035
tielens@dusty.arc.nasa.gov

Prof. Stanislav Svirschevsky
Head of Dept. of Aerodynamics of Flying Vehicles
Moscow State Aviation Institute
Volokolamskojo shosse, 4
Moscow 125871 Russia
shematov@inasan.rssi.ru

Alan Tokunaga
Institute for Astronomy
2680 Woodlawn Drive
Honolulu HI 96822
tokunaga@galileo.ifa.hawaii.edu

Roger Sylvester
Dept. of Physics and Astronomy
University College London
Gower St.
London WC1E 6BT England
rjs@star.ucl.ac.uk

Gary Toller
General Sciences Corporation
6100 Chevy Chase Dr.
Laurel, MD 20707
toller@tahiti.gsfc.nasa.gov

Nobuya Tajima
Dept. Earth & Planetary Physics
Faculty of Science
University of Tokyo
Tokyo 113 Japan
tajima@geoph.s.u-tokyo.ac.jp

David E. Trilling
Dept. of Planetary Science
Lunar and Planetary Laboratory at Univ of AZ
P. O. Box 210092
Tucson, AZ 85721-0092
trilling@lpl.arizona.edu

Susan Terebey
IPAC 100-22
Caltech
Pasadena CA 91125
st@ipac.caltech.edu

Frederic Trotta
LGGE 54
2c Moliere
BP96 38402
St. Martin HERES FRANCE
trotta@glaciog.grenet.fr

Robert G. Tull
McDonald Observatory
University of Texas
Austin TX 78712
rgt@astro.as.utexas.edu

Gary Walker
1812 N. Quinley Ave
Merced CA 95340

Margaret C. Turnbull
University of Wisconsin
Department of Astronomy
475 N. Charter St.
Madison WI 53706
turnbull@alizarin.physics.wisc.edu

Rens Waters
Astronomical Institute " Anton Pannekoek"
University of Amsterdam
Kruislaan 403
1098 SJ Amsterdam The Netherlands
rensw@astro.uva.nl

Mario van den Ancker
Astronomical Institute " Anton Pannekoek "
University of Amsterdam
Kruislaan 403 NL-1098 SJ
Amsterdam The Netherlands
mario@astro.uva.nl

Stuart Weidenschilling
Planetary Science Ist.
620 N. 6th Ave.
Tuscon AZ 85705-8331
sjw@psi.edu

Setsuke Wada
University of Electro-Communications
2-31-1
Sengoku, Suge, Tama-Ku, Kawasaki-shi
Kanagawa Japan
wada@e-one.uec.ac.jp

Doug Whittet
Dept. of Physics, Applied Physics & Astronomy
Rensselaer Polytechnic Institute
Troy, NY 12180
doug@whittet.phys.rpi.edu

Christoffel Waelkens
Institute for Astronomy
Celestijnenlaan 200 B
B-3001 Leuven (Belgium)
christoffel@ster.kuleuven.ac.be

Francis P. Wilkin
Astronomy Department
University of California
Berkeley CA 94720
fwilkin@astro.berkeley.edu

Darren M. Williams
Dept. of Astronomy and Astrophysics
Penn State
525 Davey Lab
University Park, PA 16802
dwilliams@astro.psu.edu

Stephanie L. Woissol
Millikin University
886 West Wood Street #7
Decatur IL 62522
swoissol@mail.millikin.edu

Donald Wilson
Process Technology and Development
3637 Countrywood Ct.
San Jose CA 95130

Diane Wooden
NASA Ames Research Center
Mail Stop 245-6
Moffett Field CA 94035
wooden@ssa1.arc.nasa.gov

Tommye Wintle
2346 Venndale Ave.
San Jose CA 95124

Dorothy Woolum
CSU Fullerton
Physics Department
Fullerton CA 92634
woolum@legs.gps.caltech.edu

Adolf Witt
Ritter Observatory
The University of Toledo
Toledo
OH 43606
awitt@anwsun.astro.utoledo.edu

Dr. Chillier Xavier
1998 Broadway #1005
San Francisco CA 94109
chillier@chemistry.stanford.edu

Fred Witteborn
NASA Ames Research Center
Mail Stop 245-6
Moffett Field CA 94035
fwitteborn@mail.arc.nasa.gov

David Yu
Student Helper
David_C._Yu@ilanet.org

Michael Zolensky
SN2 NASA
Johnson Space Center
Houston, TX 97058
zolensky@snmail.jsc.nasa.gov

Philip Zell
2126 Plaen View Drive
Iowa City IA 52246
Zell@act.org

REPORT DOCUMENTION PAGE

Form Approved
OMB No. 0704-0188

1. AGENCY USE ONLY *(Leave blank)*	2. REPORT DATE	3. REPORT TYPE AND DATES COVERED
	October 1996	Conference Publication

4. TITLE AND SUBTITLE

From Stardust to Planetesimals: Contributed Papers

5. FUNDING NUMBERS

188-40-01

6. AUTHOR(S)

M. E. Kress, A.G.G.M. Tielens, and Y. J. Pendleton

7. PERFORMING ORGANIZATION NAME(S) AND ADDRESS(ES)

Ames Research Center
Moffett Field, CA 94035-1000

8. PERFORMING ORGANIZATION REPORT NUMBER

A-965145

9. SPONSORING/MONITORING AGENCY NAME(S) AND ADDRESS(ES)

Natinal Aeronautics and Space Administration
Washington, DC 20546-0001

10. SPONSORING/MONITORING AGENCY REPORT NUMBER

NASA CP-3343

11. SUPPLEMENTARY NOTES

Point of Contact: A.G.G.M. Tielens, Ames Research Center, MS 245-3, Moffett Field, CA 94035-1000; (415) 604-6230

12a. DISTRIBUTION/AVAILABILITY STATEMENT

Unclassified - Unlimited
Subject Category 89

12b. DISTRIBUTION CODE

13. ABSTRACT *(Maximum 200 words)*

On June 24 through 26, 1996 a scientific conference entitled From Stardust to Planetesimals was held at the Westin Hotel, Santa Clara, CA coinciding with the 108th annual meeting of the Astronomical Society of the Pacific. This conference was made possible by generous grants from the Astrophysics and Exobiology Programs of the National Aeronautics and Space Administration. This conference brought together 153 scientists from 14 different countries. This is a highly interdisciplinary field where astronomy, physics and chemistry meet. This is reflected in the varied background of the participants. The active participants included astronomers involved in observations of the star formation process and/or interstellar dust, planetary scientists studying cometary or asteroidal bodies or modeling the formation of the Solar System, and chemists and physicists studying astronomical analogs or analyzing material isolated from meteorites in the laboratory. During the course of the meeting, 33 invited and 79 contributed papers were presented. This is a collection of the contributed papers. The invited papers will be published separately by the Astronomical Society of the Pacific as part of their Conference Series.

14. SUBJECT TERMS	15. NUMBER OF PAGES
Stardust, Planetesimals, Star formation	275
	16. PRICE CODE: A12

17. SECURITY CLASSIFICATION OF REPORT	18. SECURITY CLASSIFICATION OF THIS PAGE	19. SECURITY CLASSIFICATION OF ABSTRACT	20. LIMITATION OF ABSTRACT
Unclassified	Unclassified		